Geochronology and geochemistry of rare-element pegmatites from the Superior Province of Canada

Thesis

Geochronology and Geochemistry of Rare-Element Pegmatites from the Superior Province of Canada

A thesis presented for the degree of Doctor of Philosophy

Stephen Raymond Smith BSc. (Hons.)
Royal Holloway, University of London

Department of Earth Sciences
The Open University

November 2001

'Are all these tales such cobwebs and moontalk?'

from *The Jungle Book*,
R. Kipling

Acknowledgements

This project was joint funded by The Open University and Ontario Geological Survey. Firstly, I would like to thank Andy Tindle, Simon Kelley and Fred Breaks for their enthusiastic supervision and for being down to earth.
I acknowledge P. Thurston at the OGS for coordinating the project proposal.
I am also grateful to Rolf Romer for help and discussion with TIMS analyses of columbites at GFZ, Potsdam. LA-MC-ICP-MS analyses of columbites were funded by 'Isotopic Analytical Support' from the Natural Environment Research Council and were performed at NIGL, keyworth. Gavin Foster, Steve Noble and Matt Horstwood are thanked for their help and discussion during columbite analyses at NIGL.
Ray Burgess and Nigel Harris are thanked for taking time to read the thesis and their constructive comments.

Avalon Ventures Ltd., Champion Bear, Emerald Fields Resource Corp. and Houston Lake Mining provided access to surface samples and core material. Thanks must go to Perry, Al, Phil and Dick (EFR) for lots of tequila and laughs in Kenora.
Also in Canada, I'm indebted to Roddy Ornella for keeping me sane in the field and to the Ornella's in Sudbury for being so welcoming and friendly.

At the Open University, I thank Jo Wartho, Sarah Sherlock and Hazel Roberts for their help in the Ar-Ar laboratory. Thanks to Aaron Venables for being a great office mate and his copy of the 'pedants bible' ! My house-mates over the past 3 years have been great fun to live with, Vanessa, Marc, Fred, Yuxing, and the vicarage badgers ....Cheryl, Rick, Yvette, Phil, Trevor, Deborah.
Graham, Rom, Vic, Hannah, Matt, Amy, Retro, Bazza, Kate, Tim, JP, Helen, Glyn, Lee, Charlie, Nicky, Yvonne, Q, Gav, Mike B and Russ have all been good mates.

Many of the Staff at the OU have been a great help at one time or another- CJ, Janet, Holbrook, Liz, Kay, Brian, Mike, John, JT, Andy Lloyd to mention a few.

My parents have given me continued love and support throughout my education and for this I cannot thank them enough.

Special thanks goes to Siobhán, GRAND !

Abstract

The crystallisation age and thermochronology of late- to post-orogenic, rare-lithophile element (Li, Cs, Ta) pegmatites that are chemically associated with peraluminous granites have been determined from U-Pb TIMS and LA-MC-ICP-MS analyses of columbite-tantalite, and UV-laser $^{40}Ar/^{39}Ar$ analyses of mica.

In the northwest Superior Province, U-Pb ages reveal that the Pakeagama Lake pegmatite crystallised at 2673 ±8Ma. Rare-element pegmatites in the western Superior Province yield crystallisation ages of 2649 ±4Ma and 2644 ±8Ma for the Separation Rapids group, and 2665 ±10Ma for the Mavis Lake group, showing that they are temporally associated with adjacent peraluminous granites. Replacement zones of columbite-tantalite grains from the pegmatites show disturbance to the U-Pb system, probably caused by interaction with residual fluids and sub-solidus metasomatic processes that lasted for ~30Ma after crystallisation.

Mica from rare-element pegmatites is characterised by distinct compositional zoning with muscovite cores and F-, Li- and Rb-rich zinnwaldite/lepidolite rims. The zinnwaldite/lepidolite rims that replace the original muscovite were most likely precipitated from a residual melt or fluid phase during the late-magmatic to hydrothermal period of pegmatite formation.

Within these micas, $^{40}Ar/^{39}Ar$ apparent ages young towards the grain boundary and also towards the core - rim boundary, which suggests that the compositional zones form separate argon diffusion domains. However, similar $^{40}Ar/^{39}Ar$ apparent ages are found within F-rich zinnwaldite/ lepidolite and coexisting muscovite indicating that diffusion rates may be comparable.

Mica from rare-element pegmatites of the Superior Province yield intra-grain $^{40}Ar/^{39}Ar$ apparent age variations of up to 800Ma within single crystals. Theoretical slow cooling models do not match the measured $^{40}Ar/^{39}Ar$ profiles and cannot account for the large apparent age variations. Thermal history models that produce the best fit to apparent age profiles include two re-heating events; a minimum 350°C re-heating at ~2450Ma and *circa* 300°C re-heating at 1850Ma, both for a period of at least 10Ma. These apparent ages are concordant with two major Proterozoic events affecting the Superior Province; intrusion of the Matachewan - Hearst dyke swarms and the Trans Hudson Orogeny, respectively.

Contents

1. Geology of the Superior Province

1.1 Introduction

The Superior Province forms a large proportion of the Precambrian shield of North America (figure 1.1) and is the largest single Archæan craton in the world, covering an area of 1.6 million km^2. The craton is exposed mostly within the province of Ontario, although it stretches from Quebec in the NE, to Manitoba in the west and to Minnesota (U.S.A.) in the south.

Topographically, the Superior Province is typified by low relief features. The region has relatively low elevation, less than 500m above sea level, although the craton itself is uplifted and generally more resistant than the surrounding borderlands. Major drainage features include Hudson Bay and James Bay to the north, and the Great Lakes and St. Lawrence River to the south and east. In Ontario, the craton has been divided into three geographic areas, namely the northwestern, western and southern Superior Province, displayed in figure 1.2.

The Archæan sequences of the northwest and western Superior Province are unconformably overlain by Lower Palaeozoic strata of the Hudson Bay Lowland to the northeast. The southern Superior Province is the region to the east of Lake Superior and includes the Sudbury hills of the Proterozoic Penokean Orogeny. The Laurentian Highlands form the southernmost part of the Canadian Shield, a slightly elevated region that is unconformably overlain by Palaeozoic cover sequences to the south.

Boreal Forest dominates the landscape in the Superior Province along with numerous lakes and rivers. Black Spruce grows in poorly drained areas, whereas jack pine is more prevalent in dryer sandy soils. Deciduous species include white birch and poplar, often seen along lake shores and growing on glacial deposits. Forest fires have led to large areas of the western Superior Province regenerating with thick young jack pine (Stone 1998). Quaternary glaciation has played a key role in shaping the landscape of Ontario. Twenty thousand years ago, the Laurentide Ice Sheet covered much of Canada and extended into the northern U.S.A. (Barnett 1991). Glaciers have removed pre-existing soils and sediment, smoothed bedrock surfaces and are responsible for many landforms.

- *Fieldwork and current mining activity*

Detailed mapping and sample collection of rare-element pegmatites and associated granites for this project was carried out during the summers of 1998 and 1999 as part of the continuing collaboration between The Open University and Ontario Geological Survey. Much of the Superior Province in Ontario is accessible by Highway and forestry tracks as far north as the town of Red Lake. North of Red Lake, in the northwestern Superior Province, access in the summer is only possible by float plane or helicopter. Fieldwork in the Pakeagama Lake and Favourable Lake areas was done from tent camps established on lakes and re-supplied by float equipped aircraft (bush planes) from Red Lake. Boats and canoes were used to access exposures along lake shores. In addition, extensive stripping and high-pressure jet washing of key exposures was undertaken to remove shallow soils and organic material which obscured important parts of the pegmatites.

In the Separation lake area, near the town of Kenora, Ontario, the discovery and documentation of the Separation Rapids pegmatite field has been led by Breaks and Tindle (1993, 1994, 1996, and 1997). In recent years, several junior mining companies have undertaken surface stripping and associated exploration activities, recognising the regions high economic potential. Individual dykes have been assayed for rare-element concentration and drilling projects have ascertained subsurface continuation of dykes and ore quantities.

Mining companies involved in the development of the Separation Rapids pegmatite field are Avalon Ventures Limited, Champion Bear Resources and Emerald Fields Resource Corporation. At Pakeagama Lake, in the northwestern Superior Province, Houston Lake Mining currently hold the claim block containing the main exposure of the pegmatite. Detailed reports on the exploration history and economic potential of the Separation Rapids pegmatite group are available in Breaks *et al.* (1999b), Breaks and Tindle (*in press*) and on the Pakeagama Lake pegmatites, Breaks *et al.* (1999a).

- *Litho-tectonic domains of the Superior Province*

The mid- to late-Archæan Superior Province is divided into several subprovinces (figure 1.3). These subprovinces are defined as individual litho-tectonic domains with varying lithologies, structural attributes and tectonic setting.

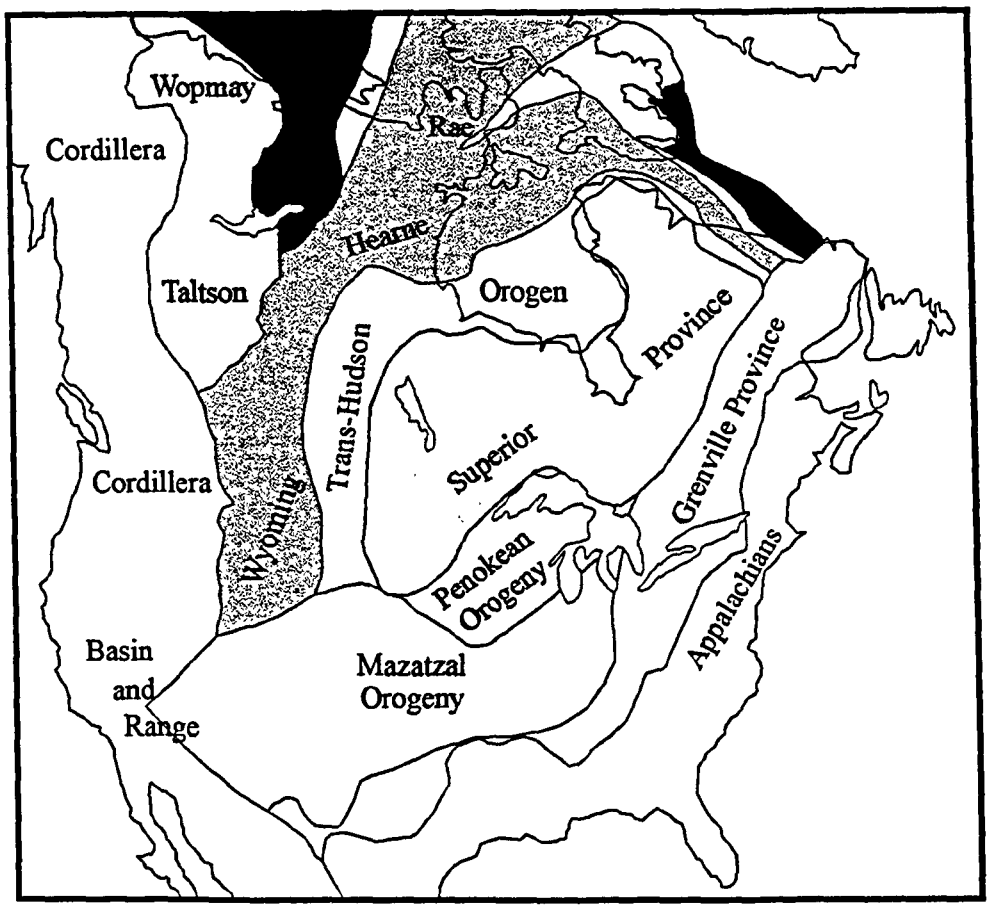

Figure 1.1 Simplified tectonic map of North America. Note the Archæan terrains are separated by Proterozoic orogens. These form the Precambrian Shield against which outlying Phanerozoic terrains were accreted. After Hoffman (1989).

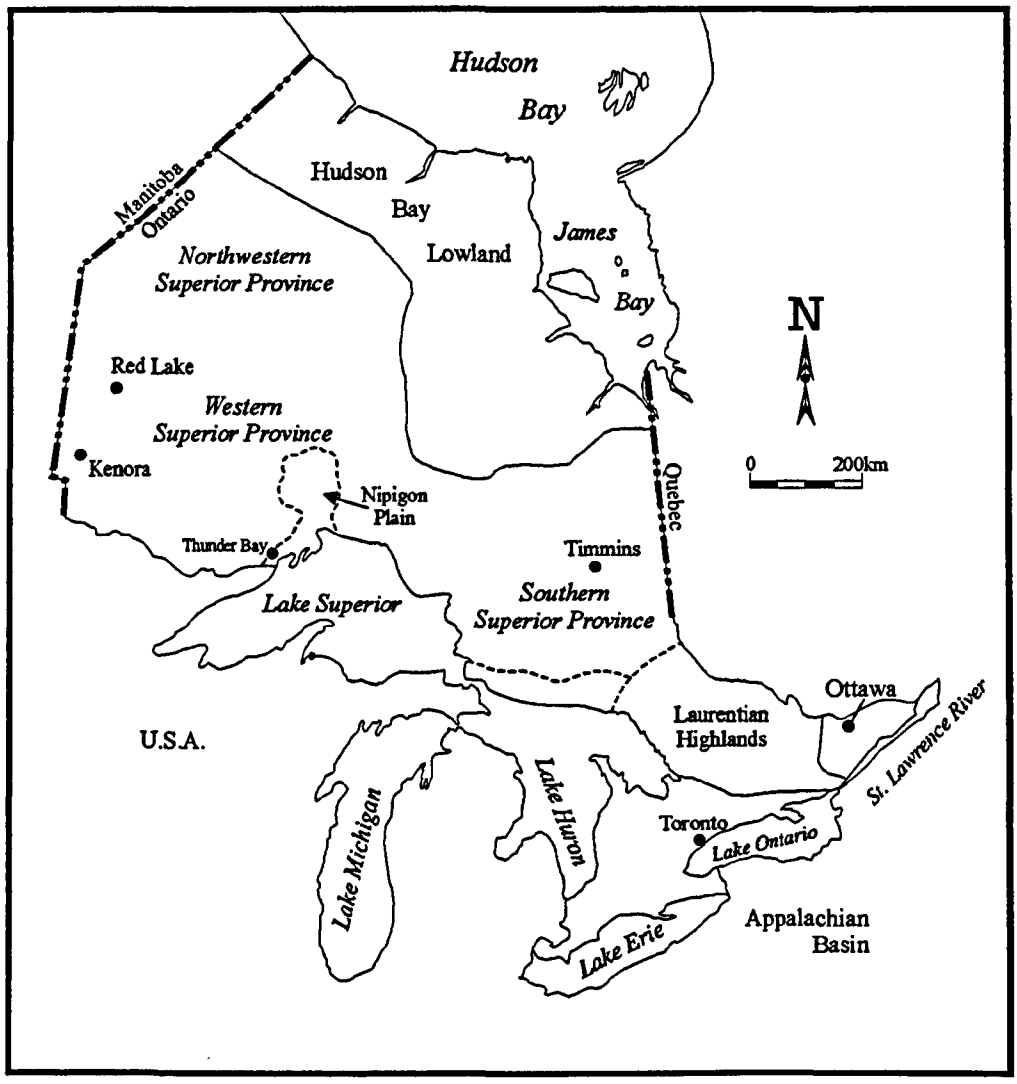

Precambrian Canadian Shield

Phanerozoic Borderlands

Figure 1.2 Map of Ontario showing the geographical regions of the Superior Province and surrounding borderlands. After Thurston et al. (1991).

A comprehensive summary of the Superior Province is provided by the Ontario Geological Survey, Special Volume 4 - Geology of Ontario, to which the reader is referred for detailed information.

- *Rare-element pegmatites*

Pegmatites are distinguished from other intrusive rocks primarily by their coarse grain size (centimetre to metre scale), but perhaps more importantly by internal heterogeneity. Common features include abrupt variations in grain size, mineralogy and textures. Granitic pegmatites are by far the most common composition, and of these, the rare-element class display the most diversified structures and compositions (Cerný 1992). Rare-element pegmatites are characterised by exotic mineralogy e.g. lithium aluminosilicates (petalite, spodumene), Nb-Sn-Ta oxides, and a highly evolved chemical composition enriched in rare-lithophile elements such as Nb, Y, F, Li, Cs and Ta. These complex intrusive bodies are associated with peraluminous granites and are commonly found within upper greenschist to cordierite-amphibolite facies rocks (Cerný 1991).

The aim of this chapter is to discuss the regional geology and tectonic setting of subprovinces/terrains that host rare-element pegmatites in the Superior Province. The approach taken here is to describe the relevant subprovinces/terrains i.e. those from which rare-element pegmatites have been sampled, within the framework of the Superior Province.

1.2 Northwest Superior Province

The original subdivision of the northwest Superior Province was proposed by Card and Ciesielski (1986). These authors delineated a greenstone-rich domain, the Sachigo Subprovince in the north, and a region dominated by granitoid plutons, the Berens River Subprovince, further south. However, Thurston *et al.* (1991) revised this model and provided a terrain analysis based on newly available geochronology, reconnaissance mapping and the use of regional scale shear zones as boundaries. As such, the northwest Superior Province is divided into 7 terrains separating areas of differing age, litho-stratigraphic association and structural trends (figure 1.3). In this

section; much of the discussion regarding pre 2.7Ga lithologies and tectonic interpretation is a summary of the work of Thurston *et al.* (1991) and Stone (1998).

The North Caribou Terrain is composed of 2.9Ga sandstone and carbonate platform sequences deposited on older volcanic arc assemblages, including the Favourable Lake and North Spirit Lake greenstone belts. Thurston *et al.* (1991) reported that other terrains of the northwest Superior Province are characterised by 2.8Ga tonalitic plutons and greenstone belts that record 300Ma of geological history over the period 3.0Ga to 2.7Ga. These terrains were all accreted to the North Caribou Terrain by at least 2700Ma to form the stable cratonic nucleus, against which further volcanic arc terrains formed the Superior Province. Examples include the Island Lake Terrain and the Pickle Terrain (figure 1.3), both interpreted as volcanic arcs accreted to the North Caribou Terrain on the north and south margin, respectively. The present study is concerned with the evolution and tectonic interpretation of the North Caribou Terrain: in particular, the Favourable Lake and North Spirit Lake greenstone belts, which are found along the Bear Head Fault Zone (figure 1.4).

- *Favourable Lake greenstone belt*

The Favourable Lake greenstone belt is composed of komatiite lavas of the Setting Net assemblage interpreted as oceanic volcanism at 2926 ±2Ma (Corfu and Ayres 1991). Younger sequences include shallow water sediments and andesitic strata typical of a volcanic arc setting, the 2870Ma +8/-2Ma (Corfu and Ayres 1991) South Trout assemblage. Corfu and Ayres (1991) also describe the pillow basalts and turbidite fan deposits of the youngest, 2725Ma, North Trout assemblage. In the western arm of the Favourable Lake greenstone belt, the Gorman assemblage contains quartz arenites and argillaceous units correlative with the Setting Net assemblage, possibly representing a >2800Ma platform sequence (Thurston *et al.* 1991).

Stone (1998) has delineated peraluminous two-mica granites within the western arm of the Favourable Lake greenstone belt. More detailed field investigation by Breaks *et al.* (1999a) revealed the presence of rare-element pegmatites (figure 1.4) containing accessory garnet, tourmaline and molybdenite. These are termed the Severn River pegmatites, consisting of small boudinaged dykes with a maximum width of 10m. Typical textures include blocky K-feldspar crystals (30cm diameter) and radial quartz - tourmaline intergrowths.

- *North Spirit Lake greenstone belt*

Ultramafic to felsic volcanic rocks and abundant metasedimentary sequences characterise the North Spirit Lake greenstone belt. These are divided into several assemblages, which include some of the oldest supracrustal rocks in the Superior Province (Thurston *et al.* 1991). The 3023 ±2Ma (Nunes and Wood 1980) North Spirit assemblage is comprised of mafic flows, ironstones and felsic pyroclastics. Structural relations between assemblages are unclear and often equivocal; the Nemakwis assemblage and the Makataiamik assemblage contain basal conglomerates, quartz arenites, mudstones and marbles suggesting a submarine platform depositional setting. Corfu and Wood (1986) report that the source of sediments in the North Spirit Lake greenstone belt was older than 2980Ma, based on detrital zircon ages. The Bijou Point assemblage is the youngest sequence, comprising fluvial sediments and volcanic units of possible shoshonitic affinity, dated at 2731 ±2Ma (Corfu *et al.* 1998).

Stone (1998) describes the North Spirit Lake greenstone belt as being located between the Bear Head Fault to the northwest and an unnamed shear zone to the southeast. Figure 1.4 shows that these fault zones curve and dissipate within the vicinity of the greenstone belt. Stone (1998) also describes a series of *en echelon* fault splays, internal to the greenstone belt. It is evident that the greenstone sequences may represent a pull-apart basin resulting from the dextral strike-slip movement of these two transcurrent faults. However, the earliest age of movement on the Bear Head Fault is unknown and may post date the deposition of several assemblages in the North Spirit greenstone belt.

Peraluminous granites are intruded into the highly attenuated western and northwestern arms of the North Spirit Lake greenstone belt. These are located at Margot Lake and Pakeagama Lake, respectively (figure 1.4). Primary muscovite and accessory garnet are rare within the Margot Lake pluton indicating a moderately peraluminous composition. A monazite U-Pb age of 2697 ±2Ma obtained for the Margot Lake pluton, has been interpreted as the age of crystallisation of the peraluminous suite in the North Caribou Terrain (Corfu and Stone 1998a).

The Pakeagama Lake pluton is a peraluminous granite (2 x 15km) containing accessory garnet and tourmaline (Breaks *et al.* 1999a). The pluton is moderately sheared and displays a granoblastic texture induced by deformation and recrystallisation associated with the closely situated Bear Head fault zone. The pluton is also the likely

parent granite to the Pakeagama Lake rare-element pegmatite, based on overlapping K/Rb feldspar compositions and mineralogical similarities (Breaks *et al.* 1999a).

- *Tectonic interpretation*

The evolution of the North Caribou microcontinent began with the development of primitive oceanic arcs and the extrusion of the 3023Ma North Spirit assemblage. Partial melting of subducted oceanic crust produced tonalitic magmas intruded at around 3000Ma Thurston *et al.* (1991). The intrusion of tonalite magmas into the oceanic arcs caused the arcs to become larger, more buoyant and rigid. The arcs were thus able to resist subduction and form a basement on which platform sediments were deposited, such as the <2986Ma Nemakwis assemblage (Corfu and Wood 1986).

This new tectonic element was different to the simple conveyor belt process of pre- 3Ga times when oceanic crust was produced rapidly, transported and subducted at primitive arcs (Thurston *et al.* 1991). Microcontinental fragments acted as stable buttresses, against which volcanic arc material could be accreted to the margins. Lateral crustal growth continued via accretion of other microcontinental fragments; and vertical growth occurred with the intrusion of large batholiths such as the 2925Ma tonalite intrusion of North Spirit Lake (Stevenson 1995). At this stage (~2.9Ga), continental growth changed from dilation of arcs into continental fragments, to accretion of fragments to form the North Caribou microcontinent (Stone 1998).

The large North Spirit - Favourable Lake greenstone chain developed as an arc-trench environment at a continental margin pre- 2.9Ga, which may have been an early suture zone (Stone 1998). This is a major greenstone chain that was long-lived with episodic volcanism at 2870, 2858 and *circa* 2734Ma (Corfu and Stone 1998a). The Favourable Lake and North Spirit Lake greenstone belts are thus a complex structure which are not well understood, but may be interpreted as a back arc basin and perhaps one of the last microcontinental boundaries to close (Stone 1998).

After 2.8Ga, growth of the North Caribou Terrain was achieved by the development of continental margin magmatic complexes as opposed to earlier accretion of microcontinental fragments and ocean basins (Stone 1988). This is also recognised in the source of tonalite magmatism, as post 2.8Ga tonalite and hornblende suites were derived from melting of basaltic underplate rather than from melting of subducted slab as was the case prior to 2.8Ga (Stone 1988).

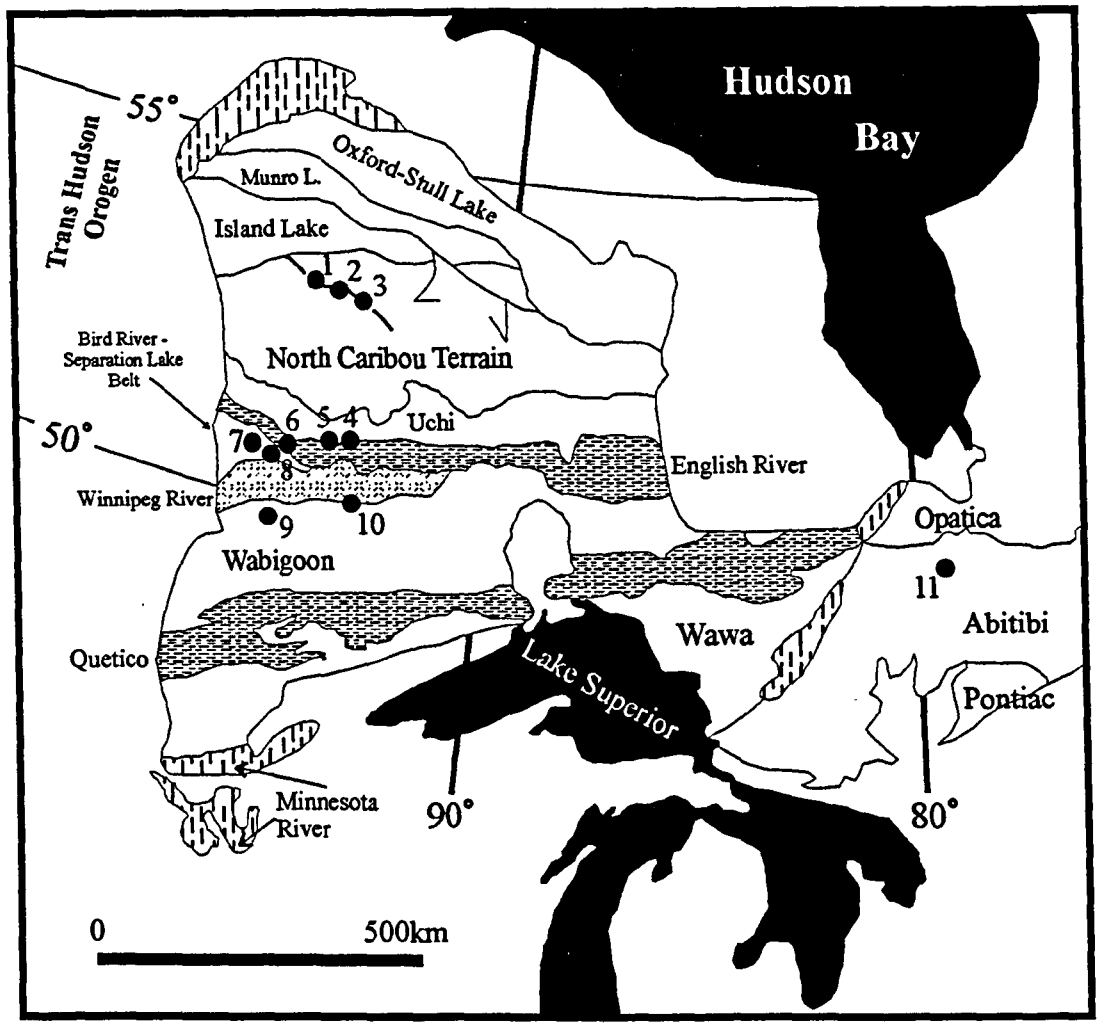

Archæan Subprovince type

- Plutonic
- Granite-greenstone
- Metasedimentary
- High-grade gneiss

Peraluminous granites and pegmatites sampled;

1. Severn River pluton and pegmatite.
2. Pakeagama Lake pluton and pegmatite.
3. Margot Lake pegmatite.
4. Wenesaga pegmatite.
5. Sandy Creek pegmatite.
6. Treelined Lake pegmatite.
7. Skidder pluton.
8. Separation Rapids pluton and pegmatite group.
9. Graphic Lake pegmatite.
10. Ghost Lake batholith and Mavis Lake pegmatite group.
11. Case pegmatite.

Figure 1.3 Location of peraluminous granites and pegmatites discussed in the text. Subprovinces of the Superior Province are from Card and Ciesielski (1986); Thurston et al. (1991).

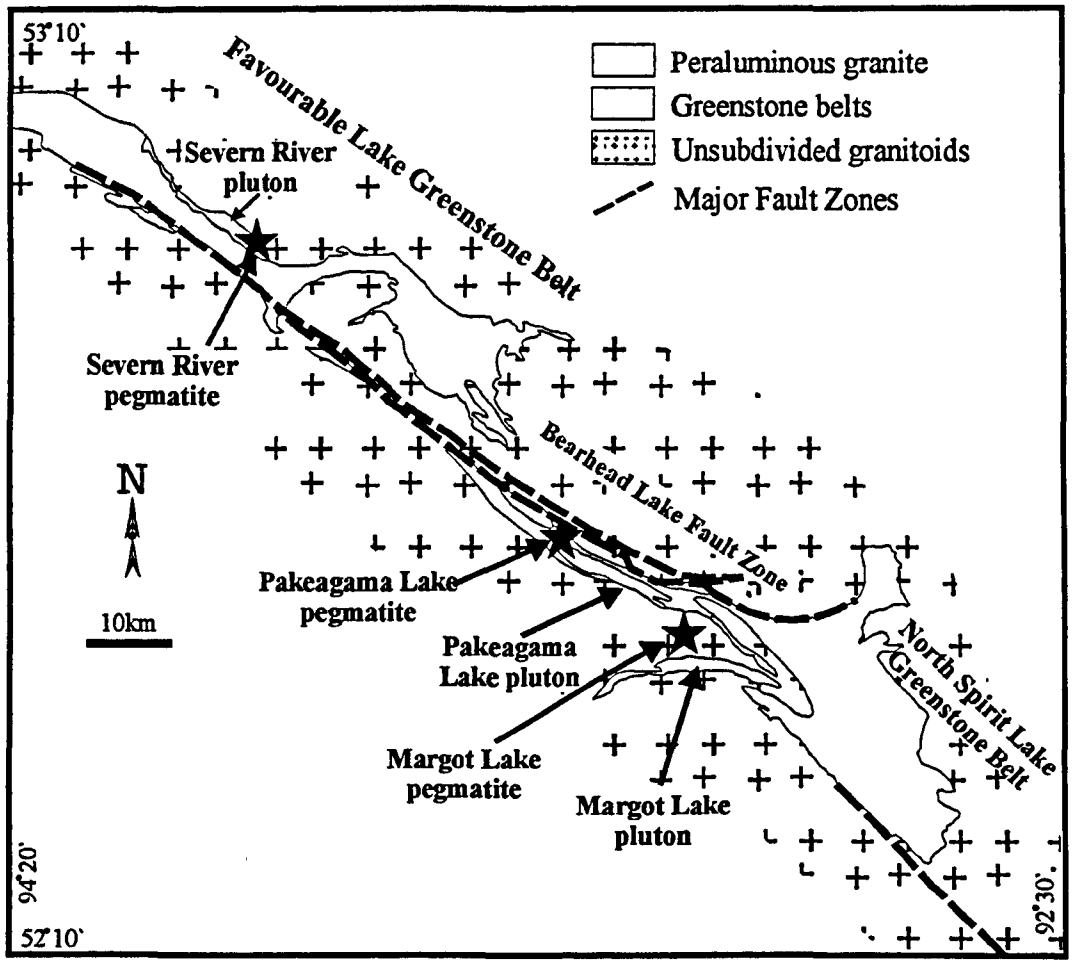

Figure 1.4 Part of the North Caribou Terrain within the NW Superior Province showing the locations of peraluminous granite plutons and associated rare-element pegmatites in relation to greenstone belts and the Bearhead Lake fault, a dextral sense shear zone (after Breaks et al. 1999).

Following collision of microcontinents (*circa* 2.9Ga) and the change to continental margin magmatism after 2.8Ga, subduction along the southern margin of the North Caribou continent produced volcanic assemblages dated at 2750 - 2735Ma (Corfu and Stone 1998a). This marks the time when a back arc basin opened in the North Spirit - Favourable Lake area due to extensional forces, perhaps created by a steep angle of subduction (Stone 1998).

Volcanic activity in the back-arc basin ceased during the period 2735 - 2725Ma as compressional regimes took over, resulting from collision with the Winnipeg River continent to the south (Stone 1988). Intrusion of intermediate to felsic plutonic magmas into the North Caribou Terrain was followed closely by collision related trans-tensional strike-slip faulting, marked by deposition of the Bijou Point assemblage sediments at 2731Ma (Corfu *et al.* 1998).

Voluminous hornblende granite and biotite granite melts were emplaced during the period 2725 - 2697Ma (Corfu and Stone 1998a). This marked the end of subduction as magmas became increasingly assimilated with crustal material. Emplacement of the LILE and LREE enriched 'sanukitoid' suite between 2700 - 2686Ma represents the final mantle derived magmas, enriched in LILE such as K, Rb, Sr from a metasomatised mantle wedge (Corfu and Stone 1998a).

The transition from mantle derived magmas to crustal melting occurred after subduction terminated at approximately 2700Ma (Stone 1998). Crustal thickening was induced by compressional tectonic forces and displacement was taken up along major shear zones such as the Bear Head fault. Metamorphism and partial anatexis of supracrustal sequences generated suites of peraluminous granites and rare-element pegmatites during the final stages of orogenesis. As discussed by Corfu and Stone (1998a), the spatial association of the peraluminous suite with sedimentary assemblages suggests that anatexis of the latter could provide the source of the peraluminous suite. Indeed, Sylvester (1998) suggested that such Archæan sandstone - siltstone sequences are feasible protoliths of peraluminous granites.

Constraints on the post-magmatic thermal evolution of the felsic plutonic domains of the North Caribou Terrain are given by U-Pb titanite and apatite. Ages between 2660 - 2630 are interpreted as the timing of retrogressive growth of titanite and disturbance to apatite U-Pb systematics from localised re-heating and/ or fluid movement ages (Corfu and Stone 1998b).

1.3 Western Superior Province

The western Superior Province is loosely defined as the area north of Lake Superior. From north to south this includes the Uchi, English River, Bird River, Winnipeg River, Wabigoon, Quetico and Wawa Subprovinces (figure 1.3). The Uchi Subprovince is a greenstone-rich domain comprising 3.0 - 2.7Ga metavolcanic - metasedimenatry sequences intruded by granitoid batholiths (Card and Ciesielski 1986). To the south, the English River Subprovince is composed predominantly of high-grade clastic metasediments and derived migmatites formed at approximately 2.7Ga (Breaks 1991). The Bird River Subprovince is a *circa* 2.7Ga greenstone domain located along the English River - Winnipeg River Subprovince boundary (Beakhouse 1991). Tonalite gneiss and granitoid plutons with ages in the range 3.1 - 2.8Ga are the main lithologies of the Winnipeg River Subprovince (Beakhouse 1991). Blackburn *et al.* (1991) have described the Wabigoon Subprovince, characterised by two regions with broad expanses of greenstone belts, separated by a dominantly granitoid central region. The Quetico Subprovince is a 2.7Ga metasedimentary terrain composed of detrital volcanic material from the adjacent Wawa, Wabigoon and Abitibi Subprovinces (Card and Ciesielski (1986).

A detailed multi-disciplinary study of these terrains has recently been undertaken by the Lithoprobe Transects (Harrap and Helmstaedt 1995; 1999), involving geophysical, geochemical and bedrock mapping techniques. In the present study, samples have been collected from the English River, Bird River, Winnipeg River and Wabigoon Subprovinces in the western Superior Province.

1.3.1 English River Subprovince

The English River Subprovince (ERS) is an 800km long, 50km wide, E-W trending linear belt composed mainly of clastic sedimentary rocks and derived high-grade migmatites (Breaks 1991). The ERS can be traced from Lake Winnipeg in Manitoba to the James Bay Lowlands in the east, where it is unconformably overlain by Phanerozoic sequences (figure 1.3). The width of the English River Subprovince narrows to 1.5km where the NE striking Miniss River fault intersects with the NW striking Pashkokogan fault zone. The contact with the granite-greenstone Uchi Subprovince to the north is marked by the Sydney Lake-Lake St. Joseph fault in Ontario

(figure 1.5). To the south, the boundary is locally defined by greenstone belts of the Wabigoon Subprovince in the west and the Bird River Subprovince to the east. Between these two areas, metasediments of the English River Subprovince lie in juxtaposition with the tonalites of the Winnipeg River Subprovince (WRS) suggesting a complex tectonic boundary (Breaks 1991).

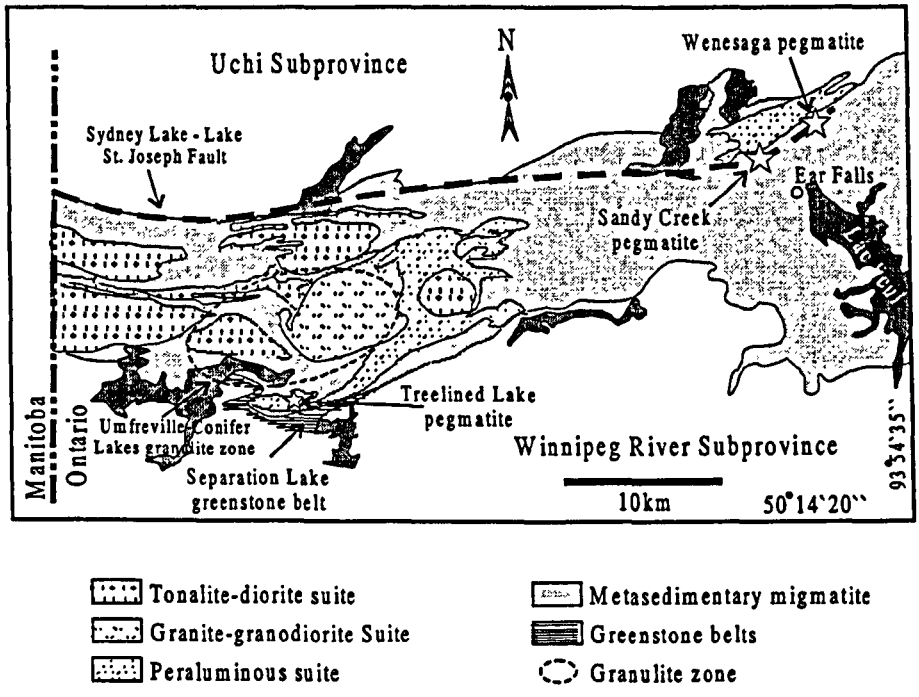

Figure 1.5 Simplified geological map of the English River Subprovince and adjacent Separation Lake greenstone belt, showing the location of the Wenesaga, Sandy Creek and Treelined lake pegmatites. After Breaks (1991).

- *Lithologies*

Supracrustal sequences make up approximately 60% of the English River Subprovince and consist of metamorphosed greywacke and mudstone. These metasediments were interpreted as turbidites deposited in a submarine fan environment, with a provenance from dacite volcanic sequences in the adjacent Uchi Subprovince (Breaks 1991). The timing of sedimentary deposition in the ERS is constrained by detrital zircon U-Pb ages, Corfu *et al.* (1995) suggest that the main assemblages were deposited in the period 2720 - 2700Ma.

Plutonic suites within the ERS include a diorite - tonalite - granodiorite suite with ellipsoidal exposure shapes and long axes oriented E-W, parallel to the regional deformation fabric (Breaks 1991). The Fletcher Lake batholith is an example of the diorite - tonalite - granodiorite suite (figure 1.6). Geochemically, these plutons have

characteristics of 'sanukitoids' i.e. LILE and LREE enriched with elevated Mg and Cr, interpreted as being derived from metasomatised mantle (Stern and Hanson 1991). U-Pb zircon ages for the diorite - tonalite - granodiorite suite plutons indicate a 2698 ±2Ma age of crystallisation (Corfu *et al.* 1995).

A peraluminous granite suite forms approximately 10% of the ERS, recognised by a distinctive assemblage containing two micas (muscovite and biotite) with accessory minerals including garnet, cordierite, sillimanite, and tourmaline (Breaks 1991). The combination of these minerals produces Al_2O_3/ ($CaO + Na_2O + K_2O$) or A/CNK ratios >1, typical of peraluminous granites, using the classification of Sylvester (1998). The Churchill Lake batholith (2200km^2) is the largest example of the peraluminous granite suite. Corfu *et al.* (1995) report a crystallisation age of 2692 ±2Ma (U-Pb monazite) for peraluminous suite rocks in the eastern Lac Seul region. However, numerous dykes, stocks and small peraluminous batholiths are emplaced along the subprovince boundary zones within low- to medium-grade metasediments. This localised magmatism continued until *circa* 2669Ma (Corfu *et al.* 1995).

The Treelined Lake granite is an irregular shaped peraluminous intrusion centred on the Umfreville-Conifer Lakes granulite zone (Pan and Breaks 1997). A prominent apophysis of the Treelined Lake granite outcrops to the southwest of the main mass, along the boundary with the Separation Lake greenstone belt (figure 1.6). Breaks (1991) described complex enclaves or "clots" of sillimanite + cordierite + biotite ± garnet ± plagioclase, within the Treelined Lake granite, interpreted as restite material from a pelite protolith. Pan and Therens (1997) calculated that the Treelined Lake granite was generated from 30 - 60% partial melting of the ERS metasediments with a garnet, cordierite, sillimanite residue, indicating melting at a mid-crustal depth. Partial melting of ERS metasediments is thought to be an indirect result of intrusions such as the Fletcher Lake batholith, which could have supplied a heat source great enough to induce anatexis (Pan and Therens 1997).

A number of peraluminous granites and rare-element pegmatites occur along the boundary zones of the English River Subprovince, which are the chemically evolved derivatives of the peraluminous granite suite (Breaks 1991). The granites occur as small plutons and dykes in low- to medium-grade greenstone belts immediately adjacent to the metasedimentary migmatites of the English River Subprovince. In the western portion of the English River Subprovince, the Wenesaga Lake stock outcrops along the Sydney Lake - Lake St. Joseph Fault Zone along the northern boundary of the ERS with

the Uchi Subprovince. Spatially associated with the Wenesaga Lake stock are a field of pegmatites including the Wenesaga pegmatite and Sandy Creek beryl type pegmatite (figure 1.5).

- *Structural Geology*

The structural analysis of the English River Subprovince by Breaks (1991) provides a synthesis of regional events. Regional mineral foliation trends towards the east, often dipping sub-vertically. The migmatites of the English River Subprovince record three phases of folding and a long-lived phase of shearing and faulting (Breaks 1991 and references therein).

D_1 deformation is represented by metre scale, shallow plunging, tight to isoclinal folds observed in rocks of low metamorphic grade. D_2 deformation is recognised by regional disharmonic folding and a strongly developed axial planar fabric (S_2) that is parallel to the regional east striking foliation. The tectonic significance of D_2 deformation is most likely a compressional event that affected the whole subprovince (Breaks 1991). West plunging lineations at the English River Subprovince - Winnipeg River Subprovince boundary recognised by Sanborn-Barrie (1988) have been inferred as overthrusting of the Winnipeg River tonalites over the English River metasedimentary sequences.

Breaks (1991) noted that localised and contrasting styles of D_3 deformation are described e.g. Sanborn-Barrie (1988). These include sporadic kink folding with axial planes plunging steeply NW and dextral sense shear zones along the ERS-WRS subprovince boundary.

- *Metamorphism*

Metasedimentary sequences in English River Subprovince have undergone low pressure, high temperature metamorphism that reached granulite facies conditions. Breaks (1991) described the complex regional metamorphic facies series, which are commonly interrupted and telescoped by fault zones and exhumation/erosion effects. The metamorphic facies series culminate in high-grade granulite zones that occur close to, or across the ERS - WRS boundary (Breaks 1991). Geothermometry and geobarometry studies in the eastern Lac Seul granulite zone resulted in temperature estimates of 675°C to 750°C and pressure estimates of 0.74±0.1 to 0.54±0.8 GPa (Chipera and Perkins 1988). It is worth noting that peak P-T conditions are rarely

recorded in granulite facies rocks, which led Breaks (1991) to conclude that the presently exposed granulite zones are exhumed from 20km depth or more.

The timing of metamorphism within the eastern Lac Seul region has been elucidated by Krogh *et al.* (1976) and Corfu *et al.* (1995). A main phase of dynamic (syn-kinematic) metamorphism occurred between 2698 - 2691Ma, culminating *circa* 2691Ma with granuilte grade metamorphism (Corfu *et al.* 1995). This was followed by localised, post-peak metamorphism and metasomatism in the period 2690 - 2670Ma (Corfu *et al.* 1995).

In comparison, the Umfreville-Conifer Lakes granulite zone has a slightly younger main metamorphic event. A 2698 ±2Ma U-Pb zircon crystallisation age for the Fletcher Lake batholith is followed by a U-Pb monazite age of 2684 ±2Ma, inferred as the timing of granulite facies metamorphism (Corfu *et al.* 1995).

- *Geological Overview*

Corfu *et al.* (1995) have described the evolution of the English River Subprovince, which commenced with sedimentary deposition between 2720 - 2700Ma. This was closely followed by the intrusion of a diorite - tonalite - granodiorite suite at 2698Ma. A main episode of regional metamorphism ensued, culminating at ~2691Ma with the development of a regional deformation fabric (D_2), granulite-grade metamorphism, anatexis and intrusion of the peraluminous granite suite. Static metamorphism (late- to post-kinematic) continued at a local scale until approximately 2670Ma (Corfu *et al.* 1995).

There has been much discussion as to whether the English River Subprovince represents a fore-arc basin to the Uchi Subprovince or a back-arc basin to the Wabigoon Subprovince. Breaks (1991) describes a tectonic model for the western Superior Province that involves an older sialic microcontinent, the Winnipeg River Subprovince, between the English River and Wabigoon Subprovince (figure 1.3). In this scenario, the English River Subprovince must represent an 800km long fore-arc basin, as in the interpretation of Langford and Morin (1976).

The tectonic model of Breaks (1991) invokes north dipping subduction of ocean crust beneath the Uchi volcanic arc. Collision of the English River fore-arc with the Winnipeg River microcontinent arrested subduction *circa* 2698Ma and caused regional compression and partial melting of the ERS metasediments to produce the 2698 ±2Ma diorite - tonalite - granodiorite suite.

Causes of metamorphism in the English River Subprovince have been related to increased crustal thickness due to thrusting and tectonic compression during the Kenoran Orogeny. Breaks (1991) has suggested that this might explain the highest metamorphic grades present at the subprovince boundaries, where thrust stacking was most prominent. However, Breaks (1991) also noted that metamorphism outlasted collision-related deformation in the eastern Lac Seul region, where the granulite zone had overprinted the ERS-WRS boundary. A second model proposed by Corfu *et al.* (1995) suggests upwelling of the asthenosphere and subsequent underplating of the lithosphere with mafic magma as a means of inducing low pressure - high temperature metamorphism to the continental crust.

Granulite-grade metamorphism was accompanied by anatexis of clastic metasedimentary rocks (Pan and Breaks 1997), which generated peraluminous, S-type granites such as the Treelined Lake granite (described above). Pan and Breaks (1997) and Breaks and Tindle (*in press*) contend from mineralogical and chemical evidence, a link between high-grade metamorphism and the ultimate formation of peraluminous granite melts and rare-element pegmatites in the adjacent Separation Lake greenstone belt.

1.3.2 Bird River Subprovince

The Bird River Subprovince is located between the boundary of the Winnipeg River Subprovince and the English River Subprovince (figure 1.3). The overall length of the Bird River Subprovince is approximately 130km, extending into Manitoba. The average width of the subprovince is less than 200m wide in Ontario except in the Separation Lake area where it is several kilometres wide. The northern boundary of the Bird River Subprovince is characterised by faulted contacts with metasedimentary rocks of the English River Subprovince. In contrast, intrusive relationships with plutonic rocks characterise the boundary with the Winnipeg River Subprovince to the south (Blackburn and Young 1993).

- *Separation Lake greenstone belt*

The Separation Lake greenstone belt is composed of a sequence of highly deformed mafic - felsic volcanics and greywackes. Blackburn and Young (1993) interpreted the Separation Lake greenstone belt to be an eastward extension of the 2750

- 2715Ma (Timmins *et al.* 1985) Bird River Subprovince of Manitoba. All supracrustal rocks of the Separation Lake greenstone belt have been subjected to medium grade regional metamorphism, 500-550°C and 3-4kbar, (Pan *et al.* 1996). The supracrustal rocks of the Separation Lake greenstone belt are intruded by a suite of granitic dykes and sills. Diorite to gabbroic sills and dykes are also present and are analogous to the chromite-bearing Bird River Sill (Cerný *et al.* 1981).

The characteristic feature of the Separation Lake greenstone belt is the relatively high concentration of rare-element class pegmatites; the Separation Rapids pegmatite group described by Breaks and Tindle (1996; *in press*), Tindle and Breaks (1998) and Breaks *et al.* (1999b). The location of the 13.5km^2 Separation Rapids pegmatite group is shown in figure 1.6. Two spatially separated subgroups were recognised (Breaks and Tindle 1996) which cluster around the 2646 ±2Ma (Larbi *et al.* 1999) peraluminous Separation Rapids pluton. This highly fractionated, zoned, S-type leucogranite pluton was suggested to be the parent granite of the pegmatites, based on bulk chemical and mineralogical data (Breaks 1993, Pan and Breaks 1997, Breaks and Tindle, *in press*).

- *Bird River greenstone belt*

The Bird River greenstone belt consists of metavolcanic and metasedimentary rocks of the Rice Lake Group (Cerný *et al.* 1981). These include sediments containing clasts of volcanic provenance that have undergone greenschist facies metamorphism and a metabasaltic sequence with a suite of intrusive rocks including the gabbroic Bird River sill. Unconformably overlying older formations are lithic arenites and pebble conglomerates metamorphosed to amphibolite facies, together with minor turbidites interlayered with ironstones (Cerný *et al.* 1981 and references therein). Timmins *et al.* (1985) report a U-Pb zircon age of 2741Ma for volcanic assemblages in the Bird River area in Manitoba and infer sedimentary deposition at >2715Ma, based on detrital zircon ages.

The Lac du Bonnet batholith and the Cat Lake - Winnipeg River pegmatite field are intruded into the Bird River greenstone belt in Manitoba (figure 1.6). Goad and Cerný (1981) describe the most fractionated and complex pegmatite group at Bernic Lake, which includes the Tanco pegmatite, one of the world's largest economic deposits of lithium and tantalum. Baadsgaard and Cerný (1993) report a U-Pb age of 2640 ±7Ma for tantalite from the Tanco pegmatite.

- *Tectonics and terrain status*

The status of the Bird River 'Subprovince' as a separate subprovince in its own right as proposed by Card and Ciesielski (1986), is not universally accepted. Sanborn-Barrie (1988) considered the 'Bird River belt' to be part of the Winnipeg River Subprovince, based on structural observations. Other workers (Beakhouse 1991; Breaks 1991) have noted that metasediments of the English River Subprovince can be traced continuously into the Bird River and Separation Lake greenstone belts, suggesting that they were part of a single depositional environment during part of their development. However, Beakhouse (1991) supports the Bird River Subprovince status, based on the application of subprovince defining principles used elsewhere in the Superior Province by Card and Ciesielski (1986).

Beakhouse (1991) concluded that the Bird River Subprovince developed in a volcanic setting at 2750 - 2715Ma (Timmins *et al.* 1985). This was followed by tectonic transport and interaction with the older (~3Ga) Winnipeg River Subprovince. Furthermore, Beakhouse (1991) interprets the Bird River Subprovince as an allocthonous block, inferred from the faulted contact of the belt. Lack of evidence for an unconformity and the presence of basal formations containing volcaniclastic facies as opposed to high-grade gneisses and tonalitic material of the Winnipeg River Subprovince, is further evidence for this proposal (Beakhouse 1991).

Tectonic transport of the Bird River Subprovince is inferred to post-date the intrusion of the tonalite plutonic suite of the Winnipeg River Subprovince i.e. <2.83Ga and predate the emplacement of granitic suite, which intrudes both the Bird River Subprovince and Winnipeg River Subprovince, 2.66 to 2.71Ga (Beakhouse 1991).

1.3.3 Winnipeg River Subprovince

The Winnipeg River Subprovince (WRS) is a dominantly granitoid terrain located in the western part of the Superior Province (figure 1.3). Card and Ciesielski (1986) defined the terminology and boundaries with the dominantly metasedimentary English River Subprovince to the north and the granite-greenstone domain, the Wabigoon Subprovince, to the south. Although peraluminous granites and rare-element pegmatites are present only within the boundary zones of the Winnipeg River Subprovince, this terrain forms a key tectonic element of the western Superior Province and thus deserves some description.

- *Lithologies*

The Winnipeg River Subprovince consists of supracrustal remnants including massive and pillow basalts along with sedimentary sequences intruded by, and tectonically included in a metaplutonic suite (Beakhouse 1991). These metaplutonic rocks are divided into a tonalitic gneiss suite and a tonalitic plutonic suite with an age range from 2.83Ga to 3.17Ga (Krogh *et al.* 1976). The gneissic suite is very heterogeneous, with enclaves of mafic volcanic rocks and deformed granitic sheets. The plutonic suite is comparatively homogeneous and forms well defined intrusive bodies (Beakhouse 1991).

Further intrusive rocks include a granitic suite and a mafic suite (diorite to granodiorite) that were emplaced between 2.66Ga and 2.71Ga. The granitic suite underlies ~40% of the Winnipeg River Subprovince (Breaks 1991). The 2702 ±4Ma Lount Lake batholith (figure 1.7) is representative of the granite suite, characterised by abundant granodiorite - granite with enclaves of the older tonalite gneiss suite (Beakhouse 1991). The granitic suite batholiths are generally undeformed and contain primary mineralogical and textural features suggesting that they were intruded subsequent to the last regional deformation/metamorphism.

- *Structural Geology*

The Winnipeg River Subprovince is characterised by polymetamorphic gneiss, which has an arcuate exposure pattern around tonalitic intrusions and strikes parallel to the subprovince boundary, broadly E-W. An early phase of horizontal tectonics resulting in thrust faulting and recumbent folding, tightly constrained at 2707±8Ma (Corfu 1988; Beakhouse 1991), were later deformed in a phase of upright folding and doming. Transcurrent E-W shear faulting along the subprovince boundaries commonly has a dextral displacement sense consistent with northwest directed regional compression (Beakhouse 1991).

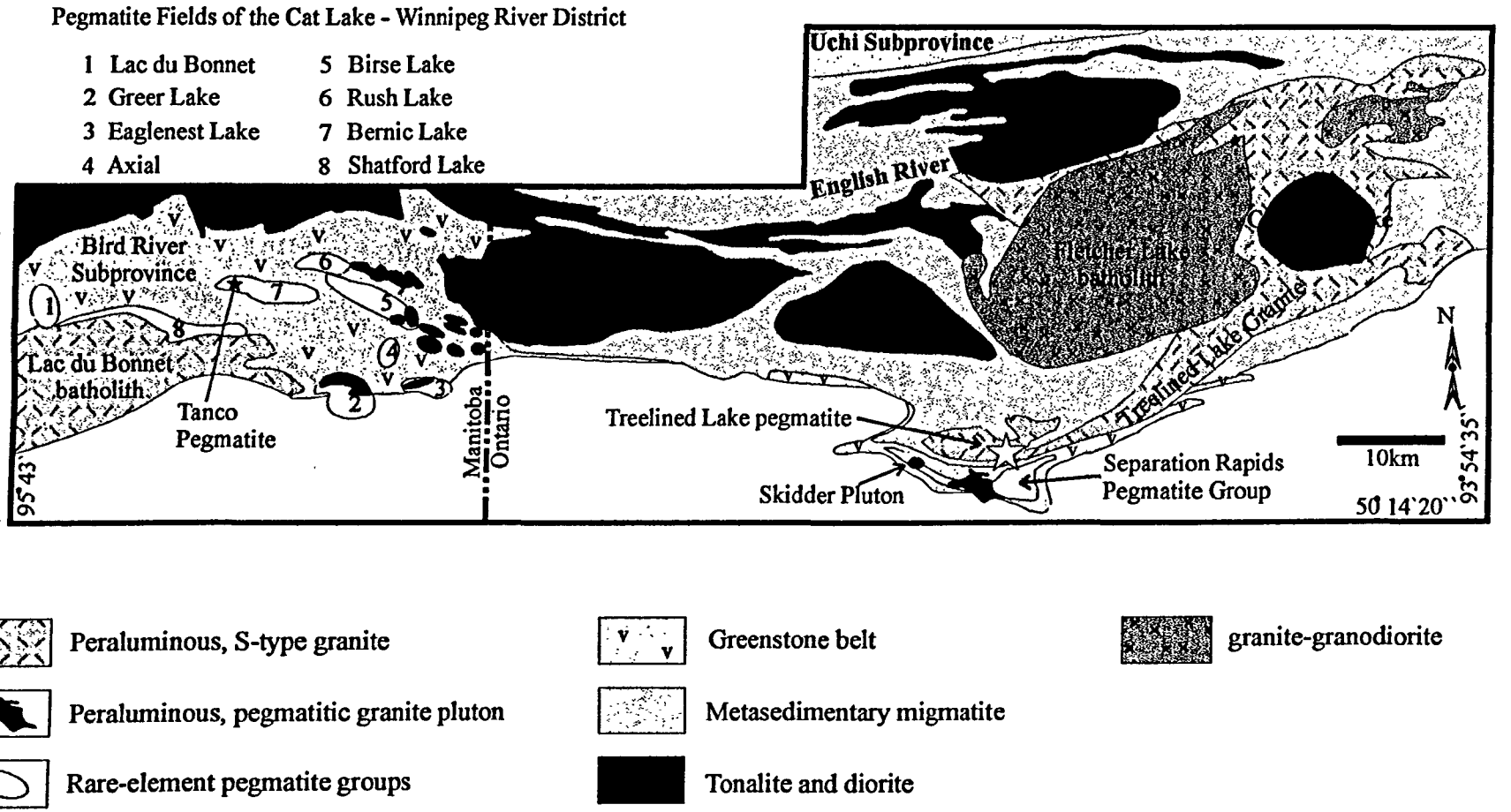

Figure 1.6 Geological map of the western English River Subprovince and Bird River Subprovince, in NW Ontario and adjacent Manitoba. Note the Z-shaped exposure of the Separation Lake greenstone belt, characteristic of regional scale D_2 folding. After Breaks and Tindle (in press).

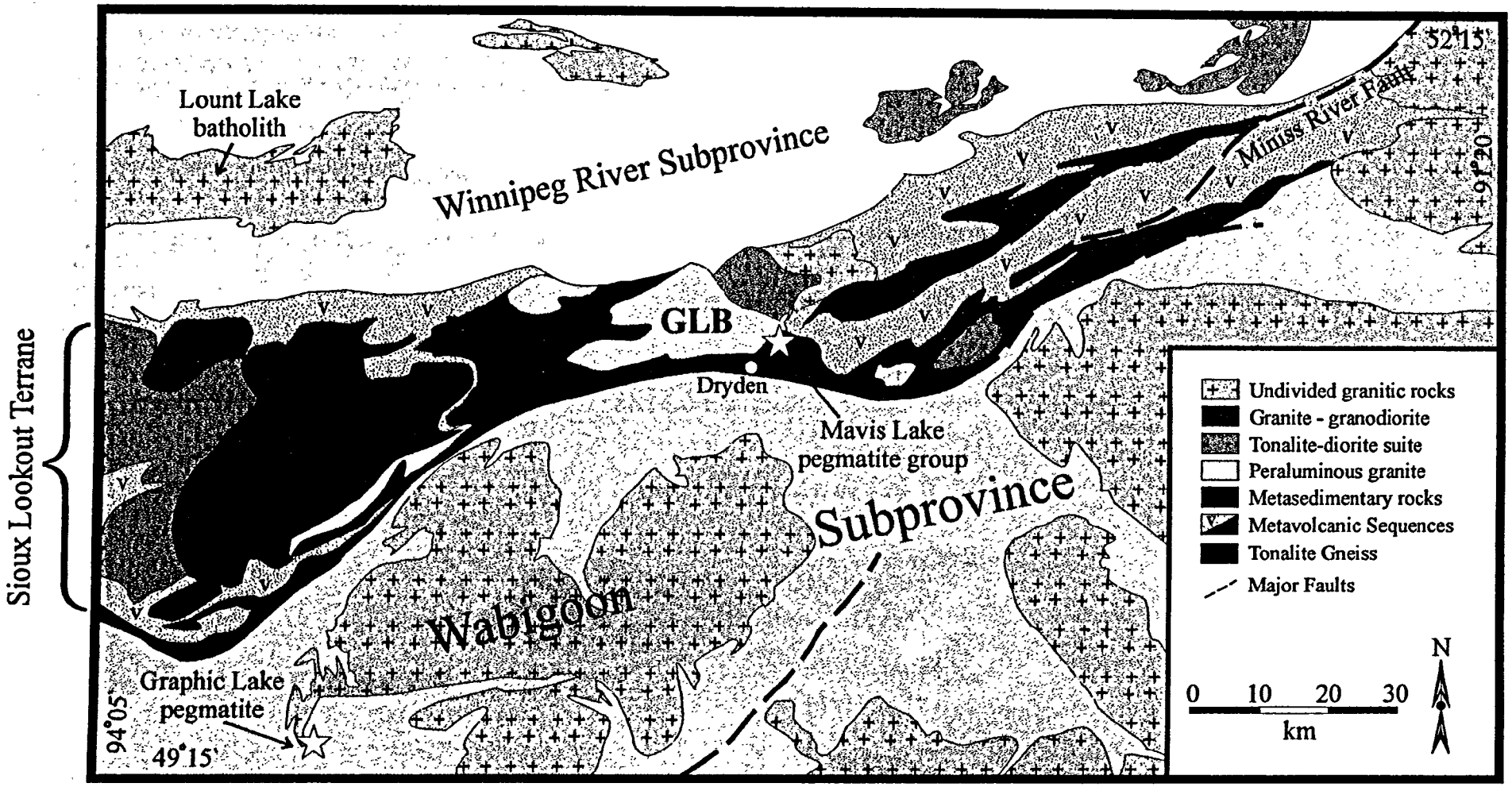

Figure 1.7 Simplified geological map of the Winnipeg River - Wabigoon Subprovince boundary, showing the location of the Ghost Lake batholith (GLB) and associated Mavis Lake pegmatite group, and the Graphic Lake pegmatite. After Breaks and Moore (1992).

Beakhouse (1991) also reported that faults along the Winnipeg River - Wabigoon Subprovincial boundary record a final movement of north-side up, dip slip movement on sub-vertical faults. The subprovince bounding faults remained active until the latest Archæan, most likely caused by isostatic compensation for tectonically thickened crust in the Winnipeg River Subprovince.

- *Metamorphism*

Medium- to high-grade metamorphism has affected the early supracrustal remnants, the gneissic suite and some of the tonalite plutonic suite. Detailed investigation of the eastern Lac Seul granulite zone produced estimates of peak metamorphic conditions at 650 to 750°C at 350 to 600MPa (Harris and Goodwin 1976) and greater than 770°C at 400 to 600MPa (Breaks 1991).

The duration and number of metamorphic events within the Winnipeg River Subprovince is however, uncertain. Corfu (1988) suggested that a relatively late metamorphism affected the entire subprovince at 2709 ±2Ma, with subsequent differential cooling. Metamorphic zircons within tonalite gniess have a U-Pb age of 2790 ±9Ma, which may correspond to an earlier metamorphic event (Beakhouse 1991). Constraints on metamorphic conditions indicate that the present erosion surface has been exhumed from between 14km - 21km depth (Breaks 1991).

- *Geological Overview*

Crustal evolution in the Winnipeg River Subprovince before 2.83Ga is characterised by bimodal basalt-tonalite suites. These suites were produced by a two-stage process involving mantle derived tholeiitic volcanism followed by melting of the basalts, which produced tonalite plutonism (Beakhouse 1991). At approximately 2710Ma, the crust of the Winnipeg River Subprovince was tectonically thickened by thrust faulting and nappe development. Thickening induced high-grade metamorphism and intracrustal melting of the gneissic tonalite and plutonic suites producing a granodiorite to granite phase of plutonism emplaced over a period of 40Ma (Beakhouse 1991).

1.3.4 Wabigoon Subprovince

The Wabigoon Subprovince is a 900km long, 150km wide granite - greenstone terrain in the western Superior Province (figure 1.3). The greenstone belts are composed of metavolcanic - metasedimentary sequences that are surrounded and intruded by granitoid batholiths. The subprovince is bounded to the north by the Winnipeg River Subprovince and English River Subprovince; the Quetico Subprovince lies to the south. Blackburn *et al.* (1991) have distinguished three geographic regions based on the relative quantities of the major lithologic units; 1) western Wabigoon region, composed of extensive greenstone belts and oval granitoid batholiths. 2) central Wabigoon region, characterised by large areas of gneissic tonalites and granitoid batholiths. 3) eastern Wabigoon region, which comprises isolated greenstone belts surrounded by lobate granitoid batholiths (figure 1.8).

For the present study, the Ghost Lake batholith - Mavis Lake rare-element pegmatites, and the Graphic Lake pegmatite were sampled from the western Wabigoon region. Therefore, further discussion here will be focused on this region.

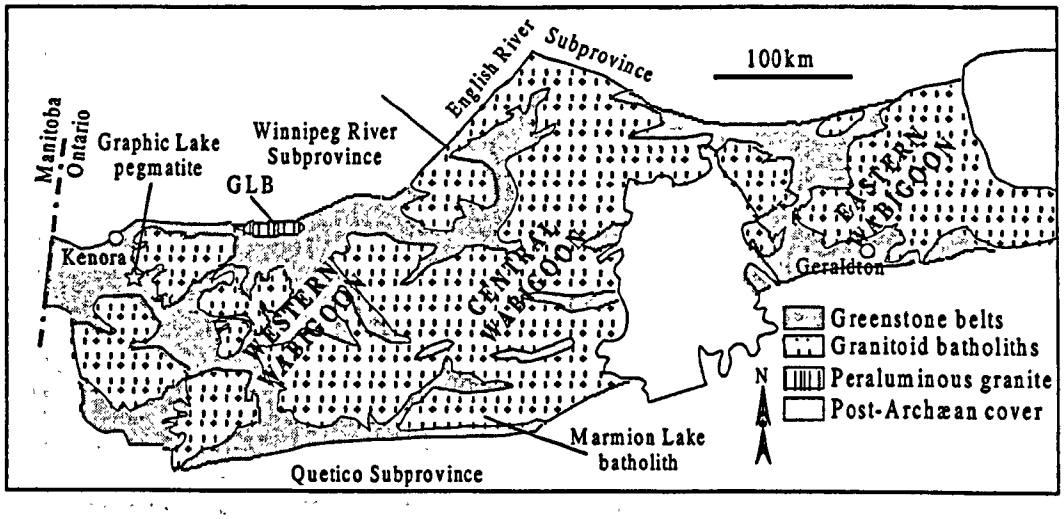

Figure 1.8 Simplified geological map of the Wabigoon Subprovince showing the location of the Ghost Lake batholith (GLB) and the Graphic Lake pegmatite. After Blackburn et al. (1991).

- *Western Wabigoon region - lithologies*

The western Wabigoon region (WWR) is characterised by a network of interconnected greenstone belts, surrounded and intruded by syn-volcanic granitoid

batholiths and post-tectonic granitic plutons (Blackburn *et al.* 1991). Greenstone assemblages are divided into four main sequences:

1. Lower ultramafic komatiites and tholeiitic basalts, the oldest dated at 2775 ±1Ma (Davis *et al.* 1988).
2. Intermediate to felsic calc-alkaline metavolcanics with subordinate andesite - rhyolite pyroclastic assemblages. U-Pb ages between 2745 - 2711Ma (Davis *et al.* 1985).
3. Upper mafic assemblages of tholeiites and komatiites.
4. Assemblages of turbidites and alluvial - fluvial metasediments, deposited in the period 2710 - 2695Ma (Davis *et al.* 1988).

Plutonic rocks in the Wabigoon Subprovince are divided into three suites based on their geochemical and age relationships with adjacent greenstone belts (Blackburn *et al.* 1991). Tonalitic orthogneiss domes and granitoid batholiths are abundant within the central Wabigoon region (figure 1.8). These lithologies are thought to represent a basement complex to unconformably overlying greenstone assemblages e.g. the 2999 ±1Ma Marmion Lake batholith (Davis and Jackson 1988).

Within the WWR, syn-volcanic granitoid batholiths intrude the greenstone belts. The Dryberry batholith is representative of these internal granitoids, which comprises a core of 2663 ±4Ma granodiorite surrounded by older, 2716 ±2Ma tonalite units (Blackburn *et al.* 1991).

A suite of late- to post-tectonic granite plutons intrude and surround the greenstone belts. The 2685Ma peraluminous, S-type Ghost Lake batholith and associated Mavis Lake rare-element pegmatites (Breaks and Moore 1992) are located along the Wabigoon - Winnipeg River Subprovince boundary zone, immediately north of Dryden (figure 1.7). This region has been termed the Sioux Lookout Terrain (Beakhouse 1991), and is characterised by repeated stratigraphy of metavolcanic - metasedimentary assemblages.

- *Metamorphism and structural geology*

Throughout the interior parts of the Wabigoon Subprovince, low-grade metamorphic mineral assemblages are prevalent, recording greenschist to lower amphibolite facies conditions. The distribution of metamorphic grades is spatially

associated with granitoid batholiths; highest grades are found adjacent to these batholiths (Blackburn *et al.* 1991).

The subprovince margins are characterised by steep metamorphic gradients, ~50°C/km (Blackburn *et al.* 1991). In the Sioux Lookout Terrain, the Zealand group metapelites (figure 1.7) contain a facies series ranging from a chlorite - biotite zone to sillimanite - K-feldspar migmatites. Peak metamorphic conditions of 550 - 750°C at a pressure of approximately 0.4GPa have been determined from the Zealand group metapelites (Breaks and Moore 1992). Recent studies of the Wabigoon - Winnipeg River Subprovince boundary have distinguished three episodes of metamorphism, with peak conditions recorded *circa* 2685Ma and a retrograde metamorphism at 2652 ±1Ma (Menard *et al.* 1997).

Structural features are also different in the interior of the subprovince compared with the margins. Long, sinuous shear zones with complex brittle and ductile deformation cut through the subprovince interior. These central shear zones may be 250km in length and up to 3km wide, with several associated splay faults. In contrast, the subprovince boundary zones are characterised by long, relatively narrow, shear zone bounded panels of supracrustal rocks. Metavolcanic - metasedimentary assemblages have been subjected to layer-parallel shearing and have a repeated outcrop pattern consistent with tectonic stacking (Blackburn *et al.* 1991).

- *Geological Overview*

Early development of greenstone belts within the Wabigoon Subprovince may have begun with rifting of an older continental mass represented by 3Ga tonalite basement preserved in the central Wabigoon region (Blackburn *et al.* 1991). Geochemical constraints suggest that the mafic volcanic sequences are plume related (Tomlinson *et al.* 1998). The tectonic model proposed by Blackburn *et al.* (1991) commences with the opening of a micro-ocean, which produced the 2.78 - 2.72Ga mafic volcanic sequences. Closure of the ocean basin was associated with subduction beneath continental gneissic terrains, the Winnipeg River Subprovince and central Wabigoon region. This led to the development of island arcs and the production of calc-alkaline magmatism (volcanic and plutonic) in the period 2745 - 2711Ma (Davis *et al.* 1985). Syn-volcanic granitoid batholiths have ε_{Nd} (T) values as high as +2, suggesting an origin from melting of juvenile basaltic crust (Larbi *et al.* 1999).

Arc - continent collision is the most likely explanation for the transition to a compressional regime indicated by east-trending asymmetric folding and thrust stacking along the Wabigoon - Winnipeg River Subprovince boundary. Uplift and erosion produced the alluvial - fluvial sedimentary assemblages, deposited in the period 2710 - 2695Ma (Davis *et al.* 1988).

Emplacement of a post-tectonic granite suite included the Ghost Lake batholith. Breaks and Moore (1992) suggested that this peraluminous granite was derived from partial anatexis of the adjacent Zealand group metapelites. Recent Sm-Nd work has confirmed this hypothesis; the isotopic signature of the Ghost Lake batholith and Zealand sediments are similar, ε_{Nd} (T) +1 to –1 (Larbi *et al.* 1999). An initial phase of metamorphism and partial melting concentrated incompatible rare-lithophile elements into leucosome fractions of migmatites. Crustal thickening related to the collision of the Wabigoon arc with the Winnipeg River 'microcontinent' led to a second, more extensive partial melting event and the generation of S-type granitic melts. Breaks and Moore (1992) also describe the subsequent chemical differentiation of the Ghost Lake batholith. Rare-lithophile elements (F, Li, Sn, Ta), boron and H_2O were concentrated in residual melts and 'ponded' within the cupola zone of the batholith. Ultimately, this led to the dispersion of rare-element pegmatites, the Mavis Lake group, emplaced along earlier formed shear zones (Breaks and Moore 1992).

1.4 Southern Superior Province

1.4.1 Abitibi Subprovince

The Abitibi Subprovince is a granite - greenstone terrain located in the southern part of the Superior Province (figure 1.3). The Abitibi Subprovince is bordered to the north by the metasedimentary and plutonic rocks of the Opatica Subprovince, to the south by the metasedimentary Pontiac Subprovince, to the west by the mid-crustal granulites of the Kapuskasing Uplift, and to the east by the Meso-proterozoic Grenville Province.

The western Abitibi Subprovince in Ontario is dominated by the Abitibi greenstone belt. This is the largest greenstone belt in the world and is divided into a

northern portion dominated by granitoid batholiths and a southern portion with more abundant supracrustal sequences (figure 1.9).

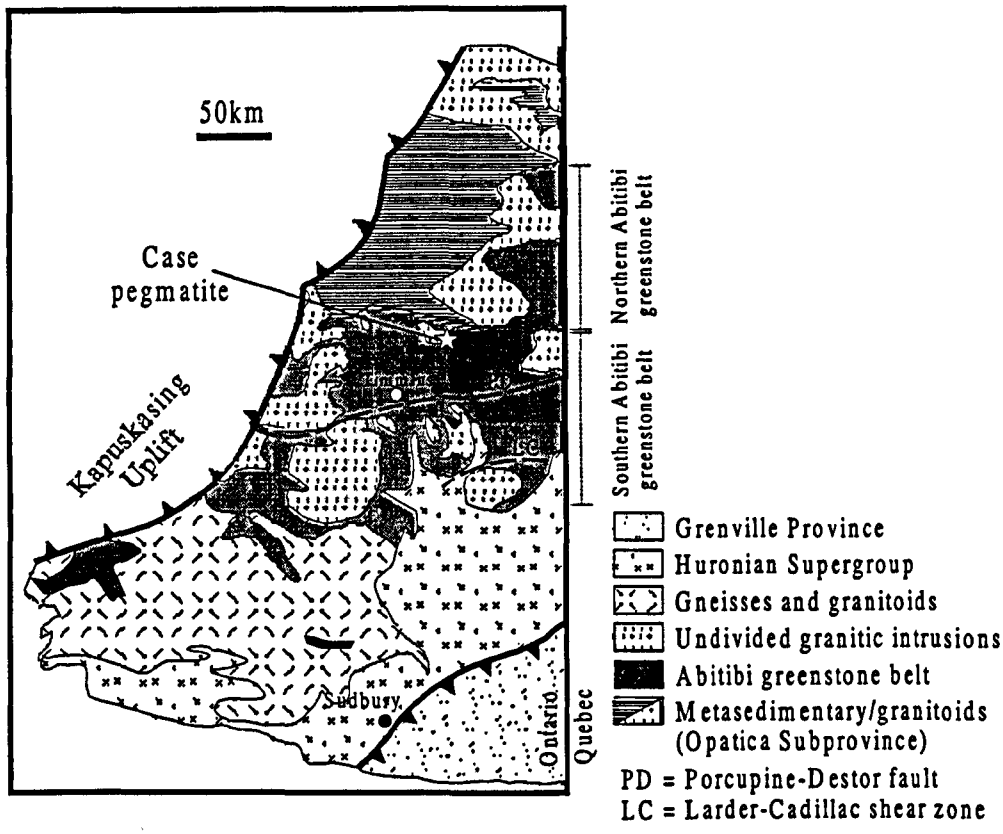

Figure 1.9 Simplified geological map of the Abitibi Subprovince showing the location of the Case pegmatite. After Jackson and Fyon (1991).

- *Abitibi greenstone belt - lithologies*

Supracrustal sequences of the Abitibi greenstone belt are dominated by ultramafic komatiite and tholeiite volcanic assemblages, with ages between 2750 - 2700Ma (Corfu *et al.* 1989). Overlying metasedimentary turbidite sequences were deposited in the period 2.7 - 2.68Ga. Calc-alkaline volcanic assemblages and alluvial - fluvial sedimentary assemblages formed between 2685 - 2675Ma (Corfu *et al.* 1989).

Intrusive suites include 2.74 - 2.69Ga tonalite-trondhjemite-granodiorite (TTG) batholiths such as the 35 x 50km Lake Abitibi batholith (Corfu *et al.* 1989). These batholiths commonly consist of two major phases of intrusion, an older gneissic tonalite phase and a younger massive granodiorite phase. Geochemically, the TTG suites are LREE enriched (~10 to 50 x chondrite). A suite of alkali-rich syenite plutons intrude the Abitibi greenstone belt. These minor plutons are also LREE enriched (~20 to 500 x chondrite) with emplacement ages between 2.69 - 2.67Ga (Corfu *et al.* 1989).

Along the boundary of the northern and southern portions of the Abitibi greenstone belt, a spodumene-bearing rare-element pegmatite is emplaced within the Case batholith, part of the Opatica Subprovince (figure 1.9). The Case pegmatite is a 30m x 25m body characterised by spodumene blades up to 30cm long. The tonalitic Case batholith has no mineralogical similarities with the Case pegmatite and is therefore considered unlikely to be chemically or genetically associated. Metasedimentary and metavolcanic sequences of the Scapa and Steele assemblages are in close spatial association with the Case pegmatite. In particular, the Scapa assemblage is a 5 to 12km wide, 100km long clastic metasedimentary dominated assemblage, which coincides with the boundary between the northern and southern portions of the Abitibi greenstone belt (Jackson and Fyon 1991). The linear exposure of the Scapa assemblage and association with several high-strain shear zones is a common feature of subprovince boundary zones, which are often the sites of emplacement of rare-element pegmatites. The Scapa and Steele assemblages are tentatively suggested as the source rocks for the Case pegmatite.

The Preissac, Lamotte and Lacorne leucogranites are located within the southern Abitibi greenstone belt in Quebec. Ducharme *et al.* (1997) determined U-Pb monazite and titanite ages for these S-type granite plutons. The Preissac leucogranite yields ages between 2681 - 2640Ma, indicating plutonic activity over a 40Ma period. In comparison, the Lamotte and Lacorne leucogranites are distinctly younger, with crystallisation ages between 2645 - 2630Ma. A beryl - columbite-tantalite - spodumene pegmatite associated with the Lamotte pluton has a U-Pb monazite age of 2639 ±2Ma (Ducharme *et al.* 1997).

- *Metamorphism and structural geology*

In general, regional metamorphism in the Abitibi greenstone belt is at greenschist grade or lower. The timing of this regional metamorphism is loosely constrained at 2690 - 2700Ma based on the age of rocks affected by the metamorphism (Jackson and Fyon 1991). Additionally, large granitoid batholiths are surrounded by amphibolite - hornfels contact aureoles.

Two structural styles are recognised in the Abitibi greenstone belt. Mesoscopic (outcrop scale) folds and thrust faults are related to the emplacement of tonalite-trondjhemite-granodiorite (TTG) suite batholiths. Regional scale shear zones such as the Porcupine-Destor fault and the Larder-Cadillac shear zone developed during and after

emplacement of TTG batholiths (figure 1.9). These shear zones strike E-W to NE-SW and are associated with lode-gold mineralisation (Jackson and Fyon 1991).

- *Geological Overview*

The Abitibi Subprovince is a late-Archæan granite - greenstone terrain that developed between 2.8 - 2.6Ga (Jackson and Fyon 1991). There has been considerable discussion regarding the tectonic setting of the Abitibi greenstone belt. The 2750 - 2700Ma ultramafic - mafic asemblages may be derived from mid-ocean ridge, island arc or mantle plume volcanism (Jackson and Fyon 1991). An island arc setting has been invoked for the production of calc-alkaline (TTG) magmatism, which has Pb isotopic signatures indicating contamination with crustal material (Gariepy and Allegre 1985).

The origin of post-collisional leucogranites in the southern Abitibi greenstone belt has been determined by the Sm-Nd isotopic studies of Ducharme *et al.* (1997). The Preissac, Lamotte and Lacorne leucogranites have isotopic signatures ε_{Nd} (T) –1 to +3, consistent with an origin from melting of a juvenile sedimentary sequence, probably derived from the Abitibi arc. The 2681Ma emplacement age for the post-tectonic Preissac leucogranite places a minimum constraint on the timing of collision with the Pontiac Subprovince to the south (Ducharme *et al.* 1997).

1.5 Proterozoic events affecting the Superior Province

Several geological events have affected the Superior Province since its initial formation during the Archæan. During the Proterozoic, the Trans-Hudson Orogeny welded the Superior Craton to the Archæan Hearne and Wyoming Provinces (figure 1.1). Subsequently, the Penokean and Grenville Orogens accreted juvenile crust to the south and southeast margins of the Superior Province between 1.9 - 1.6Ga to form the Laurentian supercontinent (Hoffman 1989). Additionally, more than 12 swarms of Proterozoic mafic dykes occur throughout the Superior Province, ranging in age from 2.5 to 1.1Ga (Osmani 1991). A brief summary of the main events is provided below.

- *Brittle fault reactivation*

Kamineni *et al.* (1990) have investigated the Rb-Sr sytematics of late-orogenic plutons, 2700 - 2665Ma (U-Pb zircon) in the western Superior province. The Eye-

Dashwâ pluton, located in the Wabigoon Subprovince (figure 1.8) is cut by fracture zones that yield an imprecise whole-rock Rb-Sr isochron of 2280 ±167Ma. Similarly, the Lac du Bonnet batholith within the Bird River Subprovince (figure 1.6) is affected by steeply dipping epidote-bearing fault zones with Rb-Sr isochrons that cluster around 2.3Ga. Still younger dates are obtained from the Sydney Lake fault, which marks the ERS-Uchi Subprovince boundary (figure 1.5); pseudotachylite samples have a Rb-Sr isochron of 2183 ±74Ma.

Overall, these brittle fractures and fault zones must be related to compressive stresses. However, extensional regimes are thought to predominate at the margins of the Superior Craton *circa* 2.3Ga. Kamineni *et al.* (1990) suggest regional variations in stress across the craton might have produced the brittle structures (figure 1.10a).

- *Matachewan - Hearst dyke swarm*

The Matachewan - Hearst dyke swarm covers an area of 500 by 700km (figure 1.10b). Individual dykes are generally 10m wide and mainly composed of quartz dolerite (Osmani 1991). Emplacement of the Matachewan - Hearst dyke swarm is closely constrained by a baddeleyite U-Pb age of 2452 +3/-2Ma (Heaman 1997). The NW trending dyke swarm is located around the central and southern Superior Province but extends as far as the Uchi Subprovince - North Caribou Terrain boundary (Osmani 1991).

Heaman (1997) suggested the Matachewan - Hearst dyke swarm may be the surface expression of large scale mafic magmatism. Basaltic underplating of the lithosphere and thermal metamorphism at the base of the crust spanning a period of at least 30Ma, *circa* 2.45Ga, are proposed (Heaman 1997).

- *Huronian Supergroup*

The Huronian Supergroup comprises sedimentary sequences with subordinate flood basalts and intrusive rocks, located on the southern edge of the Superior Province (figure 1.10b). Conglomerates, mudstones, siltstones and sandstones are intercalated with mafic to felsic volcanic rocks and a suite of dolerite - gabbro sills and dykes (Bennett *et al.* 1991). The Huronian Supergroup formed between 2.5 - 2.2Ga (Krogh *et al.* 1984), and was initiated by rifting along the margin of the Superior Craton, followed by passive margin deposition of sedimentary sequences. Rocks of the Huronian Supergroup were subjected to folding and metamorphism at amphibolite

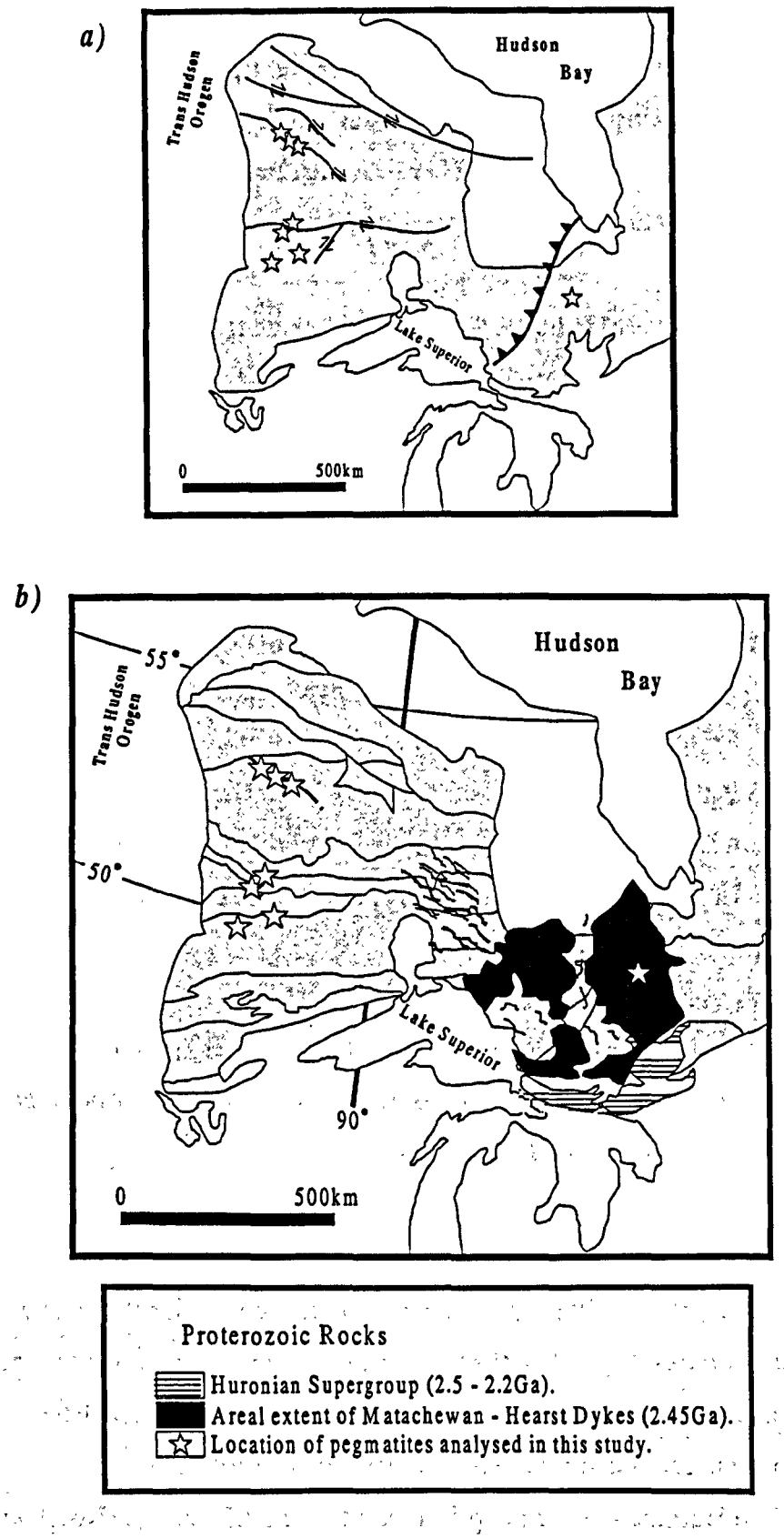

Figure 1.10 Proterozoic events affecting the Superior Province. a) Major faults active during the period 2.5 - 1.8Ga, after Kamineni et al. (1990); Osmani (1991). b) Matachewan-Hearst dyke swarms and Huronian Supergroup, after Osmani (1991).

facies during the 1.86 - 1.83Ga Penokean Orogeny (Hoffman 1989). The Penokean Orogeny is described as a fold belt resulting from the collision of a Proterozoic island arc terrain with the Superior Craton (Bennett *et al.* 1991).

- *Trans-Hudson Orogeny*

During the Proterozoic, the Trans-Hudson Orogeny welded the Superior Craton to the Archæan Hearne Province. Collision with the western and northwestern margin of the Superior Province occurred during the period 1860 - 1790Ma (Hoffman 1989). The NW directed compressional forces acting on the Superior Province created reactivation of major faults that is well documented from disturbances to isotopic systems. In particular, Corfu and Ayres (1984) reported 1850 Ma U-Pb zircon lower intercept ages from batholiths along the Bear Head fault zone within the North Caribou Terrain (figure 1.4).

1.6 Summary

Tectonic models for the formation of the Superior Province were originally developed by Langford and Morin (1976), and later refined by Card and Ciesielski (1986). They considered the striped pattern of subprovinces to be the product of island arc and intervening sedimentary basin accretion to a sialic micro-continent, now described as the North Caribou Terrain (Thurston *et al.* 1991). The majority of lithologies within each subprovince were created between 3Ga - 2.7Ga, with the craton wide Kenoran Orogeny occurring at about 2.7Ga. A progressive younging of pre-orogenic magmatism towards the south has been revealed by geochronological studies (Corfu and Davis 1991), which Hoffman (1989) suggested was analogous to the evolution of the cordillera of western North America.

During the latest stages of collision and tectonic thickening of the crust, perlauminous granite melts and associated rare-element pegmatites were generated by partial melting of metasedimentary - metavolcanic assemblages. Subprovince boundaries and regional scale shear zones are common sites for the emplacement of these S-type crustal melts. The period of emplacement of peraluminous granites and associated rare-element pegmatites is coeval with the transition from collision related compressional deformation to post-collision crustal melting. Therefore, peraluminous

granites and rare-element pegmatites are distinctive markers for the final craton-forming processes of the Superior Province. Figure 1.11 illustrates the tectonic evolution of the northwestern and western Superior Province, with emphasis on the sites of peraluminous granites and rare-element pegmatites.

1.6.1 Aims for this study

- *Description of the field relations, mineralogy and internal zoning of peraluminous granites and rare-element pegmatites of the Superior Province.*

Chapter 2 describes the petrogenetic processes by which rare-element enriched magmas originate. Following this is a description of the peraluminous granites and associated rare-element pegmatites sampled in this study.

- *Determining the chemical evolution of Superior Province pegmatites.*

Chapter 3 discusses two of the most economically important occurrences of rare-element mineralisation, the Pakeagama Lake pegmatite and the Separation Rapids pegmatite group, using electron microprobe analysis of muscovite - lepidolite mica species.

- *Constraining the emplacement age and the timescales of magmatic fractionation and secondary mineralisation processes of peraluminous granite - rare-element pegmatite systems.*

High-precision ages from U-Pb isotope dating of columbite-tantalite minerals are presented in Chapter 4. Emplacement ages are obtained from rare-element pegmatites from the northwestern and western Superior Province to constrain the timing of final accretion processes. Furthermore, results of dating columbite-tantalite from both primary magmatic and from replacement assemblages give an estimate for the timescales over which the rare-element pegmatites were active.

- *Understanding the post-orogenic thermal history of the Superior Province.*

The focus of this thesis is to use $^{40}Ar/^{39}Ar$ geochronology to determine thermal histories of rare-element pegmatites across the Superior Province, which is presented in Chapter 5. The location of rare-element pegmatite emplacement makes them useful for the study of post-orogenic thermal histories along subprovince boundaries and regional shear zones.

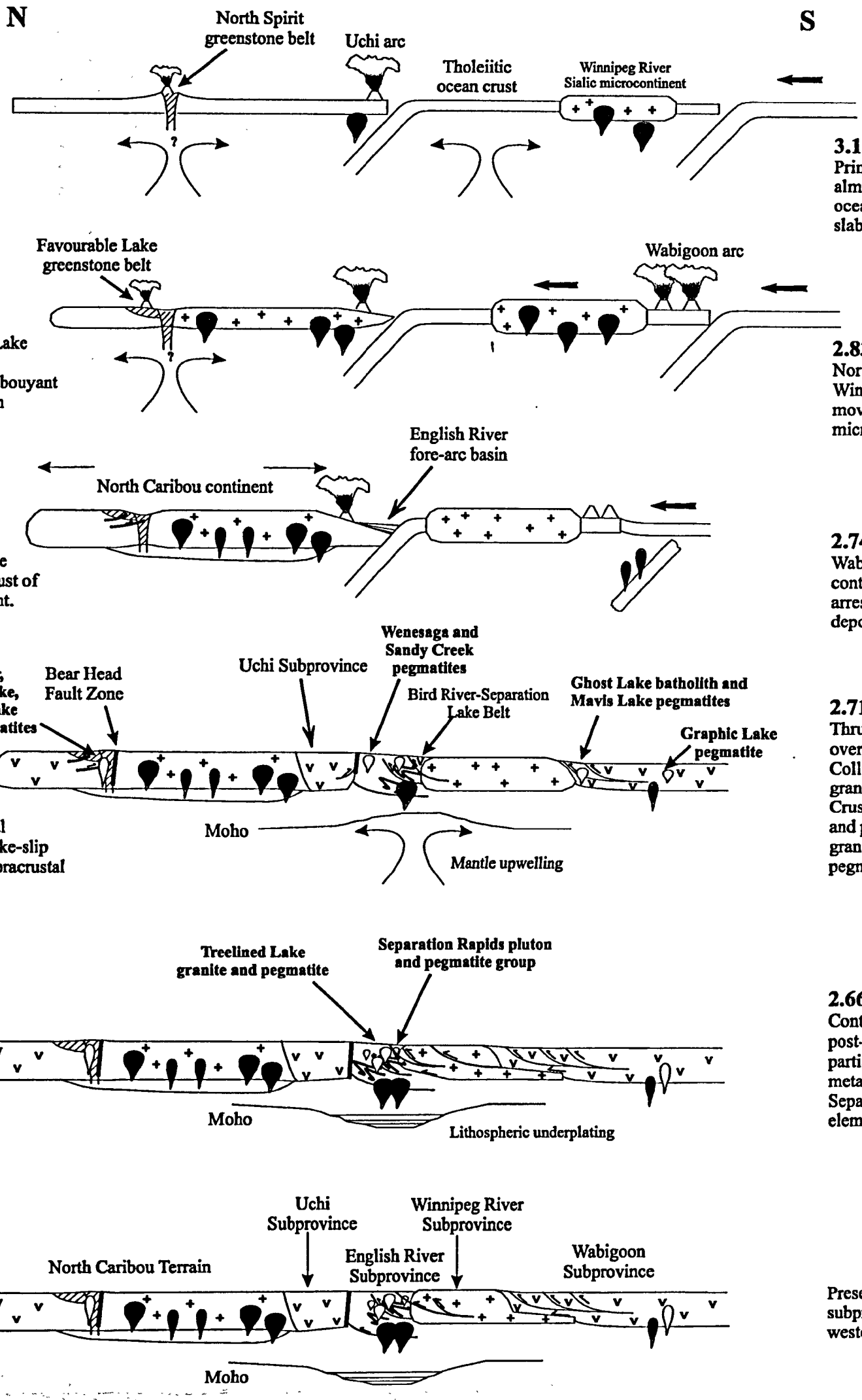

North Spirit-Favourable Lake back arc basin develops. Tonalite intrusions create bouyant arcs which accrete to form micro-continents.

Basaltic underplating of the lithosphere thickens the crust of the North Caribou continent.

Transition to compressional tectonic regime creates strike-slip faulting and anatexis of supracrustal sequences

3.17 - 2.83Ga
Primitive arc formation with almost complete recycling of oceanic crust through subduction slab melting.

2.83 - 2.74Ga
North dipping subduction as Winnipeg River micro-continent moves towards the North Caribou microcontinent.

2.74 - 2.71Ga
Wabigoon arc - Winnipeg River continent collision, subduction arrested. English River sediments depostied over ~20Ma.

2.71 - 2.66Ga
Thrust-stacking of Wabigoon arc over Winnipeg River tonalites. Collision related compression and granulite metamorphism in ERS. Crustal melting in collision zones and pruduction of peraluminous granites and rare-element pegmatites.

2.66 - 2.64Ga
Continent - mature arc collision, post-tectonic metamorphism and partial melting of ERS metasediments to produce Separation Rapids pluton and rare-element pegmatites.

Present configuration of subprovinces in the northwest and western Superior Province.

Figure 1.11 Schematic diagrams to illustrate the simplified tectonic evolution of the Northwest Superior Province with emphasis on the emplacement of peraluminous granites and rare-element pegmatites. Based on information from references cited in the text.

2. Rare-Element Pegmatites

2.1 Introduction

This chapter provides a concise review of the petrogenetic processes involved in the formation of rare-element bearing granitic melts. Following on from this is a description of the peraluminous granites and pegmatites sampled in this study, all from the Superior Province of Ontario. Descriptions are based on the field investigation of mineralogical content, internal zoning and relation to host-lithologies.

2.1.1 Peraluminous granite - rare-element pegmatite associations

Peraluminous granites are considered parental to rare-element pegmatites, based on mineralogical and geochemical similarities (Cerný and Meintzer 1988; Breaks and Moore 1992). The term 'fertile granite' has been used extensively in the literature to describe peraluminous granites derived from upper crustal rocks undergoing their first melting event (e.g. Cerný 1989). Peraluminous leucogranites have bulk compositions that tend towards low temperature melts at the minima of experimental systems. Peraluminous granites display the following facies variations; biotite granite → fine grained leucogranite → sodic aplite → potassic pegmatite → rare-element pegmatite.

Common minerals found within peraluminous leucogranites are quartz, K-feldspar, Ca-poor, Na-rich feldspar (albite), <0.1wt% CaO; ~3wt% Na_2O. Also present are Fe-rich, Mg-poor biotite and Li-, F-rich muscovite. Accessory phases include Mn-rich garnet (spessartine), pseudomorphs of cordierite, beryl, tourmaline, Nb-Ta-Sn bearing phases (columbite-tantalite, cassiterite) and phosphates (fluorapatite, monazite) (Cerný and Meintzer 1988).

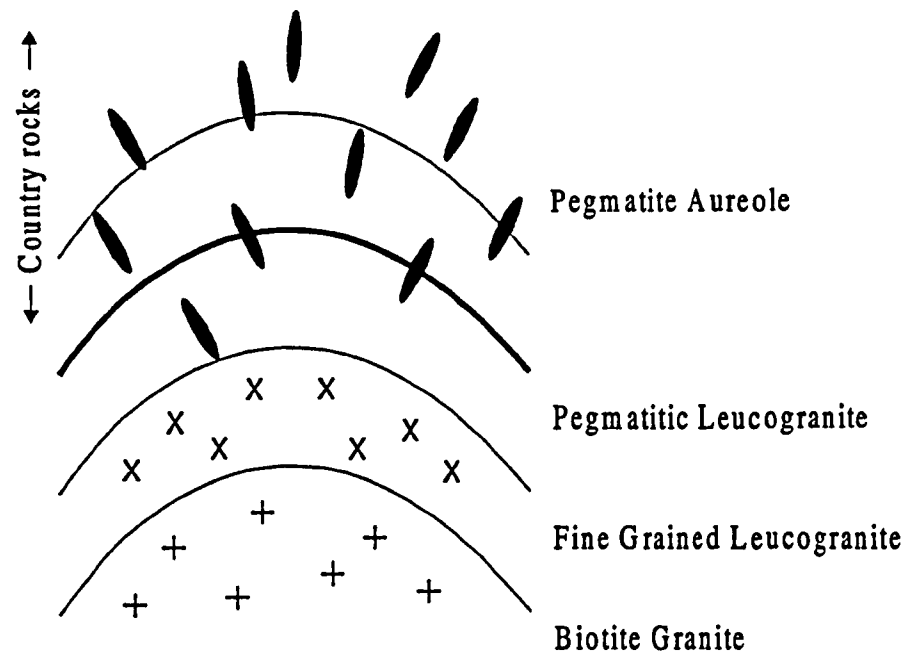

Figure 2.1 Idealised vertical section through a peraluminous granite intrusion with associated pegmatite aureole, after Cerný and Meintzer (1988).

Salient chemical features of peraluminous granites include high silica content >70wt% and high Al_2O_3 >14wt%. Peraluminous granites are alkali rich, >3wt% Na_2O, >4wt% K_2O with low CaO, MgO, Fe_2O_3, FeO, MnO and variable K_2O/ Na_2O. The strongly peraluminous chemistry, with A/CNK $\geq$ 1.1 suggests a sedimentary source (Cerný 1991).

Considering the trace elements, the K/Rb ratio is often used as a measure of the degree of fractional crystallisation of peraluminous leucogranites. Strontium and barium contents are extremely variable, but are usually lower than in calc-alkaline granites. Lithium values are similarly variable and often dependant on mica composition. Concentrations of Cs and Be are usually higher than those found in calc-alkaline granites, with average values of 10-20ppm Cs and up to 60ppm Be. Zn, Zr and Hf are variable but generally low. In contrast, Ga and the Al/Ga ratio increase with fractionation, as does the concentration of Sn. Nb and Ta (values ~150ppm and ~40ppm, respectively) are highly enriched relative to average calc-alkaline granites. Similarly, phosphorus is relatively enriched with P_2O_5 up to 0.3 - 0.6 wt%. Boron and fluorine contents are often dependent on the presence of tourmaline and micas, respectively (Cerný and Meintzer 1988).

The characteristic feature of rare-earth elements in peraluminous granites is their low abundance, generally in the 1 to 20 range of chondrite normalised values. REE patterns are typically winged, with prominent negative Eu anomalies. Some HREE depletion is observed in relatively primitive facies, which may be a result of accessory phase crystallisation, such as garnet (Cerný and Meintzer 1988).

2.1.2 Rare-element pegmatites

Pegmatites of the rare-element class are characterised by abrupt variations in grain size, mineral assemblages and enrichment in rare-lithophile elements (Li, Cs, Ta, Nb, Y, F). Individual pegmatite bodies occur as intrusive dykes at metre to km scale and are often associated with chemically evolved peraluminous granites.

Ginsburg *et al.* (1979) set out a classification scheme for granitic pegmatites, defined by their depth of formation, geological setting and petrology:

1. *Abyssal class* - migmatitic products of partial melting, upper amphibolite to granulite facies (4 - 9kb)
2. *Muscovite class* - partial melting and restricted differentiation, amphibolite facies (5 -8kb)
3. *Rare-element class* - associated with chemically evolved peraluminous granites. Upper greenschist to cordierite-amphibolite facies (2 - 4kb); main source of lithophile rare-element mineralisation among all pegmatite categories.
4. *Miarolitic class* - overlap with rare-element class environment (1.5 - 2kb).

- *Classification of rare-element pegmatites*

The exotic mineralogy that characterises pegmatites of the rare-element class may include the following species: beryl, lithium aluminosilicates (petalite, spodumene), Nb-Ta oxides (columbite-tantalite), borosilicates (tourmaline), phosphates (amblygonite-montebrasite, monazite, fluorapatite), lithium mica (lepidolite) and the rare caesium mineral, pollucite. Based on this mineralogical variety, rare-element pegmatites are divided into several types and subtypes (Cerný 1990).

Pegmatite Type	Subtype	Common Minerals and chemical formulae
Rare-Earth	Allanite, monazite	Allanite $(Y, Ce, Ca)_2(Al, Fe)_3(SiO_4)_3(OH)$, monazite $(Ce,Th)PO_4$
	Gadolinite	Gadolinite $Y_2FeBe_2Si_2O_{10}$, euxenite $(Y,Ca,Ce,U,Th)(Nb,Ta,Ti)_2O_6$
Beryl	Beryl - columbite	Beryl $Be_3Al_2Si_6O_{18}$, columbite-tantalite $(Fe,Mn)(Ta,Nb)_2O_6$
	Beryl-columbite-phosphate	Beryl, columbite-tantalite, triphylite $LiFePO_4$
Complex	Spodumene	Spodumene $LiAlSi_2O_6$, beryl, tantalite, pollucite $(Cs,Na)_2Al_2Si_4O_{12}H_2O$
	Petalite	Petalite $LiAlSi_4O_{10}$, beryl, tantalite
	Lepidolite	Lepidolite $K(Li,Al)_3(Si,Al)_4O10(F,OH)_2$, topaz $Al_2SiO_4(F,OH)_2$, beryl, microlite $(Ca,Na)_2Ta_2O_6(O,OH,F)$, pollucite
	Amblygonite	Amblygonite-Montebrasite $(Li,Na)Al(PO_4)(F,OH)$, beryl, tantalite, pollucite
Albite-spodumene		Albite $NaAlSi_3O_8$, spodumene, cassiterite SnO_2, beryl
Albite		Albite, cassiterite, beryl

Table 2.1 Classification of the rare-element class pegmatites, after Cerný (1990).

A more simplified classification scheme was also proposed by Cerný (1992). This division of rare-element pegmatites into two families is based on the dominant chemical signature of pegmatites, namely NYF (niobium, yttrium, fluorine) and LCT (lithium, caesium, tantalum). All pegmatites in this study are of the LCT family, which are derived from peraluminous granites, in turn originating from melting of undepleted upper to middle supracrustals and basement gneisses.

- *Internal zoning of rare-element pegmatites*

The classic zoning pattern of rare-element pegmatites is generally agreed upon and contains any or all of the following units;

1. Fine to medium grained aplite border zone rich in albite + quartz + muscovite.
2. Coarse grained graphic zone of K-feldspar + quartz + albite wall zone.
3. Blocky K-feldspar + quartz intermediate zone.
4. Quartz-rich core zone, with megacrystic spodumene ± petalite ± pollucite.
5. Layered pegmatite-aplite unit.

6. Replacement units of fine to coarse grained K-feldspar + albite + quartz with Li-bearing micas.

2.2 Petrogenetic models

Peraluminous granites occur in compressional regimes of orogenic belts, within volcanic arc terrains, or sedimentary troughs along cratonic margins or rifts (Cerný and Meintzer 1988). In the early stages of orogenesis, basin closure leads to crustal thickening and melting of the lower crust, producing tonalite magmas. Following orogenic collapse, temperature gradients continue to increase until anatectic temperatures are reached in the mid- to upper crust. Partial melting of previously un-melted sedimentary and volcanic sequences ensues from the thermal effects of ascending batholiths and frictional heating along fault systems. Peraluminous granites originate from partial melting of aluminosilicate (muscovite) bearing source rocks. Enrichment in rare - alkali metals Li, Rb and Cs and other rare - lithophile elements such as Sn, Ta and Nb are consistent with a pelitic metasedimentary source (Cerný and Meintzer 1988). Hydrous, S-type peraluminous magmas are channelled along crustal-scale fault zones, which often have steep thermal gradients allowing the volatile enriched melts to differentiate, with highly evolved liquids ponding at the top of the melt column.

The processes that lead to the generation of pegmatites and their textures are less well understood and have been the subject of much discussion (London 1996). Jahns and Burnham (1969) recognised that fractional crystallisation alone could not account for the origin of pegmatites. More recently, London *et al.* (1989) presented a model based on experimental petrology data.

- *Jahns - Burnham model*

Jahns and Burnham (1969) developed a model which promoted a magmatic origin for pegmatites but also emphasised the role of hydrothermal fluids or 'vapours'. Simultaneous crystallisation of quartz, plagioclase and alkali feldspar was thought to occur in eutectic proportions, but in spatially separated zones. Jahns and Burnham (1969) viewed the transition from granitic to pegmatitic textures as a consequence of exsolution of a supercritical aqueous fluid (vapour), due to its saturation in the melt. The separated vapour phase transports residual elements as hydroxyls or halide complexes

and was proposed as the driving mechanism for partial replacement of crystalline phases and the development of pegmatite textures.

- *Non-eutectic crystallisation (London et al. 1989)*

In contrast, recent experimental petrology studies (London *et al.* 1989; London 1992) have demonstrated that there is no causal relationship between aqueous vapour saturation and the development of pegmatite textures. Instead, the London *et al.* (1989) model suggests that pegmatite crystallisation, in particular those of the rare-element class, results from distinctly non-equilibrium crystallisation caused by undercooling of a borosilicate, peraluminous melt. Undercooling of the melt can be caused by significant concentrations of non-haplogranite components such as lithium, boron, fluorine and phosphorus, which are capable of modifying melt properties, namely liquidus temperatures (London 1992), viscosity and density (Dingwell *et al.* 1996). These elements form stable hydroxide complexes with alkalis and Al, $[NaAl(OH)_3F]$, which considerably enhances Al mobility (Tagirov and Schott 2001) and thus inhibits crystal nucleation (especially feldspars) leading to larger pegmatitic crystals.

London (1996) noted that addition of lithium to granitic melts decreases the eutectic point by approximately 50°C. Boron, fluorine and phosphorus also lower solidus temperatures and thus extend magmatic crystallisation down to low temperatures, probably <500°C (London 1987; London *et al.* 1993). This undercooling of the melt and inhibiting of crystal nucleation means that even fractional crystallisation cannot be assumed. Instead, crystallisation of pegmatites is controlled by opposing factors of nucleation energy of the phases versus ligand strengths in the melt (London 1996).

Rare-element pegmatites are produced from the most evolved, mobile and low temperature melt. The timing of separation of the pegmatite melt from the parent granite is dependant on melt pressure and the structural behaviour of surrounding lithologies. Dynamic stress conditions are often prevalent because the level of pegmatite emplacement is commonly within the brittle-ductile transition zone of the crust (Dingwell *et al.* 1996). Primary crystallisation of rare-element pegmatites begins at upper stability limit of petalite and spodumene, in the range 700 - 600°C (London 1984, 1986), but transitional magmatic-hydrothermal activity may continue down to much lower temperatures.

- *Vapour phase*

Fluid inclusion studies, reviewed by London (1996), consistently reveal that the vapour phase of rare element pegmatites is dominantly aqueous with minor CO_2. In the Tanco rare-element pegmatite of Manitoba, London (1986) demonstrated that complete miscibility between melt and H_2O exists, and thus there may be a continuous transition from magmatic to hydrothermal conditions in the temperature range 470 - 420°C.

The crystallisation of tourmaline is critical to the timing and extent of exsolution of an aqueous vapour phase. Tourmaline crystallisation removes boron, a major flux component, which increases the solidus temperature of the remaining silicate liquid and causes a 'boron quench' (London 1986). Following this, exsolution of an aqueous fluid leads to precipitation of other alkali aluminosilicates (e.g. lithium mica/ lepidolite). The components remaining after tourmaline crystallisation will be divided according to the partition coefficients between the melt and vapour phase. Available data show that fluorine and phosphorus preferentially partition into melt, $D(F)^{melt/vapour} \approx 3$, $D(P)^{melt/vapour} \approx 10$, (London *et al.* 1993). However, the incompatibility of these components in crystalline phases often means they are enriched in late-stage pods, veins and hydrothermal haloes (London 1996).

From experimental studies, London (1996) suggested that rare-element pegmatite melts contain >2 wt% Li_2O and B_2O_3 in order to attain saturation in lithium aluminosilicates (petalite, spodumene) and tourmaline, respectively. Similarly, P_2O_5 concentrations probably reach 0.5 - 2.5 wt%, whereas F content of LCT family pegmatites may be around 1 wt% or less.

- *Interaction with country rocks*

Components such as B, Li, F and P are often lost to surrounding host rocks via an exsolved vapour phase. The most common products of this are veins and disseminated metasomatic haloes of holmquistite (Li-amphibole) or tourmaline, developed at near- solidus conditions (Shearer and Papike 1988).

Contamination of pegmatite melts with host rocks is perhaps less well studied (Shearer *et al.* 1986). However, where there is assimilation of country rocks into a pegmatite melt, clearly this could have significant effects on the compositional evolution of phases. In particular, the addition of Fe from mafic volcanic rocks or Fe-rich sediments (banded ironstones) may influence the composition of columbite-tantalite and tourmaline (Tindle and Breaks 1998; Tindle *et al.* in press).

2.3 Description of peraluminous granites and pegmatites in this study

The regional setting of peraluminous granites and pegmatites is discussed in Chapter 1. In this section, the mineralogy, textures and zoning of the granites and pegmatites are described, with particular attention paid to the samples used for $^{40}Ar/^{39}Ar$ and U-Pb geochronology.

2.3.1 Northwestern Superior Province

Rare-element pegmatites and associated peraluminous granites analysed in the NW Superior Province include the Severn River, Pakeagama Lake and Margot Lake suites. The Severn River peraluminous suite is intruded into the Favourable Lake greenstone belt, approximately 50km northwest of the Pakeagama Lake suite and 75km northwest of the Margot Lake suite. The Pakeagama Lake and Margot Lake suites are intruded into the highly attenuated northwestern and western arms of the North Spirit Lake greenstone belt. All of these suites are proximal to the Bear Head fault, a NW-SE trending shear zone within the North Caribou Terrain (figure 1.4).

- *Severn River pluton and pegmatites*

The Severn River pluton is a two-mica, tourmaline-bearing granite with dimensions of 10km long and a variable width between 0.5 - 2km (figure 1.4). The granite is foliated (190°), parallel with the regional trend. The dominant assemblage is quartz, K-feldspar, biotite and muscovite. Sample SS73 is a muscovite grain (4mm diameter) used for $^{40}Ar/^{39}Ar$ dating. Detailed field investigation by Breaks *et al.* (1999a) revealed the presence of garnet - biotite granitic pegmatites containing accessory muscovite, tourmaline and molybdenite. These deformed, boudinaged dykes strike parallel to the foliation of the host lithologies at 120°, with a maximum width of 10m. Host lithologies include tonalites and mafic metavolcanic sequences.

A second group of undeformed pegmatitic dykes contain biotite, garnet and abundant radial muscovite books suggesting a more fractionated composition. Contacts with the host rocks trend E-W, cross-cutting the main foliation suggesting that these are younger than the deformed pegmatites. Typical textures include blocky K-feldspar

crystals (30cm diameter), and radial quartz - tourmaline intergrowths. Sample SS70 is a coarse (10mm) muscovite grain used for $^{40}Ar/^{39}Ar$ dating.

- *Pakeagama Lake pluton and pegmatites*

The Pakeagama Lake pluton is a peraluminous granite (2 x 15km) locally containing accessory garnet and tourmaline (Breaks *et al.* 1999a). This medium- to coarse-grained pluton is moderately sheared and displays a granoblastic texture induced by deformation and recrystallisation associated with the closely situated Bear Head fault zone. Biotite granite in the SE contains abundant black enclaves rich in garnet and biotite, which are most probably derived from metavolcanic - metasedimentary source lithologies and are stretched parallel to the foliation within the granite, trending 110°. Progressive fractionation of the pluton occurs to the NW, with muscovite-bearing leucogranite becoming the dominant rock type. Sample 98-21a is a granite whole-rock sample containing fine grained (1 - 2mm) muscovite used for $^{40}Ar/^{39}Ar$ dating. The Pakeagama Lake pluton is also the assumed parent granite to the partially enclosed pegmatite located at the NW tip of the pluton, based on compositional and mineralogical similarities (Breaks *et al.* 1999a).

The Pakeagama Lake pegmatite is a heterogeneously deformed, steeply dipping, strongly zoned pegmatite body with associated pegmatite and aplite dykes. Breaks *et al.* (1999a) classified the pegmatite as a complex type - petalite subtype pegmatite. The present exposure of the pegmatite has a width of 50m and a strike length of 250m (figure 2.2). Five internal units were recognised within the main body, a complex type - petalite subtype pegmatite, with two types of related dykes outside the main pegmatite.

Internal Units

- Layered spodumene + quartz pegmatite - aplite

In the northwestern portion of the exposed pegmatite body, a layered pegmatite - aplite unit contains spodumene + quartz, with minor white mica and cassiterite. Sample SS107, taken from this unit, contains mica used for $^{40}Ar/^{39}Ar$ analysis. The contact of the aplite unit with the host rock banded ironstones is complex, in parts the boundary is sharp, in other areas gradational, with evidence of melting and assimilation of the ironstones. Metasomatic alteration of the ironstones is also evident, with tourmaline and biotite both occurring in the ironstone within 1 - 2m of the contact.

- Blocky K-feldspar (potassic) zone

This unit is exposed adjacent to the core zone and is dominated by K-feldspar megacrysts (up to 1m diameter). Similar to the core zone, original petalite megacrysts have now been replaced by fine-grained spodumene + quartz intergrowth, although these occur only sporadically. Minor quartz, white mica and green tourmaline occur interstitial to the K-feldspar megacrysts; SS100 is a mica sample used for $^{40}Ar/^{39}Ar$ analysis. Original textural relationships appear to be largely undeformed, although partial replacement of original phases by Na-rich albite has occurred around several K-feldspar megacrysts.

- K-feldspar + petalite zone

The majority of the pegmatite body is represented by this unit, comprised of K-feldspar megacrysts (up to 0.5m diameter) enveloped by fine-grained aggregates of spodumene + quartz replacing petalite pseudomorphs. Locally this unit is intensely deformed, exhibiting metamorphic shear fabrics. Samples SS20, SS94, SS106a, SS115 and SS116 were selected for $^{40}Ar/^{39}Ar$ analysis. SS20 and SS94 are taken from the undeformed part of this unit in the southeastern portion of the pegmatite exposure, containing the assemblage quartz + K-feldspar + apatite + muscovite. Towards the central part of the main pegmatite mass, sample SS106a was taken from a mica + green tourmaline vein, within the K-feldspar + petalite zone.

Samples SS115 and SS116 were taken from a highly deformed part of the pegmatite containing the assemblage quartz + K-feldspar + tourmaline + muscovite ± garnet. Mica is commonly <5mm and is aligned parallel to the metamorphic fabric as in sample SS115 or else deformed around K-feldspar megacrysts as in sample SS116. Quartz porphyroblasts are aligned with long axes parallel to the shear orientation, whereas tourmaline crystals are randomly oriented and appear to have grown post-deformation. A manganotantalite grain with dimensions of 4 x 2 x 2mm, which occurred as an inclusion within a former petalite megacryst was collected for U-Pb isotopic analysis (sample SS137).

- Quartz-rich wall zone

The wall zone has dimensions of 40m by 13m. The mineralogy of the wall zone is dominated by generally anhedral quartz grains (70-80 modal %) that are enveloped by

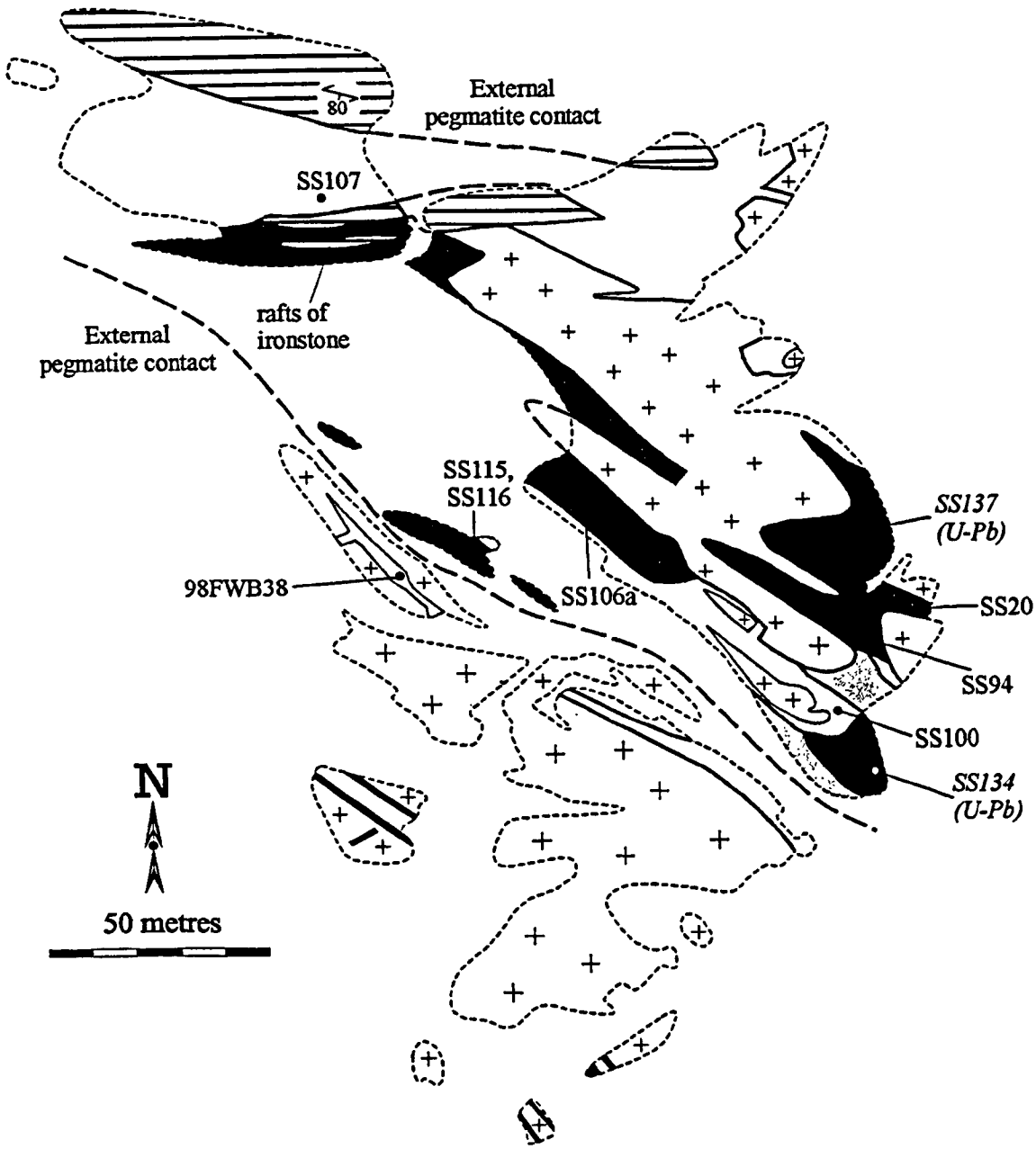

Figure 2.2 Exposure map of the Pakeagama Lake pegmatite, modified from Breaks et al. (1999a) showing the location of mica samples used in $^{40}Ar/^{39}Ar$ geochronology and columbite-tantalite grains collected for U-Pb geochronology (shown in italics).

External lithologies

- Banded ironstones
- Peraluminous granite
- Tourmaline + muscovite aplite dykes
- Tourmaline + K-feldspar + albite ± pollucite dykes

Internal pegmatite units

- Blocky K-feldspar (potassic) zone
- K-Feldspar + petalite zone
- Spodumene + quartz pegmatite-aplite
- Quartz-rich wall zone
- Spodumene + quartz core zone

centre of the pegmatite. A parent granite to the Sandy Creek pegmatite has not been recognised.

A series of small (<1m width) boudinaged dykes occur approximately 20km east of the Sandy Creek pegmatite. A sample of muscovite (SS1) was taken from a pegmatite containing abundant tourmaline, herein named the Wenesaga pegmatite. The dyke obliquely cross-cuts the foliation of the host rock banded ironstones. The Wenesaga Lake stock is the only exposed S-type granite pluton that might be considered parental to these pegmatites.

- *Treelined Lake pegmatite*

The Treelined Lake granite is an irregularly shaped peraluminous pluton located in the core of the Umfreville - Conifer Lakes granulite zone of the English River Subprovince (Pan and Breaks 1997). Mineralogical content of the Treelined Lake granite is variable, grading from orthopyroxene - garnet bearing granite in the main suite, into muscovite - biotite granite within a prominent apophysis to the southwest. Close to the contact with the Separation Lake greenstone belt, the southwest apophysis of the Treelined lake granite contains several *in-situ* pegmatites that contain rare-element enriched minerals. The most notable occurrence is a 1m wide beryl-type pegmatite segregation with miarolitic cavities containing tourmaline, fluorapatite and topaz. A graded contact with the biotite - garnet granite is observed. Sample SS42b (figure 2.3) is a muscovite crystal (10mm) taken from the core zone of quartz + biotite + K-feldspar (20cm).

- *Separation Rapids pluton and pegmatites*

In the Separation Lake area of the western Superior Province, the boundary between the metasedimentary English River Subprovince to the north and the tonalite gneiss dominated Winnipeg River Subprovince to the south is interjected by the Separation Lake greenstone belt.

Intruded into the Separation Lake greenstone belt are several beryl type and complex type - petalite subtype rare-element pegmatites, collectively named the Separation Rapids pegmatite group (Breaks and Tindle 1996). The pegmatites are clustered around the peraluminous, S-type granite, Separation Rapids pluton (figure 2.3). Tindle and Breaks (1998) consider the Separation Rapids pegmatite group to be an

eastward extension of the Cat Lake - Winnipeg River pegmatite field, which contains the Tanco rare-element pegmatite at Bernic Lake, Manitoba.

Separation Rapids pluton

The Separation Rapids pluton is a 4km^2 oval shaped intrusion that contains a core of K-feldspar porphyritic, garnet bearing granite enveloped by a larger area of pegmatitic leucogranite interlayered with potassic pegmatite, sodic aplite and fine grained leucogranite. Mineralogy and textures within the outer zone of the pluton are heterogeneous, containing the assemblage muscovite + garnet ± cordierite ± tourmaline. Grain sizes range from 2 - 5mm within aplites, whereas pegmatitic facies contain K-feldspar megacrysts up to 1m in diameter.

Within the Separation Rapids pluton, two localities were sampled for mica $^{40}Ar/^{39}Ar$ analysis. Sample SS35b is a coarse (7mm) muscovite grain from pegmatitic leucogranite at locality 93-249 within the outer zone of the pluton. Situated at the eastern end of the pluton, this locality is notable for cordierite pseudomorphs up to 8cm across, replaced by garnet + chlorite + biotite. Interlayered with the pegmatitic leucogranite are fine grained leucogranite and potassic pegmatite.

SS36 is a sample of muscovite (6cm diameter) from the 3m thick potassic pegmatite at locality 93-260, along the southwest margin of the pluton. Muscovite grows on the periphery of large, elongate (35cm by 1m) K-feldspar megacrysts oriented perpendicular to layering. These textures, together with the presence of rare-element enriched pods of muscovite + quartz + albite, led Breaks and Tindle (*in press*) to suggest that this represents the apical part of the pluton.

Separation Rapids pegmatite group

Systematic documentation of over 70 rare-element mineral occurrences and a comprehensive study of mineral chemistry has been carried out by Breaks (1993); Breaks and Tindle (1996, 1997); Tindle and Breaks (1998, 2000). This led to the recognition of two distinct pegmatite swarms surrounding the Separation Rapids pluton (figure 2.3); named the eastern subgroup and southwestern subgroup (Breaks and Tindle 1997). Within each of these subgroups, beryl type and complex type - petalite subtype pegmatite zones were recognised.

Subsequent investigation of the Separation Rapids pegmatite group enabled Tindle and Breaks (1998) to characterise individual pegmatites on the occurrence of Fe-

or Mn- varieties of the columbite-tantalite group. This led to the classification of Fe-suite and Mn-suite pegmatites within the same pegmatite field, although, as stated by Tindle and Breaks (1998), neither of these suites equate solely with beryl or petalite pegmatites, nor are they spatially separated.

Eastern pegmatite subgroup

Pegmatite 265 is one of the eastern subgroup, beryl zone pegmatites. Mica sample SS34a was collected from the wall zone of this undeformed, 8m wide fluorapatite + garnet + biotite + muscovite pegmatite, which also contains albite pods with minor beryl, tourmaline, microlite and wodginite. Tindle and Breaks (1998) report the occurrence of almost end member manganotantalite, making pegmatite 265 part of the Mn-suite.

Within the petalite zone, Marko's pegmatite is an undeformed, 8 by 130m, Mn-suite dyke that displays exceptional internal zoning (figure 2.4). Five primary units are dominated by a 3 - 6m wide core zone of megacrystic K-feldspar + petalite, enveloped by a 1m thick wall zone containing the assemblage beryl + muscovite + albite + quartz, with sparse pollucite. Accessory mineralogy of the wall zone includes several Nb-Ta phases: wodginite, microlite and columbite-tantalite (Tindle and Breaks 1998). Replacement units occur as oval patches and veins that clearly crosscut the core zone megacrysts. Two samples of white mica were taken from Marko's pegmatite for $^{40}Ar/^{39}Ar$ analysis. SS37 was recovered from the wall zone and SS40 from the core zone. In each case, care was taken to select samples that were clearly part of the primary assemblage rather than the replacement units. Sample 94-44MU5 is a manganotantalite grain used for U-Pb isotopic analysis, collected from the wall zone.

Proximal to the boundary of the Separation Lake greenstone belt with the English River Subprovince, several petalite subtype pegmatites display a hetrogeneous, dextral, ductile shear fabric (Breaks and Tindle, *in press*). James' pegmatite is a deformed, petalite subtype pegmatite, located approximately 4km northeast of the Separation Rapids pluton (figure 2.3). Ferrotantalite is the dominant oxide species, which places James' pegmatite as part of the Fe-suite of Tindle and Breaks (1998). Sample 93-276 is a coarse (9mm) undeformed white mica crystal from the wall zone, used for $^{40}Ar/^{39}Ar$ dating.

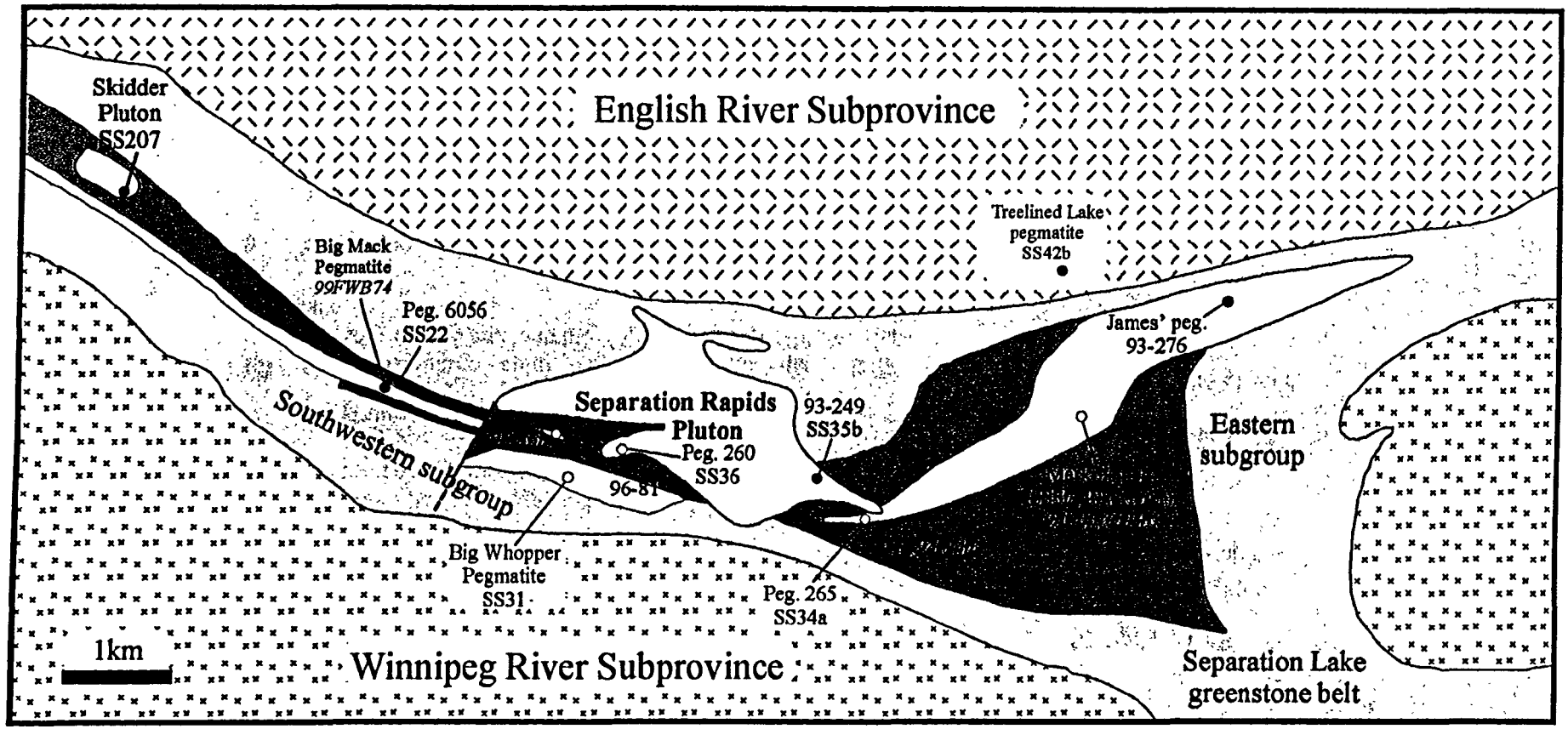

Figure 2.3 Map of the Separation Rapids pegmatite group showing the location of mica samples used in Ar-Ar analysis (circles) and columbite-tantalite used in U-Pb analysis (italics). Pegmatite names are followed by sample numbers (e.g.SS34a). After Breaks and Tindle (in press). N.B. sample 96-86b used for Ar-Ar and U-Pb analysis.

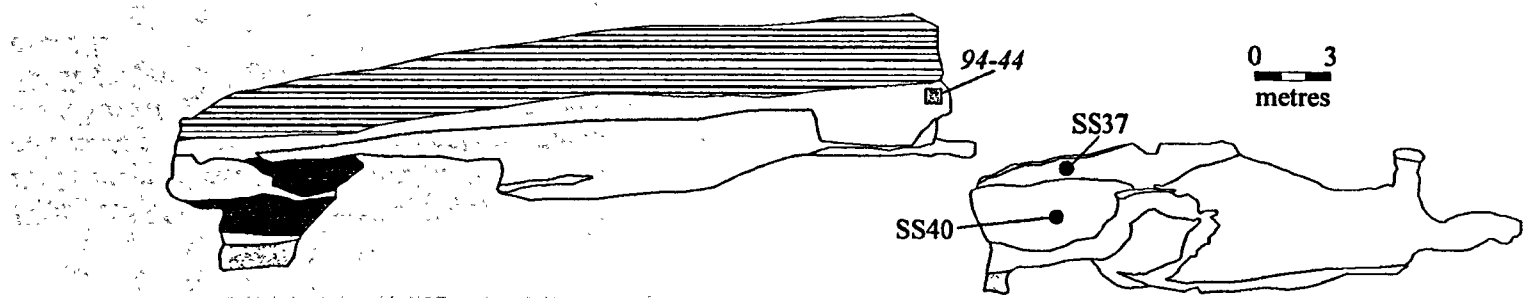

Primary Units

Wall Zone: beryl + muscovite + albite + qtz ± tourmaline ± wodginite ± apatite

Core Zone: Petalite megacrysts, blocky K-feldspar interstitial qtz + muscovite

Fine-grained granite

Layered pegmatite - aplite: beryl + muscovite + qtz + albite accessory apatite and tantalite. Contains garnet + biotite rich-veins

Columbite-tantalite sample for U-Pb geochronology

Muscovite sample for $^{40}Ar/^{39}Ar$ geochronology

Secondary Unit

Muscovite + albite replacement unit

Host Rocks

Banded ironstones

Mafic metavolcanics

Figure 2.4 Marko's pegmatite (main exposure) from the eastern petalite zone of the Separation Rapids pegmatite group. Unpubished map of F.W. Breaks, Ontario Geological Survey.

Southwestern pegmatite subgroup

The SW subgroup comprises several narrow (3m wide) beryl type pegmatites, with larger bodies of pegmatitic leucogranite up to 300m in length. Sample 96-86b is taken from a late-magmatic pod within a 150 by 300m oval stock of undeformed pegmatitic leucogranite, outside the Separation Rapids pluton. This pegmatitic granite body is part of the Fe-suite of Tindle and Breaks (1998). Coarse-grained muscovite (10mm) was collected for $^{40}Ar/^{39}Ar$ analysis and a single euhedral columbite grain (1 x 3 x 5mm) was separated for U-Pb dating. Sample SS22 is a 5cm diameter mica crystal taken from pegmatite 6056, an undeformed beryl type pegmatite. Pegmatite 6056 is part of the Fe-suite of Tindle and Breaks (1998). Pegmatite 96-81 (Fe-suite) is also an undeformed beryl type pegmatite from which two grains (1mm) of white mica were used in $^{40}Ar/^{39}Ar$ analysis.

Complex type - petalite subtype pegmatites in the SW subgroup are characterised by intensely deformed *en-echelon* pegmatite lenses. The largest of these bodies are the Big Whopper pegmatite (Mn-suite), 60 by 350m, and the Big Mack pegmatite (Fe-suite), 30 by 250m (figure 2.3). Both pegmatites are targets for economic recovery of rare-lithophile elements, e.g. Li, Cs, Ta (Breaks and Tindle *in press*). The mineralogical and structural features of the Big Whopper and Big Mack pegmatites are described by Breaks and Tindle (1997). Strong ductile deformation is evident throughout both pegmatites, which has induced recrystallisation of petalite and K-feldspar. Isoclinal folding of mafic metavolcanic 'rafts' indicates that structural thickening may have doubled the original width of the pegmatites. It is worth noting that there are many similarities between the Big Whopper/ Big Mack pegmatites and other 'giant' rare-element pegmatites such as Bikita, Zimbabwe (Cooper 1964) and Greenbushes, Australia (Partington 1990; Partington *et al.* 1995). Comparable primary minerals such as petalite and low temperature minerals such as eucryptite ($LiAlSiO_4$) and the zeolite mineral, bikitaite ($LiAlSi_2O_6H_2O$) indicate prolonged crystallisation/hydrothermal histories. Structural features include heterogeneous ductile deformation and boudinaged lenses, which suggest emplacement within the brittle-ductile transition zone of the crust.

Mica sample SS31 was recovered from the petalite + K-feldspar + muscovite + quartz core zone of the Big Whopper pegmatite. Two small grains (2mm) that are part of the ductile deformed fabric, characteristic of the main mass of the pegmatite were used in $^{40}Ar/^{39}Ar$ analysis.

Within the quartz + K-feldspar + petalite core zone of the Big Mack pegmatite, quartz-rich patches up to 0.3 by 1m occur sporadically and contain rare platy black oxide grains. Sample 99FWB74 is a 1 x 1 x 10mm columbite-tantalite grain used for U-Pb dating, from a quartz-rich replacement patch containing recrystallised petalite.

Deformation in the Separation Rapids group

As noted by Breaks and Tindle (1997), intense ductile deformation has affected a number of pegmatites in the Separation Rapids group. This has induced recrystallisation of petalite, K-feldspar, quartz and garnet with pressure shadow mineral growth within the two largest pegmatites, the Big Whopper and Big Mack pegmatites. Furthermore, boudinage of large pegmatite bodies into several *en echelon* lenses suggests emplacement within a high strain zone. However, not all of the pegmatites within the Separation Rapids group are deformed. In particular, Marko's pegmatite (described above) shows well developed primary pegmatite textures and a complete absence of ductile deformation. Similarly, the Separation Rapids pluton is undeformed suggesting that deformation was extremely localised.

- *Skidder Pluton*

The Skidder pluton is a small body of muscovite + biotite-bearing, peraluminous granite (figure 2.3), initially mapped by Blackburn and Young (1993). The northwestern part of this 0.3 by 1.5 km stock reveals apophyses of medium- to coarse-grained granite that contain *in situ* segregations of beryl type pegmatite. Biotite grains (2 –3mm) were selected for $^{40}Ar/^{39}Ar$ analysis (sample SS207), taken from the main mass of biotite granite.

- *Graphic Lake pegmatite*

The Graphic Lake pegmatite is located within the Wabigoon Subprovince (figure 1.8). Fine to medium grained (<5mm) garnet - muscovite granite is crosscut by the Graphic Lake granitic pegmatite, which displays heterogeneous deformation and is largely barren of rare-element mineralisation. Sample SS89 is a coarse (8mm) muscovite grain from the pegmatite.

- *Ghost Lake batholith and Mavis Lake pegmatite group*

The Ghost Lake batholith has been described as a late-tectonic, peraluminous S-type granite that displays genetic links with the nearby Mavis Lake group rare-element pegmatites (Breaks and Moore 1992). The regional setting of this batholith and its associated pegmatites is between two major litho-tectonic domains, namely the tonalite-gneiss dominated Winnipeg River Subprovince and the greenstone-rich Wabigoon Subprovince (figure 1.8). Foliation within the batholith is consistent with the broadly E-W striking regional foliation.

The Ghost Lake batholith is made up of eight internal units containing cordierite-biotite granite in the most primitive units, grading into chemically evolved tourmaline - muscovite bearing pegmatitic granite (figure 2.5). Breaks and Moore (1992) describe the geochemical features, which include high SiO_2 (>70%), Al_2O_3 (14 – 20 wt%), with low CaO, MgO and Fe. The Ghost Lake batholith has Al_2O_3/ (CaO + Na_2O + K_2O) ratios between 1.19 - 1.48, which is within the range of strongly peraluminous granites defined by Sylvester (1998).

Segregation of blocky K-feldspar + quartz pegmatite occurs sporadically within the Ghost Lake batholith (figure 2.5). These irregular masses are usually <0.5m width and up to 2m length. Sample SS50a is a muscovite book (1cm diameter) taken from a muscovite + tourmaline bearing pegmatite unit GLB-2, which cross-cuts the primitive biotite granite, unit GLB-1 of Breaks and Moore (1992).

Chemically more evolved leucogranites occur at the eastern end of the Ghost Lake batholith (figure 2.5), units GLB-4 to -8 of Breaks and Moore (1992). A large outcrop situated close to the Dryden Airfield, off Highway 601, consists of fine-grained leucogranite (GLB-5) with accessory garnet and tourmaline. SS55 is a sample of muscovite collected from pegmatitic leucogranite, situated near the margin of the batholith within the interior beryl pegmatite zone. The leucogranite grades into and is cross-cut by potassic pegmatite units GLB-6 and -7 containing K-feldspar crystals up to 15cm diameter that project into quartz masses. Accessory phases include euhedral tourmaline, garnet and green beryl up to 3 by 8cm.

The Mavis Lake group pegmatites comprise an 8km by 1.5km zone extending eastward from the most evolved portion of the Ghost Lake batholith. Systematic changes in mineralogy and chemistry enabled Breaks and Moore (1992) to define four pegmatite zones including (1) Interior beryl zone, (2) Beryl - columbite zone, (3) Spodumene - beryl - tantalite zone, (4) Albite type pegmatite zone.

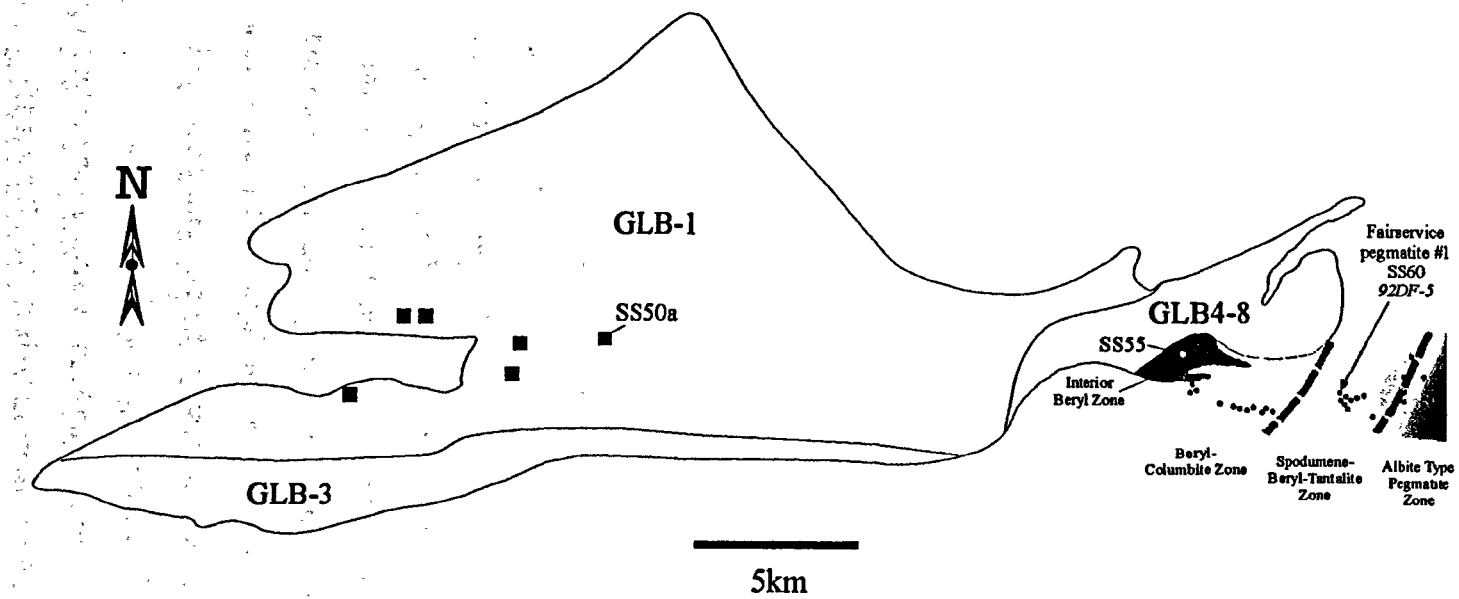

GLB-1 Cordierite-biotite granite

■ GLB-2 internal pegmatites

• External Mavis Lake group pegmatites

GLB-3 Biotite-muscovite-garnet granite

GLB4-8 Tourmaline-muscovite leucogranite and potassic pegmatite units.

Figure 2.5 Internal units of the Ghost Lake batholith and zones of the Mavis Lake pegmatite group, after Breaks and Moore (1992). Mica sample locations for Ar-Ar and U-Pb geochronology are shown (columbite sample for U-Pb in italics).

Fairservice pegmatite #1 is the most notable occurrence, located within the Spodumene - beryl - tantalite zone. This albite - spodumene type pegmatite, which displays crude internal zoning, has exposed dimensions of 12 by 76m. The contact of the dyke has a strike at 074°, sub-parallel to the foliation of the host mafic metavolcanic sequences.

Breaks and Janes (1991) have previously described the detailed mineralogy of Fairservice pegmatite #1, which includes the following features. A *Quartz-rich core zone* characterised by blocky K-feldspar up to 30cm, green primary spodumene with albite-rich rims and lesser tourmaline, garnet and beryl. SS60 is a muscovite sample taken from the Quartz-rich core zone, used for $^{40}Ar/^{39}Ar$ dating. A *Spodumene + albite + quartz zone* envelops the core zone and comprises almost 50% modal abundance of spodumene with minor feldspar and pockets of sodic aplite. Sample 92DF-5 is a manganocolumbite grain with dimensions of 3 x 2 x 2mm taken from the spodumene + albite + quartz unit of Fairservice pegmatite #1, selected for U-Pb isotopic analysis. A third primary internal *potassic pegmatite zone,* rich in K-feldspar with minor interstitial spodumene occurs mainly in the SE portion of the pegmatite. Irregular masses of *albite-rich replacement zones* occur within the dyke and commonly contain green mica, white beryl and albite after spodumene.

2.3.3 Southern Superior Province

- *Case pegmatite*

Located in the north of the Abitibi Subprovince (figure 1.9), the Case pegmatite is a 30m wide, undeformed, complex type - spodumene subtype pegmatite. This pegmatite is situated within the Case batholith, which, because of its tonalitic composition is considered an unlikely parent. The Case pegmatite contains quartz, metre sized K-feldspar crystals, green spodumene blades up to 20cm long, beryl, columbite and muscovite. Sample SS45 is 9mm muscovite grain collected for $^{40}Ar/^{39}Ar$ geochronology.

2.4 Summary

The complex petrogenetic processes involved in the formation of peraluminous granites and rare-element pegmatites commence with partial melting of supracrustal sequences to produce a peraluminous granite melt. Ascent and fractional crystallisation of the granite is followed by escape of the most chemically evolved residual melts into surrounding country rocks that produces a swarm of pegmatitic dyke intrusions. High concentrations of flux components (Li, B, F and P) dramatically reduces solidus temperatures and allows magmatic processes to continue below 500°C. This promotes extreme levels of enrichment in other rare-elements (Nb, Ta, Cs). The silicate melt may be completely miscible with a vapour phase throughout much of the crystallisation history, co-existing until the latest stages of magmatic processes and perhaps even down to nominally 'hydrothermal' temperatures, 470 - 420°C (London 1986). At this stage, the primary magmatic assemblages may be replaced or altered by secondary processes such as exsolution and precipitation of a vapour phase.

As a result of these complex processes, rare-element class pegmatites develop a heterogeneous mineral assemblage including quartz, feldspar, mica, lithium aluminosilicates (petalite, spodumene), beryl, Nb-Ta phases (columbite-tantalite), borosilicates (tourmaline), phosphates (amblygonite-montebrasite, apatite) and rare caesium minerals (pollucite).

In the next chapter, chemical data from electron microprobe analysis of white mica is used to determine the crystallisation history of the Pakeagama Lake and Separation Rapids pegmatites. These pegmatites display a wide range of mineralogy and textures typical of rare-element pegmatites.

3. Geochemistry of Mica in the Pakeagama Lake and Separation Rapids Pegmatites

3.1 Introduction

Understanding the petrogenesis of rare-element pegmatites first requires knowledge of the different mineralogical zones of a pegmatite or group of pegmatites. Once this is established, geochemical studies of pegmatites often focus upon a specific mineral group in order to determine compositional changes during crystallisation and processes such as interaction between the melt and a fluid phase or contamination from host rocks.

This chapter considers the geochemical evolution of micas in the muscovite - lithium muscovite - zinnwaldite - lepidolite series. Micas are one of the most common rock-forming mineral groups, stable over a wide range of pressure and temperature. They have a wide range of possible compositions and an ability to exchange components with fluids or solid phases as external conditions change (Tischendorf *et al.* 1997). Micas are also hydrous and therefore chemically responsive to changes in oxygen fugacity, water, fluorine and other volatiles. As such, micas are good indicators of the physico-chemical environment in which they grew. This is particularly important in the case of peraluminous granites and rare-element pegmatites, which may have undergone a long history of crystallisation under non-eutectic and non-equilibrium magmatic conditions (London 1992).

3.2 Petrographic descriptions

3.2.1 Pakeagama Lake pegmatite

The Pakeagama Lake pegmatite is a complex type - petalite subtype pegmatite. Enrichment of the pegmatite in rare-elements is reflected in the mineralogy as described

by Breaks *et al.* (1999a). Petalite pseudomorphs, replaced by spodumene + quartz intergrowth attests to the lithium-aluminosilicate saturation common to all complex type rare-element pegmatites. The occurrence of tourmaline, amblygonite-montebrasite, fluorapatite and topaz within the Pakeagama Lake pegmatite is evidence for significant amounts of boron, phosphorus and fluorine in the melt. There is also mineralogical evidence for appreciable concentrations of caesium, from the presence of pollucite (Breaks *et al.* 1999a). White mica is a common phase within all zones of the pegmatite, which allows a wide range of samples to be analysed from the locations shown in figure 3.1.

K-feldspar + petalite zone (Samples SS17, SS20, SS94, SS98, SS99, SS113, SS114, SS116, SS117)

Mica from this zone displays varied texture and grain size. Towards the southeast portion of the exposed pegmatite, coarse books (1-2cm) of colourless mica occur within petalite megacrysts and within quartz + K-feldspar + apatite assemblages. Mica forms well developed books grown in random orientation suggesting magmatic growth. Backscattered electron images reveal that mica grains have core zones surrounded by compositionally distinct rims (figure 3.2a).

The assemblage quartz + tourmaline + K-feldspar + muscovite occurs within the central portion of the pegmatite exposure. Minerals form an aligned deformation fabric containing fine-grained micas (<5mm). Garnet + tourmaline + mica aplite veins within this zone contain coarse muscovite porphyroblasts up to 1cm width. Aplite veins with the assemblage quartz + tourmaline + mica have highly sheared fabrics and contain mica books (>5mm) with undulose extinction, which may represent deformation related metamorphic mineral growth. Zoning is present, but commonly occurs along fractures or as thin rims (figure 3.2b).

Blocky K-feldspar (potassic) zone (Samples SS100, SS101)

Mica from this zone occurs as two distinct types recognisable in the field. The first is transparent mica that forms small books (5-7mm) as inclusions within K-feldspar megacrysts. The second type occurs as interstitial grains between large (0.5m) K-feldspar megacrysts. These micas are lavender coloured with a fine-grained (1-2mm) aggregate texture, which occurs in thin veins approximately 2mm wide. Compositional zoning occurs in both types of mica, with distinct core zones and rims.

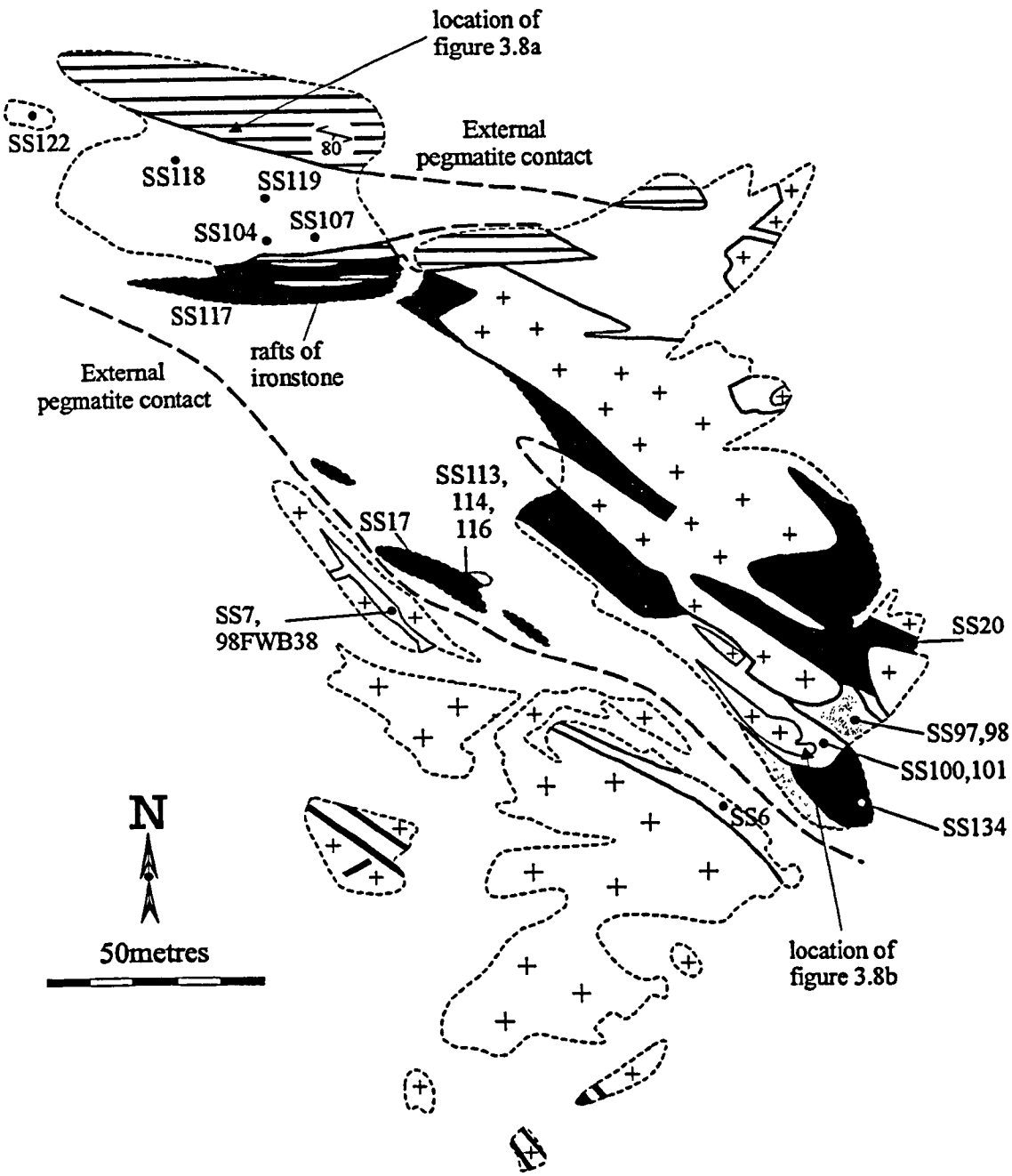

Figure 3.1 Exposure map of the Pakeagama Lake pegmatite, modified from Breaks et al. (1999a) showing the location of mica samples used in electron microprobe analysis.

External lithologies

- Banded ironstones
- Peraluminous granite
- Tourmaline + muscovite aplite dykes
- Tourmaline + K-feldspar + albite ± pollucite dykes

Internal pegmatite units

- Blocky K-feldspar (potassic) zone
- K-Feldspar + petalite zone
- Layered spodumene + quartz pegmatite-aplite
- Quartz-rich wall zone
- Spodumene + quartz core zone

Layered (spodumene + quartz) pegmatite - aplite (SS104, SS107, SS118, SS119, SS122)

This unit dominates the NW part of the exposure (figure 3.1). Coarse books (5-7mm) of colourless mica are associated with feldspar and spodumene, mainly within the pegmatitic layers. At the boundary with fine-grained aplite layers, mica displays undulose extinction indicating deformation. Zoning of the micas is present, but with only very thin rims (figure 3.2c).

Quartz-rich wall zone (SS97, SS98)

Mica occurs as coarse-grained books (5mm) within the quartz + amblygonite (montebrasite) + beryl + apatite + tourmaline primary assemblage of the wall zone. Also present are fine-grained aggregates (1-2mm) of lavender coloured mica, found between monomineralic quartz patches and beryl crystals. Zoning is prevalent in all mica from this zone, with well developed rims that are wider when proximal to fractures.

Spodumene + quartz-rich core zone (SS134)

Mica is relatively uncommon within the main part of the core zone. However, cross-cutting veins contain abundant, fine-grained (1-2mm), lavender coloured mica. These micas have widespread development of rims, displaying sharp boundaries with the cores (figure 3.2d). Mica grows as interstitial grains between monomineralic quartz masses.

Tourmaline + muscovite aplite dykes (SS6, SS7, 98FWB38)

These external dykes contain a fine-grained K-feldspar + quartz aplite assemblage, with porphyroblasts of muscovite (7-10mm), tourmaline and apatite. An aligned mineral fabric is prevalent with quartz and feldspar separated into bands. Porphyroblasts occur along the boundaries of these bands. Zoning in the mica from this dyke does not persist along the whole boundary of grains (figure 3.2e).

- ***Backscattered electron images***

Backscattered electron (BSE) images collected with the electron microprobe reveal compositionally distinct cores and rims (figure 3.2). Chemical analyses confirm that the cores are muscovite, whereas the rims are commonly lithian-muscovite, zinnwaldite or lepidolite composition (table 3.1). In the majority of grains analysed, the

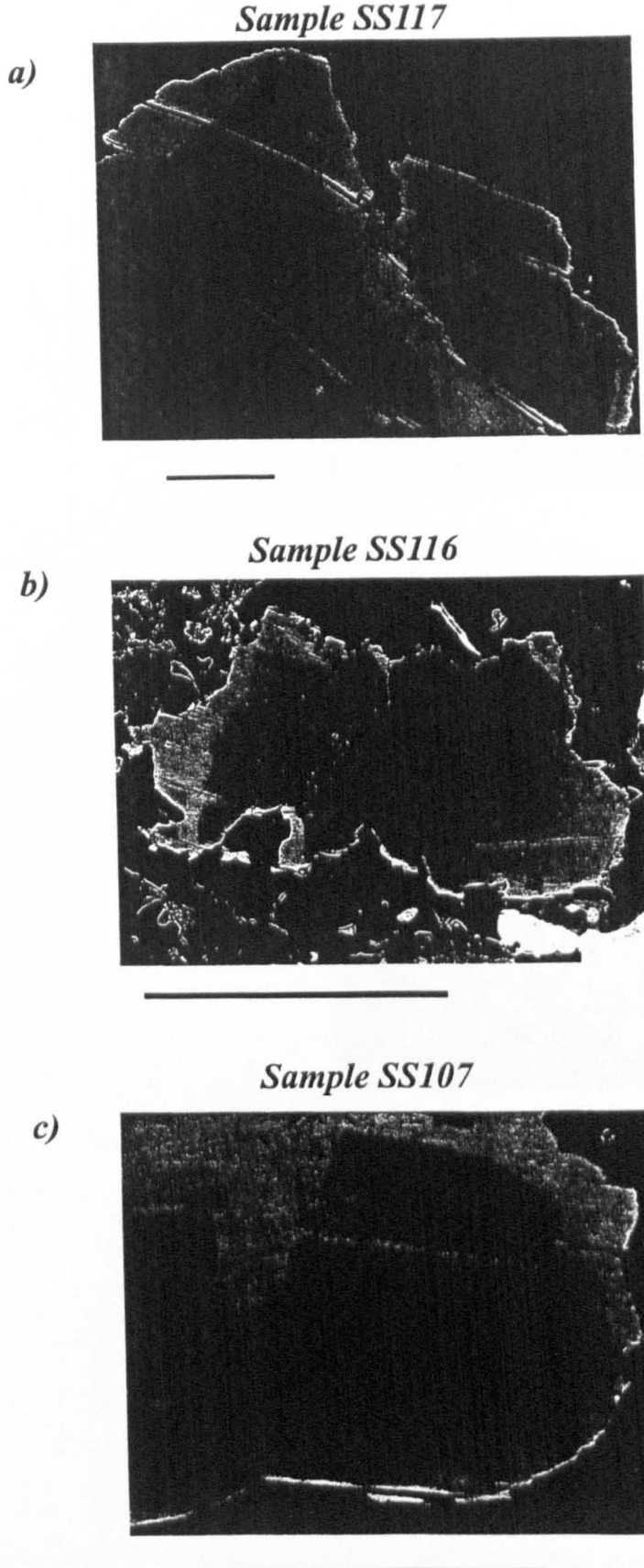

Figure 3.2 Backscattered electron images of micas from the Pakeagama Lake pegmatite; a) and b) K-feldspar + petalite zone. c) Layered spodumene + quartz pegmatite-aplite. Dark grey areas are muscovite, light grey areas are Li-muscovite - lepidolite composition. Note the variable width of the rim zones and propogation along fractures indicating replacement of original muscovite. Scale bars are 500 microns.

Sample SS134

d)

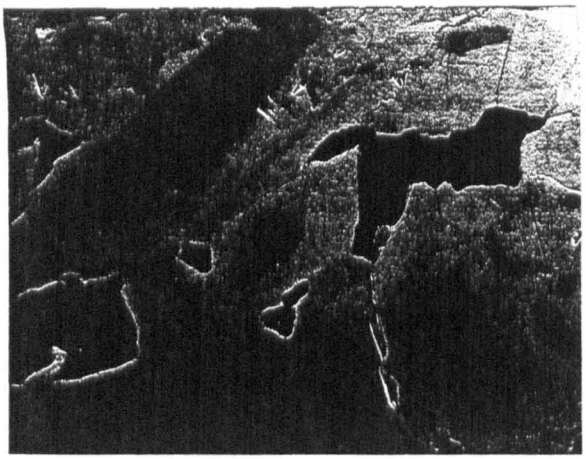

Sample 98FWB38

e)

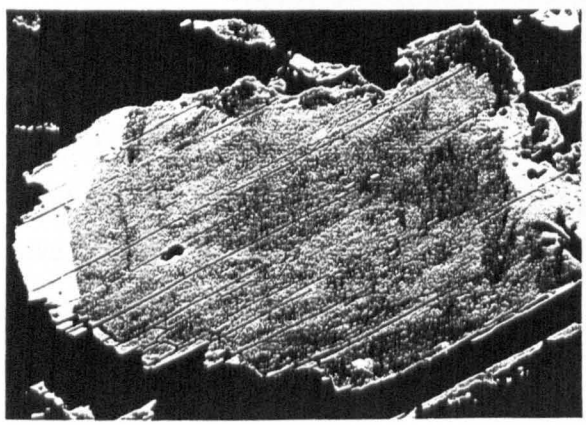

Figure 3.2 continued. Backscattered electron images of micas from the Pakeagama Lake pegmatite; d) Lepidolite vein cross-cutting the core zone. e) Tourmaline + muscovite aplite dyke. Dark grey areas are muscovite, light grey areas are Li-muscovite - lepidolite composition. Scale bars are 500 microns.

boundary between core and rim is sharp, which could indicate a hiatus in mica crystallisation, over which time the melt had changed composition. However, the Li-muscovite - lepidolite rims have not formed on all grain margins. Propagation of the zoning along fractures is common, but cleavage is continuous through the zones, suggesting that these could be a replacement of the original grain by a secondary process. Clearly, the Li-muscovite - lepidolite rims represent significant changes in the composition of the pegmatite melt-fluid. These features are examined further in section 3.3.2, using BSE images and chemical analyses to quantify chemical variations of the different mica species.

3.2.2 Separation Rapids pegmatite group

The Separation Rapids pegmatite group comprises beryl type and complex type - petalite subtype pegmatites of the rare-element class. Tindle and Breaks (1998, 2000) have divided the Separation Rapids pegmatite group into two suites, *viz.* Fe-suite and Mn-suite, based on the occurrence of Fe- and Mn- varieties of columbite-tantalite minerals. The occurrence of fluorine-rich minerals such as microlite, topaz and fluorite led Tindle and Breaks (1998) to conclude that the Mn-suite pegmatites crystallised from a melt with higher fluorine concentration than the Fe-suite pegmatites, which exhibit a restricted occurrence of F-rich minerals.

Muscovite is abundant in many of the >70 rare-element pegmatites of the Separation Rapids group. For this study, mica has been analysed from selected pegmatites, shown in figure 3.3, that are representative of the spatial, mineralogical and chemical subgroups defined by the previous studies.

Fe-suite (SS35b, 96-81, SS22, Big Mack pegmatite, 93-276)

White mica samples have been analysed from the following locations; pegmatitic leucogranite (sample SS35b) from the Separation Rapids pluton containing the assemblage quartz + K-feldspar + biotite + muscovite + garnet + cordierite. Pegmatite 96-81 and 6056 are beryl type pegmatites containing the assemblage quartz + K-feldspar + biotite + muscovite + garnet + beryl. Mica from pegmatite 96-81 is fine-grained (~2mm) whereas large books (5cm) form part of the primary assemblage in pegmatite 6056 (sample SS22).

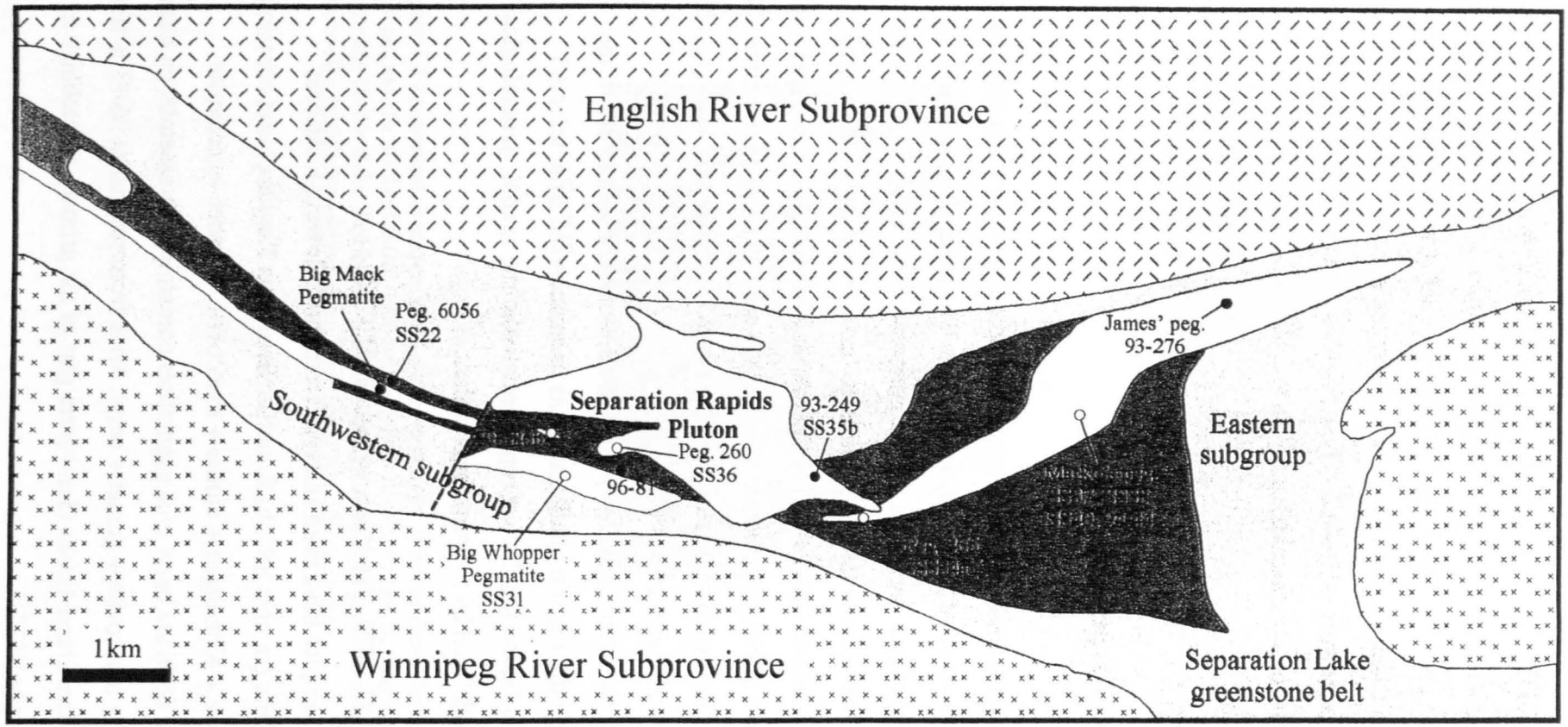

Figure 3.3 Map of the Separation Rapids pegmatite group showing the location of mica samples analysed by electron microprobe. Pegmatite names are followed by sample numbers (e.g.SS34a). After Breaks and Tindle (in press).

Sample SS34a

a)

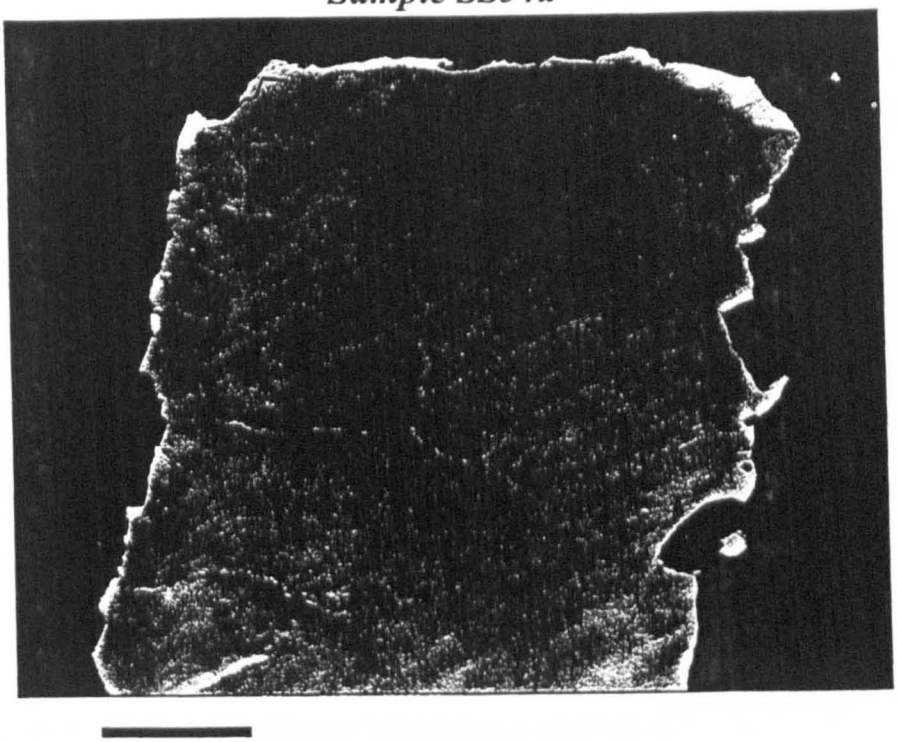

Sample SS34a

b)

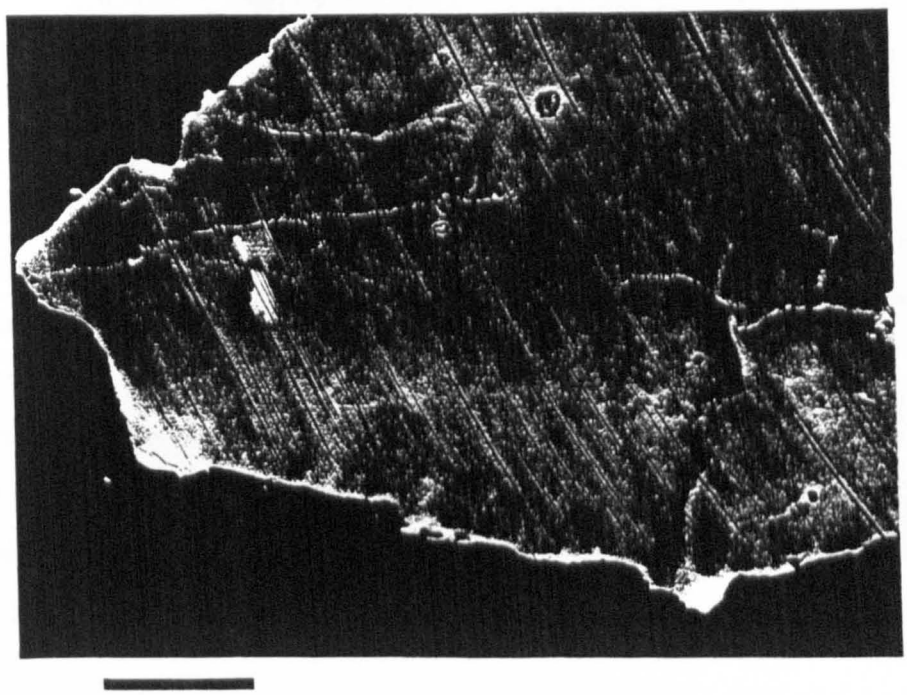

Figure 3.4 Backscattered electron images of mica from the Separation Rapids pegmatite group. a) and b) Mica sample SS34a from pegmatite 265, part of the Mn-suite. Note the thin rim zones (bright regions) and sub-grain boundaries. Scale bars are 500 microns.

Sample 94-44

c)

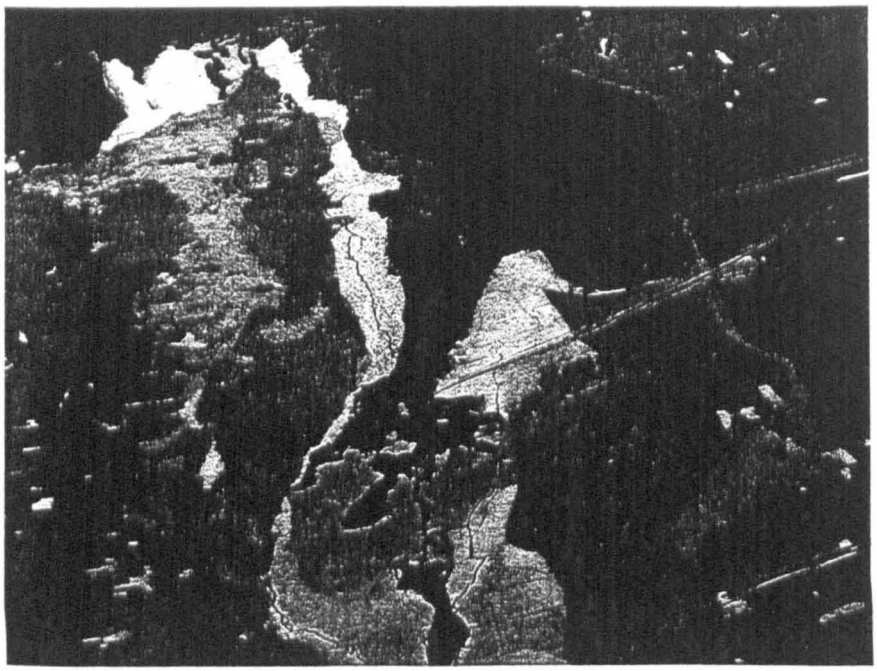

Sample 94-44

d)

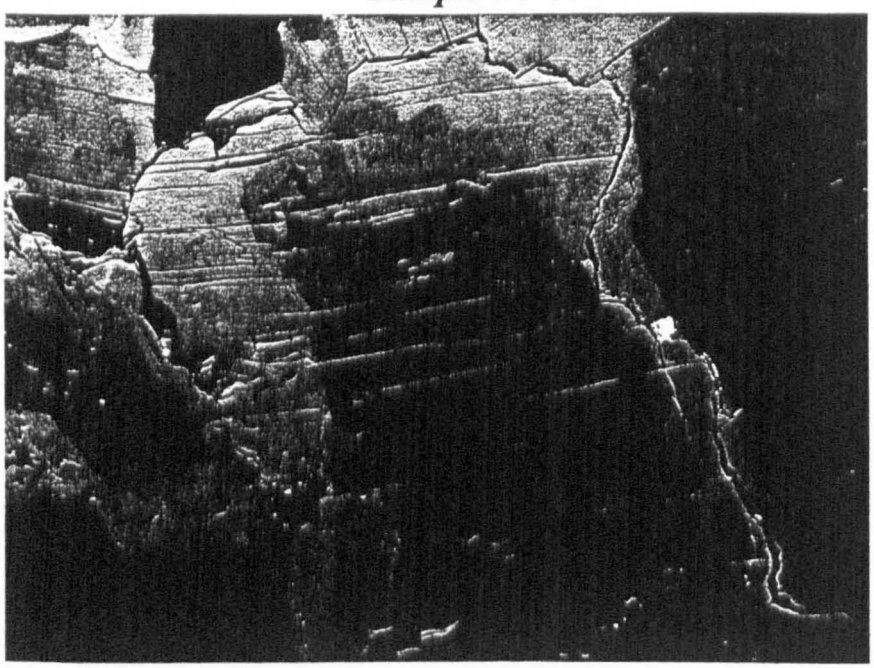

Figure 3.4 continued. Backscattered electron images of mica from the Separation Rapids pegmatite group. c) and d) Mica sample 94-44 from Marko's pegmatite, part of the Mn-suite. Note the mottled texture in c) indicating partial replacement and the sharp zoning boundaries in d) suggesting an abrupt chemical change. Scale bars are 500 microns.

The Big Mack pegmatite is one of the largest petalite subtype pegmatites in the Separation Rapids group (Breaks *et al.* 1999b). Eleven individual mica samples have been analysed. Muscovite from the Big Mack pegmatite occurs as fine-grained aggregates (<1mm) within the quartz + K-feldspar + albite aplite wall zone and as coarse-grained books (~5mm) in the quartz + K-feldspar + garnet + biotite border zone. James' pegmatite is also a petalite subtype pegmatite that exhibits ductile deformation with recrystallisation of the original pegmatite fabric. Muscovite is present in the wall zone of the pegmatite (sample 93-276).

Mn-suite (96-86b, SS34a, SS36, SS37, SS38, SS40, 94-44, SS31)

Sample 96-86b is a mica grain from a quartz + K-feldspar + muscovite + albite pod that texturally overprints a pegmatitic leucogranite stock outside the Separation Rapids pluton. Pegmatite 265 is an 8m thick, fluorapatite + garnet + biotite + muscovite pegmatite within the beryl zone. Fine-grained muscovite was collected from the wall zone (sample SS34a). Within the Separation Rapids pluton, locality 93-260 (sample SS36) is notable for a 3m thick potassic pegmatite containing K-feldspar megacrysts and muscovite + quartz + albite segregations.

The Big Whopper pegmatite and Marko's pegmatite are petalite subtype pegmatites. The core zone of the Big Whopper pegmatite contains the assemblage petalite + K-feldspar + muscovite + quartz. Muscovite grains (2mm) are part of the ductile deformed fabric (sample SS31). Marko's pegmatite contains coarse books (1cm) of mica within the wall zone (sample SS37). In the core zone, micas occur as interstitial grains between K-feldspar megacrysts (samples SS38, SS40) and in mica + albite spherical pods (figure 3.8c), which overprint the core zone assemblage and are interpreted as immiscible melt-fluid pockets (Tindle and Breaks 1998). Analyses of mica from these spherical pods have been incorporated into the present study using unpublished data of A.G. Tindle, The Open University (full data set presented in Appendix A).

- ***Backscattered electron images***

Backscattered electron (BSE) images of mica samples show that the compositional zoning observed in mica from the Pakeagama Lake pegmatite is not widespread in the Separation Rapids pegmatites. Mica from the Fe-suite pegmatites is commonly unzoned. In mica samples from the Mn-suite pegmatites, compositionally

distinct rims are thin (figure 3.4a,b). Marko's pegmatite, one of the Mn-suite dykes, contains mica with zoning similar to that seen in mica from the Pakeagama Lake pegmatite (figure 3.4c,d). Rare species such as the Cs-mica, nanpingite, tend to occur sporadically along cleavage planes, fractures and in small aggregates as late-stage replacement/alteration products (Breaks and Tindle, *in press*).

3.3 Electron microprobe results

Electron-probe microanalysis is the technique most commonly used for chemical analysis of minerals. A full description of operating conditions used for this study are given in Appendix A. The electron microprobe has the distinct advantage of enabling analyses of single grains or even compositional variation within individual grains. In contrast, 'wet' chemical techniques can provide only bulk analysis of samples that can be misleading due to inclusions, overgrowths or zoning. Mica from rare-element pegmatites is commonly analysed for concentrations of SiO_2, TiO_2, Al_2O_3, FeO total, MnO, MgO, CaO, Na_2O, K_2O, SrO, BaO, Rb_2O, Cs_2O, ZnO, SnO_2, Ga_2O_3, F and Cl. Representative analyses are given in tables 3.1 and 3.2, and the full data set of mica analyses is presented in Appendix A.

3.3.1 Estimating lithium concentrations

A disadvantage of the electron microprobe is the inability to determine lithium concentrations, which may make up a significant proportion in both dioctahedral and trioctahedral micas, particularly those in rare-element enriched granite - pegmatite systems. Fortunately, Li correlates well with several elements in mica that can be analysed by the electron microprobe and this allows an estimation of the Li_2O content via a regression line equation. Tindle and Webb (1990) determined an empirical relationship between Li_2O and SiO_2 for trioctahedral micas based on 250 published wet chemical analyses. This was confirmed by a subsequent study (Tischendorf *et al.* 1997), which also provided similar regression equations for dioctahedral micas based on correlations between Li_2O and F.

Eqn. 3.1a $Li_2O = (0.289SiO_2) - 9.658$ for trioctahedral micas e.g. lepidolite.

Eqn. 3.1b $Li_2O = 0.3935F^{1.326}$ for dioctahedral micas e.g. muscovite.

Equations 3.1a and 3.1b : Regression equations for the estimation of Li_2O from SiO_2 and F in trioctahedral and dioctahedral micas, respectively (Tischendorf et al. 1997).

Transitional muscovite - lepidolite crystals that are common in rare-element pegmatites have mixed-layer forms of dioctahedral and trioctahedral structure. However, the use of different regression equations when calculating Li_2O content is discouraged as this can produce artificial breaks in the Li_2O variations (Tischendorf *et al.* 1997). Since determining the compositional variation of mica is the main goal of this study, only one equation has been used to estimate Li_2O concentration. Tischendorf *et al.* (1997) suggest using the regression equation that applies to the most primitive sample from any given dataset and thus the Li_2O calculations are based on the dioctahedral equation shown above (equation 3.1b). One drawback of this approach is that Li_2O concentrations in trioctahedral lepidolite will be underestimated. This is easily recognised from percentage totals of these analyses, which are often significantly below 100% (Appendix A).

3.3.2 Pakeagama Lake pegmatite

Representative analyses of mica from the Pakeagama Lake pegmatite have been compiled for each of the samples and are reported in table 3.1.

- *Classification*

A mica classification diagram based on the octahedral cations in micas has been developed by Tischendorf *et al.* (1997). The diagram uses combinations of two components on both axes, thereby allowing the effects of four variables to be shown on a two-dimensional plot. The axis variables are [Mg-Li] and [Fe_{tot}+Mn+Ti-Al^{vi}]. This allows Mg and Fe to be separated and is based on the strong negative correlation of Mg and Li plus a similar relationship for total Fe (Fe*) and Al^{vi} (*see* Tischendorf *et al.* 1997 for full description of diagram). Advantages to the diagram are that a full range of micas

can be plotted, all the important octahedral cations are used and unlike triangular plots, absolute and not relative concentrations are shown.

Figure 3.5 is a plot of mica data from the Pakeagama Lake pegmatite using the lower left (Li-Al mica) quadrant of the Tischendorf *et al.* (1997) classification diagram. Data extends into all fields except phengite in the Li-Al mica quadrant, representing the wide variation in composition. Two trends are apparent and it is clear from the diagram that the bulk of data extends from the muscovite field through lithium muscovite and zinnwaldite to lepidolite. Samples from the quartz-rich wall zone, K-feldspar + petalite zone, tourmaline + muscovite aplite dykes and lepidolite vein cross-cutting the spodumene + quartz core zone fall along this trend, interpreted as the main compositional variation of mica. A second trend runs through the Li-phengite, zinnwaldite and lepidolite fields, with correspondingly higher values of the $Fe^{*}+Mn+Ti-Al^{vi}$ parameter compared with the main compositional path. Micas from the layered spodumene + quartz pegmatite-aplite and in part, the blocky K-feldspar (potassic) zone make up this separate trend. Chemical data from other mineral phases (columbite-tantalite and tourmaline) also suggests significant differences in the composition of the layered spodumene + quartz pegmatite-aplite compared with the rest of the pegmatite (Tindle *et al., in press*).

- *Variation diagrams*

Variation diagrams of major elements plotted against Si reveal the overall geochemical trends of mica from the Pakeagama Lake pegmatite (figure 3.6). Positive correlations exist between Si and Mn, Rb, Cs, and F. In contrast, total Al has a strong negative correlation with Si. Similar trends for these elements have been reported for mica from other rare-element pegmatites (Jolliff *et al.* 1987; Roda *et al.* 1995). Data for Fe *versus* Si define two trends. Plotting the data with different symbols for each pegmatite zone reveals that the layered spodumene + quartz pegmatite-aplite and in part, the blocky K-feldspar (potassic) zone follow a trend that is separate from the rest of the pegmatite zones (Figure 3.7).

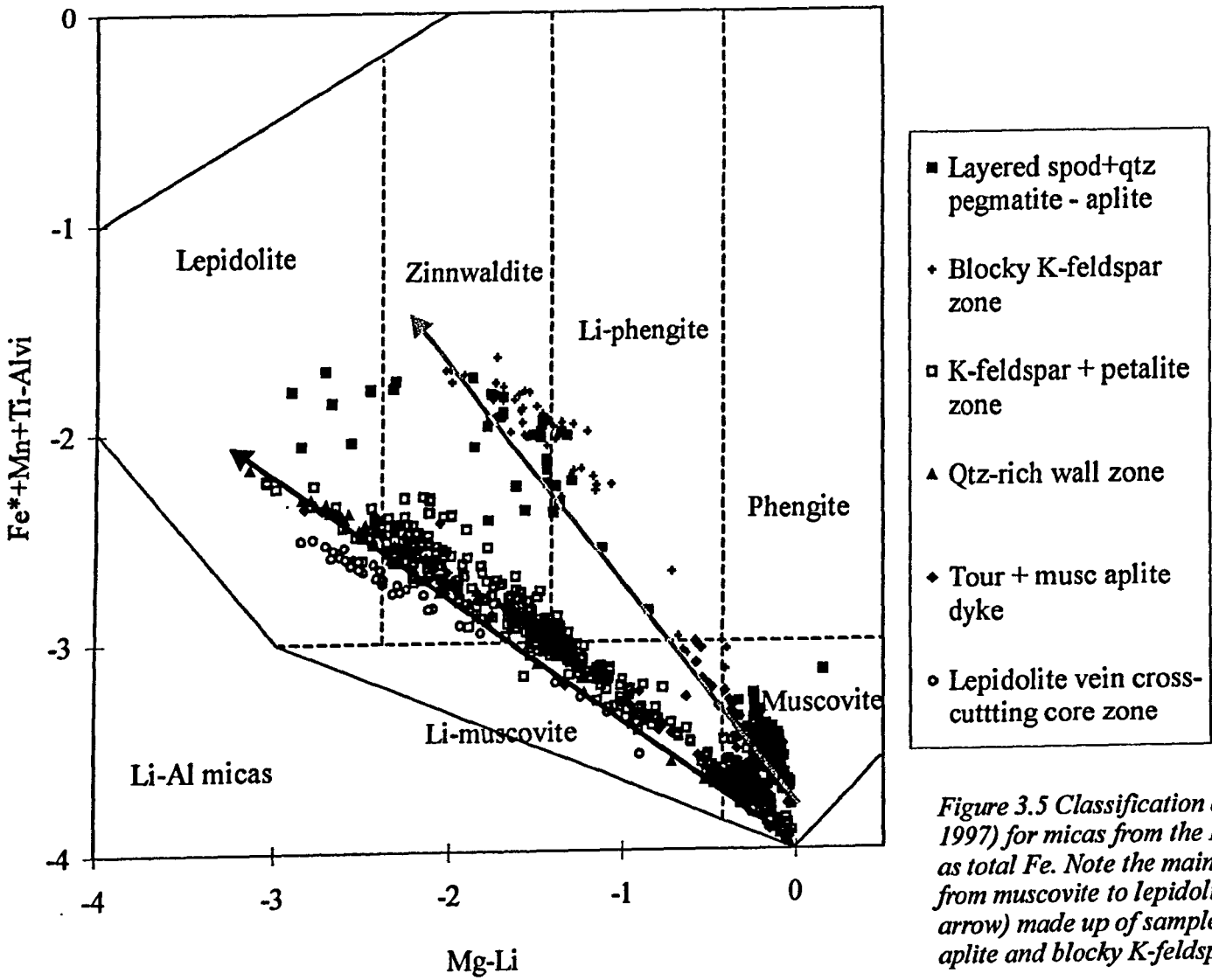

Figure 3.5 Classification diagram (after Tischendorf et al. 1997) for micas from the Pakeagama Lake pegmatite. Fe as total Fe. Note the main compositional trend (red arrow) from muscovite to lepidolite and a second trend (blue arrow) made up of samples from the layered pegmatite-aplite and blocky K-feldspar zone.*

Table 3.1 Representative analyses and structural formulae (based on 22 oxygens) of micas from the Pakeagama Lake pegmatite.

	Blocky K-feldspar zone				K-feldspar + petalite zone									
Sample	SS100	SS100	SS101	SS101	SS17	SS17	SS20	SS20	SS94	SS94	SS99	SS99	SS113	SS113
Location	core	rim	core	rim	core	rim	core	rim	core	rim	core	rim	core	rim
	musc	zinn	musc	zinn	zinn	lepid	musc	zinn	musc	zinn	musc	zinn	Li-musc	zinn
SiO_2	45.84	49.39	45.64	51.10	49.02	52.50	47.89	52.45	47.13	50.57	46.44	51.68	49.09	49.32
TiO_2	0.20	0.05	0.01	0.02	0.04	0.01	0.03	0.00	0.03	0.05	0.00	0.00	0.07	0.06
Al_2O_3	34.69	24.83	36.74	24.02	27.16	22.60	33.87	24.48	34.40	24.79	35.72	23.62	29.11	27.96
FeO	1.90	5.85	0.18	0.88	1.89	1.37	0.34	1.06	0.76	2.37	0.21	1.03	1.43	1.72
MnO	0.33	1.14	0.14	0.77	1.16	0.92	0.24	0.89	0.29	1.03	0.11	0.80	0.84	0.96
MgO	0.03	0.09	0.00	0.02	0.07	0.05	0.01	0.03	0.01	0.04	0.03	0.01	0.06	0.07
CaO	0.00	0.01	0.00	0.00	0.01	0.00	0.00	0.00	0.00	0.00	0.00	0.00	0.01	0.00
Na_2O	0.22	0.12	0.48	0.14	0.23	0.13	0.19	0.13	0.21	0.10	0.20	0.11	0.16	0.15
K_2O	10.30	9.71	9.80	9.81	9.74	10.04	9.81	9.90	10.21	9.86	10.32	9.92	9.32	9.50
SrO	0.02	0.03	0.03	0.05	-	-	0.06	0.01	0.02	0.04	0.05	0.02	0.06	0.00
BaO	0.00	0.00	0.00	0.00	0.00	0.00	0.00	0.00	0.00	0.00	0.00	0.00	0.00	0.00
Rb_2O	1.38	1.56	1.29	2.34	0.00	0.00	1.60	2.01	1.76	2.28	1.44	2.27	2.08	1.92
Cs_2O	0.11	0.29	0.13	0.43	0.30	0.71	0.14	0.62	0.09	0.45	0.13	0.62	0.19	0.20
ZnO	0.10	0.20	0.03	0.07	0.11	0.08	0.05	0.07	0.08	0.18	0.01	0.11	0.10	0.07
SnO2	0.05	0.02	0.02	0.01	0.03	0.00	0.04	0.00	0.07	0.03	0.05	0.01	0.07	0.05
Ga_2O_3	0.06	0.03	0.05	0.05	0.02	0.00	0.05	0.02	0.05	0.01	0.03	0.02	0.05	0.04
F	0.78	4.20	0.39	5.36	5.03	7.00	1.57	5.96	1.45	5.38	0.74	6.01	4.08	5.01
Cl	0.01	0.01	0.00	0.01	0.01	0.01	0.00	0.00	0.00	0.00	0.01	0.00	0.01	0.01
Li_2O*	0.28	2.64	0.11	3.65	3.35	5.19	0.72	4.19	0.64	3.67	0.26	4.24	2.54	3.33
H_2O*	4.08	2.40	4.28	1.84	2.03	1.15	3.75	1.69	3.81	1.88	4.12	1.58	2.53	2.10
O=F,Cl	0.33	1.77	0.16	2.26	2.12	2.95	0.66	2.51	0.61	2.27	0.31	2.53	1.72	2.11
Total	100.06	100.78	99.16	98.30	98.08	98.81	99.69	101.03	100.38	100.47	99.56	99.51	100.08	100.34

*Li_2O Calculation from Tischendorf *et al.* (1997); H_2O calculation from Tindle and Webb (1990).

Si	6.178	6.744	6.122	6.990	6.650	7.036	6.394	6.967	6.292	6.836	6.220	6.991	6.589	6.607
Al iv	1.822	1.256	1.878	1.010	1.350	0.964	1.606	1.033	1.708	1.164	1.780	1.009	1.411	1.393
Al vi	3.690	2.739	3.931	2.864	2.994	2.607	3.724	2.800	3.706	2.786	3.859	2.758	3.196	3.022
Ti	0.020	0.005	0.001	0.002	0.004	0.001	0.003	0.000	0.003	0.005	0.000	0.000	0.007	0.006
Fe	0.214	0.668	0.020	0.100	0.214	0.153	0.037	0.118	0.084	0.268	0.023	0.116	0.161	0.192
Mn	0.037	0.131	0.016	0.089	0.134	0.104	0.027	0.100	0.033	0.118	0.013	0.092	0.095	0.109
Mg	0.006	0.017	0.000	0.003	0.014	0.010	0.002	0.006	0.002	0.007	0.006	0.002	0.013	0.014
Zn	0.010	0.020	0.003	0.007	0.011	0.008	0.005	0.007	0.008	0.018	0.001	0.011	0.010	0.007
Sn	0.003	0.001	0.001	0.000	0.002	0.000	0.002	0.000	0.003	0.002	0.002	0.000	0.003	0.002
Ga	0.005	0.003	0.004	0.004	0.002	0.000	0.004	0.002	0.004	0.001	0.003	0.001	0.004	0.003
Li*	0.153	1.449	0.061	2.006	1.830	2.799	0.384	2.240	0.345	1.994	0.143	2.310	1.370	1.797
Ca	0.000	0.001	0.000	0.000	0.001	0.000	0.001	0.000	0.000	0.000	0.001	0.000	0.001	0.000
Na	0.057	0.031	0.125	0.038	0.060	0.034	0.049	0.035	0.054	0.027	0.052	0.030	0.042	0.038
K	1.770	1.691	1.677	1.712	1.686	1.717	1.670	1.678	1.739	1.700	1.762	1.712	1.596	1.624
Sr	0.002	0.002	0.002	0.004	-	-	0.004	0.001	0.001	0.003	0.004	0.002	0.005	0.000
Ba	0.000	0.000	0.000	0.000	0.000	0.000	0.000	0.000	0.000	0.000	0.000	0.000	0.000	0.000
Rb	0.120	0.137	0.111	0.206	0.000	0.000	0.137	0.172	0.151	0.198	0.124	0.197	0.180	0.165
Cs	0.006	0.017	0.008	0.025	0.018	0.040	0.008	0.035	0.005	0.026	0.007	0.035	0.011	0.011
OH*	3.666	2.184	3.834	1.680	1.839	1.033	3.338	1.498	3.389	1.698	3.684	1.428	2.266	1.875
F	0.332	1.814	0.166	2.319	2.160	2.966	0.662	2.502	0.611	2.302	0.314	2.572	1.732	2.123
Cl	0.003	0.002	0.000	0.002	0.002	0.001	0.000	0.000	0.000	0.000	0.002	0.000	0.002	0.001
TOTAL	18.093	18.914	17.960	19.061	18.968	19.473	18.058	19.194	18.140	19.154	18.001	19.266	18.694	18.992
Al total	5.511	3.996	5.809	3.873	4.344	3.571	5.330	3.833	5.414	3.950	5.639	3.767	4.606	4.415
Mg-Li	-0.146	-1.432	-0.061	-2.002	-1.817	-2.789	-0.382	-2.234	-0.343	-1.987	-0.137	-2.308	-1.358	-1.783
(Fe*+Mn+ Ti-Alvi)	-3.418	-1.935	-3.894	-2.672	-2.642	-2.349	-3.657	-2.581	-3.586	-2.395	-3.823	-2.550	-2.932	-2.714

Table 3.1 continued. Representative analyses of micas from the Pakeagama Lake pegmatite.

	K-feldspar + petalite zone						Layered spodumene + quartz pegmatite-aplite							
Sample	SS114	SS114	SS116	SS116	SS117	SS117	SS104	SS104	SS107	SS107	SS118	SS118	SS119	SS119
Location	core	rim	core	rim	core	rim	core	rim	core	rim	core	rim	core	rim
	Li-musc	zinn	musc	zinn	musc	lepid	musc	zinn	musc	zinn	musc	zinn	musc	musc
SiO_2	49.68	50.75	46.62	53.27	46.83	53.01	45.40	49.56	45.79	47.84	46.15	48.95	45.36	45.56
TiO_2	0.02	0.04	0.02	0.04	0.02	0.02	0.03	0.01	0.05	0.06	0.03	0.08	0.05	0.03
Al_2O_3	30.37	28.00	35.64	24.18	35.30	19.56	35.58	25.15	35.14	25.55	35.12	22.53	33.68	35.05
FeO	0.78	1.29	0.77	1.40	1.26	1.43	1.58	3.40	1.92	4.38	1.25	6.19	2.70	2.04
MnO	0.41	0.72	0.29	0.95	0.28	0.66	0.15	0.27	0.20	0.37	0.13	0.50	0.39	0.23
MgO	0.03	0.05	0.01	0.06	0.04	0.04	0.05	0.11	0.03	0.04	0.00	0.03	0.01	0.02
CaO	0.00	0.00	0.00	0.00	0.00	0.01	0.00	0.00	0.00	0.01	0.01	0.00	0.00	0.00
Na_2O	0.13	0.09	0.39	0.09	0.32	0.08	0.26	0.14	0.36	0.11	0.18	0.07	0.36	0.27
K_2O	9.66	9.68	9.75	9.05	9.64	9.07	10.10	9.75	9.96	9.36	10.28	9.42	9.68	9.97
SrO	0.04	0.04	0.05	0.01	0.05	0.04	0.04	0.00	0.03	0.03	0.00	0.04	0.03	0.01
BaO	0.00	0.00	0.00	0.00	0.00	0.00	0.00	0.00	0.00	0.00	0.00	0.00	0.00	0.02
Rb_2O	2.05	1.93	1.43	1.92	1.21	2.30	1.33	2.17	1.32	2.34	1.63	2.64	1.62	1.48
Cs_2O	0.17	0.29	0.04	0.77	0.04	0.67	0.04	0.18	0.05	0.78	0.06	0.57	0.07	0.05
ZnO	0.04	0.12	0.04	0.12	0.10	0.15	0.09	0.27	0.18	0.34	0.16	0.45	0.28	0.17
SnO2	0.03	0.05	0.05	0.03	0.07	0.00	0.06	0.00	0.01	0.01	0.05	0.00	0.05	0.05
Ga_2O_3	0.06	0.02	0.05	0.04	0.04	0.01	0.02	0.03	0.03	0.04	0.05	0.04	0.00	0.04
F	3.49	4.67	1.07	6.09	1.13	6.82	0.62	4.93	0.53	3.95	0.81	5.01	1.09	0.77
Cl	0.00	0.00	0.01	0.01	0.00	0.03	0.00	0.00	0.01	0.00	0.00	0.01	0.00	0.01
Li_2O*	2.06	3.04	0.43	4.31	0.46	5.02	0.21	3.26	0.17	2.43	0.30	3.33	0.44	0.28
H_2O*	2.85	2.31	3.99	1.66	3.97	1.10	4.15	2.04	4.19	2.41	4.08	1.92	3.88	4.08
O=F,Cl	1.47	1.97	0.45	2.56	0.48	2.88	0.26	2.08	0.23	1.66	0.34	2.11	0.46	0.32
Total	100.40	101.13	100.19	101.45	100.28	97.13	99.45	99.19	99.73	98.38	99.94	99.66	99.22	99.78

*Li_2O Calculation from Tischendorf *et al.* (1997); H_2O calculation from Tindle and Webb (1990).

Si	6.608	6.723	6.206	7.022	6.228	7.315	6.128	6.784	6.171	6.696	6.203	6.832	6.192	6.152
Al iv	1.392	1.277	1.794	0.978	1.772	0.685	1.872	1.216	1.829	1.304	1.797	1.168	1.808	1.848
Al vi	3.370	3.096	3.799	2.779	3.761	2.496	3.789	2.842	3.752	2.911	3.767	2.538	3.612	3.730
Ti	0.002	0.004	0.002	0.004	0.002	0.000	0.003	0.001	0.005	0.006	0.003	0.009	0.005	0.003
Fe	0.087	0.143	0.085	0.154	0.140	0.165	0.179	0.389	0.216	0.513	0.141	0.723	0.309	0.230
Mn	0.047	0.080	0.033	0.106	0.031	0.077	0.017	0.031	0.023	0.044	0.015	0.059	0.045	0.026
Mg	0.006	0.010	0.001	0.013	0.008	0.008	0.010	0.023	0.006	0.009	0.000	0.006	0.001	0.003
Zn	0.004	0.012	0.003	0.012	0.010	0.015	0.009	0.027	0.018	0.035	0.015	0.047	0.028	0.017
Sn	0.002	0.003	0.003	0.002	0.004	0.000	0.003	0.000	0.001	0.001	0.003	0.000	0.003	0.003
Ga	0.005	0.002	0.005	0.003	0.003	0.001	0.002	0.002	0.002	0.003	0.004	0.003	0.000	0.003
Li*	1.105	1.620	0.231	2.287	0.249	2.787	0.113	1.797	0.093	1.369	0.161	1.871	0.242	0.150
Ca	0.000	0.000	0.000	0.000	0.000	0.001	0.000	0.000	0.000	0.001	0.002	0.000	0.000	0.000
Na	0.032	0.024	0.100	0.024	0.081	0.022	0.068	0.037	0.094	0.028	0.046	0.019	0.094	0.071
K	1.639	1.637	1.655	1.522	1.636	1.597	1.739	1.702	1.712	1.670	1.762	1.677	1.686	1.717
Sr	0.003	0.003	0.004	0.001	0.004	0.004	0.003	0.000	0.002	0.002	0.000	0.003	0.003	0.001
Ba	0.000	0.000	0.000	0.000	0.000	0.000	0.000	0.000	0.000	0.000	0.000	0.000	0.000	0.001
Rb	0.175	0.165	0.123	0.163	0.104	0.204	0.116	0.191	0.114	0.210	0.141	0.236	0.142	0.129
Cs	0.010	0.016	0.002	0.043	0.002	0.039	0.002	0.010	0.003	0.047	0.003	0.034	0.004	0.003
OH*	2.531	2.041	3.547	1.461	3.523	1.016	3.737	1.865	3.770	2.252	3.655	1.787	3.530	3.672
F	1.469	1.958	0.451	2.537	0.477	2.978	0.263	2.134	0.228	1.748	0.345	2.211	0.470	0.327
Cl	0.000	0.000	0.001	0.002	0.000	0.007	0.000	0.001	0.002	0.000	0.000	0.002	0.000	0.001
TOTAL	18.486	18.814	18.046	19.112	18.034	19.415	18.052	19.053	18.040	18.851	18.063	19.224	18.173	18.086
Al total	4.762	4.372	5.593	3.757	5.533	3.182	5.661	4.058	5.581	4.215	5.564	3.706	5.420	5.578
Mg-Li	-1.098	-1.610	-0.230	-2.275	-0.241	-2.779	-0.103	-1.774	-0.087	-1.360	-0.161	-1.865	-0.240	-0.147
(Fe*+Mn+ Ti-Alvi)	-3.234	-2.869	-3.679	-2.514	-3.588	-2.254	-3.590	-2.420	-3.507	-2.349	-3.608	-1.747	-3.254	-3.471

Table 3.1 continued. Representative analyses of micas from the Pakeagama Lake pegmatite.

	Layered pegmatite-aplite		Quartz-rich wall zone				Core zone		Tourmaline + muscovite aplite dyke					
Sample	SS122	SS122	SS97	SS97	SS98	SS98	SS134+	SS134+	SS6	SS6	SS7	SS7	98FWB38	98FWB38
Location	core	rim	core	rim	core	rim	core	rim	core	rim	core	rim	core	rim
	musc	lepid	Li-musc	lepid	Li-musc	lepid	musc	lepid	Li-musc	zinn	musc	musc	musc	Li-musc
SiO_2	46.28	51.17	52.37	55.34	48.02	48.62	46.70	51.36	47.89	51.34	46.31	46.73	46.71	47.05
TiO_2	0.03	0.01	0.05	0.02	0.02	0.02	0.00	0.00	0.04	0.02	0.05	0.04	0.05	0.03
Al_2O_3	35.35	20.68	29.70	24.05	32.32	25.34	35.87	23.62	33.50	24.24	35.84	35.20	33.55	31.66
FeO	1.43	4.41	0.90	1.34	0.45	1.19	0.13	0.40	0.33	0.88	0.81	1.52	1.32	2.42
MnO	0.17	0.67	0.69	1.12	0.35	1.06	0.18	0.76	0.32	1.08	0.17	0.29	0.31	0.42
MgO	0.01	0.01	0.03	0.03	0.01	0.01	0.00	0.01	0.01	0.02	0.04	0.03	0.07	0.06
CaO	0.01	0.01	0.00	0.00	0.00	0.00	0.00	0.00	0.00	0.00	0.01	0.00	0.02	0.02
Na_2O	0.22	0.09	0.12	0.14	0.27	0.13	0.42	0.13	0.38	0.19	0.40	0.51	0.33	0.25
K_2O	10.16	9.92	9.97	9.90	10.19	9.74	10.03	9.82	10.19	10.12	10.18	9.71	9.78	9.77
SrO	0.03	0.04	0.01	0.04	0.00	0.05	-	-	0.01	0.06	-	-	0.02	0.07
BaO	0.00	0.00	0.00	0.00	0.00	0.00	0.00	0.00	0.00	0.00	0.00	0.00	0.00	0.00
Rb_2O	1.59	2.30	1.92	1.88	1.65	2.39	1.53	2.27	1.89	2.67	0.00	0.00	1.73	1.86
Cs_2O	0.07	0.16	0.21	0.45	0.12	0.49	0.21	0.85	0.21	0.65	0.07	0.08	0.08	0.11
ZnO	0.25	0.75	0.07	0.08	0.05	0.10	0.02	0.03	0.00	0.06	0.10	0.14	0.15	0.26
SnO2	0.01	0.00	0.05	0.01	0.04	0.01	0.05	0.02	0.06	0.00	0.05	0.04	0.53	1.23
Ga_2O_3	0.05	0.02	0.06	0.05	0.04	0.01	0.05	0.00	0.03	0.03	0.06	0.05	1.02	0.41
F	0.67	6.23	4.46	6.86	3.09	6.21	0.88	6.48	2.09	5.76	1.10	1.44	1.57	2.06
Cl	0.00	0.00	0.00	0.00	0.00	0.00	0.00	0.00	0.01	0.00	0.00	0.01	0.01	0.01
Li_2O*	0.23	4.45	2.85	5.05	1.76	4.43	0.33	4.69	1.05	4.01	0.45	0.64	0.71	1.03
H_2O*	4.16	1.40	2.57	1.46	3.03	1.42	4.08	1.35	3.51	1.71	3.97	3.83	3.74	3.47
O=F,Cl	0.28	2.62	1.88	2.89	1.30	2.61	0.37	2.73	0.88	2.43	0.46	0.61	0.66	0.87
Total	100.44	99.71	104.14	104.93	100.09	98.61	100.12	99.05	100.62	100.41	99.14	99.64	101.03	101.31

*Li_2O Calculation from Tischendorf *et al.* (1997); H_2O calculation from Tindle and Webb (1990).
+ Unpublished data of A.G. Tindle (The Open University).

Si	6.193	7.038	6.709	7.046	6.409	6.675	6.220	6.965	6.373	6.927	6.178	6.213	6.251	6.336
Al iv	1.807	0.962	1.291	0.954	1.591	1.325	1.780	1.035	1.627	1.073	1.822	1.787	1.749	1.664
Al vi	3.768	2.390	3.194	2.654	3.494	2.777	3.851	2.740	3.627	2.782	3.814	3.728	3.543	3.362
Ti	0.003	0.001	0.005	0.002	0.002	0.002	0.000	0.000	0.004	0.002	0.005	0.004	0.005	0.003
Fe	0.160	0.508	0.097	0.142	0.050	0.137	0.014	0.046	0.036	0.099	0.090	0.169	0.147	0.272
Mn	0.019	0.079	0.075	0.121	0.040	0.123	0.020	0.087	0.036	0.124	0.019	0.033	0.035	0.048
Mg	0.002	0.003	0.006	0.006	0.001	0.003	0.000	0.001	0.001	0.004	0.008	0.006	0.013	0.012
Zn	0.025	0.076	0.007	0.008	0.005	0.010	0.001	0.003	0.000	0.006	0.010	0.013	0.015	0.026
Sn	0.000	0.000	0.002	0.000	0.002	0.001	0.002	0.001	0.003	0.000	0.003	0.002	0.028	0.066
Ga	0.005	0.002	0.005	0.004	0.003	0.001	0.004	0.000	0.003	0.002	0.005	0.005	0.088	0.035
Li*	0.125	2.464	1.470	2.588	0.942	2.446	0.179	2.556	0.561	2.178	0.240	0.341	0.384	0.556
Ca	0.001	0.002	0.000	0.001	0.000	0.000	0.000	0.001	0.000	0.000	0.002	0.000	0.003	0.002
Na	0.056	0.025	0.029	0.036	0.069	0.035	0.109	0.035	0.099	0.049	0.104	0.130	0.085	0.064
K	1.733	1.740	1.628	1.608	1.734	1.706	1.704	1.698	1.730	1.741	1.732	1.647	1.670	1.678
Sr	0.003	0.003	0.000	0.003	0.000	0.004	-	-	0.001	0.004	-	-	0.002	0.005
Ba	0.000	0.000	0.000	0.000	0.000	0.000	0.000	0.000	0.000	0.000	0.000	0.000	0.000	0.000
Rb	0.137	0.203	0.158	0.154	0.141	0.211	0.131	0.198	0.162	0.232	0.000	0.000	0.149	0.161
Cs	0.004	0.009	0.012	0.024	0.007	0.029	0.012	0.049	0.012	0.037	0.004	0.005	0.005	0.006
OH*	3.716	1.289	2.194	1.239	2.696	1.304	3.627	1.222	3.117	1.540	3.535	3.393	3.335	3.121
F	0.284	2.711	1.805	2.761	1.304	2.696	0.372	2.778	0.881	2.459	0.465	0.605	0.663	0.877
Cl	0.000	0.000	0.001	0.000	0.001	0.000	0.000	0.000	0.002	0.001	0.000	0.001	0.002	0.002
TOTAL	18.042	19.505	18.688	19.351	18.490	19.484	18.028	19.415	18.274	19.261	18.035	18.083	18.171	18.297
Al total	5.575	3.352	4.485	3.609	5.085	4.102	5.631	3.775	5.255	3.855	5.636	5.516	5.292	5.026
Mg-Li	-0.123	-2.461	-1.464	-2.582	-0.941	-2.444	-0.179	-2.555	-0.560	-2.174	-0.232	-0.336	-0.371	-0.543
(Fe*+Mn+ Ti-Alvi)	-3.586	-1.803	-3.018	-2.390	-3.402	-2.515	-3.816	-2.607	-3.552	-2.557	-3.700	-3.523	-3.355	-3.038

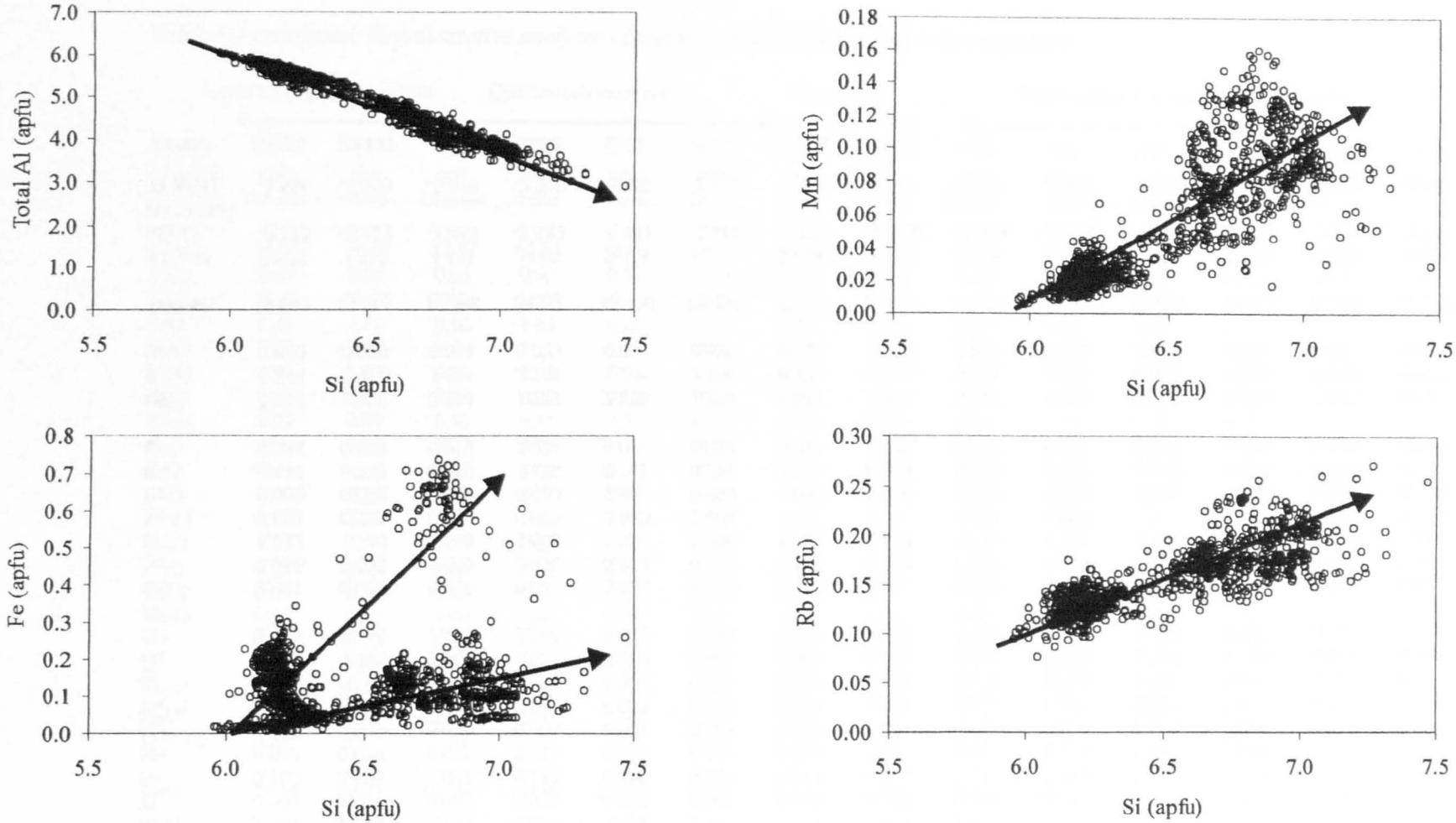

Figure 3.6 Variation diagrams for mica from the Pakeagama Lake pegmatite, apfu = atoms per formula unit (based on 22 oxygens).

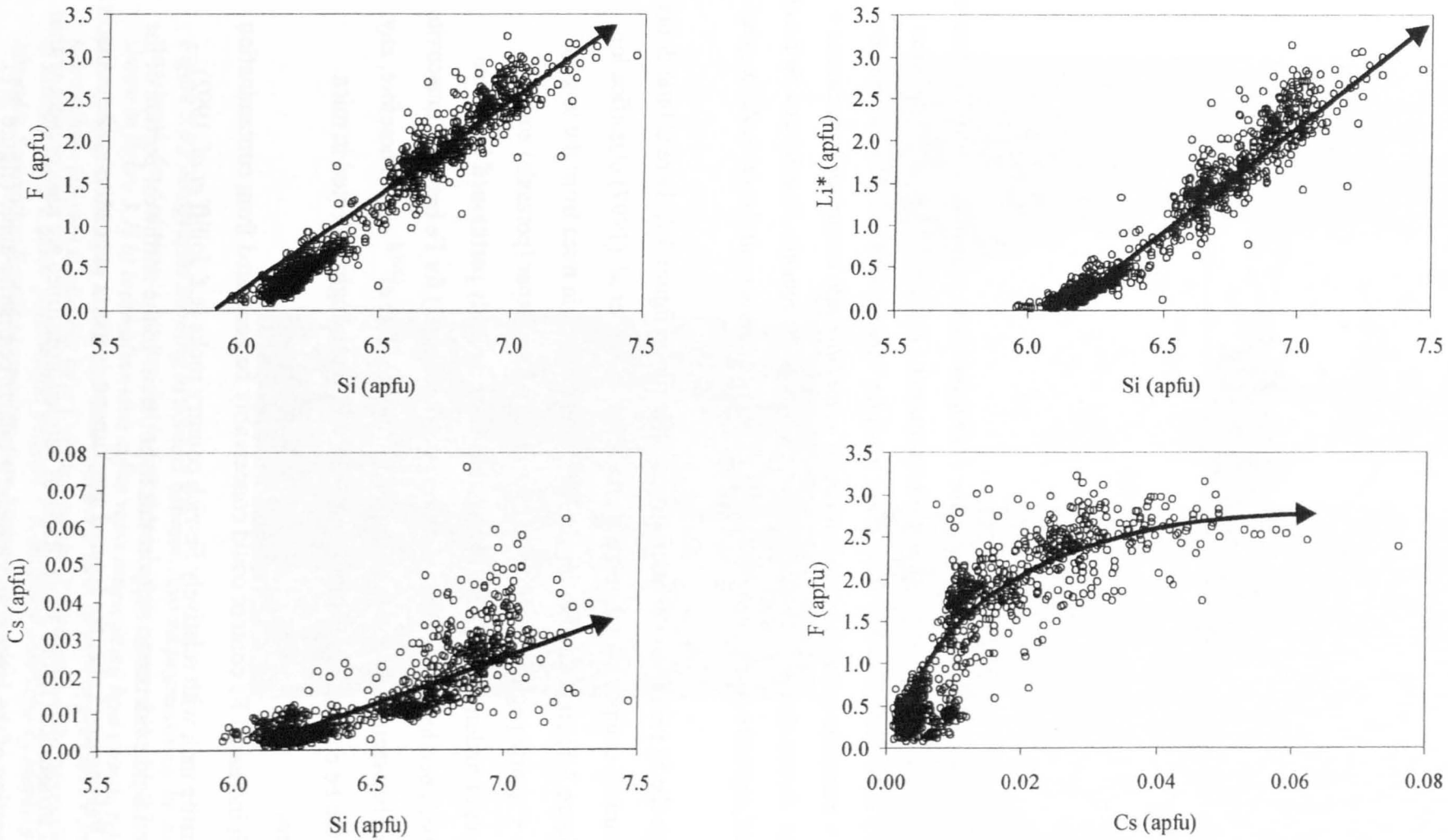

Figure 3.6 continued. Variation diagrams for mica from the Pakeagama Lake pegmatite, apfu = atoms per formula unit (based on 22 oxygens).

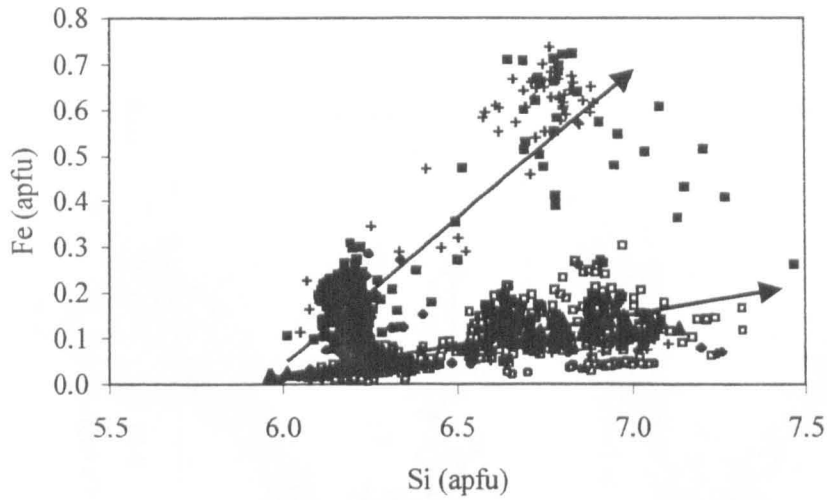

Figure 3.7 Si versus Fe plot for the micas of the Pakeagama Lake pegmatite. Filled red squares - layered spodumene + qtz pegmatite-aplite; Open squares - K-feldspar + petalite zone; plus signs - blocky K-feldspar (potassic) zone; green triangles - Quartz-rich wall zone; diamonds - tourmaline + muscovite aplite dykes; yellow circles - lepidolite vein crosscutting spodumene + qtz core zone. Arrows denote the trend of the main mass of the pegmatite (low Fe) and the trend of the layered pegmatite-aplite (high Fe), apfu = atoms per formula unit (based on 22 oxygens).

From the Si *versus* Fe variation diagram shown in figure 3.7, there is little doubt that the separated compositional trends on the Tischendorf *et al.* (1997) classification diagram (figure 3.5) are related to higher Fe concentrations in mica from the layered spodumene + quartz pegmatite-aplite and the blocky K-feldspar (potassic) zone. Icenhower and London (1995) have shown that Fe is strongly partitioned into mica coexisting with peraluminous melt; partition coefficients (D) for Fe between muscovite and glass are between 4 - 7, and even higher for biotite, $D\,(Fe)^{Bt/gl}$ ~20. Therefore, any increase in the Fe content of peraluminous melt will be strongly reflected in mica compositions.

Such increased Fe content could conceivably be generated from contamination of the pegmatite melt with relatively Fe-rich country rocks (c.f. Jolliff *et al.* 1992). There is good field evidence to support this hypothesis. In the northwest portion of the exposure at Pakeagama Lake, the layered spodumene + quartz pegmatite-aplite contacts with banded ironstones (figure 3.8a). Rafts of banded ironstones are also present within the central portion of the layered spodumene + quartz pegmatite-aplite (figure 3.1).

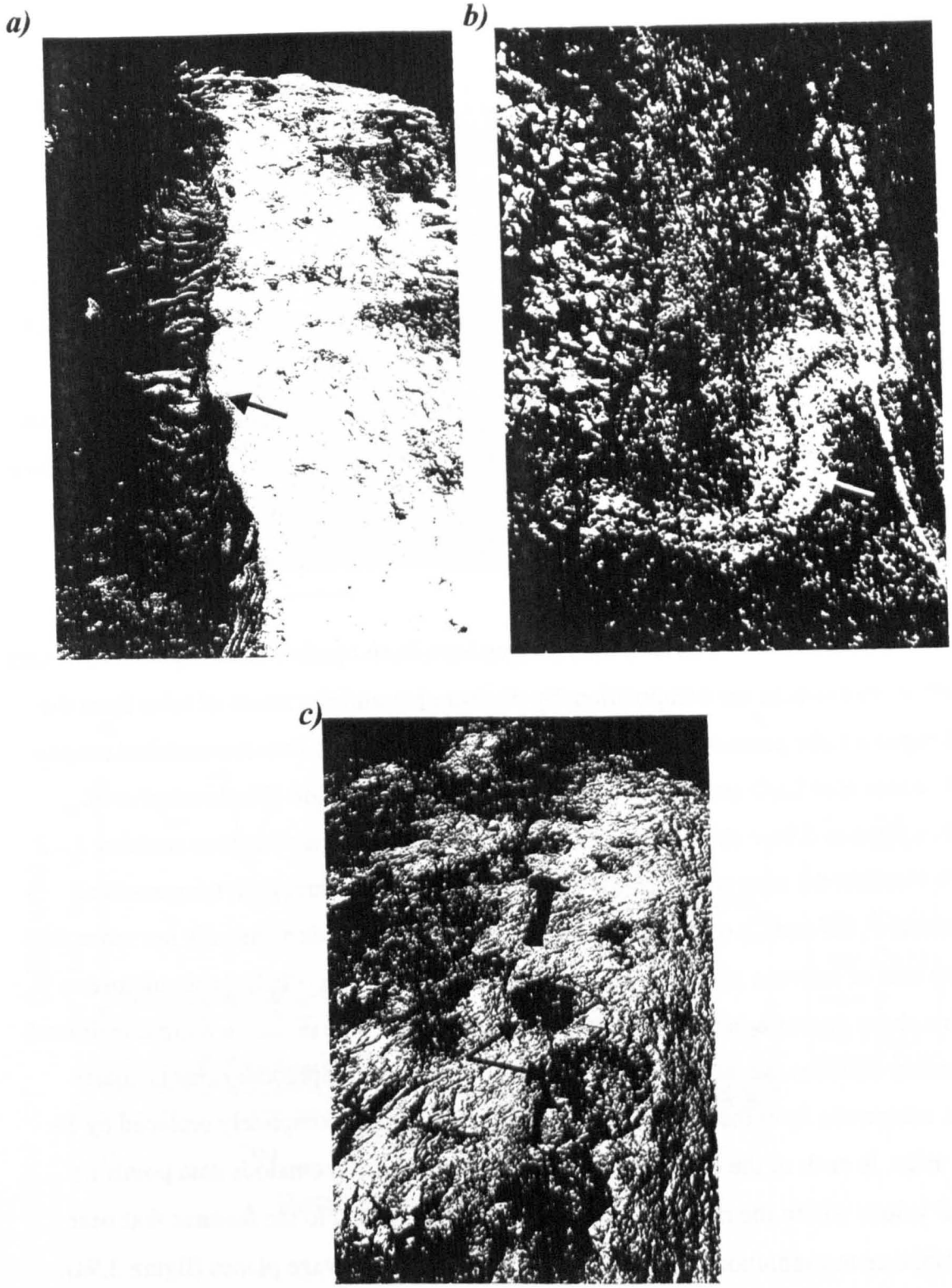

Figure 3.8 Photographs showing ***a)*** *contact between layered pegmatite-aplite and banded ironstones, field of view is approx. 2m in foreground (Pakeagama Lake pegmatite, location shown in figure 3.1)* ***b)*** *tourmaline-rich aplite veins crosscutting host granite (right side of photograph) and blocky K-feldspar zone (left part) field of view approx. 1m x 2m. The tourmaline-rich vein is also cut by a K-feldspar vein (Pakeagama Lake pegmatite).*
c) *Lithium mica + albite pods within petalite + K-feldspar core zone of Marko's pegmatite, Mn-suite Separation Rapids pegmatites, (use hammer for scale).*

Partial melting and assimilation of these Fe-rich host rocks has undoubtedly occurred with the layered spodumene + quartz pegmatite-aplite.

A plot of F *versus* Cs (figure 3.6) shows a notable change in the positive correlation trend at a value of F = 2.5 apfu. Below this value, the increase in Cs is relatively small for a given increase in fluorine. However, as F reaches 2.5 apfu, Cs values increase rapidly (0.02 - 0.06 apfu) to give a sub-horizontal trend, suggesting that a critical F content is reached in the mica structure that facilitates the incorporation of Cs. The value of 2.5 apfu F is equal to ~6wt% F and an estimated 4 wt% Li_2O using the equation for dioctahedral mica (Tischendorf *et al.* 1997). These values correspond directly with the minimum F and Li_2O concentrations of lepidolite. This indicates that the change from muscovite to lepidolite facilitates the incorporation of Cs into the mica structure.

- ***Crystal-chemical zoning***

Backscattered electron (BSE) images have been combined with quantitative spot analyses to examine the compositionally distinct core and rim zones of mica from the Pakeagama Lake pegmatite. Chemical profiles show that the rims are enriched mainly in F, hence also Li_2O since there is a direct positive correlation (Tischendorf *et al.* 1997). Figures 3.9a-c show that mica from the K-feldpar + petalite zone contains 1 - 2 wt% F within the core and up to 6 - 7wt% at the rim. The increase in the rare-alkali elements F, Rb and Cs occurs at a common and abrupt boundary, usually not more than a few tens of microns wide. Furthermore, the increase in rare-alkalis is simultaneous with a sharp decrease in calculated H_2O content. Figure 3.9c reveals a more transitional boundary between the muscovite cores and Li-muscovite - lepidolite rims. In figure 3.9d, muscovite from the blocky K-feldspar zone is almost completely replaced by F-rich mica. In each of the chemical profiles, there are some anomalous data points i.e. low F values within the rim of a grain. These may be related to the features that bear resemblance to exsolution lamellae, oriented parallel to cleavage planes (figure 3.9a).

From the textural observations described in section 3.2.1 and chemical profiles presented here, the Li-muscovite - lepidolite rims found in this study are interpreted as secondary replacement features of primary muscovite, rather than overgrowths. Similar muscovite - lepidolite micas have been found in the Bob Ingersoll pegmatite, Black Hills, South Dakota (Jolliff *et al.* 1987). Lepidolite rims are also considered to be replacement features, precipitated by an aqueous fluid derived from residual melt in the

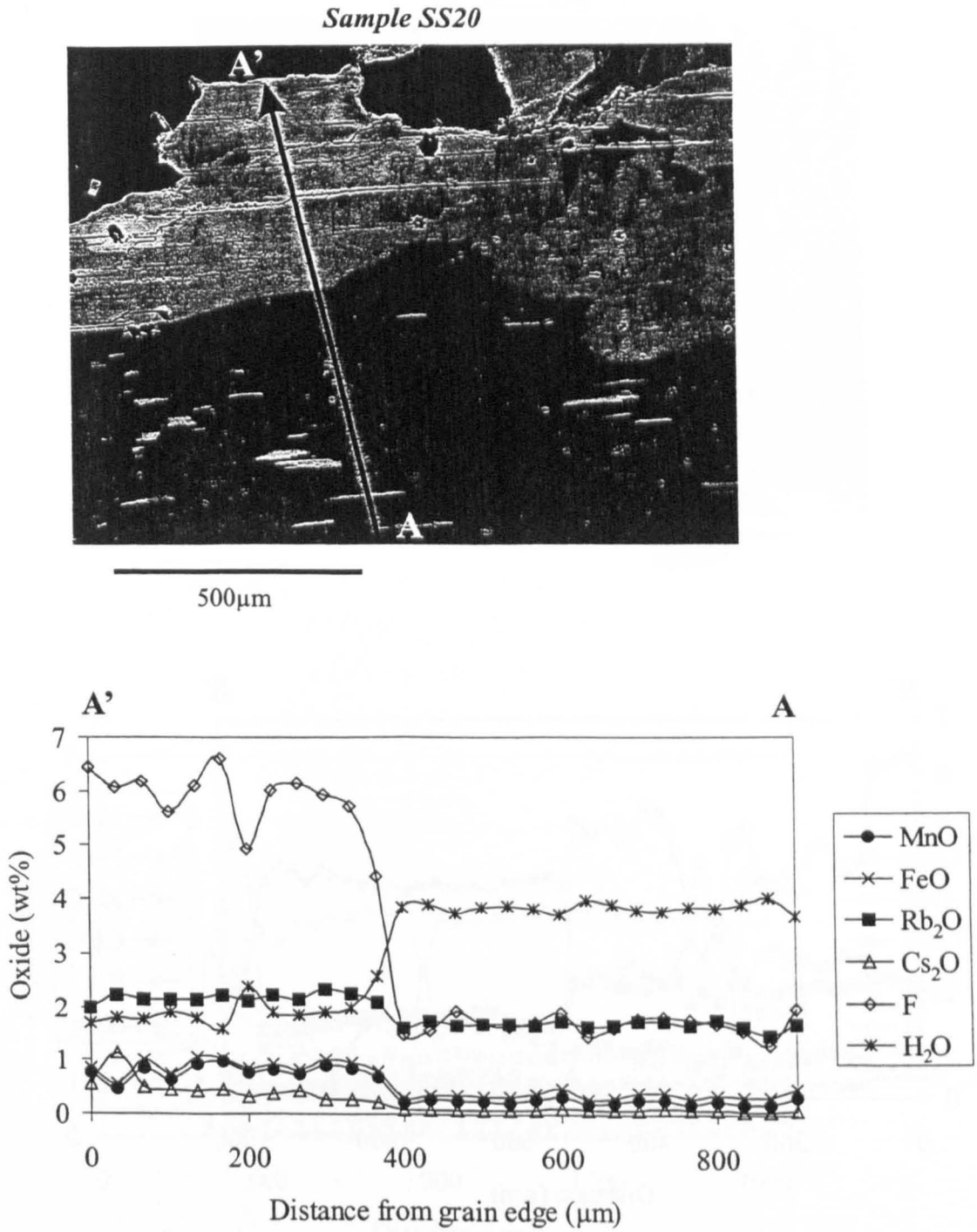

Figure 3.9a Backscattered electron image and chemical profile of a muscovite - lepidolite grain from the K-feldspar + petalite zone of the Pakeagama Lake pegmatite (sample SS20). Location of electron microprobe traverse is shown by arrow in BSE image.

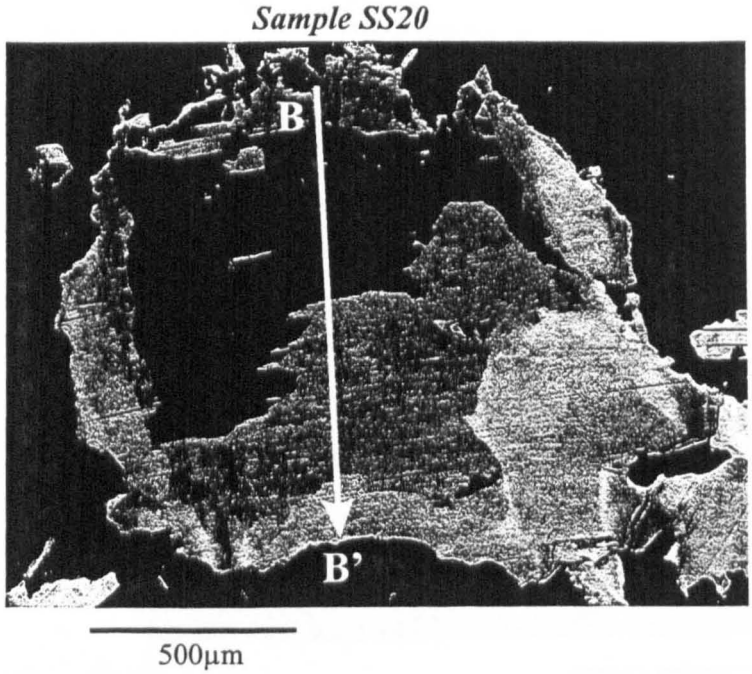

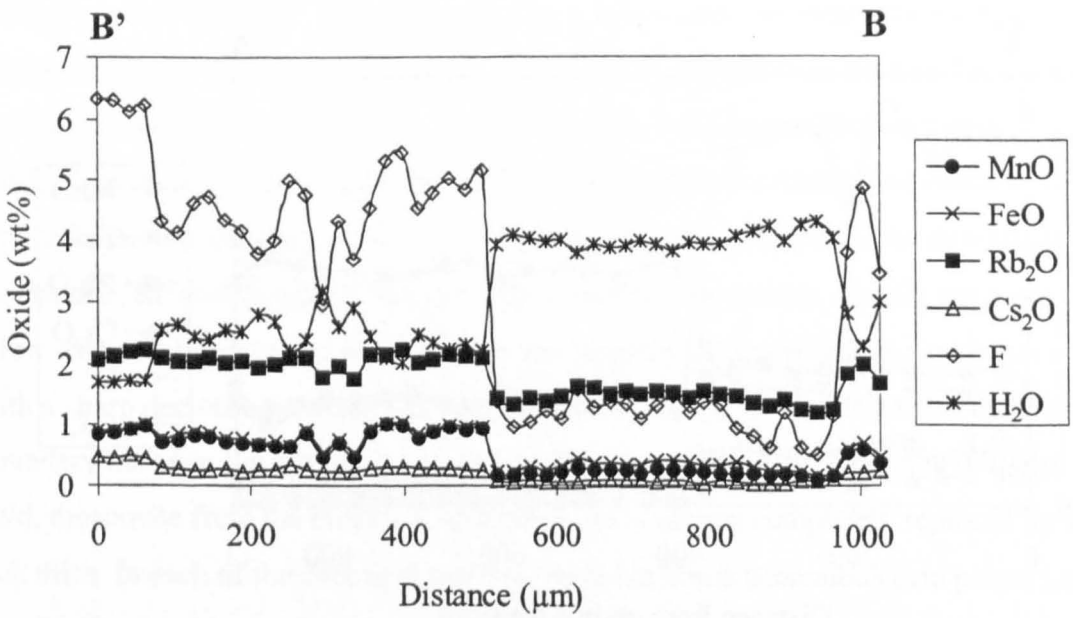

Figure 3.9b Backscattered electron image and chemical profile of a muscovite - lepidolite grain from the K-feldspar + petalite zone of the Pakeagama Lake pegmatite (sample SS20). Location of electron microprobe traverse is shown by arrow in BSE image.

Sample SS117

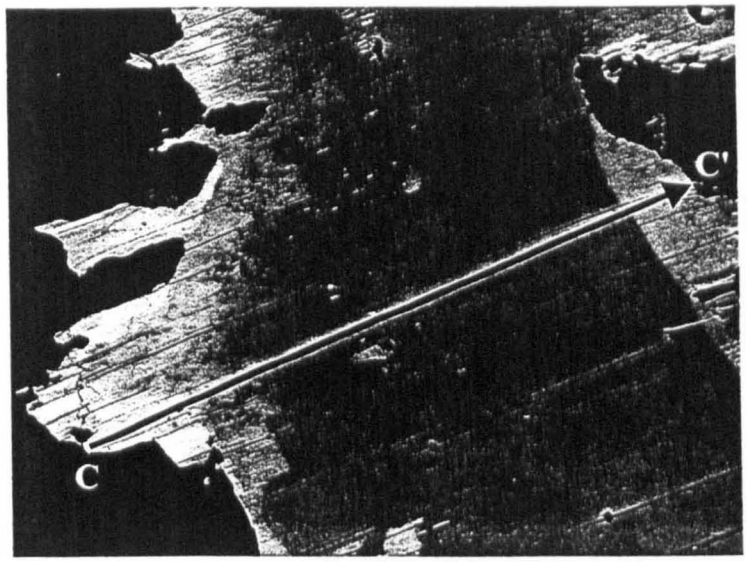

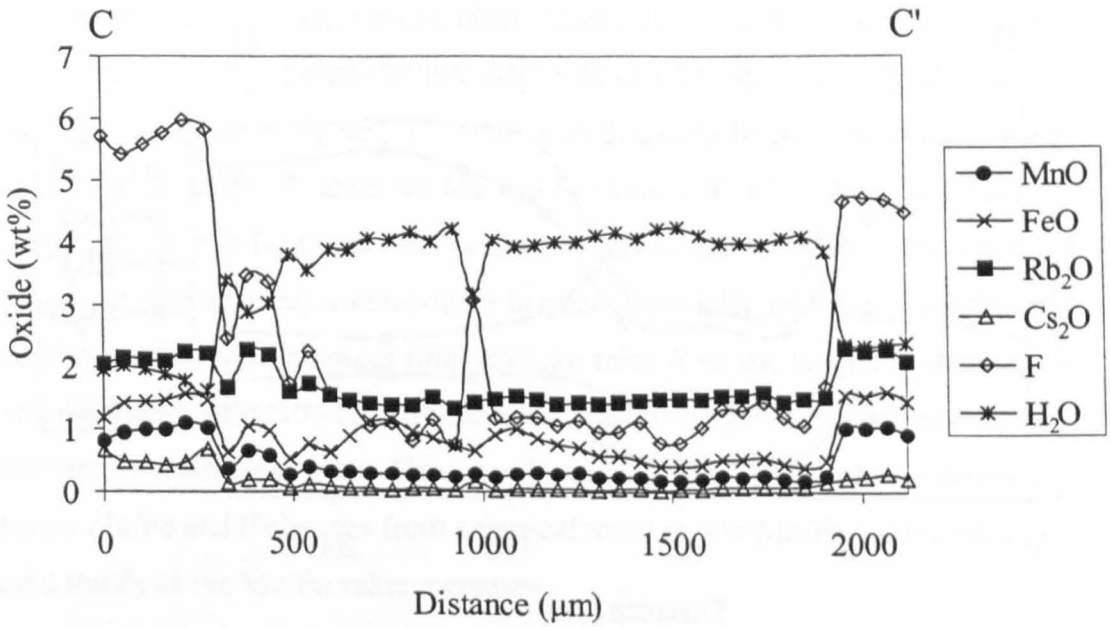

Figure 3.9c Backscattered electron image and chemical profile of a muscovite - lepidolite grain from the K-feldspar + petalite zone of the Pakeagama Lake pegmatite (sample SS117). Location of electron microprobe traverse is shown by arrow in BSE image.

Sample SS100

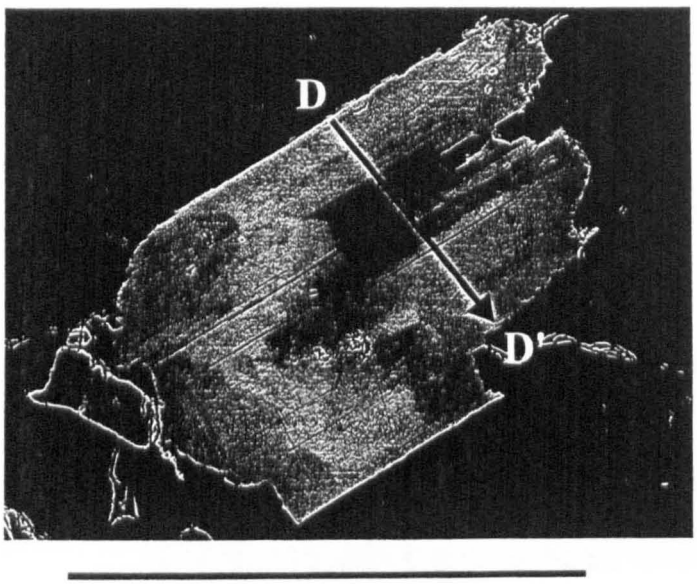

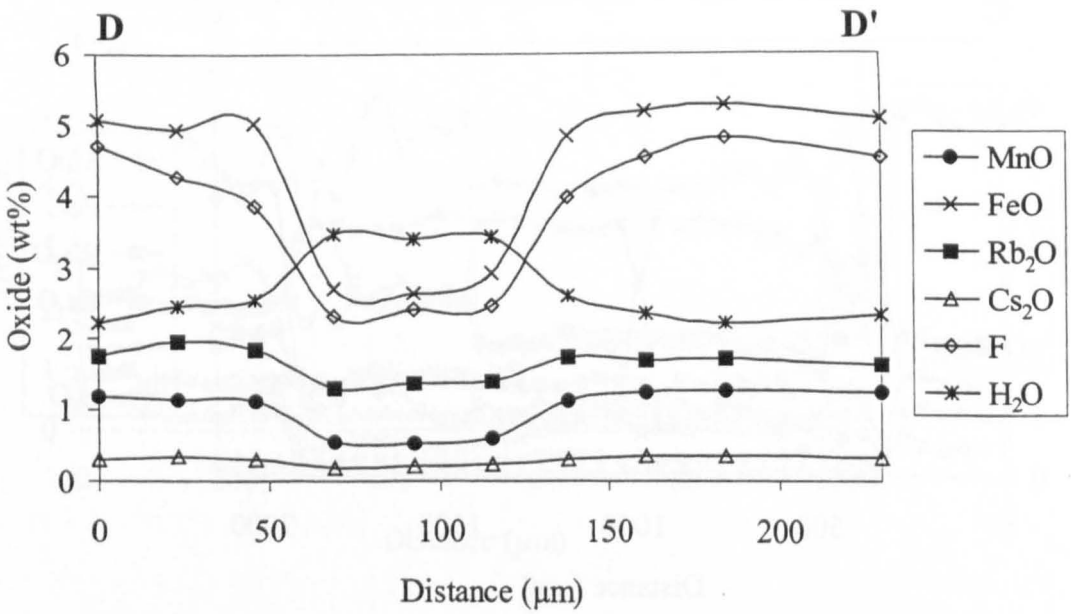

Figure 3.9d Backscattered electron image and chemical profile of a muscovite - lepidolite grain from the blocky K-feldspar zone of the Pakeagama Lake pegmatite (sample SS100). Location of electron microprobe traverse is shown by arrow in BSE image.

core zone. Jolliff *et al.* (1987) suggest that the fluid could have leached Li and F from micas in one portion of the pegmatite and redistributed these components to other pegmatite zones.

- ***Variation in mica compositions from different zones of the pegmatite***

The K/Rb ratio of K-feldspars is commonly used to decipher the degree of chemical differentiation of rare-element pegmatite fields (e.g. Cerný 1992). Figure 3.10 shows K/Rb *versus* Cs and Rb/Cs *versus* F diagrams for the micas of the Pakeagama Lake pegmatite, which display compositional variation consistent with that expected for rare-element pegmatites. There are low K/Rb ratios (5 - 25) and high Cs values up to 0.06 apfu, compared with mica from similar pegmatites (e.g. Foord *et al.* 1995). This indicates the high degree of chemical variation within different zones of the Pakeagama Lake pegmatite. Data for individual zones and dykes of the pegmatite are overlapping, which may indicate some mixing of melt-fluid between pegmatite zones. However, the K/Rb ratio is perhaps more relevant to K-feldspars as an indicator of chemical variation.

Investigating further, the chemical variation in mica from the different zones of the Pakeagama Lake pegmatite is best displayed in a new diagram with F (apfu) plotted against the ratio Mn/Fe (figure 3.11). Variation diagrams from this study show that there are a wide range of values for Mn and Fe in mica. Furthermore, contamination of the melt with Fe-rich host rocks can dramatically increase Fe concentration in mica. Fluorine can also be a major component in mica, especially within zinnwaldite and lepidolite species. Mn/Fe ranges from <0.1 for mica from the layered spodumene + quartz pegmatite-aplite to ~2.0 for mica from the late-stage vein cross-cutting the spodumene + quartz core zone. Values of F range from 0 - 3.25 apfu. The relationship between Mn/Fe and F changes from a vertical trend at low Mn/Fe values (<0.2) to curved trends as the Mn/Fe value increases.

Clearly, this diagram is superior to the commonly used K/Rb *versus* Cs plot in showing the chemical variation of mica from individual zones and dykes of the Pakeagama Lake pegmatite (figure 3.11). Backscattered electron images and chemical profiles (figure 3.9) have revealed that Mn, Fe and in particular F values increase within replacement zones of the mica and thus these trends are interpreted as the degree to which mica has been affected by replacement processes.

The distinct compositions of mica from different zones of the Pakeagama Lake pegmatite may indicate a lack of convection and mixing within the parent melt-fluid.

However, there is some field evidence to suggest that some zones may have crystallised after others, e.g. the lepidolite veins cross-cutting the spodumene + quartz core zone.

Highlighting the main trends in the F *versus* Mn/Fe diagram shows the possible sequence of crystallisation and subsequent replacement processes for the Pakeagama Lake pegmatite, summarised in figure 3.12. It is notable that some of the zones display two trends (blocky K-feldspar zone, tourmaline + muscovite aplite dykes). As a specific example, the two trends from the blocky K-feldspar zone relate to different samples. The first trend is from the analysis of colourless mica grains occurring as inclusions within K-feldspar megacrysts (sample SS100), interpreted as primary magmatic grains. The second trend is from mauve coloured interstitial mica grains (sample SS101), which may represent a second phase of mica crystallisation/precipitation.

Pegmatite Zone	*Primary Mica Crystallisation*	*Secondary Replacement*
Layered spod+qtz aplite	———	———
Blocky Kspar zone	——— - - -	———
Kspar + petalite zone	———	———
Qtz-rich wall zone	——— - - -	———
Tour + musc aplite dykes	——— ———	———
Spod + qtz core zone	———	———

Figure 3.12 Summary of the relative timing of mica crystallisation within different zones and dykes of the Pakeagama Lake pegmatite. Dashed lines indicate uncertainty.

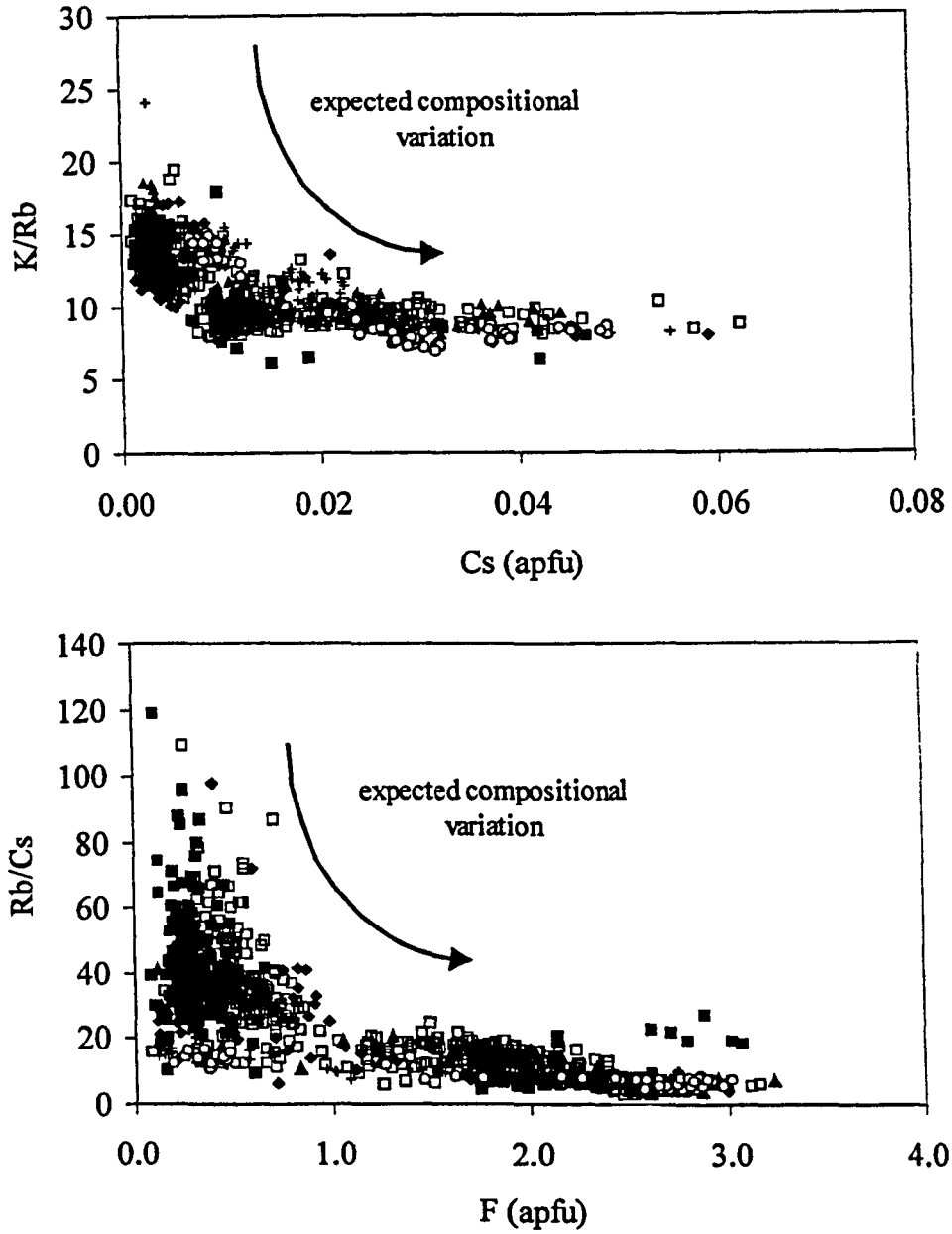

Figure 3.10 Multi-element plots for micas of the Pakeagama Lake pegmatite.
apfu = atoms per formula unit (based on 22 oxygens).
Symbols: filled (red) squares - Layered spodumene + qtz pegmatite - aplite.
Open squares - K-feldspar + petalite zone.
Filled diamonds - Tourmaline + muscovite aplite dykes.
Filled (green) triangles - Quartz rich wall zone.
Plus signs - Blocky K-feldspar (potassic) zone.
Filled (yellow) circles - Lepidolite vein cross-cutting spodumene + qtz core zone.

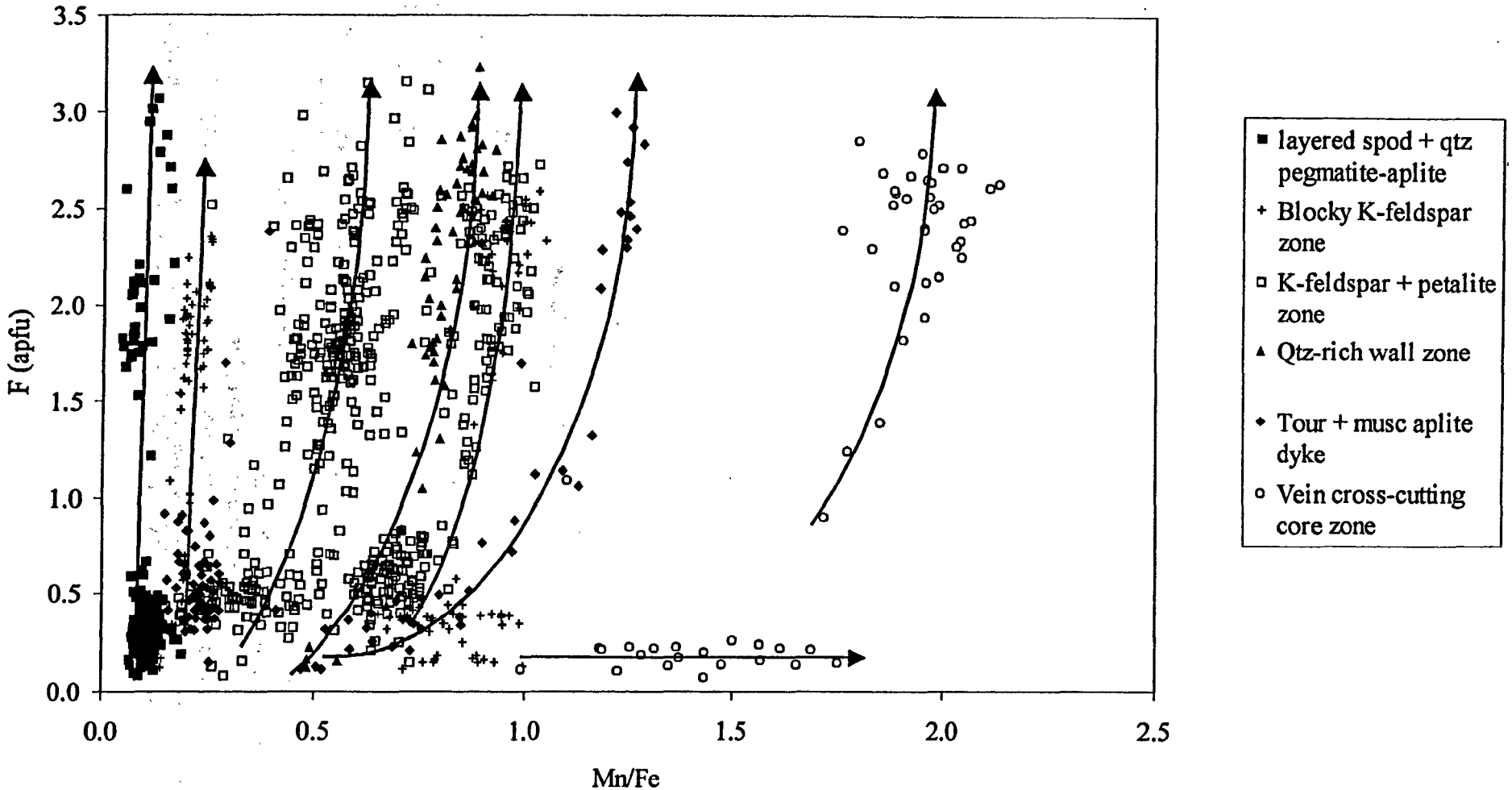

Figure 3.11 F versus Mn/Fe for mica from the Pakeagama Lake pegmatite. Arrows denote compositional trends of mica from different zones of the Pakeagama Lake pegmatite. apfu = atoms per formula unit (based on 22 oxygens).

3.3.3 Separation Rapids pegmatite group

Representative analyses of mica from the Separation Rapids pegmatite group have been compiled for each of the samples and are reported in table 3.2.

- *Classification*

The Tischendorf *et al.* (1997) classification diagram reveals a limited compositional variation among mica from the Fe-suite pegmatites (figure 3.13). Data from the Big Mack pegmatite plots almost entirely within the muscovite field indicating the limited compositional variation of mica. In contrast, the Mn-suite pegmatites define a trend from the muscovite field into the zinnwaldite field. Mica from Marko's pegmatite displays the largest compositional variation, consistent with the compositional zoning seen in BSE images. The compositional trend is similar to that of mica from the layered pegmatite-aplite zone within the Pakeagama Lake pegmatite, which has been contaminated by Fe-rich host rocks.

- *Variation diagrams*

A distinction between Fe-suite and Mn-suite pegmatites is also seen in plots of major elements *versus* Si for mica (figure 3.14). Variation in Si is comparatively restricted in the Fe-suite pegmatites resulting in near vertical trends of Mn, Rb and Fe *versus* Si. Low values of F and Li characterise the Fe-suite pegmatites. In contrast, Mn-suite pegmatites have much greater compositional variation and positive correlations between Si and Fe, Mn, Rb, F and Li; there is also a strong negative correlation with total Al.

Tindle *et al.* (*in press*) discuss significant and widespread contamination of the Separation Rapids pegmatites on the basis of tourmaline compositions. Mica from the Separation Rapids pegmatites have high Fe concentrations shown on the Si *versus* Fe variation diagram in figure 3.14 and similar trends on the classification diagram (figure 3.13) to contaminated zones from the Pakeagama Lake pegmatite. This suggests that contamination from Fe-rich host rocks has also affected the mica compositions of the Separation Rapids pegmatites. Indeed, the Separation Rapids pegmatites are intruded into the Fe-rich mafic metavolcanic and banded ironstone sequences of the Separation Lake greenstone belt. There is little doubt therefore, that interaction with host rocks has modified the composition of the parental melt from which the micas then crystallised.

- *Crystal-chemical zoning*

Backscattered electron images indicate that compositionally distinct rims only occur in the micas from the Mn-suite pegmatites. Mica from Marko's pegmatite displays compositional zoning similar to that found at Pakeagama Lake. Using unpublished data of A.G. Tindle (The Open University), it is evident that the rims are enriched in MnO, FeO, F, Rb_2O and Cs_2O relative to the core (figure 3.15). It seems likely that the zinnwaldite rims in micas from the Mn-suite pegmatites are also replacement features such as those described from the Pakeagama Lake pegmatite.

- *Variation in mica compositions from different pegmatites*

Compositional variation in micas from the Fe- and Mn-suite pegmatites are shown by the K/Rb *versus* Cs plot (figure 3.14). Mica from the Fe-suite pegmatites are characterised by a restricted range of K/Rb ratios (5 - 20) and low Cs values, <0.05 apfu. The Mn-suite pegmatites contain mica with K/Rb ratios from 38 to <5 and Cs values up to 0.27. Mica analyses from the Separation Rapids pegmatite group have been collected from several different pegmatite bodies. We would therefore not expect to find systematic compositional changes between the different pegmatites, as each will have undergone a unique history of magmatic crystallisation, fluid evolution and possible contamination from host rocks.

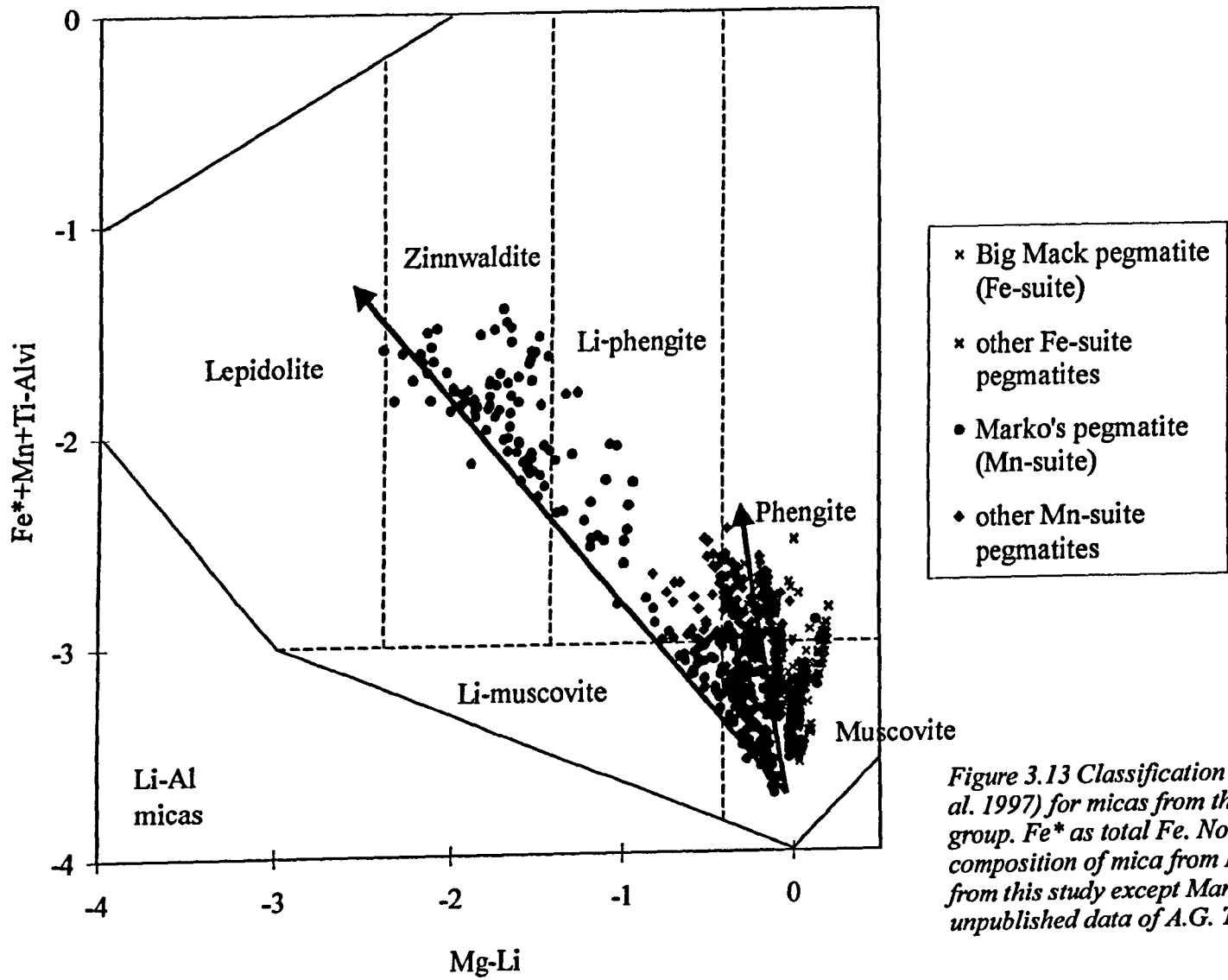

Figure 3.13 Classification diagram (after Tischendorf et al. 1997) for micas from the Separation Rapids pegmatite group. Fe as total Fe. Note the restricted variation in composition of mica from Fe-suite pegmatites. All data is from this study except Marko's pegmatite, which includes unpublished data of A.G. Tindle (The Open University).*

Table 3.2 Representative analyses and structural formulae (based on 22 oxygens) of micas from the Separation Rapids pegmatite group.

	← Fe-suite →										Mn-suite	
Sample	SS35b	SS35b	SS22	SS22	96-81	96-81	93-276	93-276	SS195	SS195	SS36	SS36
	Pluton		Pegmatite 6056		Peg. 96-81		James' pegmatite		Big Mack pegmatite		Pegmatite 260	
	muscovite	muscovite	phengite	muscovite	phengite	phengite	muscovite	muscovite	muscovite	muscovite	muscovite	Muscovite
SiO_2	44.87	44.40	42.58	43.91	45.00	45.92	45.28	44.66	44.81	43.93	44.53	44.51
TiO_2	0.06	0.02	0.04	0.00	0.05	0.04	0.27	0.12	0.02	0.04	0.04	0.03
Al_2O_3	33.97	34.11	31.77	34.61	31.46	32.82	32.31	32.45	34.44	34.15	34.25	34.34
FeO	3.31	3.39	5.23	2.52	3.40	3.15	3.09	2.84	3.16	3.33	3.59	3.31
MnO	0.06	0.06	0.35	0.28	1.70	1.52	0.06	0.08	0.02	0.03	0.07	0.08
MgO	0.09	0.11	0.26	0.01	0.09	0.08	1.23	1.28	0.22	0.24	0.18	0.15
CaO	0.01	0.00	0.06	0.01	0.00	0.00	0.01	0.02	0.01	0.01	0.00	0.00
Na_2O	0.49	0.51	0.32	0.46	0.24	0.27	0.23	0.26	0.44	0.16	0.55	0.52
K_2O	10.22	10.27	10.12	9.97	9.53	9.51	9.47	9.51	10.18	10.55	10.26	10.32
SrO	0.06	0.02	0.03	0.04	0.02	0.02	0.03	0.06	0.02	0.01	0.00	0.01
BaO	0.00	0.00	0.01	0.00	0.00	0.00	0.00	0.00	0.00	0.00	0.00	0.00
Rb_2O	0.99	1.00	1.70	1.58	1.97	1.85	3.06	3.00	1.10	0.98	1.00	0.91
Cs_2O	0.01	0.02	0.05	0.47	0.04	0.04	0.09	0.05	0.02	0.01	0.02	0.00
ZnO	0.00	0.35	0.18	0.21	0.17	0.22	0.00	0.92	0.04	0.04	0.09	0.04
SnO2	0.09	0.08	0.02	0.09	1.47	1.43	0.16	0.17	0.03	0.09	0.13	0.16
Ga_2O_3	0.03	0.06	0.06	0.03	1.50	0.77	0.05	0.06	0.05	0.02	0.01	0.06
F	0.74	0.76	1.01	0.73	1.26	1.20	0.39	0.59	0.17	0.17	0.57	0.60
Cl	0.02	0.01	0.01	0.00	0.00	0.01	0.01	0.01	0.01	0.01	0.01	0.00
Li_2O*	0.27	0.27	0.40	0.26	0.54	0.50	0.11	0.20	94.73	93.75	0.18	0.20
H_2O*	4.03	4.01	3.74	4.01	3.78	3.90	4.18	4.07	0.04	0.04	4.12	4.10
O=F,Cl	0.32	0.32	0.43	0.31	0.53	0.50	0.16	0.25	4.31	4.25	0.24	0.25
Total	99.00	99.14	97.51	98.87	101.69	102.74	99.88	100.08	99.00	97.97	99.35	99.08

*Li_2O Calculation from Tischendorf *et al.* (1997); H_2O calculation from Tindle and Webb (1990).

Si	6.137	6.086	6.049	6.053	6.153	6.162	6.216	6.148	6.123	6.084	6.087	6.089
Al iv	1.863	1.914	1.951	1.947	1.847	1.838	1.784	1.852	1.877	1.916	1.913	1.911
Al vi	3.614	3.596	3.370	3.677	3.224	3.353	3.444	3.412	3.670	3.658	3.605	3.625
Ti	0.006	0.002	0.004	0.000	0.005	0.004	0.028	0.013	0.002	0.004	0.004	0.003
Fe	0.379	0.389	0.622	0.291	0.389	0.354	0.355	0.327	0.361	0.386	0.410	0.378
Mn	0.007	0.007	0.042	0.033	0.197	0.172	0.007	0.009	0.002	0.003	0.008	0.009
Mg	0.019	0.023	0.055	0.002	0.018	0.015	0.252	0.262	0.044	0.049	0.037	0.030
Zn	0.000	0.035	0.019	0.021	0.017	0.022	0.000	0.093	0.004	0.004	0.009	0.004
Sn	0.005	0.004	0.001	0.005	0.080	0.076	0.009	0.009	0.002	0.005	0.007	0.009
Ga	0.002	0.005	0.005	0.002	0.132	0.066	0.004	0.005	0.005	0.002	0.001	0.005
Li*	0.146	0.151	0.229	0.143	0.295	0.269	0.061	0.108	0.020	0.021	0.101	0.109
Ca	0.002	0.000	0.009	0.001	0.000	0.000	0.001	0.002	0.002	0.001	0.000	0.000
Na	0.130	0.136	0.087	0.124	0.063	0.071	0.060	0.069	0.116	0.042	0.144	0.138
K	1.782	1.796	1.833	1.752	1.662	1.628	1.659	1.669	1.774	1.864	1.789	1.801
Sr	0.005	0.002	0.003	0.003	0.002	0.002	0.002	0.005	0.001	0.001	0.000	0.001
Ba	0.000	0.000	0.001	0.000	0.000	0.000	0.000	0.000	0.000	0.000	0.000	0.000
Rb	0.087	0.088	0.156	0.140	0.173	0.160	0.270	0.265	0.097	0.087	0.088	0.080
Cs	0.001	0.001	0.003	0.028	0.002	0.002	0.005	0.003	0.001	0.001	0.001	0.000
OH*	3.675	3.669	3.542	3.683	3.452	3.492	3.831	3.741	3.927	3.924	3.755	3.742
F	0.322	0.330	0.455	0.317	0.547	0.507	0.167	0.257	0.072	0.075	0.244	0.258
Cl	0.003	0.001	0.003	0.000	0.001	0.001	0.002	0.002	0.001	0.001	0.001	0.000
TOTAL	18.185	18.237	18.437	18.222	18.259	18.195	18.159	18.252	18.101	18.127	18.204	18.194
Al total	5.477	5.510	5.320	5.624	5.071	5.191	5.228	5.264	5.548	5.575	5.518	5.536
Mg-Li	-0.127	-0.128	-0.174	-0.141	-0.278	-0.254	0.191	0.154	0.024	0.028	-0.065	-0.079
(Fe*+Mn+ Ti-Alvi)	-3.223	-3.197	-2.701	-3.354	-2.632	-2.823	-3.054	-3.063	-3.305	-3.266	-3.183	-3.235

Table 3.2 continued. Representative analyses of micas from the Separation Rapids pegmatite group.

	← Marko's pegmatite →						Mn-suite		→					
Sample	SS37	SS37	SS38	SS38	SS40	SS40	94-44+	94-44+	SS31	SS31	96-86b	96-86b	SS34a	SS34a
									Big Whopper peg.		leucogranite		Pegmatite 265	
	muscovite	muscovite	muscovite	muscovite	Li-musc	phengite	zinn	musc	phengite	Li-pheng	phengite	phengite	phengite	phengite
SiO_2	43.33	43.32	44.50	44.45	44.81	44.22	46.88	46.44	44.33	45.29	44.78	44.86	43.42	43.95
TiO_2	0.47	0.43	0.30	0.30	0.54	0.54	0.12	0.27	0.06	0.05	0.04	0.05	0.04	0.05
Al_2O_3	33.47	33.61	33.92	33.99	32.64	32.55	25.39	33.17	32.66	30.61	32.03	31.75	32.56	31.50
FeO	1.67	1.72	2.29	2.30	1.85	1.82	2.67	1.28	3.32	3.51	4.29	4.79	4.58	5.26
MnO	0.53	0.57	0.82	0.85	0.85	0.91	1.95	0.85	0.73	0.86	0.37	0.42	0.29	0.35
MgO	0.42	0.44	0.07	0.05	0.58	0.60	0.73	0.48	0.00	0.00	0.13	0.16	0.24	0.27
CaO	0.01	0.02	0.00	0.02	0.00	0.01	0.01	0.00	0.00	0.00	0.01	0.02	0.01	0.01
Na_2O	0.49	0.52	0.27	0.33	0.59	0.56	0.25	0.51	0.30	0.19	0.32	0.28	0.40	0.12
K_2O	9.93	9.81	9.71	9.46	9.61	9.57	8.25	9.26	9.81	10.03	10.61	10.60	9.87	10.12
SrO	0.04	0.02	0.02	0.01	0.00	0.04	-	-	0.04	0.02	0.02	0.02	0.04	0.04
BaO	0.00	0.00	0.00	0.00	0.00	0.01	0.00	0.00	0.00	0.00	0.00	0.00	0.00	0.00
Rb_2O	1.90	1.94	2.50	2.69	1.84	1.78	3.20	1.66	2.04	2.05	0.79	0.72	1.67	1.94
Cs_2O	0.06	0.06	0.19	0.15	0.07	0.07	1.38	0.04	0.00	0.05	0.06	0.03	0.02	0.14
ZnO	0.04	0.07	0.08	0.04	0.00	1.02	0.06	0.05	0.81	1.80	0.55	0.00	0.12	0.11
SnO2	0.10	0.09	0.06	0.10	0.06	0.10	0.06	0.08	0.10	0.06	0.08	0.09	0.05	0.05
Ga_2O_3	0.05	0.06	0.07	0.06	0.05	0.04	0.02	0.02	0.04	0.08	0.03	0.02	0.06	0.08
F	1.55	1.67	0.62	0.67	2.23	2.43	5.34	1.91	1.47	2.71	1.49	1.62	0.85	1.05
Cl	0.01	0.01	0.00	0.01	0.02	0.01	0.00	0.01	0.00	0.00	0.01	0.00	0.01	0.00
Li_2O*	0.70	0.78	0.21	0.23	1.14	1.27	3.63	0.93	0.66	1.48	0.67	0.75	0.31	0.42
H_2O*	3.57	3.52	4.07	4.04	3.32	3.23	1.78	3.54	3.64	3.08	3.64	3.58	3.88	3.78
O=F,Cl	0.65	0.71	0.26	0.28	0.95	1.02	2.25	0.81	0.62	1.14	0.63	0.68	0.36	0.44
Total	97.69	97.96	99.42	99.44	99.27	99.73	99.47	99.71	99.41	100.72	99.28	99.07	98.03	98.82

*Li_2O Calculation from Tischendorf *et al.* (1997); H_2O calculation from Tindle and Webb (1990). + Unpublished data of A.G. Tindle (The Open University).

Si	6.032	6.015	6.118	6.110	6.124	6.055	6.53	6.25	6.128	6.223	6.175	6.190	6.086	6.155
Al iv	1.968	1.985	1.882	1.890	1.876	1.945	1.47	1.75	1.872	1.777	1.825	1.810	1.914	1.845
Al vi	3.523	3.515	3.614	3.616	3.382	3.308	2.692	3.519	3.448	3.181	3.380	3.355	3.465	3.355
Ti	0.049	0.045	0.031	0.031	0.055	0.055	0.012	0.028	0.007	0.005	0.004	0.005	0.005	0.006
Fe	0.195	0.200	0.263	0.264	0.211	0.208	0.311	0.144	0.384	0.404	0.494	0.553	0.536	0.616
Mn	0.063	0.067	0.096	0.099	0.099	0.105	0.230	0.097	0.085	0.100	0.043	0.050	0.034	0.041
Mg	0.088	0.091	0.014	0.011	0.118	0.122	0.152	0.096	0.000	0.000	0.028	0.032	0.049	0.057
Zn	0.004	0.007	0.008	0.004	0.000	0.103	0.006	0.005	0.083	0.183	0.056	0.000	0.013	0.012
Sn	0.005	0.005	0.003	0.005	0.003	0.005	0.003	0.004	0.005	0.003	0.004	0.005	0.003	0.003
Ga	0.004	0.006	0.006	0.005	0.005	0.004	0.002	0.001	0.004	0.007	0.003	0.001	0.005	0.007
Li*	0.393	0.433	0.114	0.127	0.628	0.702	2.032	0.503	0.365	0.816	0.369	0.415	0.177	0.238
Ca	0.001	0.002	0.000	0.002	0.000	0.002	0.002	0.000	0.000	0.000	0.001	0.003	0.001	0.001
Na	0.131	0.139	0.071	0.087	0.157	0.150	0.067	0.133	0.081	0.050	0.086	0.074	0.108	0.034
K	1.762	1.736	1.703	1.659	1.675	1.671	1.465	1.590	1.730	1.758	1.866	1.866	1.764	1.808
Sr	0.003	0.002	0.002	0.001	0.000	0.003	-	-	0.004	0.002	0.002	0.002	0.003	0.003
Ba	0.000	0.000	0.000	0.000	0.000	0.000	0.000	0.000	0.000	0.000	0.000	0.000	0.000	0.000
Rb	0.170	0.173	0.221	0.237	0.162	0.156	0.287	0.144	0.181	0.181	0.070	0.064	0.150	0.174
Cs	0.004	0.004	0.011	0.009	0.004	0.004	0.082	0.002	0.000	0.003	0.004	0.002	0.001	0.008
OH*	3.316	3.265	3.732	3.709	3.030	2.948	1.649	3.183	3.357	2.821	3.350	3.291	3.624	3.533
F	0.681	0.732	0.268	0.290	0.966	1.050	2.351	0.814	0.643	1.178	0.648	0.709	0.375	0.467
Cl	0.003	0.003	0.000	0.002	0.005	0.001	0.000	0.003	0.001	0.001	0.002	0.000	0.002	0.000
TOTAL	18.396	18.426	18.157	18.158	18.499	18.598	19.341	18.268	18.377	18.691	18.410	18.427	18.315	18.364
Al total	5.492	5.500	5.496	5.507	5.258	5.253	4.166	5.265	5.320	4.958	5.205	5.164	5.379	5.200
Mg-Li	-0.305	-0.342	-0.100	-0.116	-0.510	-0.580	-1.879	-0.407	-0.364	-0.816	-0.341	-0.383	-0.128	-0.181
Fe*+Mn+ Ti-Alvi	-3.217	-3.203	-3.223	-3.223	-3.017	-2.939	-2.140	-3.249	-2.972	-2.673	-2.838	-2.747	-2.890	-2.692

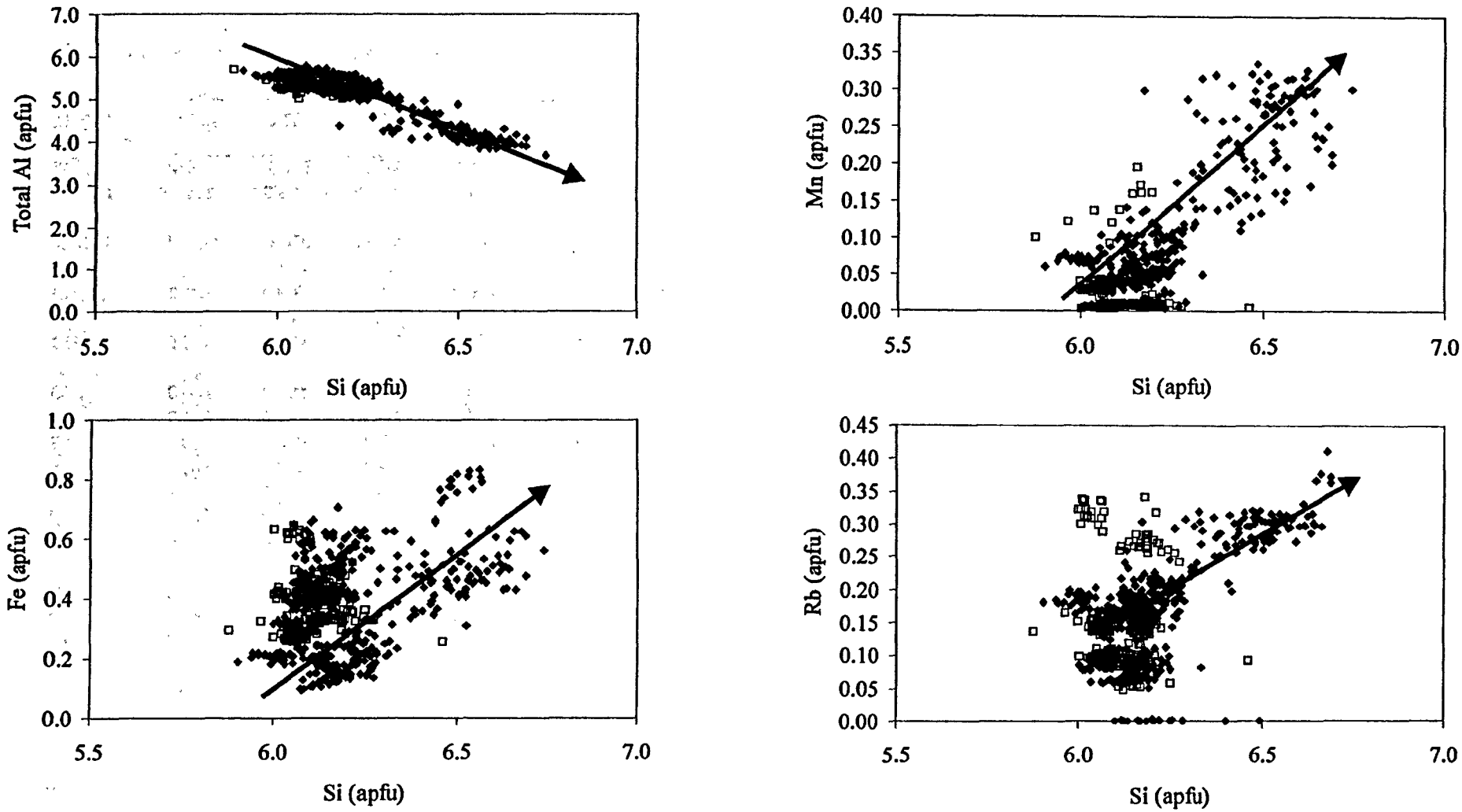

Figure 3.14 Variation diagrams for micas from the Separation Rapids pegmatite group. open squares - Fe-suite, filled diamonds - Mn-suite.

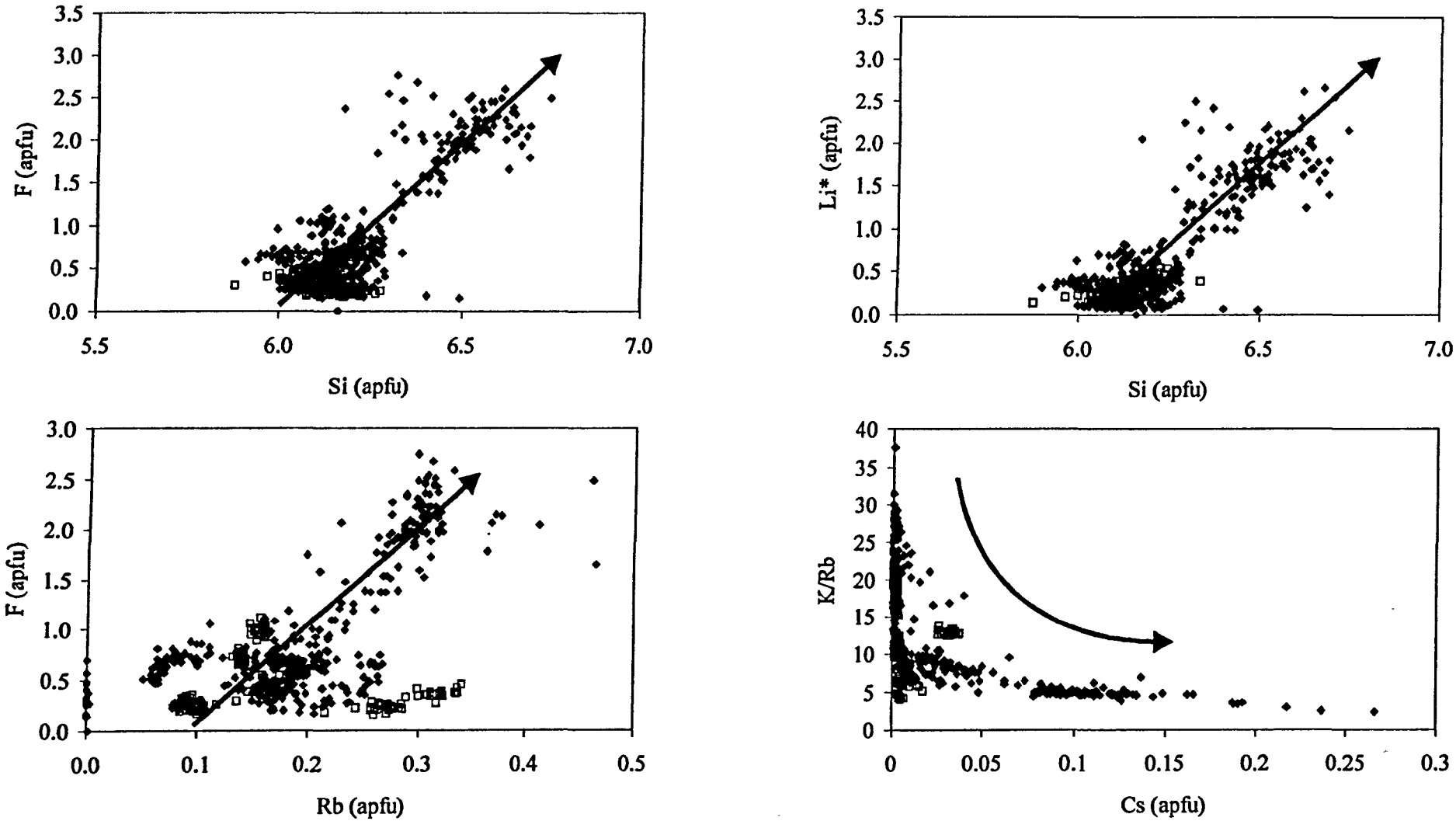

Figure 3.14 continued. Variation diagrams for micas from the Separation Rapids pegmatite group. open squares - Fe-suite, filled diamonds - Mn-suite.

Sample 94-44

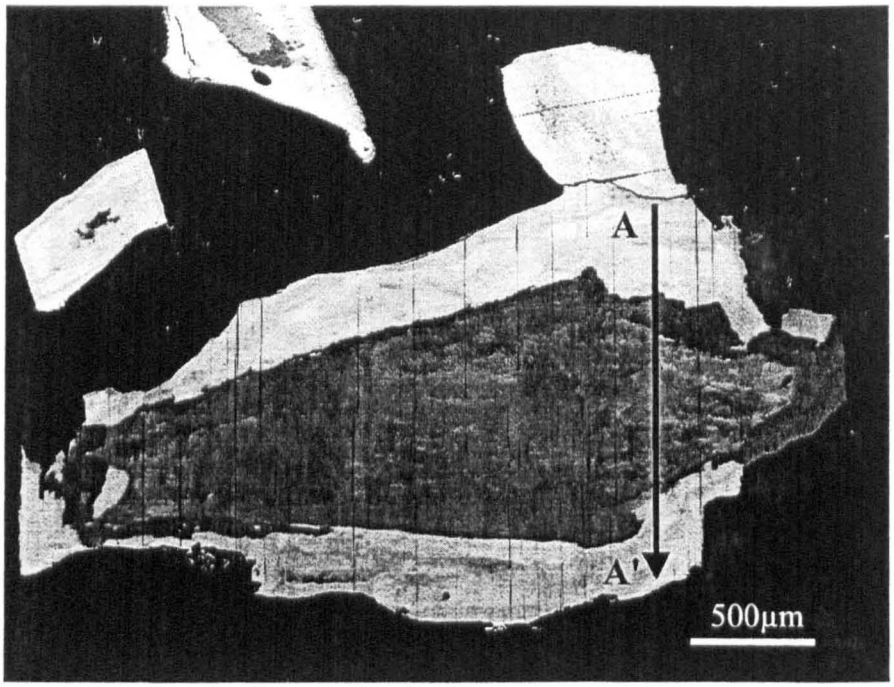

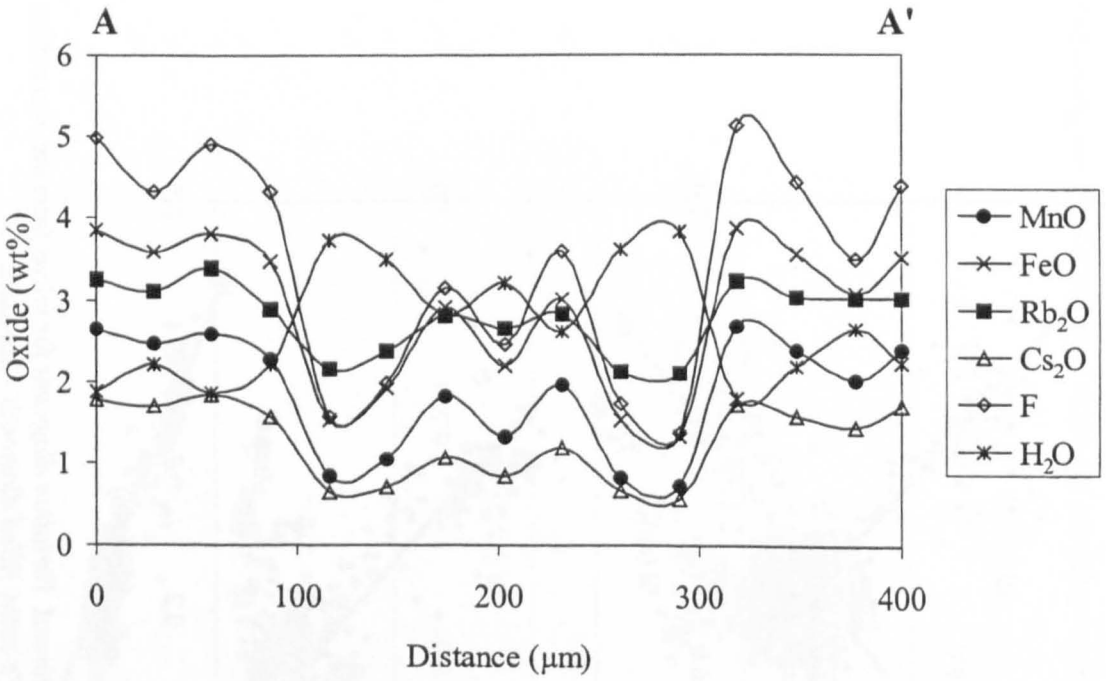

Figure 3.15 Backscattered electron image and chemical profile of a muscovite - lepidolite grain (sample 94-44) from Marko's pegmatite, Separation Rapids group, Mn-suite. Location of electron microprobe traverse is shown by arrow in BSE image. Using unpublished data of A.G. Tindle (The Open University).

3.4 Discussion and conclusions

3.4.1 Pakeagama Lake pegmatite

Electron microprobe analyses reveal the chemical characteristics of mica from different internal zones of the Pakeagama Lake pegmatite. It is likely that melting and assimilation of Fe-rich host rocks has contaminated the pegmatite melt in the layered pegmatite-aplite zone, as indicated by high Fe values in mica.

Backscattered electron images and spot analyses of mica grains reveal Li-muscovite - zinnwaldite - lepidolite rims on muscovite cores in the majority of white micas from the Pakeagama Lake pegmatite. Textural observations indicate a two-stage process beginning with primary magmatic crystallisation of muscovite. The widespread occurrence of fluorine-rich mica along grain boundaries, fractures, in interstitial grains and cross-cutting veins suggests they are secondary replacement features of magmatic muscovite.

In a study of zoned mica from the pegmatites of the Black Hills of South Dakota, Jolliff *et al.* (1987) proposed that lepidolite rims were precipitated by an aqueous fluid. The process by which a fluid phase could precipitate lepidolite is described by London (1986). Crystallisation of tourmaline removes boron (a major flux component), which raises the solidus temperature in residual silicate melt. In turn, this leads to precipitation of other alkali aluminosilicates e.g. lepidolite, and to exsolution of a relatively low density, solute-poor aqueous fluid (London 1986). Clues to when such a fluid phase might have been exsolved from the Pakeagama Lake pegmatite come from late-stage tourmaline + albite veins, which cross-cut the pegmatite and surrounding host granite (figure 3.8b; see also Breaks *et al.* 1999a). At the Tanco pegmatite in Manitoba, London (1986) has shown that similar events occurred at a temperature between 470 - 420°C and approximately 3 - 2.5kbar pressure. However, the transition from magmatic crystallisation to hydrothermal fluid precipitation could be continuous in rare-element pegmatites (London 1986). Hence, the replacement of muscovite by Li-muscovite - lepidolite may not necessarily be a sub-solidus process.

3.4.2 Separation Rapids pegmatites

The Separation Rapids pegmatite group is chemically divided into an Fe-suite and Mn-suite, based on columbite-tantalite mineral chemistry (Tindle and Breaks 1998). These authors also suggest that the Mn-suite pegmatites crystallised from a melt with higher fluorine content than the Fe-suite.

Observations from this study lend further support to this hypothesis as the Mn-suite pegmatites, represented by Marko's pegmatite, contain muscovite that is partly replaced by fluorine-rich zinnwaldite. In contrast, micas from the Fe-suite pegmatites do not display F-rich zones, suggesting that melt had a lower fluorine concentration. In both pegmatite suites, localised (wall zone) contamination of the pegmatite with Fe-rich metavolcanic and banded ironstones is suggested by Fe-rich mica compositions.

It is proposed here that the F-rich mica rims within the Mn-suite Separation Rapids pegmatites were generated by replacement of muscovite by a melt-fluid phase as at Pakeagama Lake. However, the restricted occurrence of the zinnwaldite rims indicates that the F-rich phase did not have a widespread affect on the mica crystallisation history in the Separation Rapids pegmatites. The occurrence of Li-mica + albite 'pods' within Marko's pegmatite (figure 3.8c) suggests that the F-rich phase may have been locally concentrated as an immiscible (vapour ?) segregation from the melt.

3.4.3 Comparison of Pakeagama Lake and Separation Rapids pegmatites

Comparison of the geochemical data from mica in both pegmatite suites examined indicates that mica crystallisation played a much more important role in the crystallisation of the Pakeagama Lake pegmatite than in the Separation Rapids pegmatites. This is reflected in the wide variation of mica compositions and textures within the Pakeagama Lake pegmatite and in comparison, a relatively restricted range of mica compositions and only localised evidence of melt-fluid interaction in the Separation Rapids pegmatites.

Contamination of pegmatite melts by Fe-rich host rocks is evident in both pegmatite suites. However, this is a localised feature which is only likely to have affected the pegmatite zone that is in direct contact with the host rocks.

4. U-Pb columbite-tantalite chronology of rare-element pegmatites

4.1 Introduction

Granitic pegmatites of the rare-element class are characterised by exotic mineralogy and heterogeneous textures that suggest a series of complex processes are involved in their formation. This may include multiple stages of magmatic crystallisation, precipitation of an aqueous vapour phase, and sub-solidus metasomatism (London 1996). Lithium-rich rare-element pegmatites begin primary crystallisation at the upper stability limit of the characteristic lithium aluminosilicates, petalite and spodumene, in the range 700 - 600°C (London 1984, 1986). In addition, concentration of non-haplogranite components (boron, phosphorus and fluorine) through disequlibrium fractional crystallisation involving muscovite generates a peralkaline, Na-aluminosilicate melt-vapour phase from which albite, tourmaline, F-rich micas, beryl and Nb-Ta oxides (columbite-tantalite) crystallise (London 1987). The high levels of B, P and F also lower solidus temperatures and thus extend magmatic crystallisation below 500°C (London 1987; London *et al.* 1993). Continuous transition between magmatic and hydrothermal conditions between 470 - 420°C are indicated by fluid-inclusion studies of Archæan rare-element pegmatites (London 1986).

Crystal Size Distribution (CSD) studies suggest that magmatic crystallisation of pegmatites occurs over days to years (Webber *et al.* 1999), but there are few estimates of the timescales of vapour-phase replacement and sub-solidus metasomatic processes involved in rare-element pegmatite formation. Romer and Smeds (1994) have suggested that dating of columbite-tantalite from both primary magmatic and from replacement assemblages could give the best estimate for the timescales over which rare-element pegmatites are active. Furthermore, columbite-tantalite minerals are characterised by complex zoning patterns which reflect fractionation of the melt and the multiple stages of pegmatite formation (Černý and Ercit 1985). Therefore, compositional zones within individual columbite-tantalite grains could preserve resolvable differences in U-Pb age. This study is the first to investigate the U-Pb systematics of columbite-tantalite in

relation to crystal-chemical zoning using combined electron microprobe, Thermal Ionisation Mass Spectrometry (TIMS) and high-spatial resolution Laser Ablation - Multi-Collector - Inductively Coupled Plasma - Mass Spectrometry (LA-MC-ICP-MS) techniques.

4.1.1 Columbite-tantalite mineral chemistry

The columbite-tantalite series [(Fe,Mn) $(Ta,Nb)_2O_6$] are the most common Nb-Ta species in rare-element pegmatites. The end members ferrocolumbite ($FeNb_2O_6$), manganocolumbite ($MnNb_2O_6$) and manganotantalite ($MnTa_2O_6$) are all orthorhombic minerals as is ferrotantalite (Fe>Mn) $(Ta>Nb)_2O_6$). This latter species is not an end-member however, which instead belongs to ferrotapiolite ($FeTa_2O_6$), a tetragonal species of the tapiolite series. All of these species can be represented on the columbite-tantalite quadrilateral (e.g. figure 4.3), which is commonly used to illustrate fractionation trends in rare-element pegmatites (summary in Cerný and Ercit 1985). The fractionation trend followed by columbite-tantalite minerals in rare-element pegmatites is broadly from Fe-, Nb-rich compositions to Mn-,Ta-rich compositions. This is based on the geochemical evidence that Ta substitutes for Nb, and Mn for Fe during the fractionation of a pegmatite magma (Cerný and Ercit 1985). The effect on the columbite-tantalite quadrilateral is to move from the ferrocolumbite field (lower left quadrant) to the manganotantalite field (upper right quadrant) with progressive chemical evolution.

Complex zoning patterns occur in columbite-tantalite, which can be seen to good effect using backscattered electron images. Variations in Nb and Ta content (inferred from mean atomic number variations) are readily observed as darker and lighter regions within individual crystals. Oscillatory zoning is considered to be a primary feature, produced by magmatic growth of columbite-tantalite (Cerný *et al.* 1992). An abundance of highly reactive residual fluids during the late stages of pegmatite formation subject pegmatite minerals to partial or complete replacement (London 1986). In columbite-tantalite, this results in secondary features such as convolute zoning, which overprint the primary zoning (Cerný *et al.* 1992; Abella *et al.* 1995).

4.1.2 U-Th-Pb systematics of columbite-tantalite

Columbite-tantalite minerals can accommodate considerable amounts of uranium (*circa* 500 - 1000ppm) and exclude lead almost completely, which makes them suitable for U-Pb dating (Romer and Wright 1992). The U-Pb systematics, however, are typically not straightforward; normal and reverse discordance are very common (Romer and Smeds 1994, 1996, 1997).

Previous geochronological studies have shown that columbite-tantalite minerals contain two U-Th-Pb systems; one system is bound in the crystal structure, the other is related to exsolved U-rich 'inclusions' (Romer and Wright 1992; Romer *et al.* 1996). Metamict areas within columbite-tantalite crystals are probably caused by unexsolved uranium. These areas may be open to U-Th-Pb mobility, causing the commonly observed reverse discordance of columbite-tantalite analyses (e.g. Romer and Smeds 1994, 1996). Since the columbite structure is unlikely to incorporate lead, this reverse discordance is attributed to loss of uranium, rather than lead gain (Romer *et al.* 1996). Normal discordance is also observed in U-Pb isotopic analyses of columbite-tantalite, which can be attributed to either excess uranium (perhaps from U-rich inclusions) or lead loss caused by thermal disturbance.

In some instances, this discordance can be removed by leaching prior to analysis (Romer and Smeds 1996). However, if there have been several disturbances to the U-Pb system (perhaps by interaction with residual fluids) and if the metamict regions are not preferentially dissolved, the data may show significant, non-analytical scatter. In these cases, TIMS analyses could yield intercept ages that are geologically meaningless. The LA-MC-ICP-MS technique provides a method of directly determining any age differences between primary and secondary zones in columbite-tantalite which could constrain the timing of magmatic-hydrothermal activity in rare-element pegmatites.

The closure temperature of columbite-tantalite has yet to be investigated in detail. However, Romer and Wright (1992) reported columbite-tantalite ages that were concordant with U-Pb zircon ages in an area where amphibolite facies metamorphism is known to have affected the host granites (Romer and Wright 1992). These results suggest that columbite-tantalite is a robust geochronometer, which yields reliable dates for magmatic events.

4.1.3 Analytical techniques

- *Thermal Ionisation Mass Spectrometry (TIMS)*

All isotopic analyses using TIMS were performed at GFZ Potsdam, Germany, using the procedures described by Romer and Wright (1992) and Romer and Smeds (1996) (summarised in Appendix B). All samples were leached in 20%HF for 20 minutes before ion exchange chemistry. Leaching removes surface contamination, inclusions such as feldspars and sulphides, and dissolves metamict parts of the columbite (figure 4.1). Columbite dissolves easily in 40%HF.

- *Laser Ablation - Multi-Collector - Inductively Coupled Plasma - Mass Spectrometry, LA-MC-ICP-MS (G.L. Foster, written communication)*

The LA-MC-ICP-MS analyses were performed at the NERC Isotope Geology Laboratories (NIGL, Keyworth, UK) using the procedure described by Horstwood *et al.* (2001) and is briefly summarised here. In order to preserve the replacement zones in columbite-tantalite, grains used for LA-MC-ICP-MS analyses were not leached. After cleaning to remove surface contamination, grain mounts of columbite-tantalite were placed into the ablation cell of the Merchantek Microprobe II, 266 nm, Nd:YAG laser ablation system, in an Ar environment. A large but weak laser beam (~80 μm in diameter, $kJcm^{-2}$) was briefly rastered over the surface targeted for analysis to remove any further surface contamination. A more powerful but smaller beam (approx. 30x20 μm, $kJcm^{-2}$) was then rastered over an area of 35x40 μm on the surface of the target crystal at a speed of 30 μm/sec. A pit approximately 50x50x10 μm was excavated and the ablated material was carried in a stream of Ar gas to the ICPMS source. The mass spectrometric analytical procedure included a 1 minute on-peak-zero blank acquisition prior to firing the laser, an ion counter-Faraday gain measurement, an ion-counter monitor of the Hg level in the Ar carrier gas, a measurement of mass 204 by ion-counting, and an assessment of instrumental Pb and Pb-U mass bias using a mixed Tl-^{235}U tracer solution (c.f. Horn *et al.* 2000) that was simultaneously aspirated through the laser cell. When the laser was fired Tl and Pb isotopes and ^{238}U were measured simultaneously in the multiple Faraday array of the ThermoElemental Axiom ICPMS (9 faraday collectors - one wide faraday to measure ^{238}U, and one axial ion counting detector). A single analysis typically takes less than 4 minutes to complete.

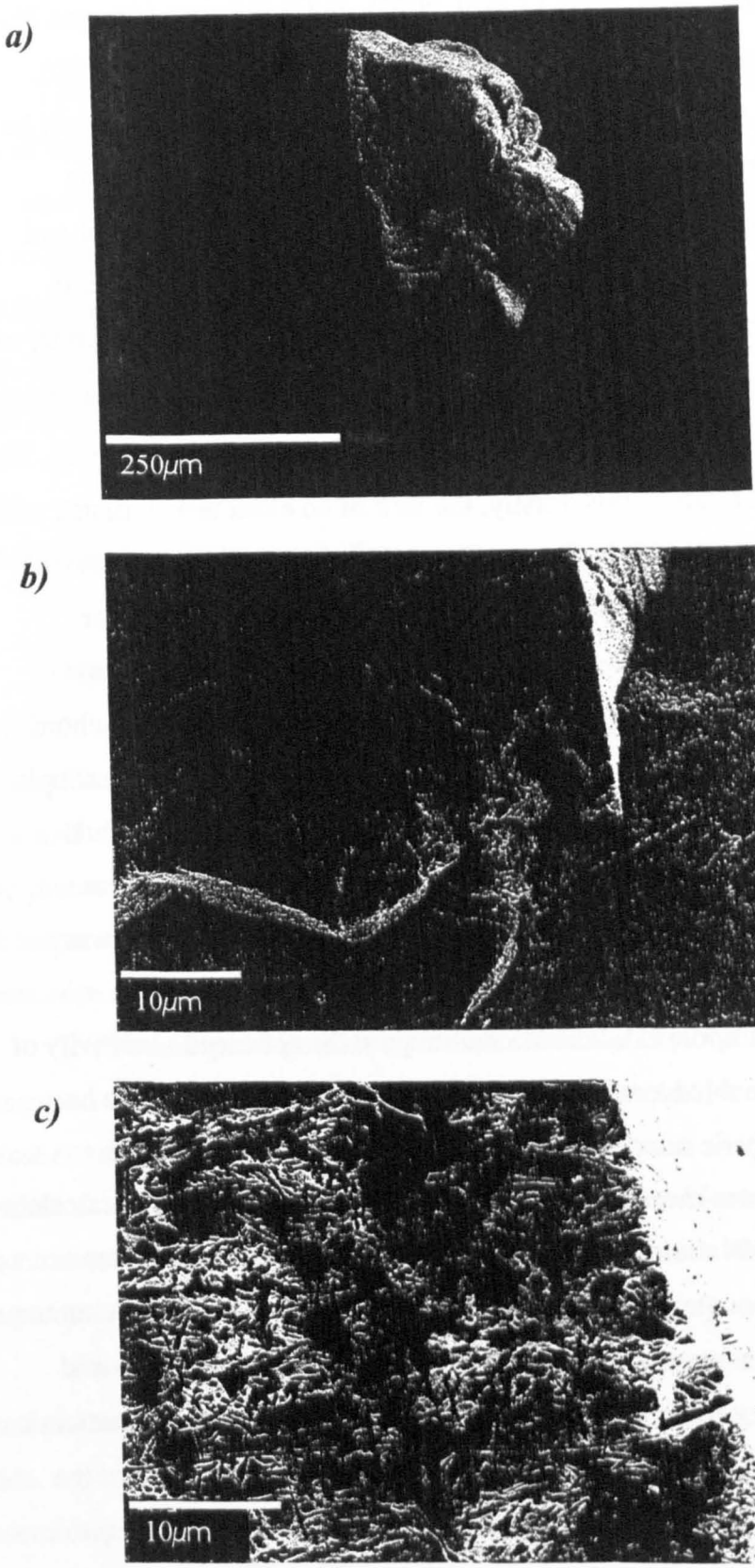

Figure 4.1 SEM images of columbite-tantalite grains after leaching in 20% HF for 20mins. a) and b) Sample SS134 Pakeagama Lake pegmatite. c) Sample 99FWB74 Big Mack pegmatite, Separation Rapids group. Note the etching of inclusions that are <10 microns in some cases.

Within run Pb/U fractionation at the site of ablation is typically removed by the rastering approach (Parrish *et al.* 1999; Li *et al.* 2001), and instrumental Pb and Pb-U mass bias is corrected using the mixed Tl-^{235}U tracer solution (Horn *et al.* 2000). However, despite these precautions and corrections, relic fractionation must still be corrected for by comparison to a standard of known age (in this case a 554 Ma monazite; R. Parrish, unpublished data) analysed under identical instrumental and ablation conditions. The reproducibility of the ^{206}Pb/^{238}U ratio of the standard is quadratically added to the internal error of each analysis reflecting the uncertainty of this correction (typically ~2-3% 2σ). Due to the unavailability of a well characterised columbite-tantalite ablation standard, a monazite standard was used in this study. There are several problems that relate to this. Firstly, the lack of an exact matrix match will effect the accuracy of the corrected U-Pb age. However, the effect of not matrix matching is small (always less than 8%), and typically reproducible with other accessory minerals (Horstwood *et al., unpublished data.*). Notably, Pb/U ratios corrected without an exact matrix match tend to be reversely discordant on a chord through the ^{207}Pb/^{206}Pb age and the origin, thus providing meaningful ages in simple cases. Secondly, whereas the rastering approach removes the laser induced Pb/U fractionation in monazite, at a similar laser fluence, minor Pb fractionation was observed in some columbite-tantalite analyses. This within-run fractionation was corrected by using the intercept method of Kosler *et al.* (in press).

In contrast to Quadrapole LA-ICP-MS techniques, the enhanced sensitivity of the Axiom MC-ICP-MS enabled a relatively precise common Pb correction to be carried out. However, isobaric interference of ^{204}Hg on ^{204}Pb complicates this correction. Here a ion counter-measurement of mass 201 (^{201}Hg) was used to calculate the ^{204}Hg present at mass 204 during the analysis and the calculated counts were stripped from the 204 ion counter-measurement and ^{204}Pb can be calculated. A common Pb correction based on this measurement and a model Pb composition (Stacey and Kramers, 1975) can then be carried out if necessary. The necessity of the correction is judged on whether the corrected ^{207}Pb/^{206}Pb lies outside of the internal errors of the uncorrected ratio. The accuracy of the common Pb correction is dependant on the amount of ^{204}Pb and ^{207}Pb. Using several crystals of known ^{207}Pb/^{206}Pb ratio, an empirical estimate of the accuracy of the correction has been generated and this is quadratically added to the internal error of the measured ^{207}Pb/^{206}Pb.

4.2 Sample descriptions

U-Pb columbite-tantalite ages are presented from three rare-element pegmatite fields of the Superior Province in Ontario, Canada (figure 4.2). All pegmatites sampled in this study are part of the lithium-cesium-tantalum (LCT) family (Cerný 1991). From north to south, these are: 1) the Pakeagama Lake pegmatite, located along the Bear Head fault zone in the North Caribou Terrain; 2) the Separation Rapids pegmatite group, English River Subprovince - Winnipeg River Subprovince boundary; 3) the Mavis Lake group, Winnipeg River Subprovince - Wabigoon Subprovince boundary.

4.2.1 Pakeagama Lake pegmatite

This variably deformed, steeply dipping, internally zoned pegmatite body is located along the Bear Head fault, a regional scale dextral shear zone within the North Caribou Terrain (Corfu and Stone 1998a). The pegmatite exposure has a width of 50m and a strike length of 250m, hosted by the assumed parental granite, the Pakeagama Lake pluton (Breaks *et al.* 1999a). Columbite-tantalite samples were collected from the K-feldspar + petalite zone and lepidolite-rich veins that cross-cut the spodumene + quartz core zone.

The K-feldspar + petalite zone forms the majority of the pegmatite body, comprised of K-feldspar megacrysts (up to 0.5m diameter), tourmaline, muscovite and garnet enveloped by fine-grained aggregates of spodumene + quartz pseudomorphs after petalite. A single euhedral grain of tantalite was collected (sample SS137) with dimensions of 6 x 4 x 2mm, which occurred as an inclusion within a former petalite megacryst.

The core zone of the Pakeagama Lake pegmatite consists of fine-grained spodumene + quartz intergrowths after petalite. Cross-cutting veins that are up to 30cm wide, replace parts of the spodumene + quartz intergrowth. These veins contain an assemblage of highly fractionated F-rich mica (lepidolite), quartz and Nb-Ta oxides, interpreted as the part of the latest stages of crystallisation from melt + F-rich fluid (vapour). A single euhedral tantalite grain was collected, with dimensions of 4 x 2 x 2mm (sample SS134).

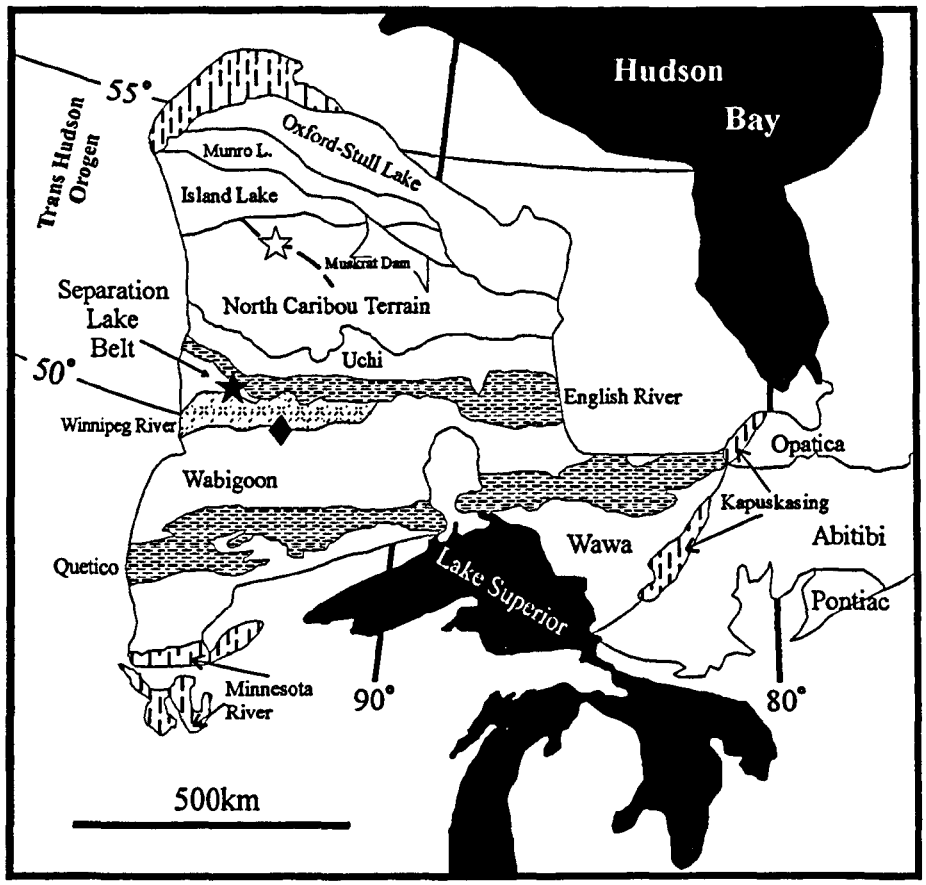

Archæan Subprovince Type

- Plutonic
- Granite-greenstone
- Metasedimentary
- High-grade gneiss

☆ Pakeagama Lake pegmatite

★ Separation Rapids pegmatite group

♦ Mavis Lake pegmatite group

Figure 4.2 Location of pegmatites sampled for U-Pb geochronology. Subprovinces of the Western Superior Province, after Card and Ciesielski (1986); Thurston et al. (1991).

4.2.2 Separation Rapids pegmatite group

The Separation Rapids pegmatite group comprises beryl-type and complex-type - petalite-subtype pegmatites hosted within the Separation Lake greenstone belt (figure 4.2). In this part of the Superior Province, the Separation Lake greenstone belt marks the boundary between the metasedimentary English River Subprovince to the north and the tonalite-gneiss dominated Winnipeg River Subprovince to the south (Breaks 1991; Beakhouse 1991).

The pegmatites are clustered around the peraluminous, S-type granite, Separation Rapids pluton. Mineralogical similarities and a continuum of fractionation trends, notably in K-feldspar and columbite-tantalite suggest a link between the Separation Rapids rare-element pegmatites and the adjacent Separation Rapids pluton (Breaks and Tindle 1996; Tindle and Breaks 1998). Although it is often assumed that rare-element pegmatites are derived from the nearest peraluminous pluton, some pegmatite fields have been found to be older than assumed parental granite (Romer and Smeds 1996). Thus, one aim of this study is to use high precision U-Pb geochronology to determine if there is a temporal as well as a spatial and geochemical link between the Separation Rapids pluton (recently dated at 2646 ± 2 Ma using monazite U-Pb; Larbi *et al.* 1999) and the Separation Rapids rare-element pegmatites.

Tindle and Breaks (1998, 2000) have divided the Separation Rapids pegmatite group into two suites, *viz.* Fe-suite and Mn-suite, based on the occurrence of Fe- and Mn- varieties of columbite-tantalite minerals. The occurrence of fluorine-rich minerals such as microlite, topaz and fluorite led Tindle and Breaks (1998) to conclude that the Mn-suite pegmatites crystallised from a melt with higher fluorine concentration than the Fe-suite pegmatites, which exhibit a restricted occurrence of F-rich minerals. In order to explain this chemical subdivision, Tindle and Breaks (1998) proposed that either a F-rich melt was separated within a layered magma chamber, or else through chemical evolution of the melt over time.

This study aims to determine if there are any resolvable differences in age between the Fe-suite and Mn-suite pegmatites of the Separation Rapids group. Sample 94-24a is a single euhedral columbite (1mm across) collected from an Fe-suite, topaz-bearing beryl-type pegmatite. The grain was extracted from the primary assemblage within this undeformed dyke. Marko's pegmatite is a Mn-suite, petalite pegmatite that is

similarly undeformed. Euhedral columbite grains (<1mm) occur as inclusions within muscovite books in the wall zone of Marko's pegmatite (sample 94-44).

An oval shaped pegmatitic leucogranite body, 250 by 300m, is exposed beyond the SW margin, and conceivably part of, the Separation Rapids pluton. Within this leucogranite body, there are several quartz + K-feldspar + muscovite + albite 'pods' that texturally overprint the main assemblage. These 'pods' are interpreted as an overprinting assemblage of the primary magmatic leucogranite (Tindle and Breaks 1998). A single euhedral columbite grain with dimensions of 1 x 3 x 5mm was extracted from one of the late-stage 'pods' (sample 96-86b).

Localised ductile deformation has affected some of the pegmatites within the Separation Rapids group. In particular the Big Mack pegmatite, a complex-type - petalite sub-type pegmatite that displays isoclinal folding and recrystallisation of original pegmatite minerals (Breaks *et al.* 1999b). Sample 99FWB74 is a 1 x 1 x 10mm single grain, collected from a recrystallised quartz + petalite assemblage within the core zone.

4.2.3 Mavis Lake group

The Mavis Lake group of pegmatites comprise an 8km by 1.5km zone of rare-element mineralisation that is chemically associated with the peraluminous, S-type granite, Ghost Lake batholith (Breaks and Moore 1992). The regional setting of the Ghost Lake batholith and Mavis Lake group pegmatites is between two litho-tectonic terrains, the greenstone-rich Wabigoon Subprovince and the tonalite-gneiss dominated Winnipeg River Subprovince (figure 4.2).

The emplacement age of the Ghost Lake batholith is constrained by a U-Pb monazite date of *circa* 2685Ma (D. Davis, unpublished data; reported in Breaks and Moore 1992). The Mavis Lake group of rare-element pegmatites are emplaced along earlier formed shear zones (Breaks and Moore 1992) and include Fairservice pegmatite #1, an albite - spodumene type pegmatite. Breaks and Janes (1991) have described the mineralogy of Fairservice pegmatite #1, which includes a quartz-rich core zone enveloped by a spodumene-albite-quartz unit. The pegmatite has exposed dimensions of 12 by 76m and is hosted by mafic metavolcanic rocks. Sample 92DF-5 is a 3 x 2 x 2mm columbite grain selected for U-Pb isotopic analysis, taken from the primary assemblage, spodumene-albite-quartz unit of Fairservice pegmatite #1.

Table 4.1 Representative electron microprobe data of columbite-tantalite minerals, structural formulae based on 6 oxygens.

	Pakeagama Lake pegmatite				Separation Rapids pegmatites								Mavis Lake group	
	Kspar+petalite zone		vein cross-cutting core zone		Fe-suite		Marko's peg. Mn-suite		quartz pod		Big Mack peg. - deformed		Fairservice peg. #1	
Sample	SS137	SS137	SS134	SS134	94-24A	94-24A	94-44	94-44	96-86B	96-86B	99FWB74	99FWB74	92DF-5	92DF-5
CaO	0.02	0.01	0.02	0.02	0.03	0.03	0.00	0.00	0.00	0.00	0.04	0.00	0.06	0.01
FeO	1.02	0.94	0.74	0.57	13.15	13.14	7.45	7.73	14.03	10.04	12.86	13.87	5.71	7.37
MnO	14.65	14.01	15.34	14.42	6.90	7.28	10.11	9.90	6.28	10.28	3.35	3.78	11.78	10.06
TiO2	0.10	0.00	0.02	0.00	1.21	1.21	2.50	2.94	0.63	0.42	0.54	0.30	0.94	0.60
Nb2O5	26.55	17.89	27.32	17.50	63.96	70.61	51.42	49.92	63.81	63.05	24.15	37.72	44.59	37.86
Ta2O5	57.30	66.03	56.34	67.85	11.23	7.39	25.16	26.27	13.76	15.01	58.22	42.91	34.06	40.77
SnO2	0.16	0.16	0.16	0.14	0.03	0.02	0.79	0.34	0.26	0.00	0.44	0.03	0.57	0.17
WO3	0.19	0.24	0.18	0.19	0.51	0.63	1.08	1.25	0.35	0.08	0.58	0.37	0.07	0.18
PbO	0.18	0.10	0.11	0.09	0.30	0.29	0.27	0.55	0.48	0.58	0.12	0.15	0.24	0.19
ThO2	0.00	0.00	0.00	0.00	0.00	0.00	0.00	0.00	0.00	0.00	0.00	0.00	0.00	0.00
UO2	0.00	0.00	0.00	0.00	0.00	0.02	0.27	0.00	0.27	0.00	0.00	0.00	0.00	0.00
Sb2O3	0.01	0.02	0.02	0.02	0.00	0.00	0.00	0.00	0.00	0.01	0.00	0.00	0.00	0.00
Bi2O3	0.00	0.00	0.00	0.00	0.00	0.00	0.05	0.45	0.00	0.00	0.00	0.00	0.00	0.00
Sc2O3	0.00	0.04	0.00	0.00	0.00	0.00	0.61	0.68	0.00	0.00	0.10	0.00	0.03	0.00
Total	100.18	99.45	100.23	100.79	99.99	100.62	99.71	100.02	99.88	99.47	100.41	99.14	98.03	97.21
Ca	0.001	0.001	0.001	0.002	0.002	0.002	0.000	0.000	0.000	0.000	0.003	0.000	0.004	0.000
Fe	0.062	0.060	0.044	0.036	0.646	0.631	0.388	0.404	0.703	0.507	0.784	0.796	0.317	0.428
Mn	0.900	0.911	0.938	0.929	0.343	0.354	0.534	0.524	0.319	0.526	0.207	0.220	0.662	0.592
Ti	0.005	0.000	0.001	0.000	0.053	0.052	0.117	0.138	0.028	0.019	0.030	0.016	0.047	0.032
Nb	0.871	0.621	0.891	0.601	1.767	1.834	1.449	1.411	1.727	1.720	0.796	1.170	1.338	1.188
Ta	1.130	1.378	1.106	1.403	0.181	0.115	0.426	0.446	0.224	0.246	1.154	0.801	0.615	0.770
Sn	0.005	0.005	0.005	0.004	0.001	0.000	0.020	0.008	0.006	0.000	0.013	0.001	0.015	0.005
W	0.004	0.005	0.003	0.004	0.008	0.009	0.018	0.020	0.005	0.001	0.011	0.007	0.001	0.003
Pb	0.003	0.002	0.002	0.002	0.005	0.004	0.005	0.009	0.008	0.009	0.002	0.003	0.004	0.004
Th	0.000	0.000	0.000	0.000	0.000	0.000	0.000	0.000	0.000	0.000	0.000	0.000	0.000	0.000
U	0.000	0.000	0.000	0.000	0.000	0.000	0.004	0.000	0.004	0.000	0.000	0.000	0.000	0.000
Sb	0.000	0.001	0.001	0.001	0.000	0.000	0.000	0.000	0.000	0.000	0.000	0.000	0.000	0.000
Bi	0.000	0.000	0.000	0.000	0.000	0.000	0.001	0.007	0.000	0.000	0.000	0.000	0.000	0.000
Sc	0.000	0.003	0.000	0.000	0.000	0.000	0.033	0.037	0.000	0.000	0.007	0.000	0.002	0.000
Total	2.981	2.986	2.992	2.981	3.007	3.004	2.994	3.005	3.024	3.029	3.007	3.013	3.005	3.021
Mn/(Mn+Fe)	0.936	0.938	0.955	0.963	0.347	0.359	0.579	0.565	0.312	0.509	0.209	0.216	0.676	0.580
Ta/(Ta+Nb)	0.565	0.689	0.554	0.700	0.093	0.059	0.227	0.240	0.115	0.125	0.592	0.406	0.315	0.393

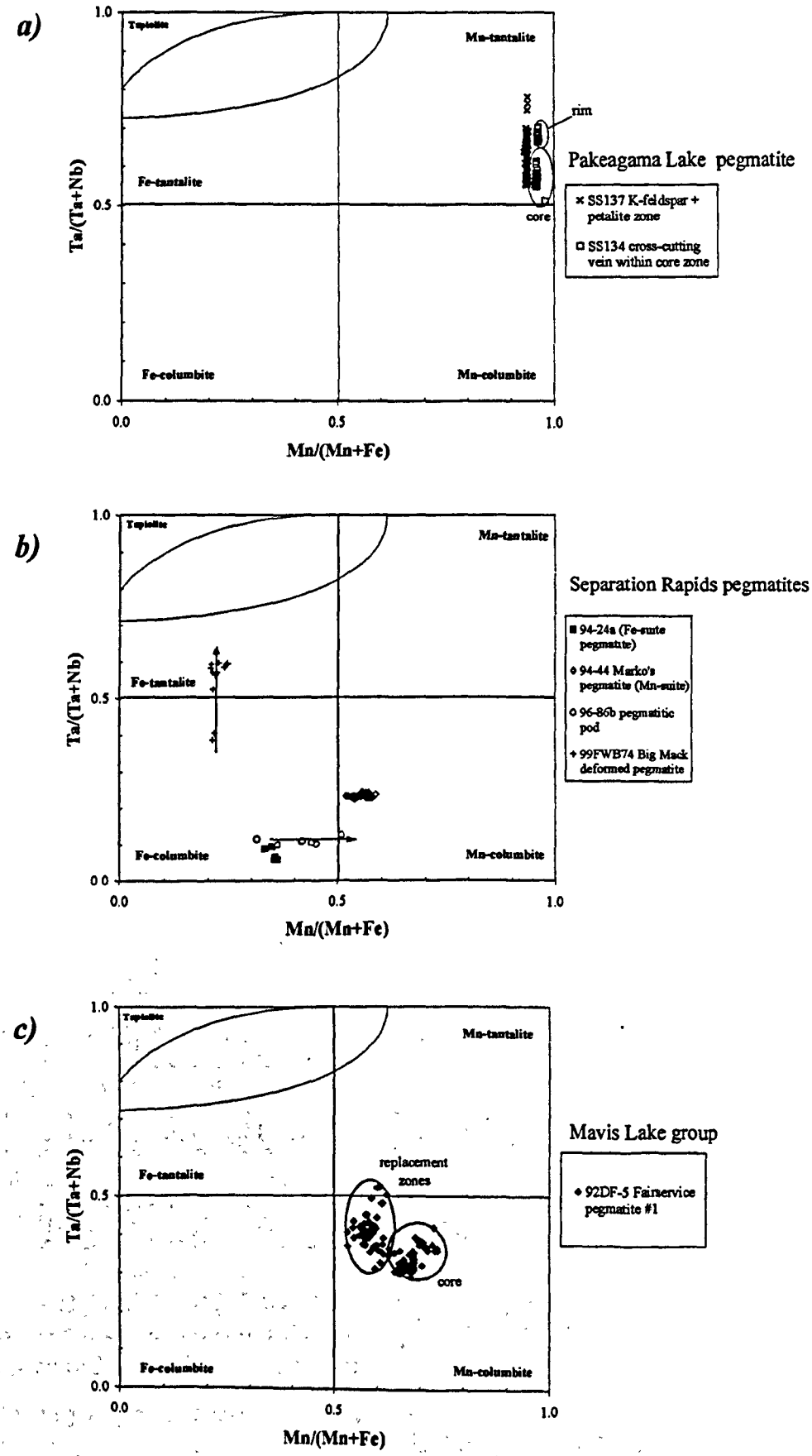

Figure 4.3 Compositions of columbite-tantalite from a) Pakeagama Lake pegmatite, b) Separation Rapids pegmatites, c) Fairservice pegmatite #1, Mavis Lake group. Fractionation of the pegmatite melt produces increasing Mn/(Mn+Fe) and Ta(Ta+Nb).

4.3 Results

4.3.1 Pakeagama Lake Pegmatite

- *Primary assemblage (Sample SS137)*

Electron microprobe data show the evolved manganotantalite composition of sample SS137, which indicates the concentration of rare-elements within the Pakeagama Lake pegmatite (figure 4.3a). Backscattered electron images of the manganotantalite grain reveal oscillatory zoning indicating primary magmatic growth (figure 4.4a).

Six raster analyses using LA-MC-ICP-MS are variably reverse discordant (figure 4.4b). The six analyses yield a good discordia (MSWD = 0.64) with an upper intercept of 2673.4 ±7.7Ma*, using a forced zero lower intercept. Despite the large data array, the intercept age agrees with the weighted mean of $^{207}Pb/^{206}Pb$ ages from all six analyses, 2673 ±6Ma (figure 4.5). The upper intercept of the discordia is therefore confidently interpreted as the crystallisation age of primary tantalite and the emplacement of the Pakeagama Lake pegmatite.

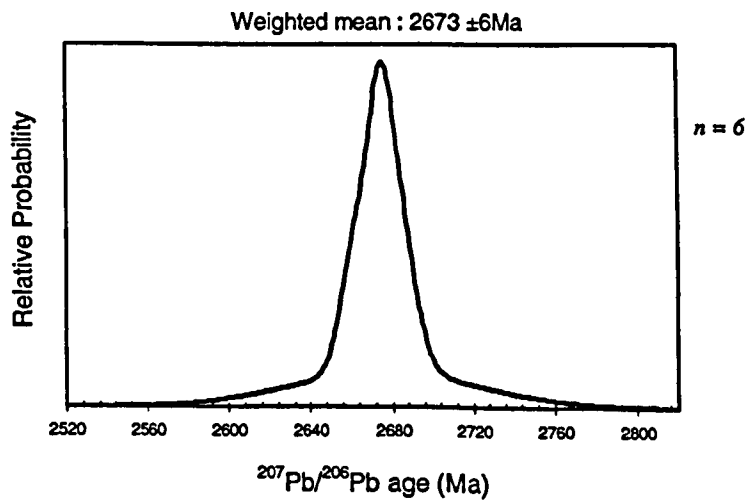

Figure 4.5 Cumulative frequency plot of $^{207}Pb/^{206}Pb$ ages from LA-MC-ICP-MS analyses of sample SS137.

* All age uncertainties are quoted at the 2σ level.

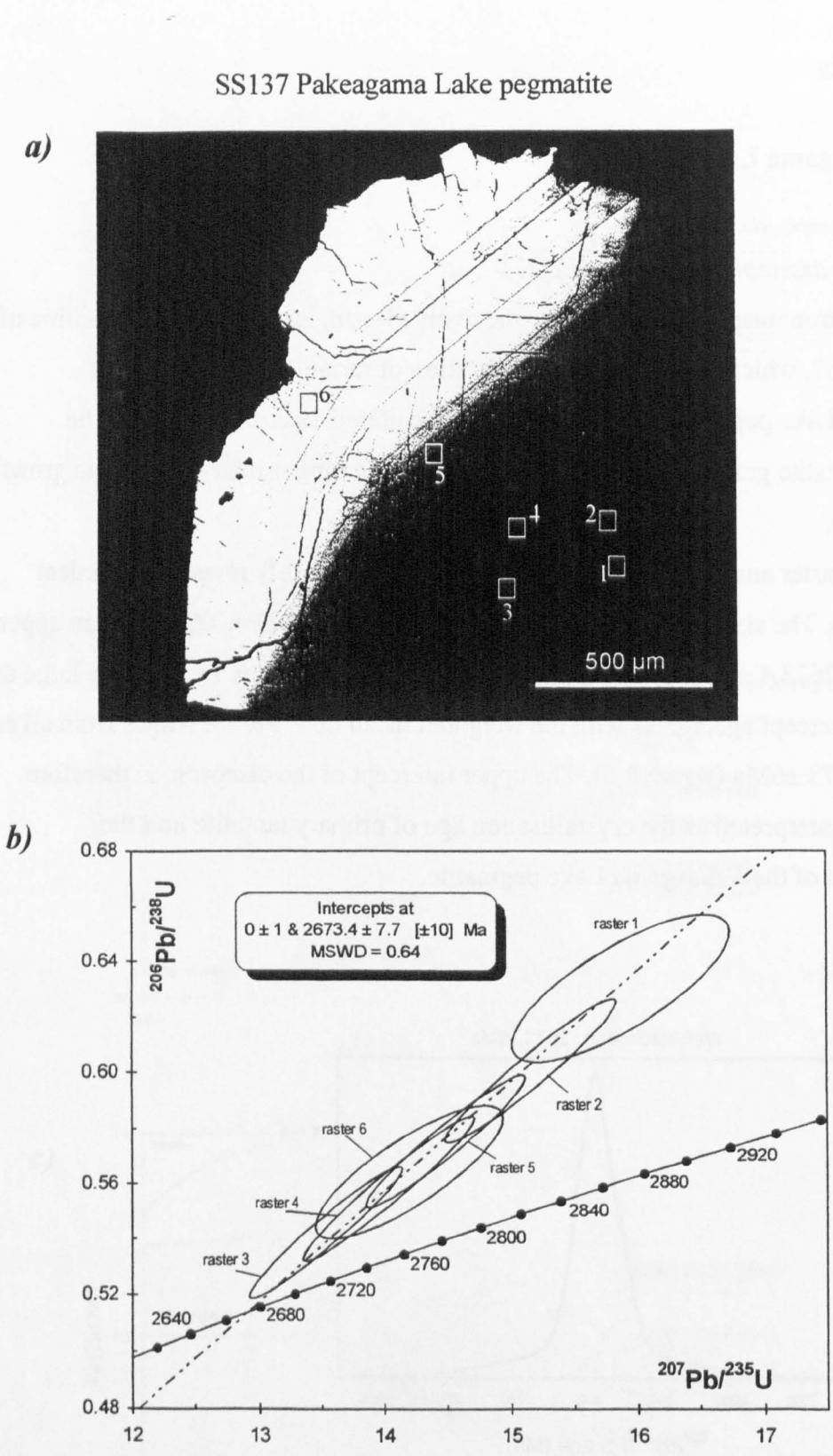

Figure 4.4 a) Backscattered electron image of sample SS137, tantalite grain from the K-feldspar + petalite zone of the Pakeagama lake pegmatite. b) Concordia plot of LA-MC-ICP-MS analyses of sample SS137, All error ellipses and age uncertainties are at the 2 sigma level. Errors in brackets include decay constant uncertainty.

Table 4.2 U-Pb isotopic data from TIMS analyses

Sample	Run	Weight	U	Pb	measured ratios			atomic ratios*			apparent ages			
		(mg)	ppm	ppm	$^{206}Pb/^{204}Pb$	$^{207}Pb/^{206}Pb$	$^{208}Pb/^{206}Pb$	$^{206}Pb/^{238}U$	$^{207}Pb/^{235}U$	$^{207}Pb/^{206}Pb$	$^{206}Pb/^{238}U$	$^{207}Pb/^{235}U$	$^{207}Pb/^{206}Pb$	2σ
Pakeagama Lake pegmatite														
SS134	882	0.06	129.1	66.7	10030	0.1802	0.0058	0.5079	12.5480	0.1792	2648	2646	2645	±1
SS134	883	0.04	114.0	59.6	6814	0.1815	0.0078	0.5126	12.7264	0.1801	2668	2660	2653	±1
SS134	885	0.07	563.6	285.8	24570	0.1787	0.0032	0.4989	12.2711	0.1784	2609	2625	2638	±1
SS134	886	0.08	55.2	29.0	5340	0.1827	0.0103	0.5136	12.7935	0.1807	2672	2665	2659	±1
Separation Rapids pegmatite group														
94-24a	877	0.08	511.4	271.8	23485	0.1800	0.0108	0.5190	12.8580	0.1797	2695	2669	2650	±1
94-24a	878	0.04	446.6	239.6	12450	0.1805	0.0120	0.5233	12.9659	0.1797	2713	2677	2650	±2
94-24a	879	0.10	419.0	226.9	16440	0.1799	0.0104	0.5287	13.0742	0.1794	2736	2685	2647	±1
94-24a	880	0.08	215.4	115.5	11530	0.1793	0.0135	0.5228	12.8654	0.1785	2711	2670	2639	±1
94-44	893	0.07	1642.0	731.5	19550	0.1783	0.0145	0.4341	10.6444	0.1779	2324	2493	2633	±1
94-44	894	0.17	1560.8	701.9	53500	0.1785	0.0144	0.4383	10.7825	0.1784	2343	2505	2638	±1
94-44	895	0.22	1287.6	697.5	29420	0.1793	0.0130	0.5280	13.0335	0.1790	2733	2682	2644	±1
94-44	896	0.04	1624.2	870.4	54660	0.1784	0.0130	0.5231	12.8616	0.1783	2712	2670	2637	±1
94-44	897	0.74	1177.6	694.7	35000	0.1801	0.0157	0.5733	14.2248	0.1799	2922	2765	2652	±1
94-44	898	0.04	1694.0	950.8	60430	0.1813	0.0141	0.5459	13.6477	0.1813	2808	2726	2665	±1
96-86b	901	0.11	62.4	33.4	2732	0.1805	0.0188	0.5177	12.5831	0.1763	2690	2649	2618	±1
96-86b	902	0.07	67.3	35.4	6462	0.1788	0.0128	0.5142	12.5596	0.1771	2675	2647	2626	±2
96-86b	903	0.23	70.6	37.5	8649	0.1784	0.0140	0.5176	12.6426	0.1771	2689	2653	2626	±1
96-86b	904	0.05	59.3	30.6	3313	0.1807	0.0196	0.5050	12.3530	0.1774	2635	2632	2629	±1
99FWB74	871	0.15	34.7	19.3	990	0.1853	0.0522	0.5157	12.3093	0.1731	2681	2628	2588	±3
99FWB74	873	0.64	11.2	5.9	3014	0.1797	0.0201	0.5090	12.3529	0.1760	2653	2632	2616	±2
99FWB74	874	0.11	40.9	21.7	1865	0.1814	0.0303	0.5084	12.2720	0.1751	2650	2625	2607	±2
99FWB74	876	0.10	45.4	23.4	2709	0.1789	0.0220	0.4987	12.0094	0.1746	2608	2605	2603	±3

*corrected for fractionation, blank, isotopic tracer, and an initial 206Pb/204Pb ratio of 13.9. Blank levels were <15pg for lead and <1pg for uranium.

Table 4.3 U-Pb isotopic data from LA-MC-ICP-MS analyses.

Sample	Raster	Uppm	%f207	Th/U calc	measured ratios			atomic ratios+		rho	apparent ages			
					$^{207}Pb/^{206}Pb^*$	$^{208}Pb/^{206}Pb$	$^{208}Pb/^{238}U$	$^{206}Pb/^{238}U$	$^{207}Pb/^{235}U$		$^{206}Pb/^{238}U$	$^{207}Pb/^{235}U$	$^{207}Pb/^{206}Pb$	2σ
Pakeagama Lake pegmatite														
SS137	1	25	2.17	0.03	0.1826	0.0071	0.4762	0.6304	15.8742	0.772	3151	2869	2677	±93
SS137	2	41	0.68	0.03	0.1831	0.0091	0.4537	0.6006	15.1580	0.962	3032	2825	2681	±16
SS137	3	63	1.37	0.00	0.1809	-0.0004	0.4096	0.5423	13.5283	0.965	2793	2717	2661	±13
SS137	4	58	0.96	0.01	0.1823	0.0031	0.4216	0.5581	14.0319	0.969	2859	2752	2674	±9
SS137	5	40	0.47	0.02	0.1826	0.0062	0.4345	0.5751	14.4819	0.960	2929	2782	2677	±19
SS137	6	30	0.13	0.00	0.1825	0.0005	0.4260	0.5640	14.1899	0.819	2883	2762	2676	±23
SS134	1	22	0.60	0.02	0.1818	0.0040	0.5013	0.6511	16.3220	0.708	3233	2896	2669	±139
SS134	2	45	0.06	-0.01	0.1805	-0.0014	0.5440	0.7067	17.5900	0.947	3446	2968	2658	±16
SS134	3	43	-0.29	0.00	0.1818	-0.0002	0.4163	0.5408	13.5571	0.937	2787	2719	2669	±45
SS134	4	71	0.75	0.01	0.1812	0.0031	0.4785	0.6215	15.5267	0.969	3116	2848	2664	±14
SS134	5	60	0.44	0.01	0.1817	0.0022	0.4469	0.5805	14.5417	0.954	2951	2786	2668	±13
SS134	6	24	2.63	-0.02	0.1779	-0.0056	0.5325	0.6917	16.9637	0.725	3389	2933	2633	±135
SS134	7	24	1.20	0.00	0.1793	-0.0011	0.5017	0.6517	16.1069	0.624	3235	2883	2646	±137
SS134	8	24	-1.35	0.05	0.1841	0.0127	0.3977	0.5167	13.1129	0.401	2685	2688	2690	±153
SS134	9	12	2.04	0.02	0.1774	0.0042	0.3815	0.4956	12.1244	0.355	2595	2614	2629	±225

*corrected for common Pb
+corrected for common Pb and Pb/U fractionation
%f207 = percentage of 207Pb as common Pb
rho : error correlation of 206Pb/238U and 207Pb/235U ratios.

Table 4.3 continued. U-Pb isotopic data from LA-MC-ICP-MS analyses.

Sample	Raster	Uppm	%f207	Th/U calc	measured ratios			atomic ratios+		rho	apparent ages			
					$^{207}Pb/^{206}Pb^*$	$^{208}Pb/^{206}Pb$	$^{206}Pb/^{238}U$	$^{206}Pb/^{238}U$	$^{207}Pb/^{235}U$		$^{208}Pb/^{238}U$	$^{207}Pb/^{235}U$	$^{207}Pb/^{206}Pb$	2σ
Fairservice pegmatite #1														
92DF-5	1	53	2.17	0.02	0.1810	0.0059	0.0059	0.7579	18.9116	0.962	3636	3037	2662	±31
92DF-5	2	58	0.68	0.02	0.1817	0.0057	0.0057	0.7494	18.7727	0.964	3605	3030	2668	±7
92DF-5	3	88	1.37	0.02	0.1822	0.0058	0.4700	0.6222	15.6303	0.798	3119	2854	2673	±90
92DF-5	4	123	0.96	0.01	0.1804	0.0032	0.4573	0.6053	15.0563	0.908	3051	2819	2657	±63
92DF-5	5	48	0.47	0.01	0.1807	0.0026	0.0026	0.7784	19.3971	0.964	3711	3062	2660	±10
92DF-5	6	111	0.13	0.02	0.1795	0.0056	0.4173	0.5524	13.6727	0.999	2835	2727	2648	±8
92DF-5	7	18	1.02	0.04	0.1711	0.0119	0.0119	0.4785	11.2873	0.715	2521	2547	2568	±43
92DF-5	8	1112	2.94	0.06	0.1338	0.0186	0.0359	0.0475	0.8754	0.909	299	638	2148	±205
92DF-5	9	163	3.36	0.05	0.1542	0.0136	0.1126	0.1490	3.1670	0.925	895	1449	2393	±228
92DF-5	10	29	4.97	0.00	0.1731	-0.0007	0.2905	0.3845	9.1805	0.569	2097	2356	2588	±331
92DF-5	11	33	4.25	0.05	0.1598	0.0139	0.0139	0.3868	8.5233	0.796	2108	2288	2454	±46
92DF-5	12	27	9.12	-0.08	0.1612	-0.0230	0.2417	0.3200	7.1111	0.491	1790	2125	2468	±615
92DF-5	13	49	3.14	0.02	0.1719	0.0053	0.3688	0.4882	11.5688	0.821	2563	2570	2576	±209
92DF-5	14	91	0.80	0.02	0.1779	0.0062	0.5211	0.6898	16.9204	0.911	3382	2930	2633	±52
92DF-5	15	120	0.09	0.03	0.1808	0.0066	0.0066	0.6765	16.8684	0.968	3331	2927	2661	±7
92DF-5	16	161	0.71	0.02	0.1799	0.0055	0.4276	0.5660	14.0357	0.959	2891	2752	2651	±46

*corrected for common Pb

+corrected for common Pb and Pb/U fractionation

%f207 = percentage of 207Pb as common Pb

rho : error correlation of 206Pb/238U and 207Pb/235U ratios.

- *Melt-vapour phase assemblage (Sample SS134)*

A single grain (4 x 2 x 2mm) from a late-stage vein that cross-cuts the core zone of the Pakeagama Lake pegmatite was split into fragments for TIMS and LA-MC-ICP-MS analyses. Backscattered electron (BSE) images reveal an oscillatory zoned core that is surrounded by a compositionally distinct rim (figure 4.7a). Electron microprobe analyses confirm the compositional difference as an increase in Ta/(Ta+Nb) within the manganotantalite field (figure 4.3a). Clearly, more than one episode of crystallisation was responsible for the zoning in sample SS134. The oscillatory zoned core indicates a primary stage of magmatic crystallisation, which has been overgrown by a thin Ta-rich rim. This may have precipitated from the fluorine-rich residual melt-vapour phase that formed the lepidolite vein.

TIMS analyses of four fractions yields one concordant fraction, two fractions that are only slightly reverse discordant, and another is normally discordant (figure 4.6). The concordant fraction lies at 2645 ±1Ma. Fitting a discordia to all four fractions (MSWD = 3.4) yields an upper intercept at 2649 ±11Ma and a poorly defined lower intercept of 1263 ±920Ma. However, the four fractions have a scattered range of $^{207}Pb/^{206}Pb$ ages between 2659 ±1Ma and 2638 ±1Ma, which are inversely correlated with U content (table 4.2). This probably indicates differential lead loss from the different zones recognised in the BSE image. Therefore, the discordia may have a fortuitous intercept and is not used further.

LA-MC-ICP-MS analyses from sample SS134 yield concordant and variably reverse discordant data (figure 4.7b). Eight raster analyses (no.'s 1 - 8) from the oscillatory zoned, primary tantalite yield a well defined discordia (MSWD = 0.41) with an upper intercept at 2664.4 ±7.8Ma. Raster 9 is located in the darker grey region of sample SS134, which is not part of the oscillatory zoned core and is therefore not used in the regression. The error ellipse from raster 9 is almost flat and lies across the concordia with a poorly defined $^{207}Pb/^{206}Pb$ age of 2629 ±123Ma. Analysis of the Ta-rich rim of SS134 was precluded by a low uranium signal (<1mV).

Clearly, the LA-MC-ICP-MS data lie along a much larger and more strongly discordant array than the TIMS data. Also, there seems to be some disparity in the ages derived by the two techniques. However, the upper intercept of 2664 ±8Ma for LA-MC-ICP-MS analyses from the core region of SS134 is within error of the oldest, and lowest U content fraction analysed by TIMS, with a $^{207}Pb/^{206}Pb$ age of 2659 ±1Ma. Furthermore, the intercept is in agreement with the weighted mean of $^{207}Pb/^{206}Pb$ ages,

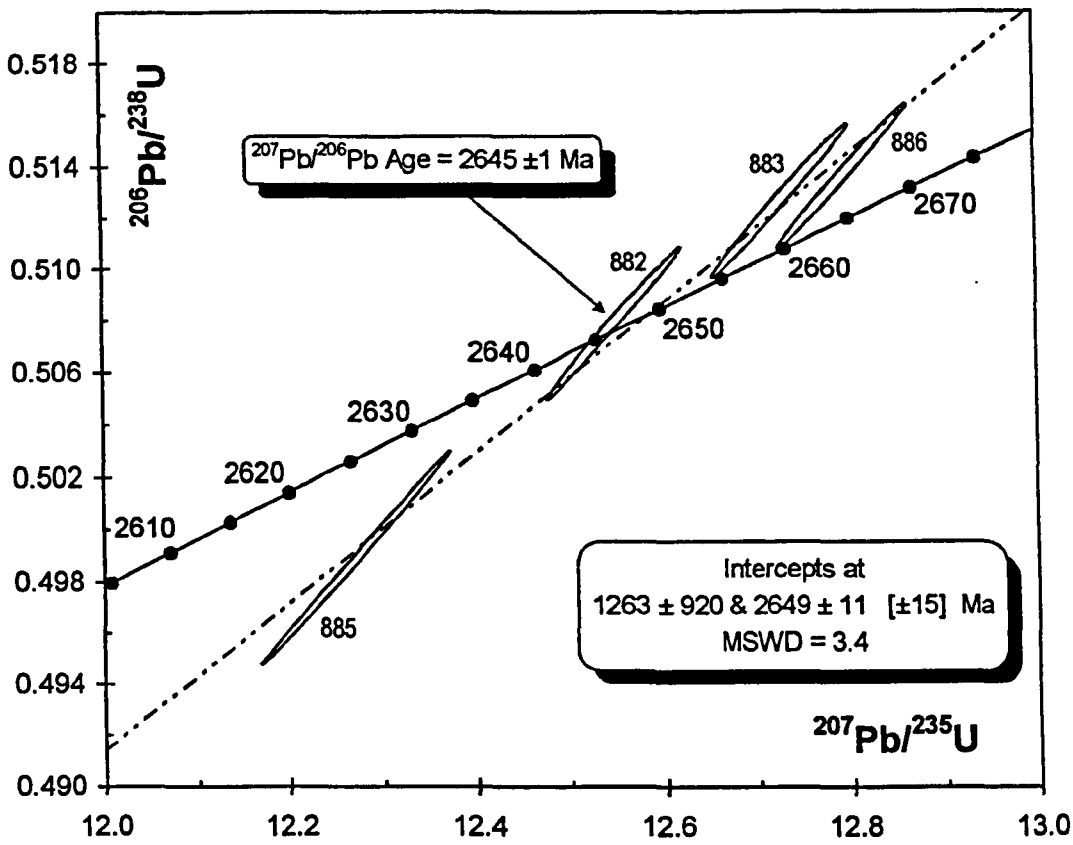

Figure 4.6 Concordia plot of TIMS analyses from sample SS134, tantalite from a lepidolite vein cross-cutting the core zone of the Pakeagama Lake pegmatite. Error ellipses and age uncertainties are at the 2 sigma level. Errors in brackets include decay constant uncertainty.

SS134 Pakeagama Lake pegmatite

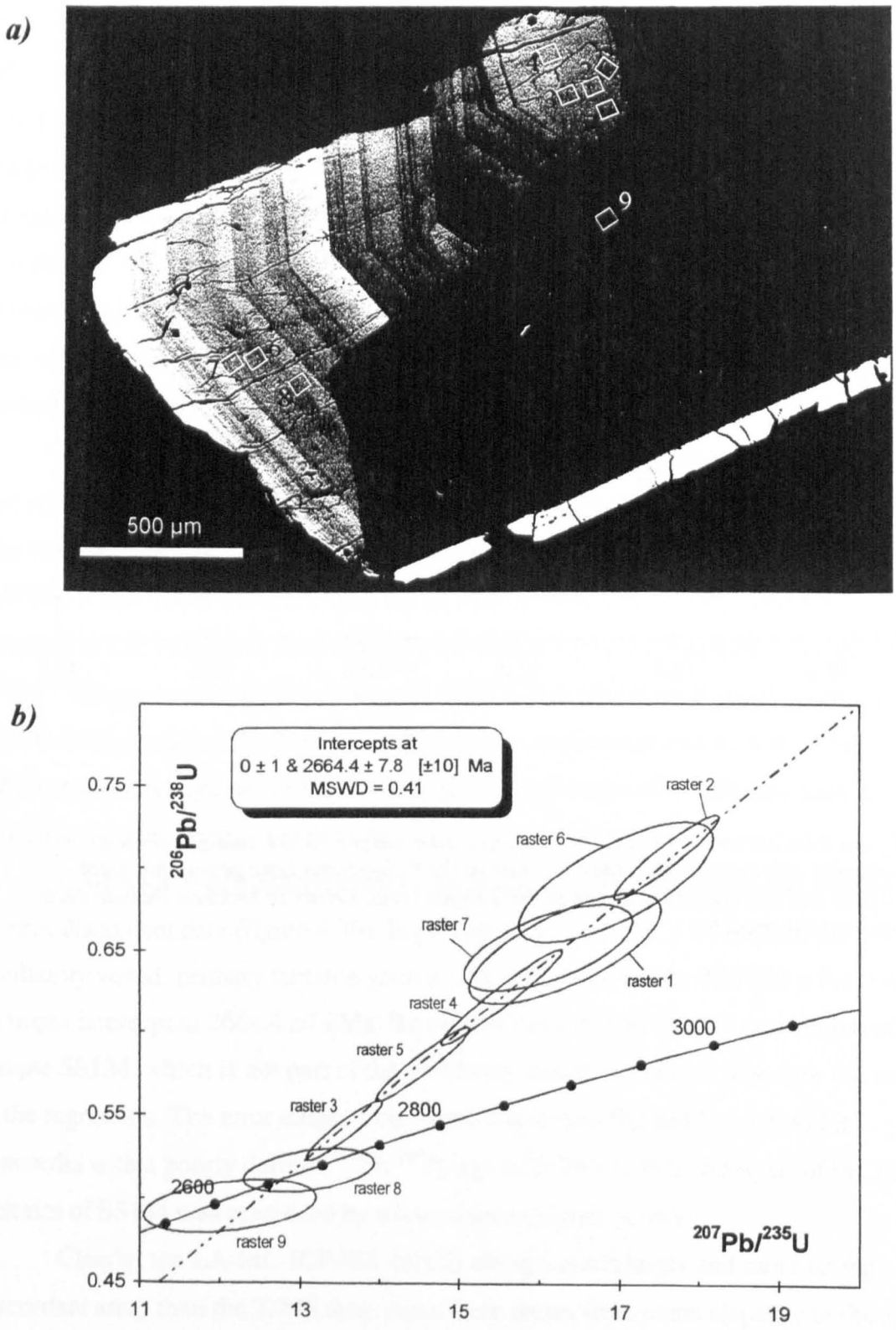

Figure 4.7 a) Backscattered electron image showing the locations of raster analyses of SS134, tantalite grain from a lepidolite vein cross-cutting the core zone of the Pakeagama Lake pegmatite. b) Concordia plot of LA-MC-ICP-MS analyses, All error ellipses and age uncertainties are at the 2 sigma level. Errors in brackets include decay constant uncertainty.

2664 ± 4Ma, from LA-MC-ICP-MS analyses (figure 4.8). The conservative estimate of 2664 ±8Ma is interpreted as the age of primary crystallisation of tantalite from the lepidolite vein cross-cutting the core zone. The TIMS data indicate variable lead loss from the replacement zones and are probably caused by disturbance to the U-Pb system from vapour phase replacement of tantalite, a minimum age for this disturbance is defined by the youngest $^{207}Pb/^{206}Pb$ age of 2638 ±1Ma.

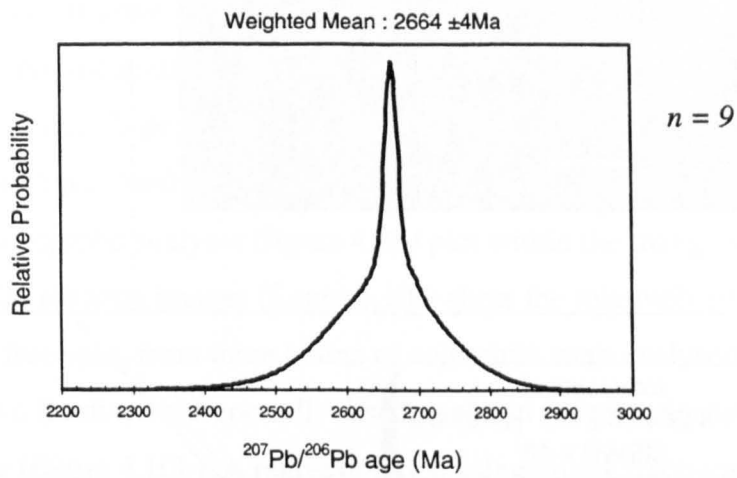

Figure 4.8 Cumulative frequency plot of $^{207}Pb/^{206}Pb$ ages from LA-MC-ICP-MS analyses of sample SS134.

4.3.2 Separation Rapids pegmatite group

- *Fe-suite pegmatite (Sample 94-24a)*

This sample is a single euhedral grain (1mm across) from a beryl-type pegmatite. Electron microprobe data plots within the ferrocolumbite field indicating that the pegmatite is part of the Fe-suite (figure 4.3b). Backscattered electron imaging reveals oscillatory zoning, indicating primary magmatic growth (figure 4.9a). There are no inclusions or any evidence for alteration, although the grain contains abundant fractures and micro-cracks. These microcracks precluded LA-MC-ICPMS analysis as they were unavoidable and increased the common Pb content of the analyses to unacceptable levels (common Pb constituting up to 98% of the measured ^{207}Pb).

Four fractions of columbite sample 94-24a were analysed by TIMS, all fractions are reverse discordant (figure 4.9b). Three fractions with U contents >400ppm fall along

94-24a Separation Rapids pegmatite group

a)

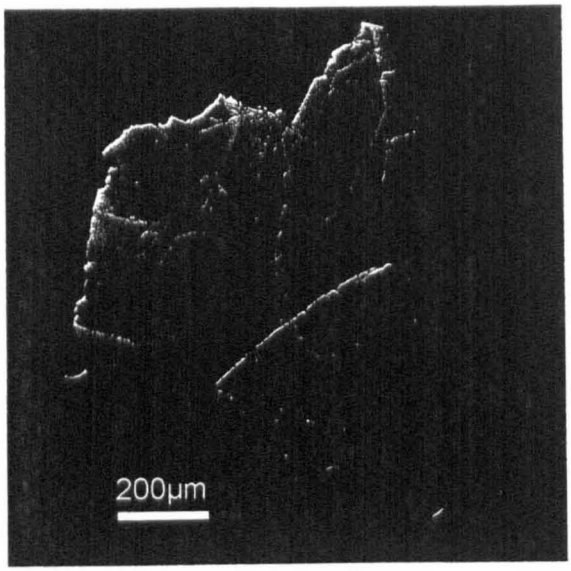

b)

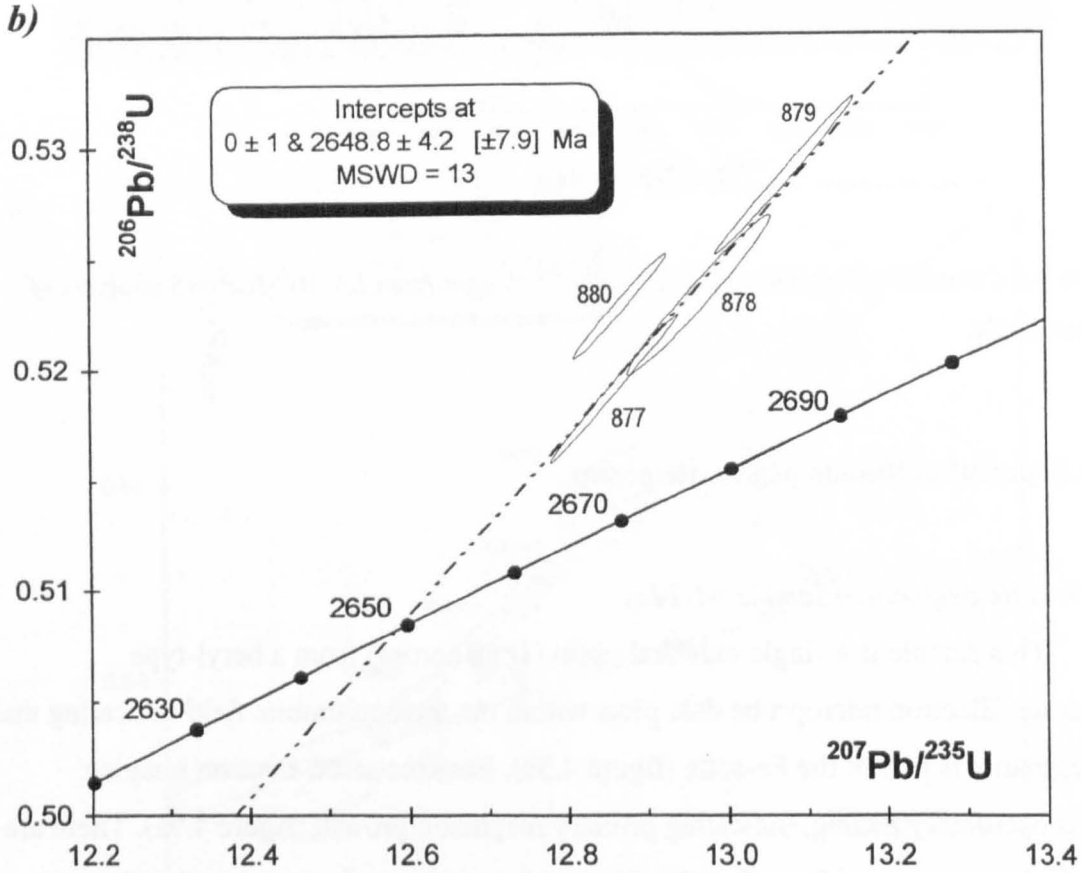

Figure 4.9 a) Backscattered electron image for sample 94-24a, ferrocolumbite from the Separation Rapids pegmatite group (Fe-suite). b) Concordia plot of TIMS analyses for sample 94-24a. All error ellipses and age uncertainties are at the 2 sigma level. Errors in brackets include decay constant uncertainty.

a trend through the origin (MSWD = 13), with an upper intercept at 2648.8 ±4.2Ma, which is interpreted as the emplacement age of the Fe-suite pegmatites. A fourth fraction lies off this discordant array, with a distinctly lower $^{207}Pb/^{206}Pb$ age of 2638.8 ±1Ma. Exclusion of this sample from the regression is substantiated by the comparatively low U content (215ppm; table 4.2). Fraction 877 is the closest to concordia and contains the highest U concentration (511ppm).

- *Mn-suite pegmatite (Sample 94-44)*

Marko's pegmatite is a Mn-suite, complex-type - petalite sub-type pegmatite. Euhedral columbite grains (<1mm) occur as inclusions within muscovite books in the wall zone of Marko's pegmatite. Monazite is also present and occurs as small (<500μm) inclusions within columbite, which were removed during crushing and hand-picking. Electron microprobe analyses (figure 4.3b) plot within the manganocolumbite field and backscattered electron images (figure 4.10a) show the relatively homogeneous grains.

Six fractions, from three grains of columbite were analysed by the TIMS method. Two fractions are normally discordant and four fractions show variable reverse discordance (figure 4.10b). A regression line using all six fractions (not shown) has a very large scatter (MSWD = 232) with upper and lower intercepts at 2646 ±12 and 186 ±260, respectively. The excess scatter is mainly due to two fractions (896 and 898) that plot away from the discordia. Excluding these two fractions from the regression yields an upper intercept age of 2644.3 ±7.1Ma and lower intercept at 144 ±140Ma (figure 4.10b). The upper intercept is interpreted as the emplacement age of Marko's pegmatite. Although there is still excess scatter (MSWD = 29), in part this may be due to the multi-grain analysis since different zones of the grain may have lost variable amounts of lead.

- *Overprinting assemblage (Sample 96-86b)*

A single euhedral columbite grain (1 x 3 x 5mm) was analysed from one of the overprinting 'pods' within leucogranite of the Separation Rapids pluton. Electron microprobe analyses (figure 4.3b) show the relatively primitive ferrocolumbite composition of 96-86b and backscattered electron images (figure 4.11a) reveal a lack of zoning in the grain and small inclusions of cassiterite.

Four fractions of columbite 96-86b were analysed by TIMS (figure 4.11b). Concentrations of U are uniformly low, 59 - 71ppm (table 4.1). Two reverse discordant fractions and one concordant fraction lie along a discordia (MSWD = 4.2) with an upper

a) 94-44 Marko's pegmatite, Separation Rapids pegmatite group

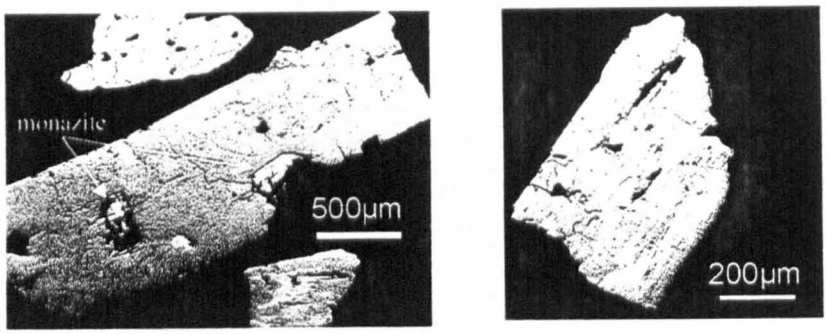

b)

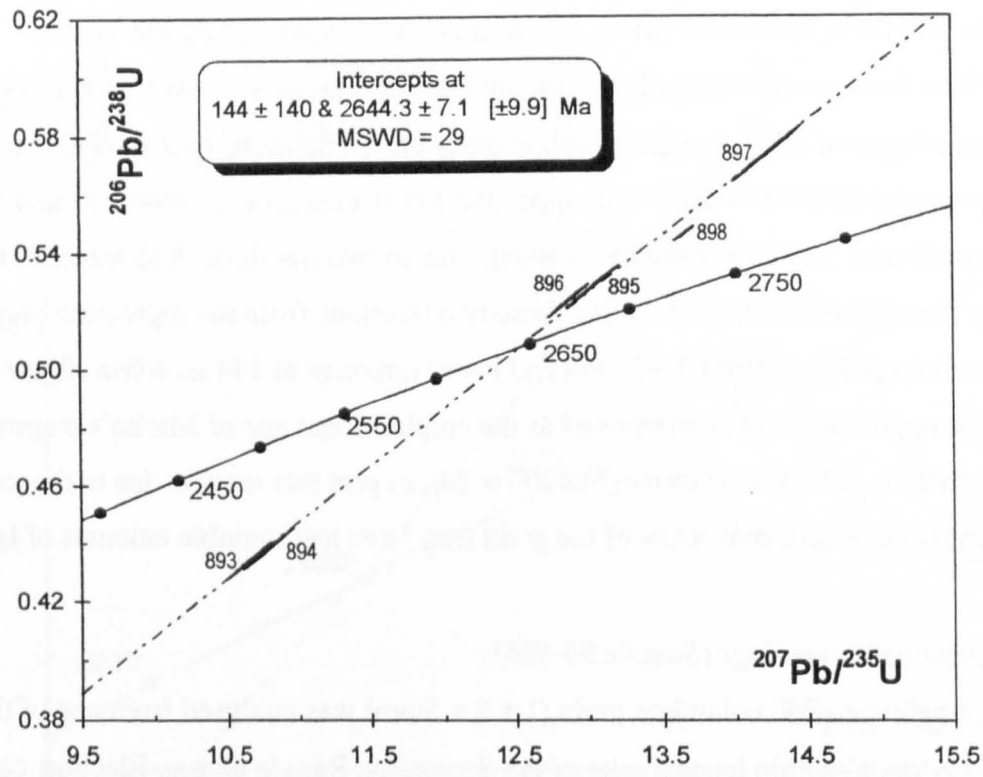

Figure 4.10 a) Backscattered electron images of sample 94-44, manganocolumbite from Marko's pegmatite, Separation Rapids group (Mn-suite). b) Concordia plot of TIMS analyses for sample 94-44. N.B. Fractions 896 and 898 are omitted from the regression. Error ellipses and age uncertainties are at the 2 sigma level. Errors in brackets include decay constant uncertainty.

96-86b Separation Rapids group

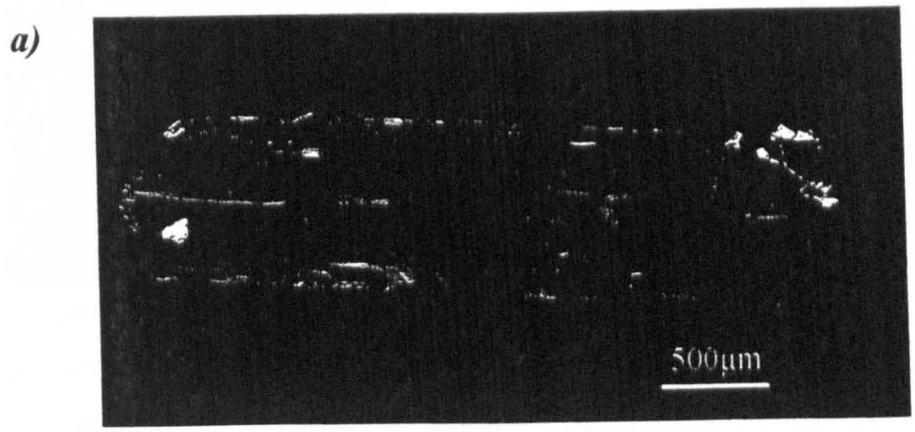

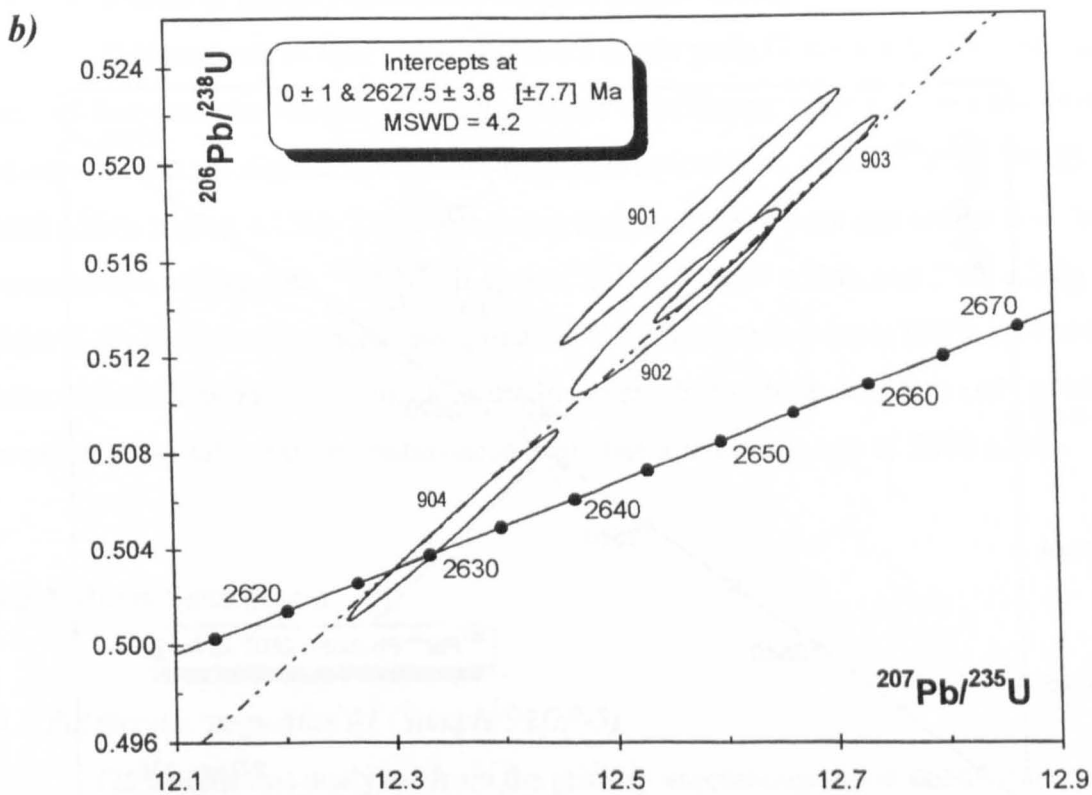

Figure 4.11 a) Backscattered electron images of columbite 96-86b from an overprinting pod assemblage within the Separation Rapids pluton. 'Bright' inclusions in the columbite are cassiterite. b) Concordia plot of TIMS analyses for columbite 96-86b, error ellipses and age uncertainties are at the 2 sigma level. Errors in brackets include decay constant uncertainty.

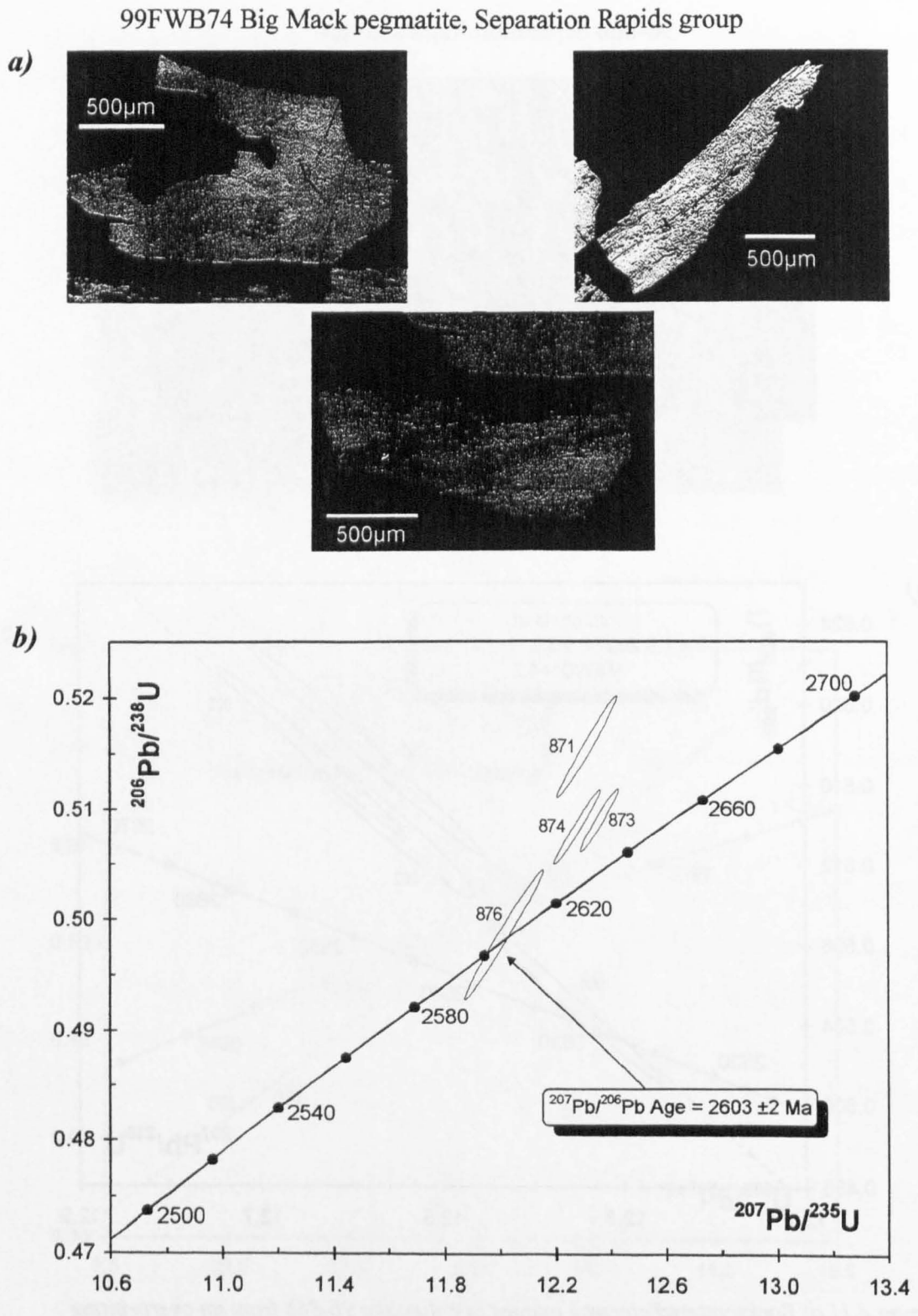

Figure 4.12a) BSE images of a single columbite-tantalite grain (1 x 1 x 10mm) split into three fragments, sample 99FWB74 from the deformed Big Mack pegmatite (Fe-suite, Separation Rapids group). Note the lack of zoning within the grain fragments. b) Concordia plot of TIMS analyses from columbite-tantalite 99FWB74, error ellipses and age uncertainties are at the 2 sigma level.

intercept of 2627.5 ± 3.8, which gives the crystallisation age of columbite within the pod. The fourth fraction has been omitted from the regression because it contains the lowest U content and plots away from the discordia.

- *Deformed pegmatite (Sample 99FWB74)*

The Big Mack pegmatite displays localised ductile deformation, isoclinal folding and recrystallisation of original pegmatite minerals (Breaks *et al.* 1999). Electron microprobe data from sample 99FWB74 plots within the ferrocolumbite and ferrotantalite fields (figure 4.3b), which is relatively primitive composition for such an evolved complex-type - petalite sub-type pegmatite. Backscattered electron images reveal that the grain fragments are unzoned, which suggests either that recrystallisation occurred under constant P-T conditions or else a metamorphic overprint has modified the composition of primary columbite-tantalite (figure 4.12a).

TIMS analysis of four fractions from a single grain (1 x 1 x 10mm) were carried out. All fractions contain low concentrations of U (<50ppm; table 4.2). Fraction 876, which contains the highest U content (45ppm) is concordant, with a $^{207}Pb/^{206}Pb$ age of 2603 ±2Ma (figure 4.12b). Three remaining fractions are reverse discordant and show considerable scatter with $^{207}Pb/^{206}Pb$ ages of 2616 ±2, 2607 ±2Ma and 2588 ±2Ma (table 4.2). The scattered data shows that the U-Pb system in sample 99FWB74 has been disturbed, probably by the deformation event. From these data, it is only possible to say that the deformation/ disturbance event has a minimum age of 2588 ±2Ma.

4.3.3 Mavis Lake group

- *Fairservice pegmatite #1 (Sample 92DF-5)*

Columbite was analysed from the primary assemblage, spodumene-quartz-albite unit of Fairservice pegmatite #1. Backscattered electron images of this single euhedral grain (3 x 2 x 2mm) reveal oscillatory zoning, overprinted by convolute zoning (figure 4.13). Electron microprobe analyses plot within the manganocolumbite field (figure 4.3c), and indicate that the replacement zones have lower Mn/(Mn+Fe) ratios than the oscillatory zoned core. Clearly, there is a complex history of crystallisation and secondary alteration/replacement recorded in this grain. Woods and Williams-Jones (1993) have suggested that these textures result from interaction with highly reactive, residual fluids during the late-stages of pegmatite formation.

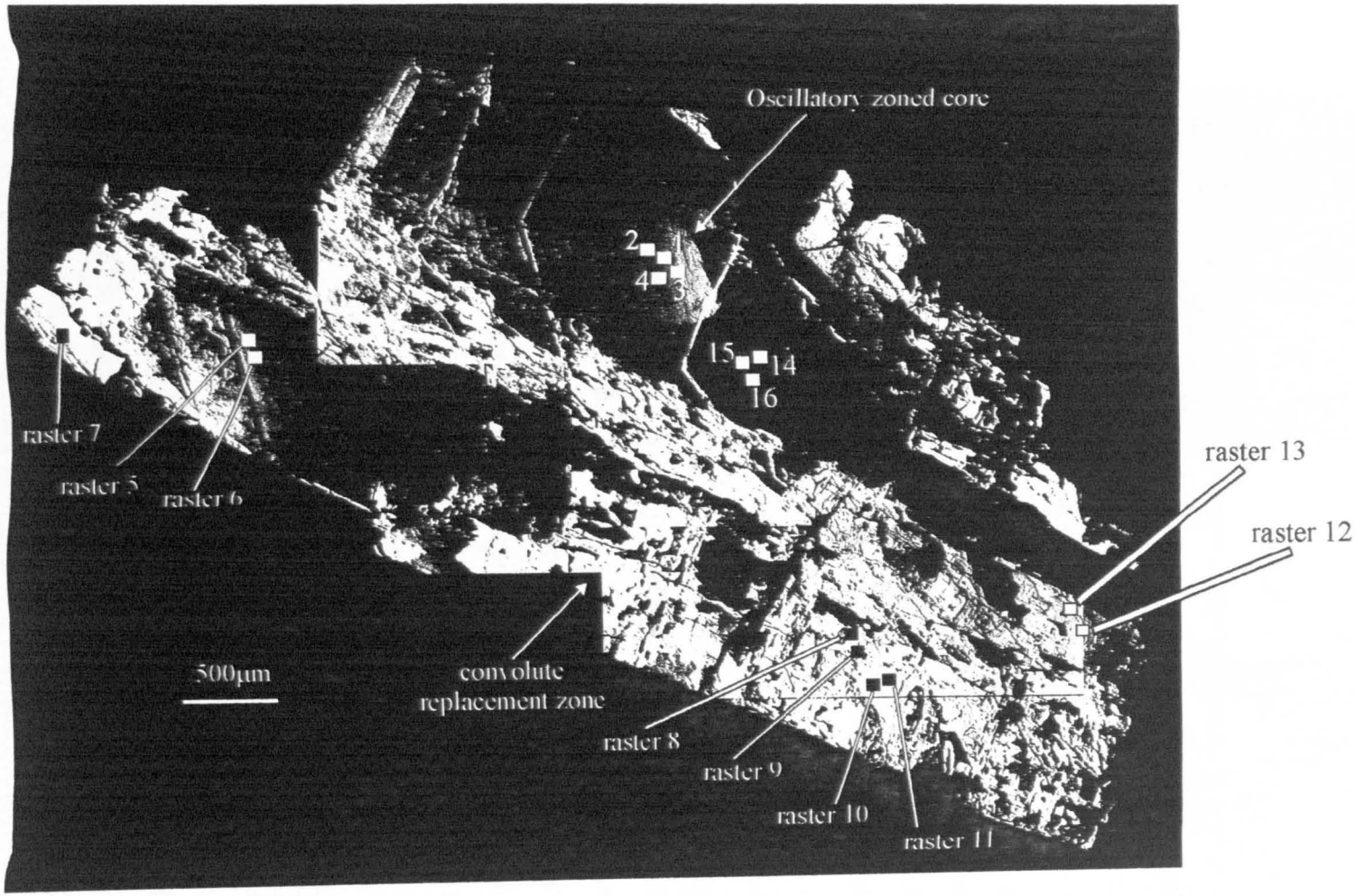

Figure 4.13 Composite BSE image of manganocolumbite from Fairservice pegmatite #1, Mavis Lake Group pegmatites (sample 92DF-5). Locations of LA-MC-ICP-MS analyses are shown (not to scale).

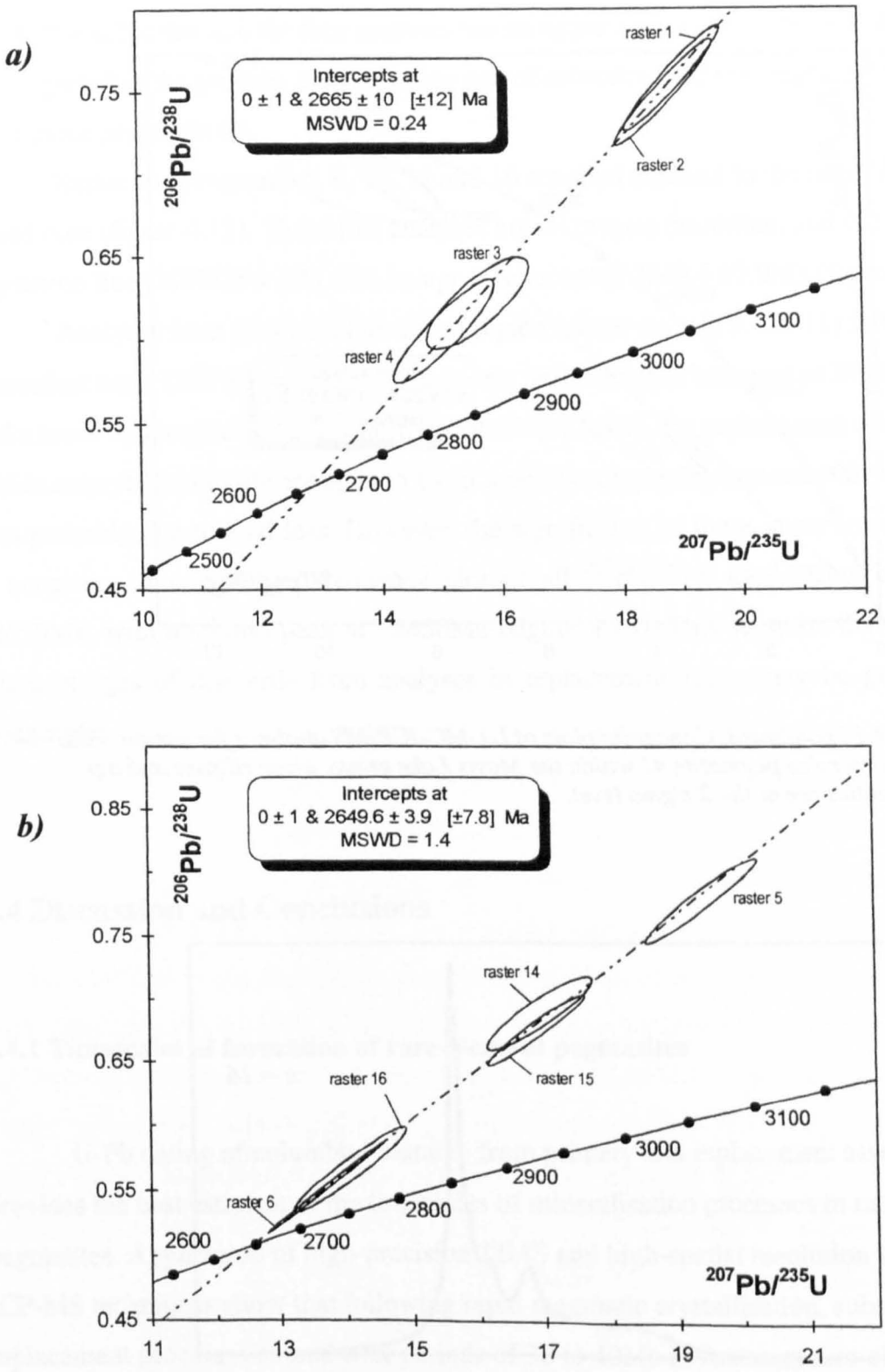

Figure 4.14 Concordia plots of LA-MC-ICP-MS analyses for sample 92DF-5 from Fairservice pegmatite #1 within the Mavis Lake group, error ellipses and age uncertainties are at the 2 sigma level. Errors in brackets include decay constant uncertainty. a) raster analyses from the primary oscillatory zoned core region. b) and c) analyses from convolute replacement zones shown in BSE image (figure 4.13).

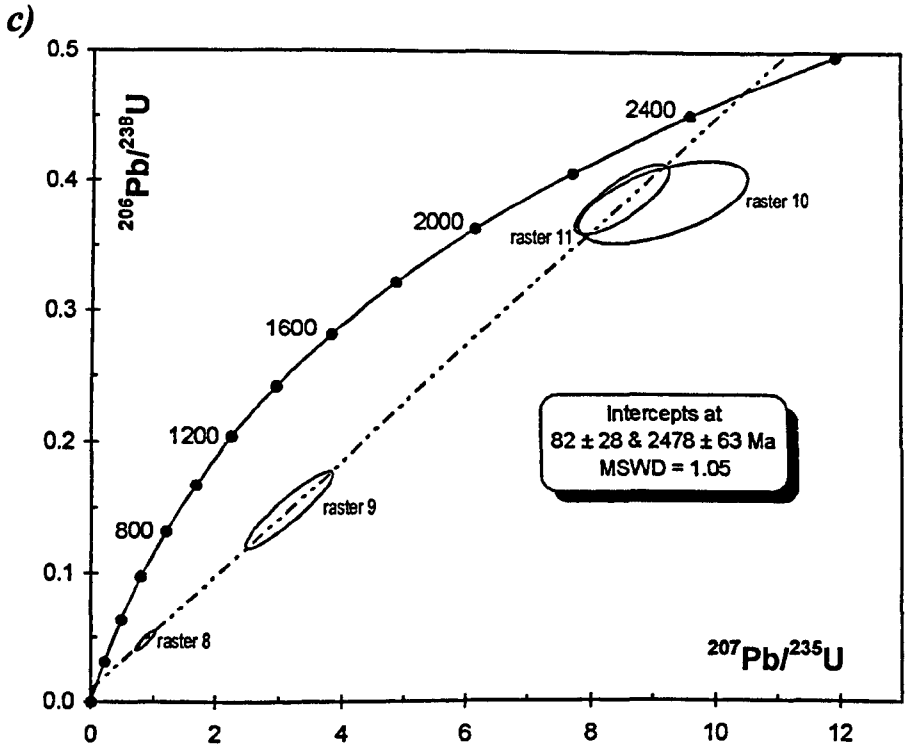

Figure 4.14 continued. Concordia plots of LA-MC-ICP-MS analyses for sample 92DF-5 from Fairservice pegmatite #1 within the Mavis Lake group, error ellipses and age uncertainties are at the 2 sigma level.

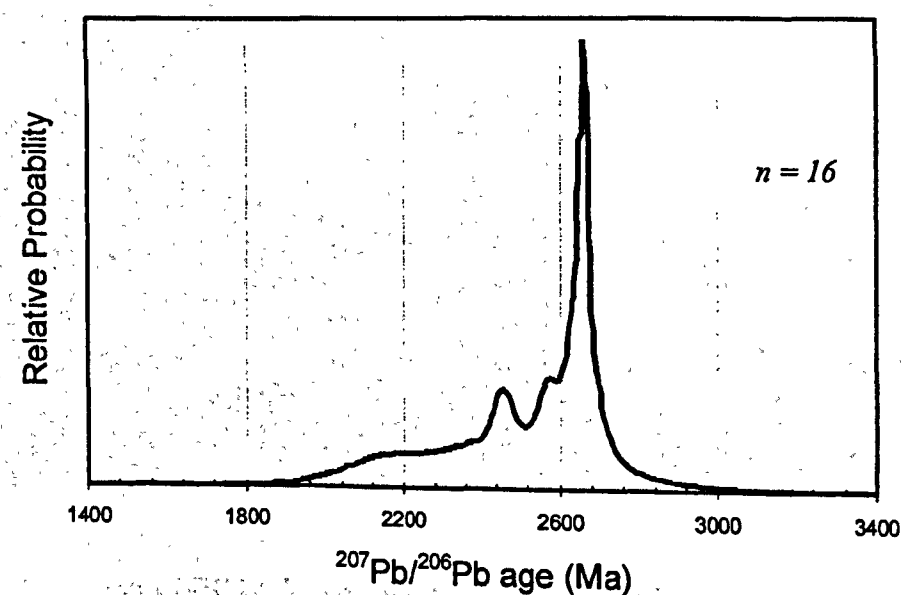

Figure 4.15 Cumulative frequency plot of $^{207}Pb/^{206}Pb$ ages from LA-MC-ICP-MS analyses of sample 92DF-5 from Fairservice pegmatite #1 within the Mavis Lake group.

Four LA-MC-ICP-MS raster analyses (1, 2, 3, 4) from the oscillatory zoned core region in sample 92DF-5 yield reverse discordant data (figure 4.14a). A regression line (MSWD = 0.24) through the four analyses has an upper intercept of 2665 ±10Ma. This is interpreted as the primary crystallisation age of columbite and the emplacement of Fairservice pegmatite #1.

Raster analyses no.'s 5, 6, 14, 15 and 16 are sited adjacent to the oscillatory zoned core (figure 4.13). These five analyses are all reverse discordant and fall on a regression line (MSWD = 1.4) with an upper intercept at 2649.6 ±3.9Ma (figure 4.14b).

Analyses from the convolute zoned region (raster no.'s 8, 9, 10, 11) fall along a discordant array (MSWD = 1.05) with a poorly defined upper intercept of 2478 ±63Ma and a lower intercept of 82 ± 28Ma (figure 4.14c). Clearly, the replacement zones within columbite-tantalite are open to U-Pb mobility, displaying normally discordant data probably due to lead loss. However, the significance of these upper intercept ages is uncertain. A cumulative frequency plot of all $^{207}Pb/^{206}Pb$ ages shows a spike at ~2650Ma, with a second peak at ~2450Ma (figure 4.15). This suggests that the upper intercept ages of discordia from analyses in replacement zones may be geologically meaningful.

4.4 Discussion and Conclusions

4.4.1 Timescales of formation of rare-element pegmatites

U-Pb dating of columbite-tantalite from primary and replacement assemblages provides the best estimate of the timescales of mineralisation processes in rare-element pegmatites. Application of high-precision TIMS and high-spatial resolution LA-MC-ICP-MS techniques show that following rapid magmatic crystallisation, subsequent replacement processes extend over periods of 30 to 40Ma in Archæan rare-element pegmatites.

In the Pakeagama Lake pegmatite, primary magmatic tantalite yields a crystallisation age of 2673 ±8Ma. Tantalite from a cross-cutting lepidolite vein which replaces parts of the core zone yields an age of 2664 ±8Ma from LA-MC-ICP-MS analyses of the primary grain core, and a range of $^{207}Pb/^{206}Pb$ ages as young as 2638

±1Ma from TIMS analyses. These data indicate differential Pb loss from tantalite over approximately 30Ma of episodic vapour-phase precipitation/ residual fluid interaction within the Pakeagama Lake pegmatite. It is worth noting that 2750 - 2700Ma (U-Pb zircon) granitoid batholiths in the North Caribou Terrain also yield U-Pb titanite and apatite ages that fall in the range 2660 - 2630Ma. These ages were interpreted as the timing of post-emplacement hydrothermal fluid flow and reheating in the region (Corfu and Stone 1998b).

Columbite-tantalite from the Separation Rapids pegmatite group yield emplacement ages of 2649 ±4Ma (Fe-suite) and 2644 ±7Ma (Mn-suite). These ages are within 2σ uncertainty of a concordant U-Pb monazite age of 2646 ±2Ma, interpreted as the crystallisation age of the adjacent Separation Rapids pluton (Larbi *et al.* 1999). This confirms the geochemical association of the Separation Rapids pluton with the Separation Rapids pegmatite group (Tindle and Breaks 1998). Furthermore, ages for the Fe-suite and Mn-suite are indistinguishable at the 2σ uncertainty level, lending support to the theory that the parent Separation Rapids granite pluton formed a layered magma chamber in which a relatively fluorine-rich melt was spatially separated from relatively fluorine-poor melt (Tindle and Breaks 1998). Columbite from a pod assemblage that texturally overprints pegmatitic leucogranite, yields a U-Pb age of 2628 ±4Ma, which is similar to a second monazite age from the Separation Rapids pluton of 2635 ±2Ma, interpreted as thermal alteration (Larbi *et al.* 1999).

Breaks and Moore (1992) reported the *circa* 2685Ma age as the crystallisation age of the primitive cordierite-biotite unit (GLB-1) of the Ghost Lake batholith. A series of complex chemical differentiation processes that concentrated rare-elements into successively residual melts and ultimately led to the dispersion of pegmatites described by Breaks and Moore (1992). Columbite from Fairservice pegmatite #1 within the Mavis Lake group yields a 2665 ±10Ma crystallisation age. Multiple disturbances to the U-Pb system are indicated by the 2650 ±4Ma and 2478 ±63Ma upper intercept ages of replacement zones within columbite 92DF-5 (Mavis Lake group). Shear zone reactivation along the Winnipeg River - Wabigoon Subprovince boundary or else a re-heating event during the Proterozoic are the most likely causes of this disturbance.

4.4.2 Regional age variation of rare-element pegmatites in the Superior Province

Pre-orogenic magmatism in the Superior Province exhibits a distinct southward younging in age, determined from regional scale U-Pb studies (Corfu and Davis 1991). In the North Caribou Terrain, pre-orogenic plutons were intruded prior to 2710Ma, whereas in the western Superior Province, similar plutons have ages between 2710 - 2690Ma. This pattern has been attributed to progressive docking of arc and microcontinental fragments (Corfu and Davis 1991). Similarly, the progression of post-collisional events can be inferred from the regional age distribution of anatectic melts such as peraluminous S-type granites and their associated LCT-family pegmatites. Rare-element pegmatites with lithium-caesium-tantalum (LCT) geochemical affinity originate from crustal melts derived from orogenically-thickened continental crust (Romer and Smeds 1997). In the Superior Province, they are commonly emplaced into the collision zones between terrains during the transition from compressional orogenesis to trans-tensional regimes.

The Pakeagama Lake pegmatite, a post-collisional rare-element pegmatite in the North Caribou Terrain was emplaced at 2673 ±8Ma. In the western Superior Province, the crystallisation ages of the Ghost Lake batholith (D. Davis, unpublished) and Mavis Lake pegmatite group (this study) constrain the timing of late- to post-collisional peraluminous magmatism at the Wabigoon - Winnipeg River Subprovince boundary to the period 2685 - 2665Ma. At the Winnipeg River - English River Subprovince boundary, also in the western Superior Province, the Separation Rapids rare-element pegmatites yield crystallisation ages of 2649 ±4Ma and 2644 ±7Ma.

The present geochronological database of peraluminous granite - rare-element pegmatite associations in the Superior Province is too small to afford any unequivocal regional conclusions. However, the existing ages indicate a craton wide onset of post-collisional, rare-element mineralisation at 2.68Ga, lasting for at least 40Ma.

4.4.3 Causes of the complexities in the U-Pb system of columbite-tantalite

This is the first application of combined TIMS and LA-MC-ICP-MS techniques to U-Pb dating of columbite-tantalite. The study gives estimates of the timescales of mineralisation processes in rare-element pegmatites and provides ages that are useful to interpretation of regional post-orogenic thermal histories. However, significant technical

problems must still be overcome in the analysis of columbite-tantalite by LA-MC-ICP-MS. For instance they are hampered by the lack of a matrix matched standard. Despite this problem, it has been shown that geologically meaningful results, consistent with TIMS analyses can be obtained by the LA-MC-ICPMS analyses of columbite-tantalite. The success of this approach allows additional conclusions to be made on the causes of the reverse discordance that is a common feature of the U-Pb analyses of columbite-tantalite (e.g. Romer *et al.* 1996).

As has been mentioned previously, the causes for the reverse discordance of columbite-tantalite in the U-Pb system are thought to be a combination of inclusion effects (mainly uraninite) and the preferential mobilisation of uranium over lead (Romer *et al.* 1996). HF leaching is known to decrease, or remove entirely, the cause of the reverse discordance (Romer and Smeds 1996). However, this leaching also removes the convolute replacement zones in columbite-tantalite, which potentially yield information on the timescales of pegmatite formation. Thus, the grain fragments analysed by LA-MC-ICPMS were untreated. Instead, by careful imaging and targeting, submicroscopic inclusions were avoided (and the zones of alteration that surround them), and cracks (with the exception of 94-24a) and yet the analyses still exhibit reverse discordance, notably to a larger degree than the TIMS analyses. The discordance is unlikely to be caused by laboratory effects as the lack of an exact matrix match has only a small (<8%) and reproducible effect on U/Pb fractionation (Horstwood *et al., unpublished data*). Although this is likely to contribute to the reverse discordance, it would be unlikely to cause the large and variable reverse discordance observed in LA-MC-ICPMS analyses. Therefore, the cause for the discordance of the *in-situ* analyses must exist at a scale that is comparable to, or smaller than, the resolution of this technique (50x50x10 μm).

Given the submicron as well as decimicron-scale of pits and grooves that are etched by HF-leaching (figure 4.1), such material is a likely candidate for generating the reverse discordance observed in LA-MC-ICPMS analyses of untreated columbite-tantalite. Work is in progress to continue the study of columbite-tantalite minerals by combining electron microprobe, TIMS and LA-MC-ICP-MS techniques. This will contribute to the broader understanding of complex U-Pb systematics in other minerals used in geochronology.

5. $^{40}Ar/^{39}Ar$ geochronology

5.1 Introduction

This chapter presents the results of UV laser microprobe $^{40}Ar/^{39}Ar$ dating of micas from rare-element pegmatites and associated peraluminous granites in the Superior Province. In section 5.2, a brief review of the main models of diffusion serves to explain the ideas on which interpretations of the data are made. Due to the large dataset obtained in this study and the competing hypotheses on data interpretation, sections 5.3 and 5.4 present the 'raw' data and descriptions, without the overlay of interpretation. This is followed by theoretical modelling of the data in section 5.5 and consideration of crystal - chemical controls in section 5.6. The implications in terms of the regional geological history and the interpretation of $^{40}Ar/^{39}Ar$ data are discussed in section 5.7. The main conclusions of the study are summarised in section 5.8. Specific methods of the data collection and techniques for analysis are reported in Appendix C.

5.2 Diffusion and the closure temperature concept

5.2.1 Volume Diffusion

Transfer of atoms in solids occurs by heat conduction (diffusion) of kinetic energy resulting from random molecular motions. In the simplest case, this will involve transfer of atoms through a homogeneous structure. This is known as volume diffusion, for which the rate limiting factor is the thermal energy (temperature) of the solid. In this case, diffusion will follow Fick's Second Law;

Equation 5.1 $$dC/dt = D\,(d^2C/dx^2)$$

Where: C = *concentration of the diffusing species*

t = *time* x = *distance* D = *diffusion coefficient*

Argon diffuses at significant rates in common rock forming minerals until they are below geologically moderate temperatures (~500°C). In igneous systems or metamorphic terrains these temperatures are well below the crystallisation temperature (~900°C) or thermal peak of metamorphism (e.g. ~750°C in granulite facies). The date obtained from the $^{40}Ar/^{39}Ar$ system is often therefore a 'cooling age', representing the time at which argon is effectively retained in the mineral i.e. not a crystallisation age. This apparent shortcoming of $^{40}Ar/^{39}Ar$ dating can be turned to advantage if the temperature at which the diffusion of Ar ceases (referred to as the closure temperature, T_c) can be assigned to the date. Thus, using a series of minerals with different closure temperatures, we can estimate Temperature *versus* time (T-t) paths for a terrain, a technique known as *thermochronology.*

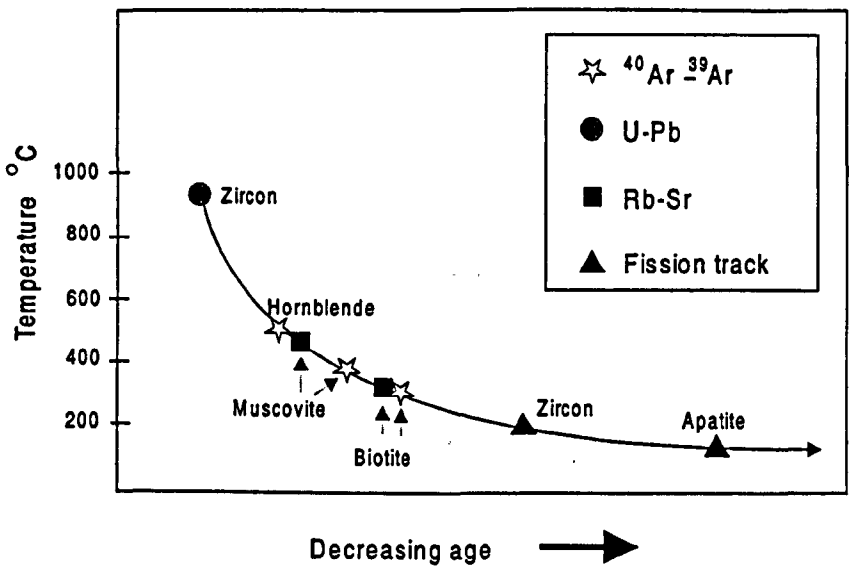

Figure 5.1 Schematic illustration of a cooling curve drawn through different minerals and isotopic systems with varying closure temperatures.

Dodson (1973) developed a mathematical formulation of the closure temperature for a uniform grain (equation 5.2). Loss of argon was assumed to be dominated by a thermally activated volume diffusion process, measured by the diffusion coefficient, *D*.

Equation 5.2

$$T_c = \frac{E/R}{\ln\left\{\left(ART_c^2 D_0/a^2\right)/EdT/dt\right\}}$$

Where T_c is the closure temperature in Kelvin, E the activation energy per mole for diffusion, R the universal gas constant, A is a geometrical constant developed by Dodson (1973) e.g. for slab, cylinder or sphere models of diffusion. D_o is the diffusion coefficient at infinite temperature; a is the effective diffusion distance and dT/dt the cooling rate at the closure temperature. D_o and E may be determined experimentally and a range of data exist for different systems (McDougall and Harrison 1999).

Figure 5.2 illustrates the closure temperature concept. During cooling from high temperature, a mineral will pass from a completely open state of diffusion (i.e. no accumulation of radiogenic Ar), through a zone of partial accumulation, represented by the curved portion of the line in the lower diagram. Eventually the mineral reaches a temperature where diffusion effectively stops and there is accumulation of radiogenic argon at a constant rate.

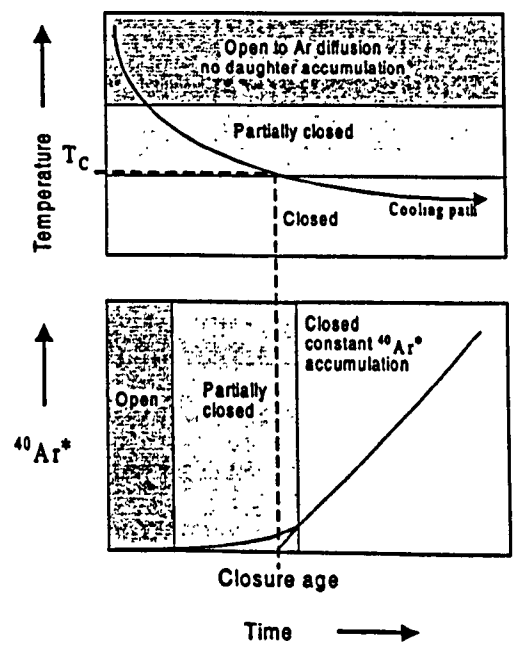

Figure 5.2 Illustration of the volume-diffusion closure temperature concept. Where Tc is the closure temperature and $^{40}Ar^*$ is radiogenic argon. The age calculated from radiogenic ingrowth reflects the time at which argon diffusion had almost ceased. After Dodson (1973).

One of the implications of the closure temperature concept is that although a mineral may have an average closure temperature, after undergoing slow cooling each radial position within the crystal has a unique closure temperature (Dodson 1986). The broader implication is that a single mineral can yield a segment of a cooling curve rather than just a single temperature - time point as in figure 5.1.

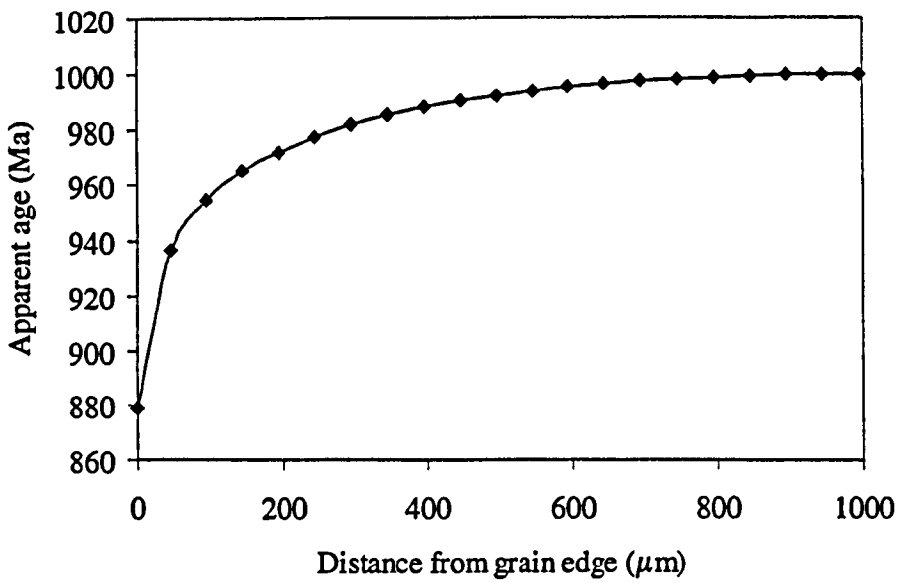

Figure 5.3 Theoretical apparent age profile for a mineral undergoing linear cooling at a rate of 10°C/Ma.

The profile in figure 5.3 shows the apparent age variation within a mineral undergoing cooling at a linear rate of 10°C/Ma. Because the transfer of energy that causes diffusion is random, the net direction of movement of diffusing atoms will be from regions of high concentration to regions of low concentration. In the simplest case, argon will escape via the grain boundary and the crystal will exhibit a $^{40}Ar/^{39}Ar$ age gradient with ages decreasing towards the grain boundary. A theoretical profile such as that shown in figure 5.3 could be fitted to the measured profile to determine the cooling history of the mineral. However, in some instances, fluids within the grain boundary network may introduce excess argon into the crystal, producing older ages at the grain boundary (Pickles *et al.* 1997).

In this study, the ultraviolet laser ablation microprobe technique is employed to measure intragrain apparent age variations in micas from rare-element pegmatites and associated peraluminous granites of the Superior Province. The short wavelength (266nm) of the UV laser means that extraction of argon from beyond the ablation pit is negligible (Kelley *et al.* 1994). Further, a 10 - 15μm beam diameter enables measurement of argon isotope concentrations, and thus apparent ages, at a high spatial resolution, allowing close control over the site of extraction within an individual mineral grain. Therefore, the UV laser microprobe enables measurement of intragrain apparent age profiles that allows determination of a T-t history (e.g. Hames and Hodges 1993; Hodges and Bowring 1995).

Closure profiles as predicted by Dodson (1973) assume loss of argon by a temperature dependant volume diffusion process. In itself, volume diffusion describes the migration of solute atoms or ions (e.g. argon) through a homogeneous crystal structure. However, crystals in nature are rarely homogeneous and contain numerous defects, chemical variations and impurities, all of which can produce non-ideal concentration gradients in minerals (Lee 1995). In $^{40}Ar/^{39}Ar$ geochronology, gas release patterns from step-heating experiments and more recently, intragrain spatial distribution of apparent ages obtained from microanalytical tools have revealed deviation from simple volume diffusion profiles (Scaillet *et al.* 1992; Kelley *et al.* 1994). This has led to a number of models being proposed to explain the anomalous concentration of argon within a mineral.

5.2.2 Multi Domain Diffusion (MDD)

Alkali feldspars are commonly used in $^{40}Ar/^{39}Ar$ geochronology because their anhydrous properties makes them stable during step-heating experiments under vacuum conditions (*summary in* McDougall and Harrison 1999). Several thermochronological studies have noted that cooling rates determined from age *versus* closure temperature diagrams deviate significantly from those indicated by individual age spectra (e.g. Heizler *et al.* 1988). In addition, the trend of data plotted on Arrhenius diagrams often contains inflections that suggest either a structural breakdown of the mineral or an important change in the diffusion characteristics.

In order to explain these features, Lovera *et al.* (1989, 1991) tested some of the fundamental assumptions of Dodson's equations. These included the assumption that the effective diffusion domain size for a given mineral is constant, denoted by the

parameter *a* in equation 5.2. Lovera *et al.* (1989) concluded that discrepancies between cooling rates and observed departures from linearity on Arrhenius diagrams could be solved by assuming a distribution of different diffusion domain sizes throughout the feldspars (figure 5.4).

There are two important implications discussed by Lovera *et al.* (1989) if a distribution of diffusion domain sizes exists. Firstly, a single closure temperature will no longer apply; large domains will 'close' at relatively high temperatures, whereas smaller domains will record closure at lower temperatures. Feldspars with a range of different size domains will have different effective closure temperatures. Secondly, age spectra will depend on the domain sizes and their volume fractions or relative proportions. The general result is that the different size components, if sufficiently distinct, can produce local plateau's in the age spectra (figure 5.4). The age of the local plateau will depend on the size of the domains and their position with respect to % ^{39}Ar released.

The multi-domain diffusion model has received a great deal of discussion in the literature. Some workers have questioned the fundamental chemical basis of alkali feldspar thermochronology (Villa 1988, 1999) and others have suggested that the MDD model is invalid, based on mineralogical features (Parsons *et al.* 1999). However, the MDD model continues to be used extensively (e.g. Lovera *et al.* 1991; Harrison *et al.* 1993) and updated (Lovera *et al.* 1997).

5.2.3 Multipath Diffusion

Volume diffusion through the crystal lattice is often the dominant transport mechanism for atoms in the solid state. However, diffusive loss of argon from minerals may also be influenced by the presence of crystal defects (e.g. exsolution lamellae, microfractures) that act as fast pathways of diffusion. In view of this, Lee (1995) developed a numerical model to describe the diffusion of a solute atom, such as argon, involving both volume diffusion and fast pathway or 'short-circuit' diffusion via defects. The combination of two or more different diffusion mechanisms operating simultaneously was given the term multipath diffusion (Lee 1995).

One of the most noteworthy predictions of theoretical models that incorporate short-circuit diffusion is the effect on cooling ages. Theoretical modelling of a cooling terrain suggests that multipath diffusion can produce significantly younger apparent ages in individual crystals than volume diffusion alone. Similarly, the effects of discrete

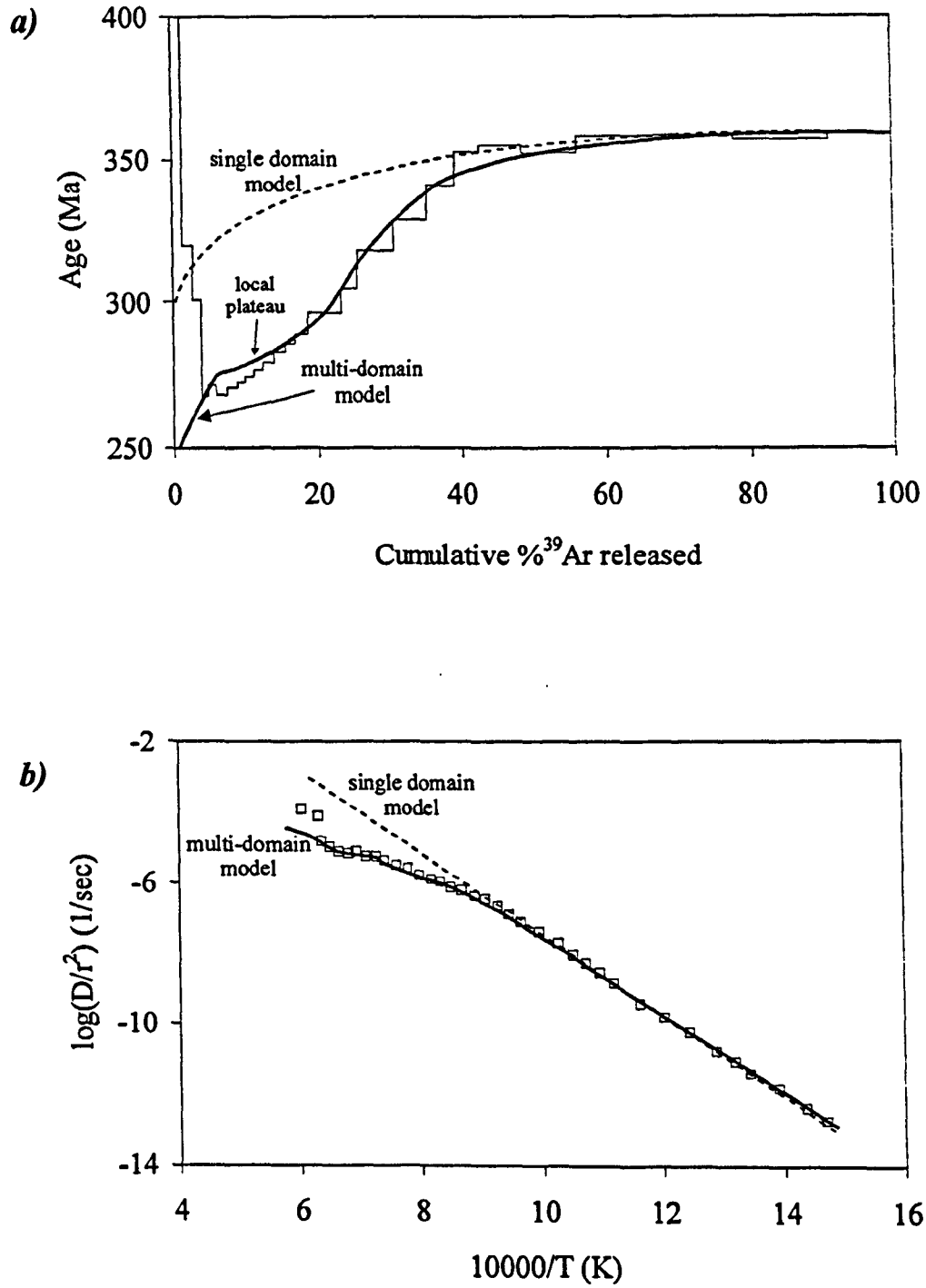

Figure 5.4 a) Diagram of age spectrum and b) Arrhenius plot for a granitoid K-feldspar sample. Note the local plateau in the age spectrum and the deviation from a linear trend on the Arrhenius plot. In both cases, theoretical curves using the multi-domain model fit the measured data. After Lovera et al. (1989).

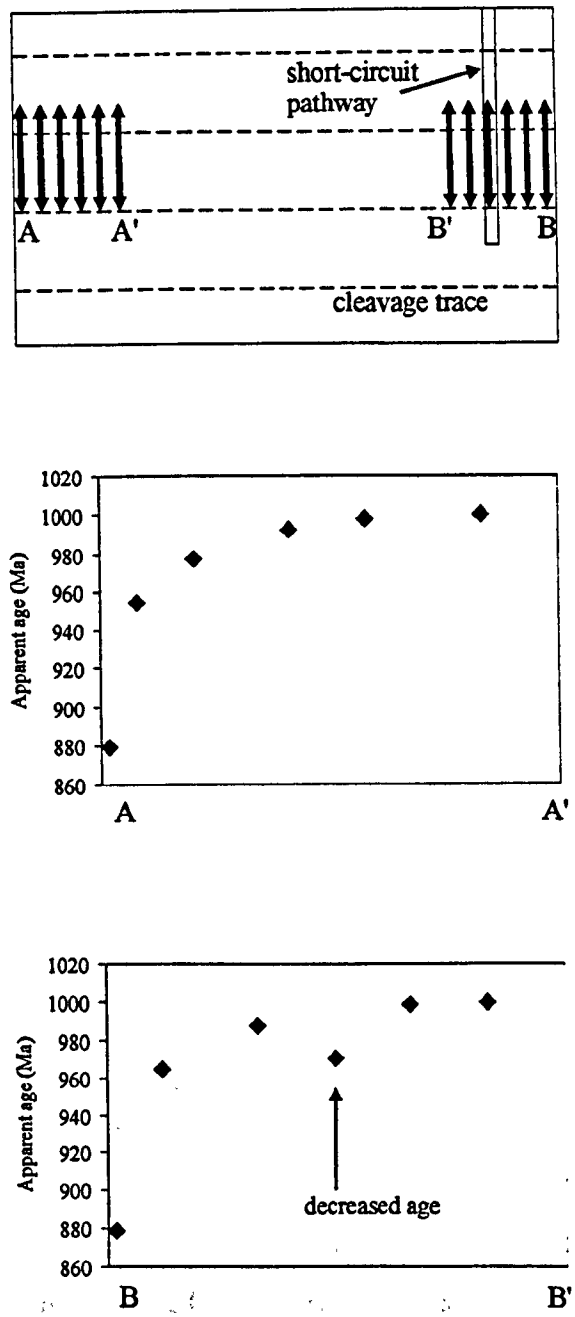

Figure 5.5 Schematic diagrams illustrating the possible affect of a crystal defect or 'short-circuit pathway' on the apparent age profile. A-A' shows the apparent age profile measured for a grain boundary undergoing simple volume diffusion. B-B' shows the apparent age variation for a profile that intersects a crystal defect with enhanced diffusion. After Pickles et al. (1997).

re-heating events or 'thermal pulses' have a much greater effect on apparent ages in crystals exhibiting multipath diffusion. Lee (1995) suggests that cooling ages and closure temperatures will be independent of the effective diffusion dimension at larger grain sizes (>70μm for hornblende).

Furthermore, multipath diffusion theory suggests that grains containing defects may yield a non-volume diffusion or non-fickian spatial distribution of radiogenic argon (^{40}Ar*). This can be measured directly with the use of a laser microprobe as shown by Kelley and Turner (1991) using hornblende grains from the Giants Range granite, Minnesota. In their study, Kelley and Turner (1991) show that Ar profiles were not produced by volume diffusion alone, but were also affected by a network of fast diffusion pathways. Similarly, Pickles *et al.* (1997) have discussed the effects of short-circuit diffusion on age profiles measured in biotite. Figure 5.5 shows the effect of argon loss from a crystal defect (e.g. crack) on the theoretical apparent age profile in figure 5.3.

The *in vacuo* step-heating experiments of Lo *et al.* (2000) and mineralogical studies of Parsons *et al.* (1999) continue to provide information supporting the application of the multipath diffusion model. However, a quantitative analysis of age profiles is precluded for this study by a lack of experimental data to constrain the parameters of short-circuit diffusion in muscovite and lithium mica.

5.2.4 Crystal-chemical controls on Ar retention

Several ^{40}Ar/^{39}Ar studies have observed that co-existing micas of different composition record different apparent ages. Harrison *et al.* (1985) recognised that variation in the Mg/Fe composition of biotite has a controlling influence on the diffusion of argon. Specifically, increasing Fe substitution weakens atomic bonds within the interlayer sheets of biotite, thereby decreasing Ar retention (Grove and Harrison 1996; McDougall and Harrison 1999).

In a study of high-pressure white mica (phengite) from the Dora-Maira nappe of the western Alps, Scaillet *et al.* (1992) also concluded that apparent age variations between lithologies were controlled largely by bulk Mg/Fe compositional differences. However, laser probe analyses revealed intragrain variation in ^{40}Ar* that was associated with spatial changes in Si^{4+} content. Furthermore, Scaillet *et al.* (1992) suggested that

variations in other major components (H^+, H_2O, O^{2-}) could also be responsible for differences in the Ar rententivity of phengite.

Although it was generally accepted that biotite is less retentive of Ar than muscovite, it was not until the *ionic porosity model*† of Dahl (1996) that a crystal - chemical explanation was provided for this observation. Based on the partitioning behaviour of trace elements, Dahl (1996) suggested three reasons why trioctahedral micas should have higher Ar diffusion rates than dioctahedral micas.

1. Biotite preferentially contains large ions (Rb, Cs), whereas muscovite partitions smaller ions (Na) into the interlayer site, indicating that biotite has a more widely spaced interlayer volume.
2. H_2O/ H_3O^+ fill many of the interlayer sites within biotite, whereas muscovite has more interlayer bonds and is therefore structurally stronger.
3. Despite a large interlayer site, Ba^{2+} is generally excluded from biotite due to an electrostatic repulsion. In contrast, muscovite favours Ba^{2+} substitution and consequently has stronger K - O interlayer bonds than biotite.

According to Dahl (1996), the weaker interlayer bonds in trioctahedral micas (e.g. biotite) are more easily stretched/broken leading to enhanced loss of radiogenic isotopes, which therefore produce younger $^{40}Ar/^{39}Ar$ cooling ages compared to dioctahedral micas (muscovite). Exceptions to this general observation occur if the trioctahedral micas contain appreciable amounts of fluorine (up to 2 wt% in the phlogopite of Dahl's study). Dahl (1996) was the first to recognise the systematic partitioning of Ba^{2+} with increasing F content in phlogopite from metapelitic assemblages. An important prediction of the ionic porosity model is that fluorine-rich trioctahedral micas would be *more* retentive of Ar than co-existing muscovite and thus produce older $^{40}Ar/^{39}Ar$ apparent ages.

Electron microprobe analyses of several mica samples in this study, presented in Chapter 3, have revealed Li-muscovite - lepidolite rims (trioctahedral structure) on muscovite cores (dioctahedral structure) in the majority of white mica from the Pakeagama Lake pegmatite. The Li-muscovite - lepidolite rims have high concentrations of fluorine, lithium, rubidium and caesium. In section 5.6, the ionic porosity model (Dahl 1996) is tested at the sub-grain scale using the UV laser microprobe.

† Dahl (1996) defines ionic porosity (Z_i) as the percentage of interlayer unit cell volume not occupied by ions.

5.3 UV-laser ablation analyses

The analytical procedure with the UV laser microprobe commenced with ablation of several square pits, usually 100μm or 50μm wide in the core of each mica grain (further details given in Appendix C). Schematic diagrams of each grain and the site of the analyses are presented in figures 5.7, 5.9, 5.10, 5.11 and an error-weighted mean age is calculated for each grain (tables 5.1 and 5.2). Errors are quoted at 1s.d.; calculated as 1.96 times the analytical error (at 1s.d.) if the probability of fit is >15%, or the *students-t* times the square root of the MSWD if the probability is less (calculated using Isoplot v. 2.22, Ludwig 2000). This also provides a 'reference age' to conduct measurement of $^{40}Ar/^{39}Ar$ profiles within individual mica grains. Analyses were excluded from the calculation of the mean if they were proximal to the grain edge, cracks or defects, or exhibited high analytical uncertainty (greater than 50Ma at the 1σ level) or were older than known U-Pb crystallisation ages.

The location of rare-element pegmatites and associated peraluminous granites from the Superior Province that are sampled in this study are shown in figure 5.6.

5.3.1 Northwest Superior Province

Three suites of peraluminous granite - rare-element pegmatite associations were studied within the NW Superior Province (figure 5.6). These are the Severn River peraluminous suite, the Pakeagama Lake suite and the Margot Lake pegmatite. The Severn River peraluminous suite intrudes the Favourable Lake greenstone belt, approximately 50km northwest of the Pakeagama Lake suite and 75km northwest of the Margot Lake suite, both of which are within the North Spirit Lake greenstone belt. All of these suites are proximal to the Bear Head Fault, a NW-SE trending shear zone within the North Caribou Terrain (Stone 1998).

U-Pb columbite-tantalite ages, presented in Chapter 4, constrain the emplacement age of the Pakeagama Lake pegmatite at 2673 ±10Ma (2σ, including decay constant uncertainties). The Margot Lake peraluminous granite has a U-Pb monazite crystallisation age of 2697 ± 2Ma (Corfu and Stone 1998a). Apparent ages older than the U-Pb age (beyond the associated analytical errors) were thus excluded from calculation of the mean age, because they must contain unsupported or excess radiogenic argon. Samples SS20, SS94, SS115, SS116, SS100 and 98FWB38 from the

Pakeagama Lake pegmatite display excess argon in ~50% of the square raster analyses (figure 5.7). Sample SS111 from the Margot Lake pegmatite also contains a minor component of excess argon (figure 5.7).

- *Severn River Peraluminous Suite (Samples SS73, SS70)*

Three analyses of sample SS73, mica from the Severn River pluton yield a poorly constrained error-weighted mean age of 2591 ± 51Ma (figure 5.7a). The error-weighted mean age for the pegmatite mica (SS70) is 2569 ± 7Ma, based on 4 analyses. This mean age is one of the youngest in the area indicating slow cooling rates (table 5.1).

Sample/ *suite*	Grain Size (mm)	Mean $^{40}Ar/^{39}Ar$ Apparent Age (Ma)	Number of analyses	U-Pb age (Ma)	Cooling Rate (°C/Ma)*
Severn River					
SS73 (pluton)	4	2591 ±51	3	*ca.*2697	3.2-10.0
SS70	10	2569 ±7	4	*ca.*2697	3.7-4.5
Pakeagama Lake					
SS20	8	2591 ±9	2	2673±10	2.0-5.6
SS94	2	2682 ±12	3	2673±10	>15.4
SS106a	4	2596 ±35	5	2673±10	1.6-10.9
SS115	3	2620 ±59	3	2673±10	>1.6
SS116 (1)	4	2620 ±116	4	2673±10	>1.1
SS116 (2)	4	2613 ±35	3	2673±10	1.9-23.3
98-21a (1) pluton	1	2593 ±10	4	2673±10	2.0-5.8
98-21a (2) pluton	2	2602 ±35	3	2673±10	1.7-13.5
SS100	4	2530 ±51	3	2673±10	1.0-4.3
SS107	6	2638 ±10	4	2673±10	3.6-23.3
98FWB38 (1)	10	2672 ±10	4	2673±10	>9.5
98FWB38 (2)	8	2672 ±28	4	2673±10	>5.1
Margot Lake					
SS111	6	2547 ±101	3	2697±2	2.0-11.2

*Table 5.1 Error-weighted mean ages (1s.d.) of peraluminous granites and rare-element pegmatites in the northwestern Superior Province. * Estimated linear cooling rates based on a closure temperature (T_c) between 350 - 400°C for Ar in muscovite (Hames and Bowring 1994). Emplacement age of the Margot Lake and Severn River pegmatites is 2697 ±2Ma (Corfu and Stone 1998a). Intrusion temperatures are assumed as 900°C for pluton samples and 600 - 700°C for pegmatite samples (London 1986).*

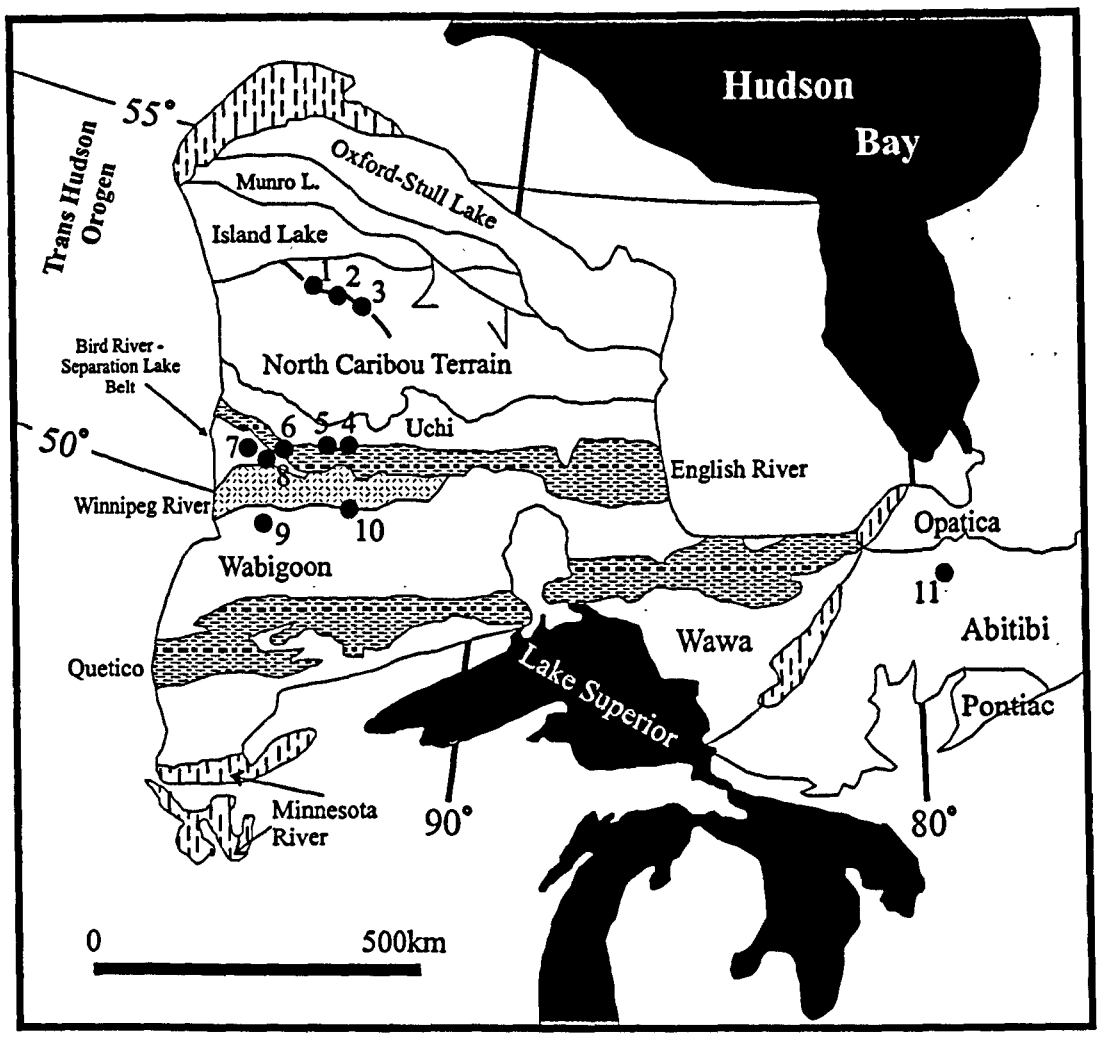

Archæan Subprovince type

- Plutonic
- Granite-greenstone
- Metasedimentary
- High-grade gneiss

Peraluminous granites and pegmatites sampled;

1. Severn River pluton and pegmatite.
2. Pakeagama Lake pluton and pegmatite.
3. Margot Lake pegmatite.
4. Wenesaga pegmatite.
5. Sandy Creek pegmatite.
6. Treelined Lake pegmatite.
7. Skidder pluton.
8. Separation Rapids pluton and pegmatite group.
9. Graphic Lake pegmatite.
10. Ghost Lake batholith and Mavis Lake pegmatite group.
11. Case pegmatite.

Figure 5.6 Location of peraluminous granites and pegmatites discussed in the text. Subprovinces of the Superior Province are from Card and Ciesielski (1986); Thurston et al. (1991).

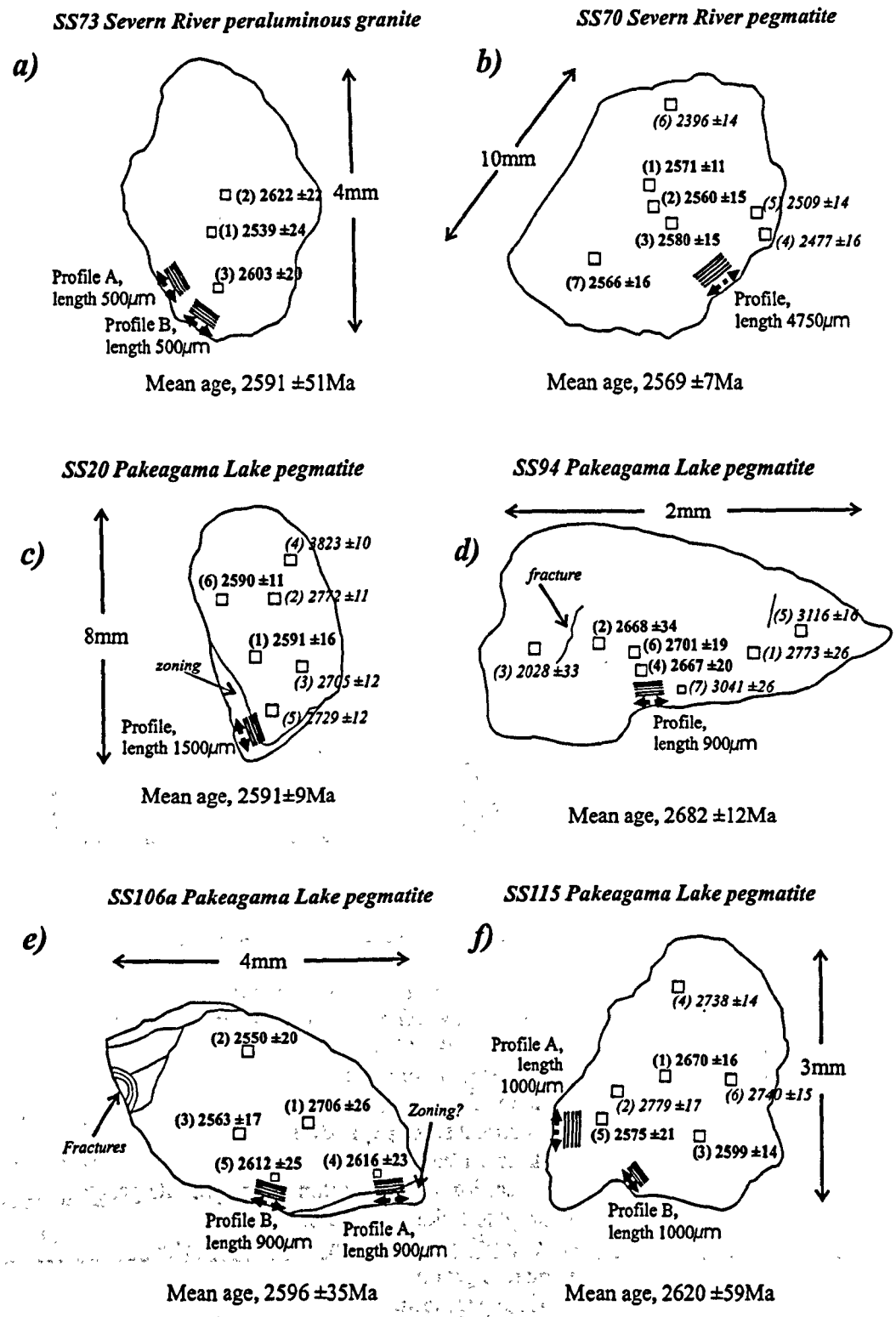

Figure 5.7 Schematic diagrams of mica grains from the NW Superior Province. Dates used in the calculation of the error-weighted mean age are highlighted in bold, those excluded from the mean age calculation are in italics. All age errors are at the 1 sigma level. The locations of apparent age profiles are indicated on each grain, presented in section 5.4.

SS116 Pakeagama Lake pegmatite

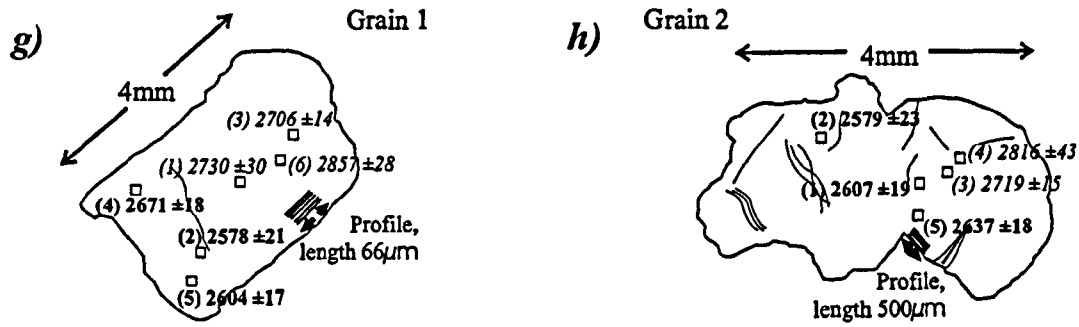

Mean age, 2620 ±116Ma

Mean age, 2613 ±35Ma

98-21a Pakeagama Lake pluton

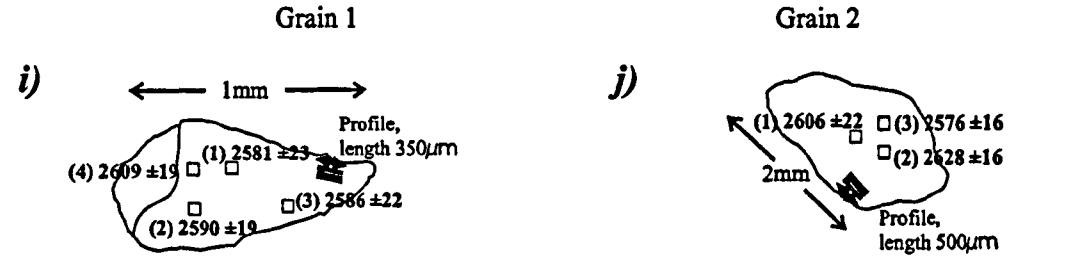

Mean age, 2593 ±10Ma

Mean age, 2602 ±35Ma

SS100 Pakeagama Lake pegmatite

SS107 Pakeagama Lake pegmatite

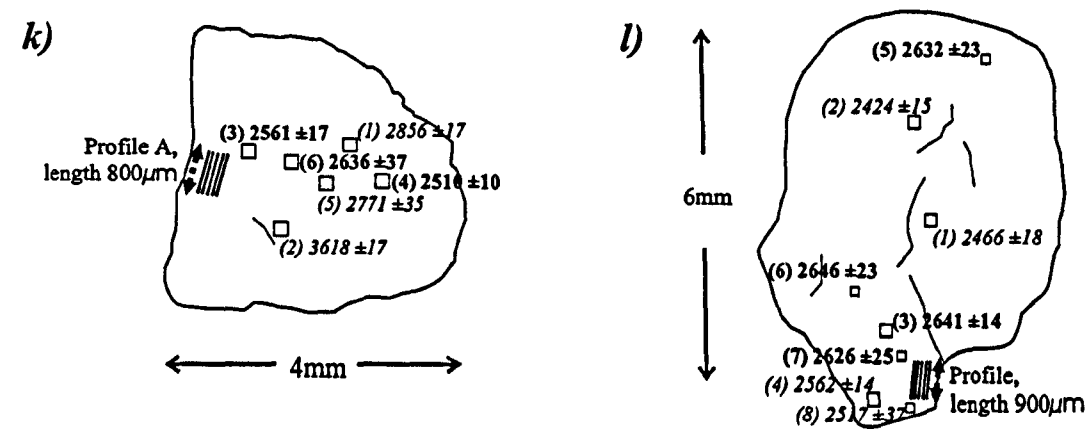

Mean age, 2530 ±51Ma

Mean age, 2638 ±10Ma

Figure 5.7 continued, schematic diagrams of mica grains from the NW Superior Province.

98FWB38 Pakeagama Lake pegmatite

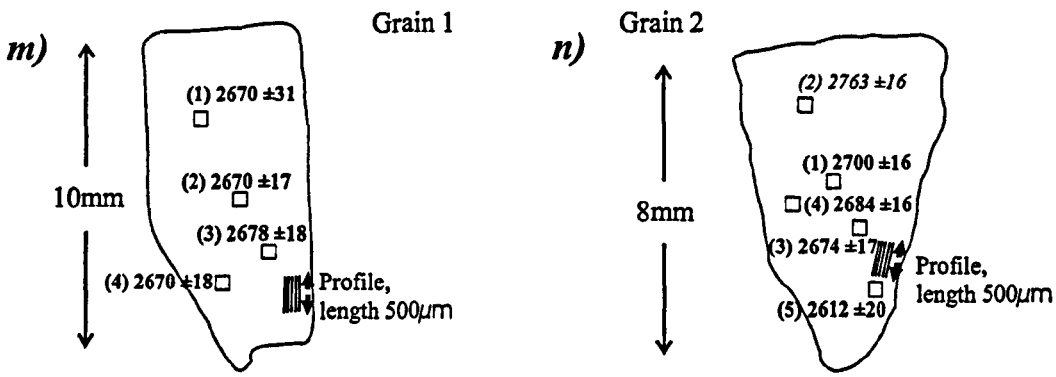

Mean age, 2672 ±10Ma

Mean age, 2672 ±28Ma

SS111 Margot Lake pegmatite

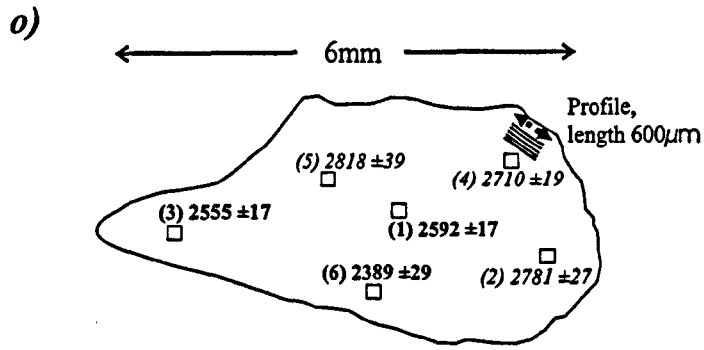

Mean age, 2547 ±101Ma

Figure 5.7 continued, schematic diagrams of mica grains from the NW Superior Province.

- *Pakeagama Lake Suite (Samples SS20, SS94, SS106a, SS115, SS116, 98-21a, SS100, SS107, 98FWB38)*

Several samples from the Pakeagama Lake pegmatites have $^{40}Ar/^{39}Ar$ ages that approach the U-Pb columbite-tantalite age of 2673 ± 10Ma (2σ, including decay constant uncertainties), interpreted as the emplacement age. Most notably, two mica grains of sample 98FWB38 from a 3m wide tourmaline-muscovite aplite dyke that is external to the main pegmatite body, give well constrained error-weighted mean $^{40}Ar/^{39}Ar$ ages of 2672 ± 3Ma and 2672 ± 28Ma (figure 5.7m, n). Mean ages of two micas from the Pakeagama Lake pluton, sample 98-21a, are much younger, 2593 ± 10Ma and 2602 ± 35Ma (figure 5.7i, j). In the first instance, these $^{40}Ar/^{39}Ar$ apparent ages from the pluton may perhaps be explained by their much smaller grain size (<2mm) compared with micas from the Pakeagama Lake pegmatite (usually >5mm). Mica grains from the pluton sample (98-21a) have a smaller effective radius of diffusion and would therefore be expected to close at lower temperature.

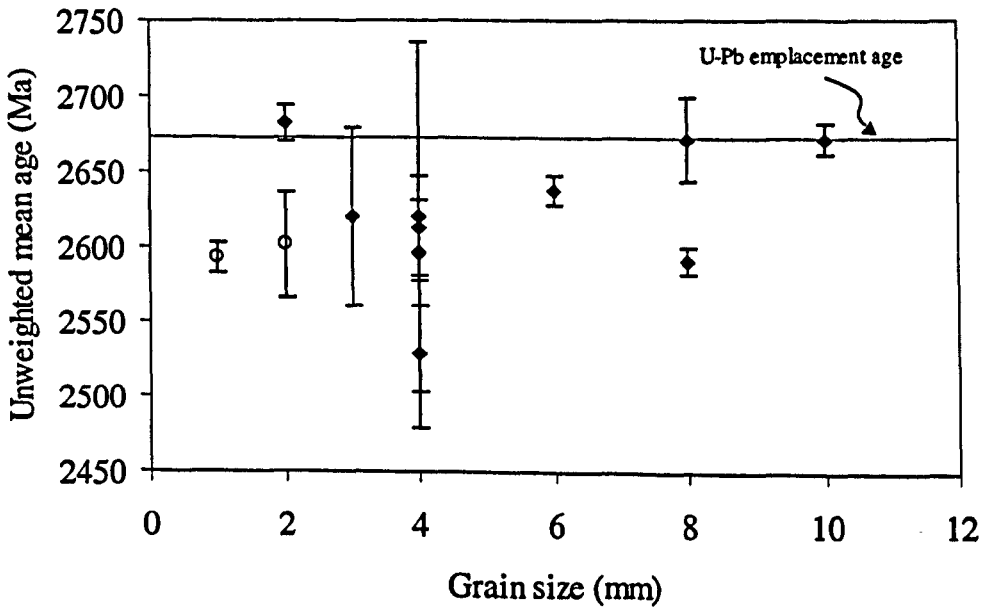

Figure 5.8 Error-weighted mean ages versus grain size for the Pakeagama Lake pluton (open circles) and pegmatite (filled diamonds). Emplacement age determined from U-Pb columbite-tantalite age (Chapter 4).

However, samples from the K-feldspar + petalite zone of the Pakeagama Lake pegmatite (SS20, SS94, SS106a, SS115, SS116) produce mean ages ranging from 2591±6 to 2682±12Ma (table 5.1). Importantly, apparent ages seem to have little correlation with grain size (figure 5.8). In part, young apparent ages could be the result of cracks and fractures that were visible within samples SS94, SS106, SS115, SS116, SS100 and SS107 (figure 5.7). These crystal defects may have acted as sub-grain boundaries as predicted by the multi-domain diffusion model or as fast diffusion pathways, indicating multi-path diffusion as described by Lee (1995). In either case, the young ages from large grain sizes suggests that the effective diffusion dimension must be on the order of μm, rather than the millimetre scale physical grain size.

- *Margot Lake Pegmatite (Sample S111)*

Three analyses from the grain core yield a poorly constrained error-weighted mean age of 2547 ± 101Ma. Three other analyses of the grain core yield anomalous older ages, up to 2818 ±39 Ma (analysis 5) and probably contain unsupported or excess radiogenic argon. For the most part however, the apparent ages fall in the same range as those for the Pakeagama Lake pegmatite (figure 5.7o).

5.3.2 Western Superior Province

Rare-element pegmatites and associated peraluminous granites occur throughout the western Superior Province. Those analysed here include the Wenesaga and Sandy Creek pegmatites, both located on the Uchi - English River Subprovince boundary; an intra-granitic pegmatite of the Treelined Lake complex, within the English River Subprovince; the Separation Rapids pluton and pegmatite group and the Skidder pluton, all located along the English River - Winnipeg River Subprovince boundary zone (the Separation Lake greenstone belt); the Graphic Lake pegmatite within the Wabigoon Subprovince; and the Ghost Lake batholith and associated rare-element pegmatite field (Mavis Lake group) located on the Winnipeg River - Wabigoon Subprovince boundary.

Sample/ *suite*	Grain Size (mm)	Mean $^{40}Ar/^{39}Ar$ Apparent Age (Ma)	Number of analyses	U-Pb age (Ma)	Cooling Rate (°C/Ma)*
Wenesaga					
SS1	10	2617±36	5	*ca.*2669	2.3-23.3
Sandy Creek					
SS2	10	2454±45	5	*ca.*2669	0.8-2.1
Treelined Lake					
SS42b (1)	10	2411±5	5	*ca.*2669	0.8-1.4
SS42b (2)	10	2432±22	5	*ca.*2669	0.8-1.6
Skidder Pluton					
SS207 (1)	2	1820±250	2	*ca.*2646	0.2-0.6
SS207 (2)	3	1953±23	3	*ca.*2646	0.3-0.5
Separation Rapids					
96-86b	10	2455±10	5	2644±10	0.9-2.1
SS34a	2	2366±12	4	2644±10	0.6-1.4
SS36	60	2367±18	4	2644±10	0.6-1.4
SS40	10	2395±25	5	2644±10	0.7-1.6
SS37	8	2423±19	8	2644±10	0.8-1.8
SS31 (1)	2	2358±144	2	2644±10	0.5-2.7
SS31 (2)	2	2330±26	3	2644±10	0.6-1.3
SS22	50	2389±5	5	2649±8	0.7-1.4
93-276	9	2445±15	5	2649±8	0.9-1.9
96-81 (1)	1	2433±5	4	2649±8	0.9-1.8
96-81 (2)	1	2411±16	3	2649±8	0.8-1.7
SS35b (pluton)	7	2435±26	1	2649±8	0.8-1.9
Graphic Lake					
SS89	8	2610±35	5	2709-2685	1.5-8.8
Ghost Lake					
SS50a	10	2549±19	4	*ca.*2685	1.9-4.7
SS55 (pluton)	4	2547±32	7	*ca.*2685	1.8-5.2
SS60	8	2563±20	8	2665±12	1.4-3.4
Southern SP					
Case					
SS45	9	2530±40	5	2639±2	1.3-5.1

*Table 5.2 Error-weighted mean ages (1s.d.) of peraluminous granite and pegmatite suites in the western and southern Superior Province. Sources of U-Pb ages for pegmatites are: Wenesaga, Sandy Creek and Treelined Lake (Corfu et al. 1995); Skidder pluton and Separation Rapids (Larbi et al. 1999 and this study); Graphic Lake (Blackburn et al. 1991); Ghost Lake (D. Davis, unpublished and this study); Case (Ducharme et al. 1997). *Estimated linear cooling rates based on a closure temperature (T_c) between 350 - 400°C for Ar in muscovite (Hames and Bowring 1994). Intrusion temperatures are assumed as 900°C for pluton samples and 600 - 700°C for pegmatite samples (London 1986).*

- *Wenesaga and Sandy Creek Pegmatites (Samples SS1, SS2)*

Square raster analyses of mica from the barren Wenesaga pegmatite and the beryl-type Sandy Creek pegmatite yield mean ages of 2617 ± 36Ma and 2454 ± 45Ma, respectively. Corfu *et al.* (1995) dated the emplacement of similar localised dykes in the English River Subprovince at 2669 ±2Ma. It is evident that these two pegmatites may have experienced quite different post-emplacement cooling histories indicated by their estimated cooling rates (table 5.2).

- *Treelined Lake intra-granitic pegmatite and Skidder pluton (Samples SS42b, SS207)*

Sample SS42b was extracted from a topaz bearing pegmatite within the Treelined Lake granite in the English River Subprovince (figure 5.6). Two muscovite grains yield error-weighted mean ages of 2411 ± 5Ma and 2432 ± 32Ma (figure 5.9c, d) which are significantly younger than the assumed emplacement age of the pegmatite, *circa* 2669Ma (Corfu *et al.* 1995).

Biotite from the Skidder pluton (sample SS207), located in the western Separation Lake greenstone belt, has mean $^{40}Ar/^{39}Ar$ apparent ages of 1820 ± 250Ma and 1953 ± 23Ma (figure 5.9e, f). The combined effect of fine grain size (2mm) and biotite composition, render these micas more susceptible to disturbance of Ar systematics from low temperature heating events. The emplacement age is assumed to be contiguous with the Separation Rapids pluton, also located in the Separation Lake greenstone belt, previously dated at 2646 ± 2Ma, U-Pb monazite age (Larbi *et al.* 1999).

- *Separation Rapids Group (Samples 96-86b, SS34a, SS36, SS40, SS37, SS31, SS22, 93-276, 96-81, SS35b)*

As shown in Chapter 4, U-Pb dating of columbite-tantalite from Separation Rapids pegmatites yields crystallisation ages of 2649±8Ma and 2644±10Ma (2σ, including decay constant uncertainties). In contrast, the maximum $^{40}Ar/^{39}Ar$ apparent age of micas in the Separation Rapids pluton and pegmatite group is 2.45Ga (figure 5.10). This suggests either that cooling rates for the region were extremely slow (<1°C/Ma), or it may imply later heating events have caused complete resetting of $^{40}Ar/^{39}Ar$ apparent ages of micas in the Separation Rapids pegmatite group.

Four samples from the Separation Rapids Group have mean $^{40}Ar/^{39}Ar$ apparent ages <2.4Ga, (SS34a, SS36, SS31 and SS22). Apparent ages of <2.4Ga from samples SS31 and SS34a can perhaps be accounted for by their relatively fine grain size (2mm),

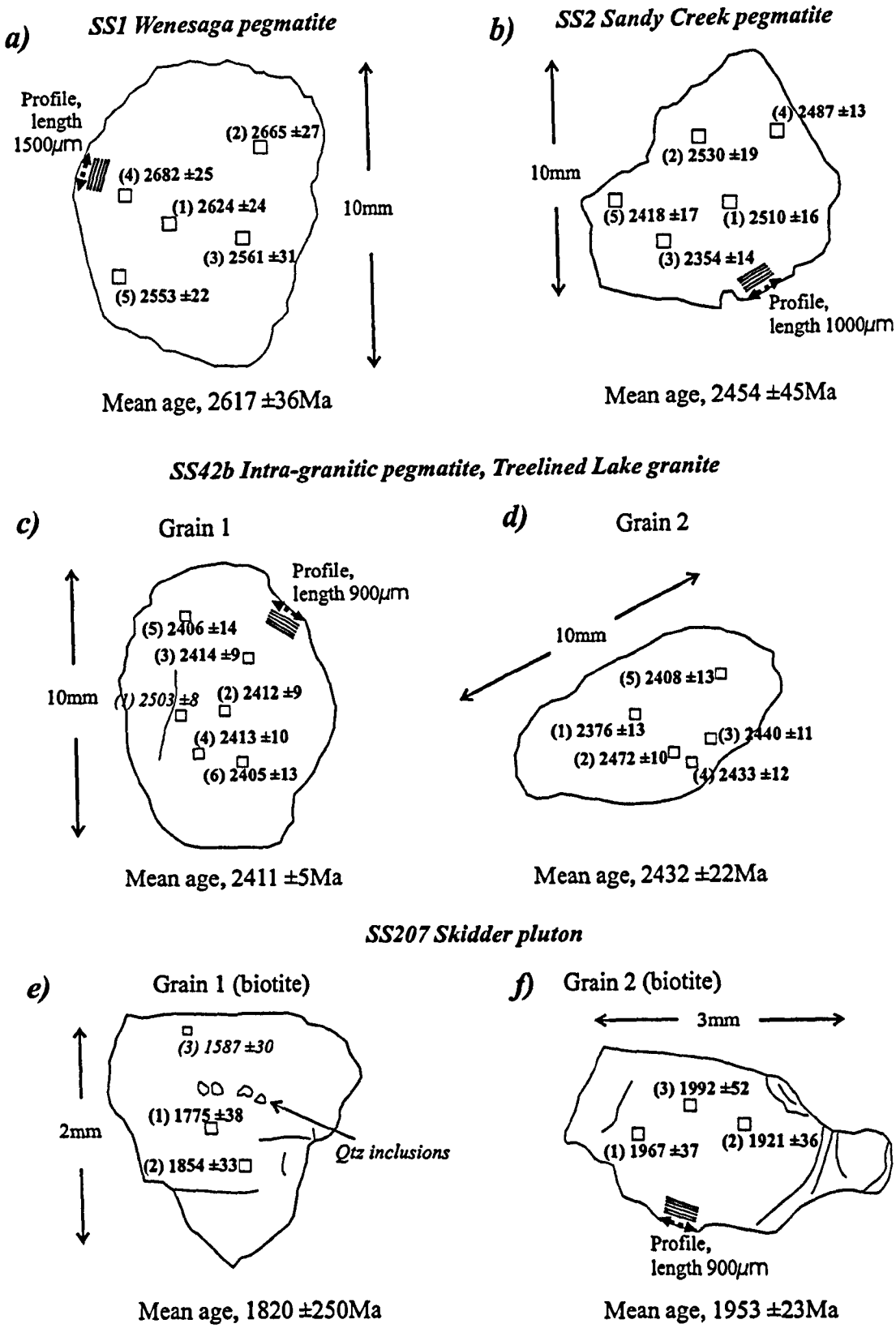

Figure 5.9 Schematic diagrams of mica grains from the western Superior Province. Dates used in the calculation of the error-weighted mean age are highlighted in bold, those excluded from the mean age calculation are in italics. All age errors are at the 1 sigma level. The locations of apparent age profiles are indicated on each grain, presented in section 5.4. All grains are white micas except where indicated.

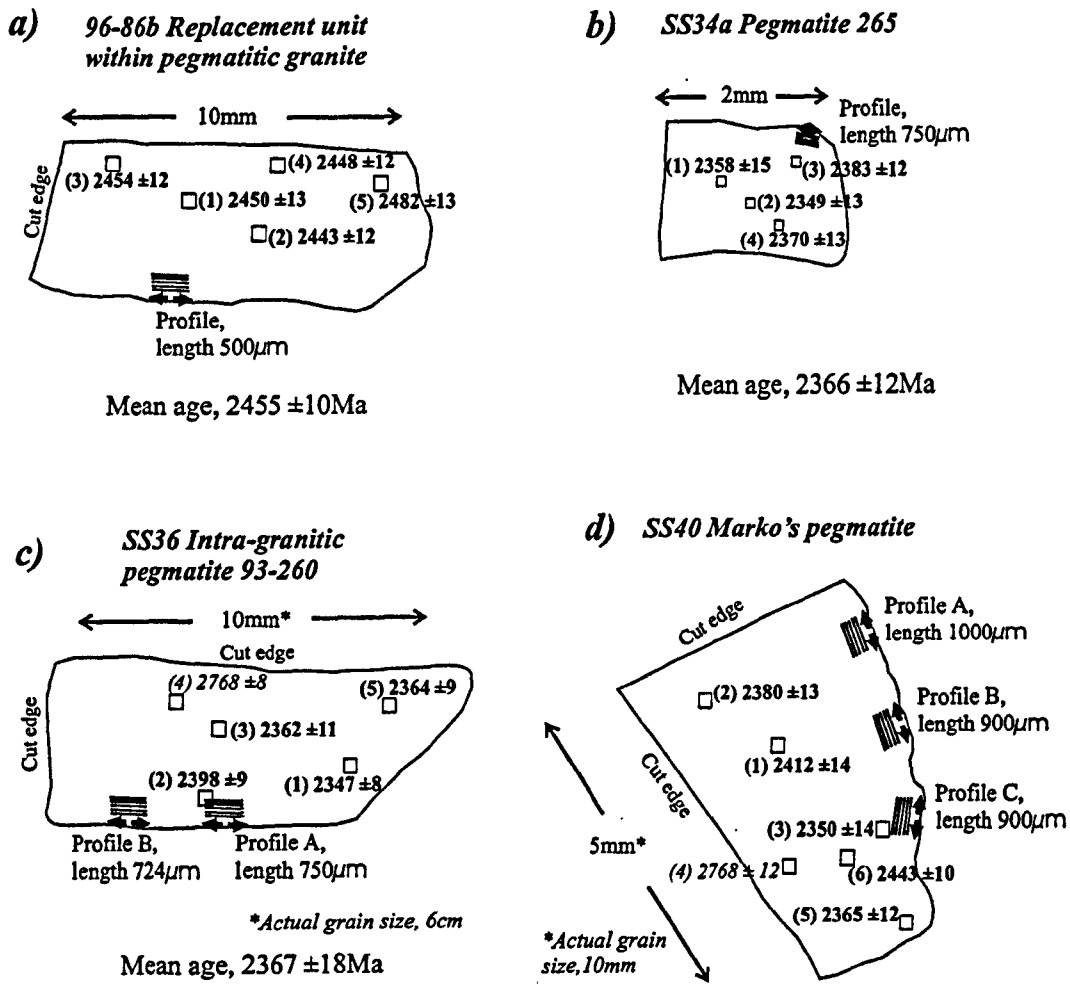

Figure 5.10 Schematic representations of mica grains from the Separation Rapids pegmatite group, western Superior Province. Dates used in the calculation of the error-weighted mean age are highlighted in bold, those excluded from the mean age calculation are in italics. All age errors are at the 1 sigma level.

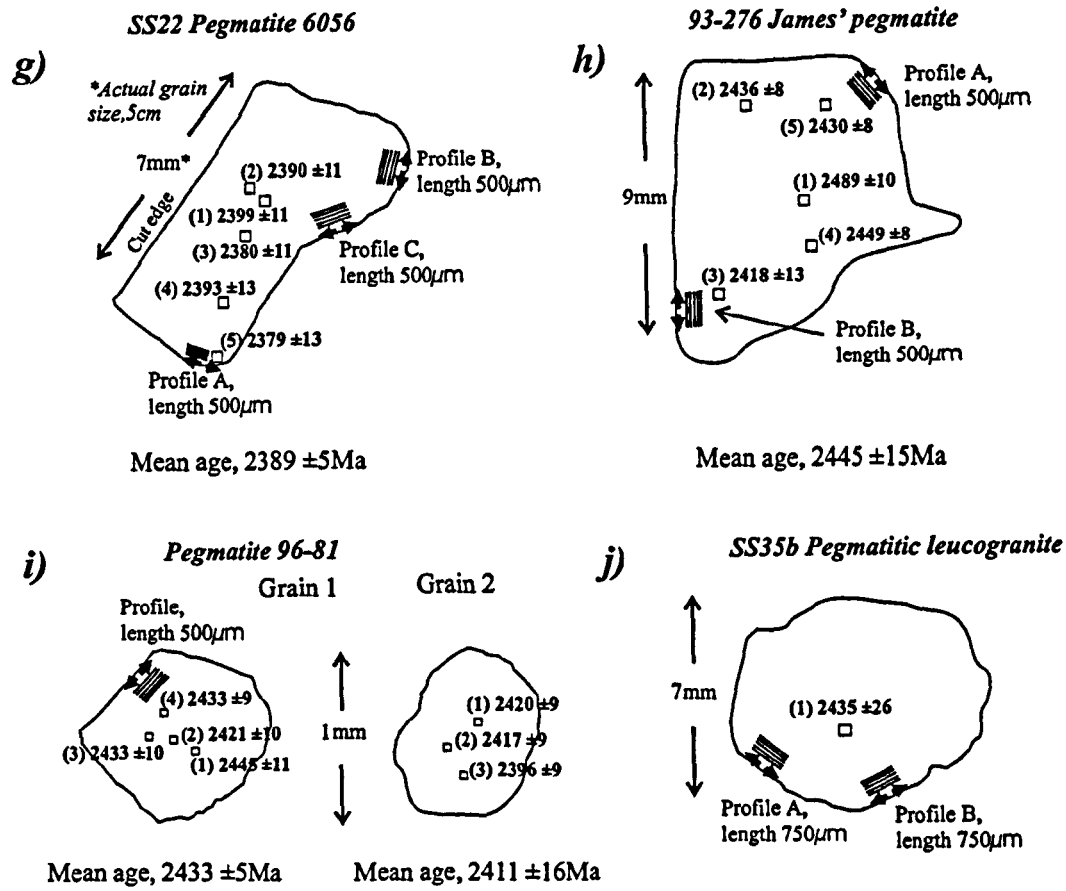

Figure 5.10 continued, schematic representations of mica grains from the Separation Rapids pegmatite group, western Superior Province.

a) ***SS89 Graphic Lake pegmatite***

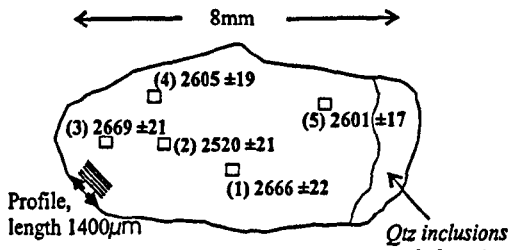

Mean age, 2610 ±35Ma

b) ***SS50a Intra-granitic pegmatite, Ghost Lake suite***

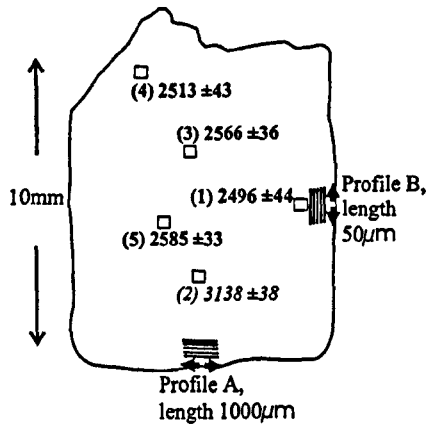

Mean age, 2549 ±19Ma

c) ***SS55 Ghost Lake batholith, GLB-7 leucogranite***

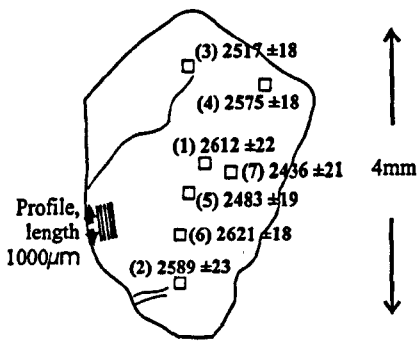

Mean age, 2547 ±32Ma

d) ***SS60 Fairservice pegmatite #1, Mavis Lake Group***

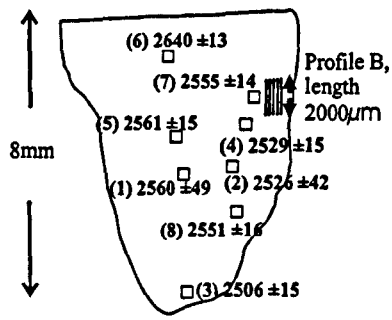

Mean age, 2563 ±20Ma

SS45 Case pegmatite, Abitibi subprovince

e)

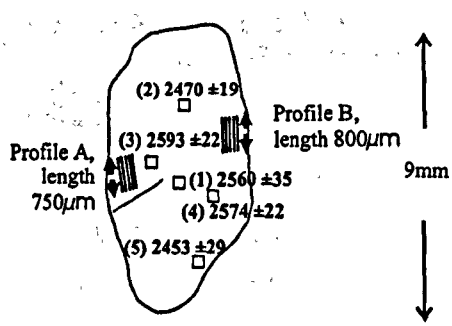

Mean age, 2530 ±40Ma

Figure 5.11 Schematic representations of mica grains from the western and southern Superior Province. Dates used in the calculation of the error-weighted mean age are highlighted in bold, those excluded from the mean age calculation are in italics. All age errors are at the 1 sigma level.

although samples SS22 and SS36 have much larger grain sizes, 5cm and 3cm, respectively (table 5.2). This implies that these micas have an effective diffusion dimension that is smaller than the physical grain size.

- *Graphic Lake Pegmatite (Sample SS89)*

Emplacement of the post-tectonic granite suite in the Wabigoon Subprovince is constrained to 2709 - 2685Ma, reported in Blackburn *et al.* (1991). Analyses of the core region of mica sample SS89 from the Graphic Lake pegmatite yield a mean $^{40}Ar/^{39}Ar$ apparent age of 2635 ±33 Ma (figure 5.11a).

- *Ghost Lake batholith and Mavis Lake group pegmatite (Samples SS50a, SS55, SS60)*

Breaks and Moore (1992) report a *circa* 2685Ma U-Pb monazite age for the primitive GLB-1 unit of the Ghost Lake batholith, obtained by D. Davis (Royal Ontario Museum). Sample SS55 from the pegmatitic leucogranite unit (GLB-7) within the Ghost Lake batholith has an error-weighted mean age of 2547 ± 32Ma (figure 5.11c). Sample SS50a taken from a pegmatite within the Ghost Lake batholith has a similar mean age of 2549 ± 19Ma (figure 5.11b).

Geochemically associated with the Ghost Lake batholith is an external zone of rare-element pegmatites termed the Mavis Lake group (Breaks and Moore 1992). U-Pb dating of columbite-tantalite (Chapter 4) from Fairservice pegmatite #1 yields a crystallisation age of 2665±12Ma (2σ, including decay constant uncertainties). Mica from the same pegmatite (sample SS60) has an error-weighted mean age of 2563 ± 20Ma. Analysis 6 (figure 5.11d) has an age of 2640 ± 13, which is nearly concordant with the U-Pb age.

5.3.3 Southern Superior Province

Ducharme *et al.* (1997) determined emplacement ages of the Preissac and Lamotte leucogranites, located in the southern Abitibi greenstone belt. Monazite and titanite from these S-type, peraluminous granite plutons yield ages between 2681 - 2630Ma indicating prolonged magmatic activity. A beryl - columbite-tantalite - spodumene pegmatite associated with the Lamotte pluton has a U-Pb monazite age of 2639 ±2Ma (Ducharme *et al.* 1997).

- *Case Pegmatite (Sample SS45)*

Analysis of rare-element pegmatites from the southern Superior Province is limited to the Case pegmatite. This is an albite - spodumene type pegmatite located at the boundary between the northern and southern Abitibi greenstone belt. Five analyses of the core region of mica sample SS45 from the Case pegmatite yields an error-weighted mean age of 2530 ±40 Ma. (figure 5.11e).

5.3.4 Summary

Square pit analyses using the UV laser microprobe yields error-weighted mean ages analogous to integrated ages from step-heating data, which can be used to constrain post-emplacement cooling rates or re-heating of individual plutons and pegmatite dykes. In contrast to bulk analysis techniques such as furnace step-heating, the use of laser 'spot' dating provides a way to map the spatial distribution of radiogenic argon. Comparison of the individual $^{40}Ar/^{39}Ar$ mica 'spot' analyses with emplacement ages of pegmatites determined by U-Pb geochronology allows us to recognise apparent ages that are anomalous i.e. older than the emplacement age or significantly younger. It is thus possible to exclude areas of grains that yield anomalous ages in the calculation of an error-weighted mean $^{40}Ar/^{39}Ar$ age.

Mica grains with physical grain sizes in the range <2mm to cm scale yield error-weighted mean ages that are independent of grain size. This suggests a micron scale maximum effective diffusion dimension, most likely defined by the mean distance between cracks or defects. This study shows that ablation pits sited close to cracks within a crystal often yield anomalous apparent ages. The anomalous older ages are interpreted as incorporating a component of excess radiogenic argon ($^{40}Ar^*$). Young ages may result from prolonged volume diffusion caused by slow cooling, or from loss of argon along fast diffusion pathways, as predicted by multipath diffusion theory (Lee 1995).

Most of the peraluminous granite pluton samples analysed from the northwestern and western Superior Province yield comparable estimated cooling rates. The Severn River pluton (sample SS73) has an estimated cooling rate between 3°C/Ma and 10°C/Ma; the Pakeagama Lake pluton sample (98-21a) yields cooling rates of 2 - 14°C/Ma. Similarly, mica sample SS55 from the Ghost Lake batholith has an estimated cooling rate between 2 - 5°C/Ma (locations shown in figure 5.6). Mica from pegmatites

in these areas have broadly similar $^{40}Ar/^{39}Ar$ ages, some of which are concordant with U-Pb ages that are interpreted as emplacement ages for the pegmatites e.g. 2672 ± 10Ma for the Pakeagama Lake pegmatite.

In contrast, micas in the Separation Rapids pegmatite group and Treelined Lake pegmatite yield $^{40}Ar/^{39}Ar$ apparent ages that are >200Ma younger than their U-Pb crystallisation age. This suggests either that cooling rates for the region were extremely slow (<1 °C/Ma), or later heating events caused complete resetting of $^{40}Ar/^{39}Ar$ apparent ages of micas in the Separation Rapids pegmatite group.

In order to investigate the differences between the mica samples from these pegmatites more thoroughly, *viz* their cooling rates and mechanisms of argon loss; the UV laser has been used to ablate traverses less than 15μm wide, enabling the measurement of apparent age variation at a very high spatial resolution. Such data are expected to reveal important information on the thermal history of a mineral that would otherwise be homogenised by bulk mineral analysis.

5.4 $^{40}Ar/^{39}Ar$ apparent age profiles

In each of the laser microprobe profiles shown in figures 5.12 - 5.18, apparent age (in millions of years) for each laser pit analysis is plotted against distance from the grain edge (in microns). Specific methods of the ablation procedure and laser parameters are reported in Appendix C. Vertical error bars represent the uncertainty in apparent age at the 1σ level. The width of ablation pits for 'spot' analyses were either 100μm or 50μm, and are represented by horizontal error bars. The width of ablation pits excavated during traversing was 10-15μm, which is commonly narrower than the data point symbol and thus horizontal error bars are often omitted for clarity.

5.4.1 Northwest Superior Province

- *Severn River peraluminous suite (figure 5.12)*

Two diffusion profiles were measured from a single grain of muscovite from sample SS73, taken from the Severn River peraluminous granite. Apparent ages range from 2.65 - 1.8Ga in profile A, and between 2.75 - 2.05Ga for profile B (figure 5.12a, b). These are the largest intragrain $^{40}Ar/^{39}Ar$ apparent age variations recorded in this

study, on the order of 700 - 800Ma difference between core and rim. The maximum apparent age is attained within 200μm from the grain edge in each profile. However, the profile is not well defined because the age variation is scattered. Profile B displays a component of excess argon in one analysis at 225μm distance from the grain edge (figure 5.12b).

In comparison, muscovite sample SS70 from a K-feldspar megacrystic pegmatite, has a well defined profile with apparent ages in the range 2.60 - 2.25Ga (figure 5.12c). Within 300μm of the grain boundary, the profile gradient is very steep, which then gradually shallows up to 1000μm distance. Between 1000μm from the grain edge and the grain core (~5000μm), apparent ages remain relatively constant at 2.6Ga. Figure 5.12d shows the first 300μm of the profile from figure 5.12c in detail. At this scale, there is a clearly marked change in the profile gradient between 150-250μm from the grain edge. This 'local plateau', perhaps analogous to that discussed by Lovera *et al.* (1989) in the Multi-Domain Diffusion (MDD) model, displays relatively constant $^{40}Ar/^{39}Ar$ ratios corresponding to an apparent age of 2.45Ga. Two anomalous data points with apparent ages that create dips in the profile are interpreted as defects in the crystal that may have lost argon via short-circuit diffusion (see figure 5.5).

- *Pakeagama Lake peraluminous suite (figure 5.13)*

Profiles from the Pakeagama Lake suite are characterised by apparent ages in the range 2.7 - 2.1Ga. Three distinctive profile patterns are recognised:

1. Profiles that display a gradual increase in apparent age with distance from the grain edge. Variation in apparent age is usually >300Ma.
2. Profiles that display relatively young apparent ages only at the grain boundary, followed by a sharp increase to older (2.6Ga) and broadly constant ages throughout the remaining traverse.
3. Profiles that display relatively little variation in apparent age (<100Ma) throughout the entire traverse.

<u>Category 1</u>

Micas from the K-feldspar + petalite zone display profiles with features of category 1. Sample SS20 is typical of such profiles with apparent age variation between 2.85 - 2.30Ga. Although the data are somewhat scattered, there is a linear trend of decreasing apparent ages towards the grain boundary (figure 5.13a).

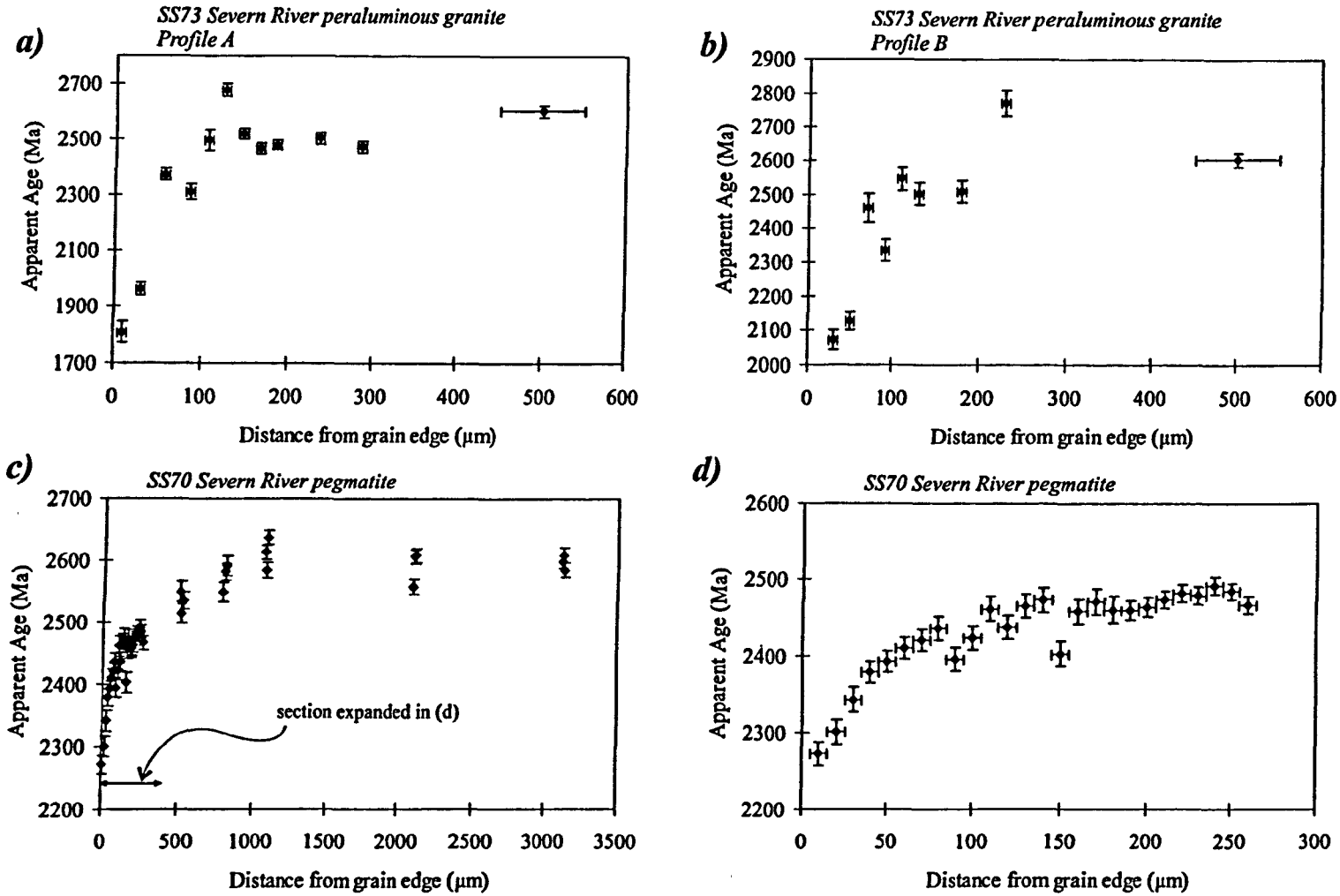

Figure 5.12 $^{40}Ar/^{39}Ar$ apparent age profiles from the Severn River peraluminous granite and rare-element pegmatite. Vertical error bars represent 1 sigma age uncertainty, horizontal bars indicate width of ablation pit. (d) shows the first 300 microns of the Severn River pegmatite mica profile (c) in detail.

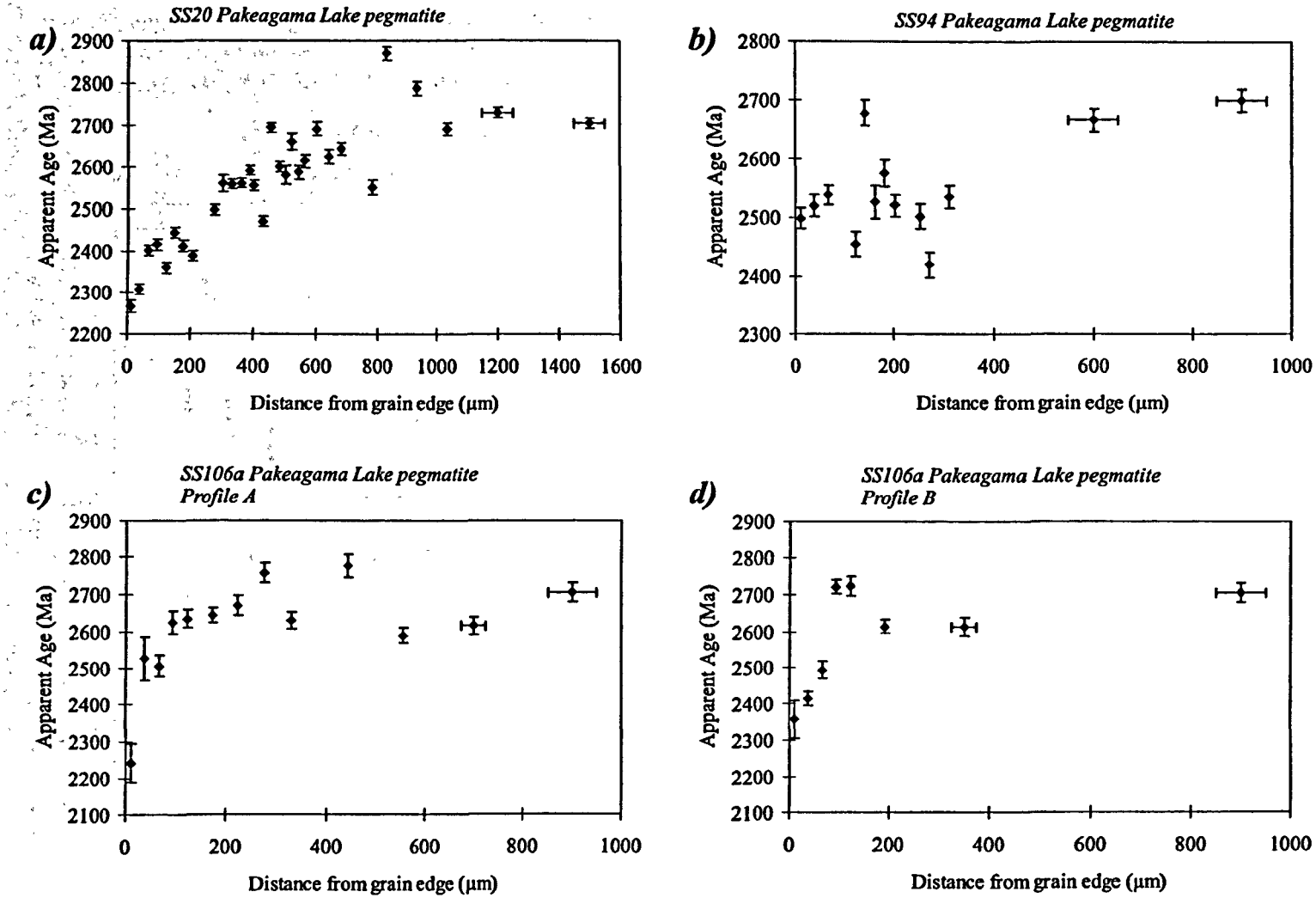

Figure 5.13 $^{40}Ar/^{39}Ar$ apparent age profiles from the Pakeagama Lake pluton and rare-element pegmatite. Vertical error bars represent 1 sigma age uncertainty, horizontal bars indicate width of ablation pit.

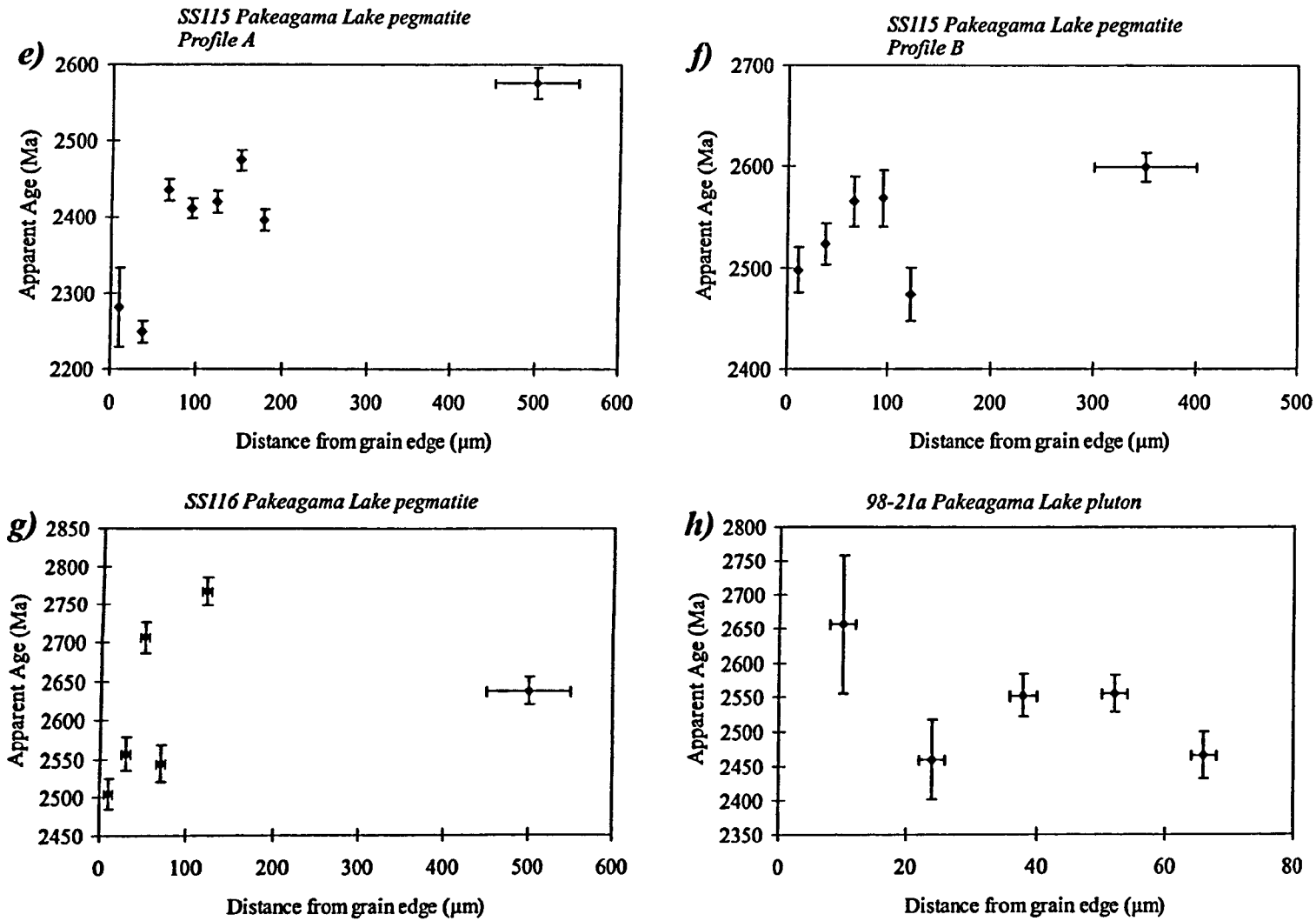

Figure 5.13 continued, $^{40}Ar/^{39}Ar$ apparent age profiles from the Pakeagama Lake pluton and rare-element pegmatite. Vertical error bars represent 1 sigma age uncertainty, horizontal bars indicate width of ablation pit.

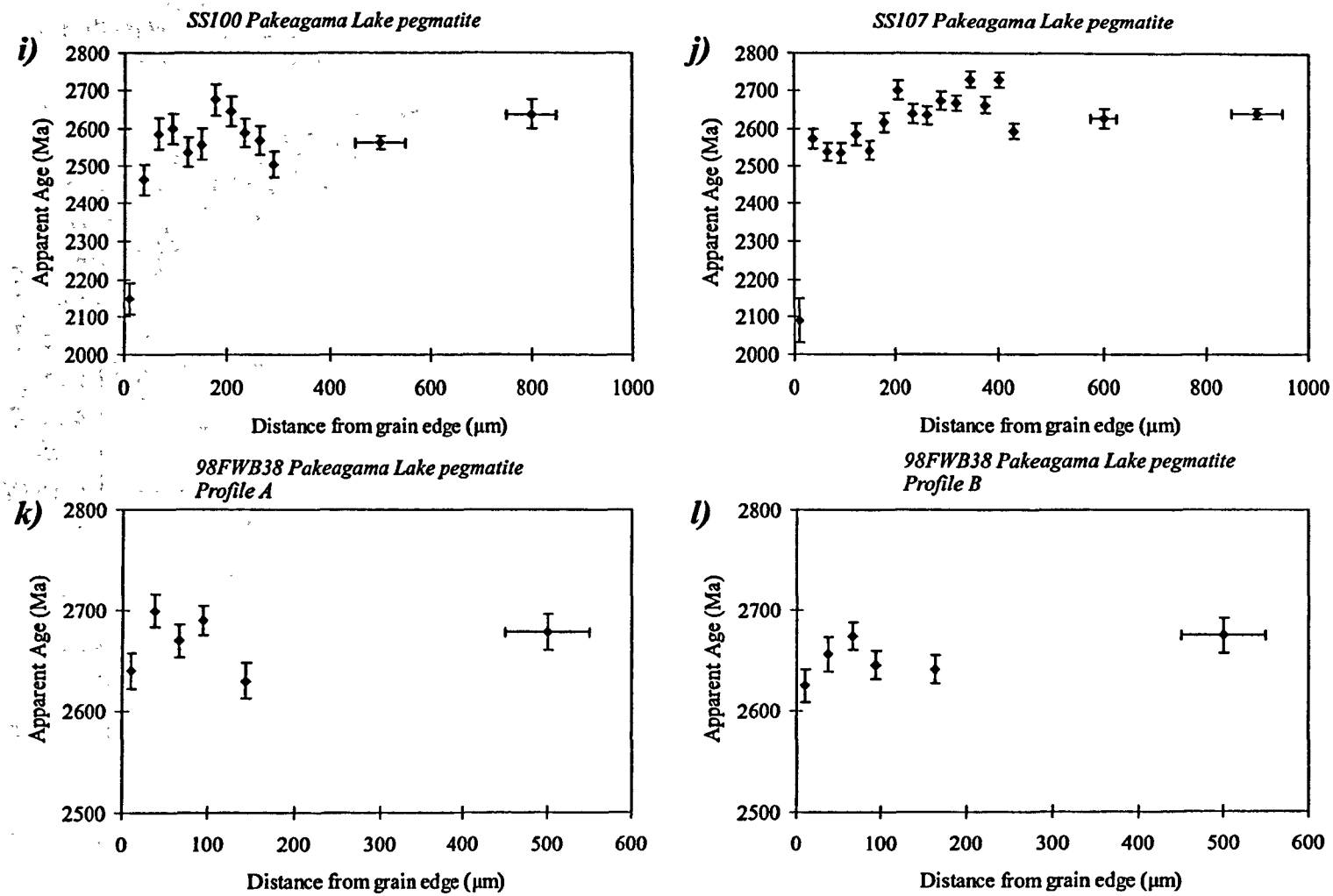

Figure 5.13 continued, $^{40}Ar/^{39}Ar$ apparent age profiles from the Pakeagama Lake pluton and rare-element pegmatite. Vertical error bars represent 1 sigma age uncertainty, horizontal bars indicate width of ablation pit.

The profile from mica sample SS94 (K-feldspar + petalite zone) has apparent ages ranging from 2.7 - 2.4Ga. There is a considerable scatter within the data, shown in figure 5.13b, although apparent ages at distances <350μm from the grain boundary are generally younger than the mean age of spot analyses within the core.

Two profiles, shown in figure 5.13c, d, were measured on a single grain of sample SS106a (K-feldspar + petalite zone). The two profiles display quite similar apparent age variations from 2.7 - 2.3Ga. Profile A has steep age gradients within ~50μm of the grain boundary (a pattern perhaps more akin to category 2) and two points >2.7Ga that probably contain excess argon. Profile B has a relatively gradual decrease in apparent ages within 200μm of the grain edge, although two points containing excess argon are displaced to >2.7Ga apparent ages.

Category 2

Two samples of mica from the Pakeagama Lake pegmatite display profiles with characteristics of category 2. Mica from the blocky K-feldspar (potassic) zone (SS100) has a profile with a single analysis at the grain edge of 2.15Ga, followed by apparent ages in the range 2.5 - 2.7Ga (figure 5.13i). Such a sharp increase in apparent age is also seen in the profile from SS107, taken from the spodumene + quartz pegmatite-aplite. Apparent ages for the majority of the profile fall in the range 2.5 - 2.7Ga, again with a much younger apparent age at the grain edge of 2.1Ga (figure 5.13j).

Category 3

Mica from the tourmaline + muscovite aplite dyke (sample 98FWB38) displays relatively little variation in apparent age. This is seen in the well constrained apparent ages from spot analyses (e.g. grain 1, 2672 ±10Ma, section 5.3.1) and is also evident from the profiles, measured on two mica grains from sample 98FWB38 (figure 5.13k, l). All analyses yield apparent ages in the range 2.6 - 2.7Ga. These profiles do not display the steep apparent age gradients at the grain edge that is common in samples from the Pakeagama Lake pegmatite and from other peraluminous suites in the NW Superior Province.

Occurrences of ages >2.7Ga (beyond analytical uncertainty) are limited to isolated analyses within samples SS20, SS106a, SS116 (figures 5.13a, c and g, respectively). These are interpreted to contain a component of excess radiogenic argon.

- *Margot Lake pegmatite (Figure 5.14)*

Apparent ages for the Margot Lake granitic pegmatite (sample SS111) fall in the range 2.75-2.15Ga. Maximum apparent ages are attained at a distance of 250μm from the grain edge, although there is some scatter amongst the data with 2.6Ga ages found at 50μm and 300μm distance (figure 5.14). As discussed in section 5.3, the Margot Lake pluton has a U-Pb monazite age of 2697 ± 2Ma (Corfu and Stone 1998a). Apparent ages >2.7Ga may thus contain unsupported or excess radiogenic argon.

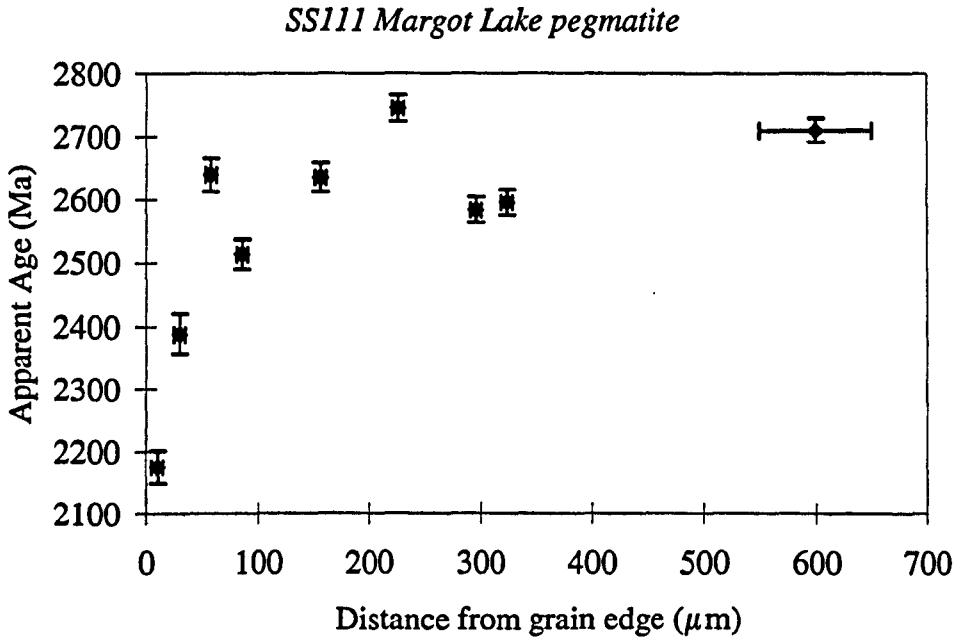

Figure 5.14 $^{40}Ar/^{39}Ar$ apparent age profile of mica from the Margot Lake pegmatite. Vertical error bars represent 1 sigma age uncertainty, horizontal bars indicate width of ablation pit.

5.4.2 Western Superior Province

- *Wenesaga and Sandy Creek pegmatites (Figure 5.15a, b)*

Profiles for the Wenesaga granitic pegmatite (SS1) and the Sandy Creek beryl-type pegmatite (SS2) display considerable differences in apparent age variation (figure 5.15a, b). Mica from the Wenesaga pegmatite has apparent ages in the range 2.7 - 2.3Ga, in comparison with 2.6 - 2.2Ga for the mica from the Sandy Creek pegmatite

(although only two points fall outside the 2.5 - 2.3Ga range). Both profiles show a single analysis at the grain boundary that is significantly younger than apparent ages throughout the remaining profiles, although there is a gradual decrease in ages towards the edge of grain SS1.

- *Treelined Lake intra-granitic pegmatite and Skidder pluton (Figure 5.15c, d)*

White mica from the Treelined Lake intra-granitic pegmatite and Separation Rapids pegmatite group (discussed below), are distinguished by apparent age profiles that attain a maximum of only 2.45Ga and reach a minimum 1.7Ga.

The profile from mica (sample SS42b) of the Treelined Lake intra-granitic pegmatite has apparent ages in the range 2.40 - 2.15Ga (figure 5.15c). The profile shows relatively constant apparent ages (2.4Ga) to within 100μm of the grain edge followed by younger apparent ages at the grain edge.

Biotite from the Skidder pluton (SS207), located approximately 5km west of the Separation Rapids pegmatite group, displays apparent ages in the range 2.1 - 1.7Ga. The data have a stepped profile with ages first rising from 1.7Ga at the grain boundary to 1.9Ga at a distance of 100μm; ages then fall back to 1.7Ga followed by a rise of ages up to 2.1Ga, beyond 400μm distance (figure 5.15d).

- *Separation Rapids pegmatite group (Figure 5.16)*

Tindle and Breaks (1998) have previously divided the Separation Rapids pegmatites into two suites based on columbite-tantalite chemistry. It is noteworthy that the two suites, the Mn-suite and Fe-suite pegmatites, display distinct $^{40}Ar/^{39}Ar$ mica apparent age profile patterns.

Mn-suite - Profiles that display apparent ages at the grain edge at least as young as 2.1Ga and commonly have well defined trends.

Within the Mn-suite, samples were analysed from a late-magmatic, pegmatitic granite assemblage (96-86b); a beryl-type pegmatite within the Separation Rapids pluton (SS36); a beryl-type pegmatite outside the pluton (SS34a); the Big Whopper petalite subtype pegmatite (SS31); and Marko's petalite pegmatite (wall zone SS37, core zone SS40). Samples 96-86b, SS34a, SS36 and SS31 display profiles with gradually decreasing apparent ages towards the grain edge (figures 5.16a, b, c, d, j, k).

Samples SS40, SS37 have steep apparent age gradients within 200μm of the grain edge (figure 5.16 e to i). Apparent ages in all profiles range from 2.45 - 1.8Ga.

Fe-suite - Profiles that display apparent ages not less than 2.3Ga with broadly flat-lying trends and/or scattered data.

Samples SS22 (beryl pegmatite), 93-276 (petalite subtype pegmatite) and 96-81 (beryl type pegmatite) are defined by relatively limited variations in apparent ages. Two profiles are presented from samples SS22 and 93-276, measured on single grains (figure 5.16l, m, n, o). Profile B from SS22 and profile A from 93-276 have broadly flat-lying trends with apparent ages between 2.45 - 2.35Ga. Data from SS22 - profile C and 93-276 - profile B are more scattered with apparent ages between 2.45 - 2.3Ga. A single profile from pegmatite 96-81 also displays relatively limited apparent age variation, in the range 2.45 - 2.3Ga. Sample SS35b (Separation Rapids pluton) is an exception to this pattern which displays apparent ages in the range 2.4 - 2.15Ga and 2.4 - 1.75Ga for profile A and B, respectively (figure 5.16q, r).

- *Graphic Lake pegmatite (Figure 5.17a)*

The Graphic Lake pegmatite is a barren granitic pegmatite. A single profile measured on mica sample SS89 has apparent ages in the range 2.6 - 2.3Ga, supplemented by a grain core spot analysis of 2.67Ga. The majority of analyses fall within the 2.4 - 2.5Ga range. Although there is some scatter to the data, there is a dominant trend of gradually decreasing apparent ages towards the grain edge (figure 5.17a).

- *Ghost Lake batholith and Mavis Lake group pegmatites (Figure 5.17)*

The peraluminous, S-type Ghost Lake batholith comprises eight internal units, from relatively primitive cordierite-biotite granite to evolved pegmatitic leucogranite. Spatially and chemically associated with the Ghost Lake batholith is a zone of rare-element pegmatites termed the Mavis Lake group pegmatites, which includes the albite - spodumene-type Fairservice pegmatite #1 (Breaks and Moore 1992).

Two profiles are presented for the Ghost Lake batholith and one profile from Fairservice pegmatite #1 (figure 5.17b, c, d). All profiles display apparent ages lying within the 2.6 - 2.3Ga range. Sample SS50a is taken from an intra-granitic pegmatite within the Ghost Lake batholith; the profile shows gradually decreasing ages towards

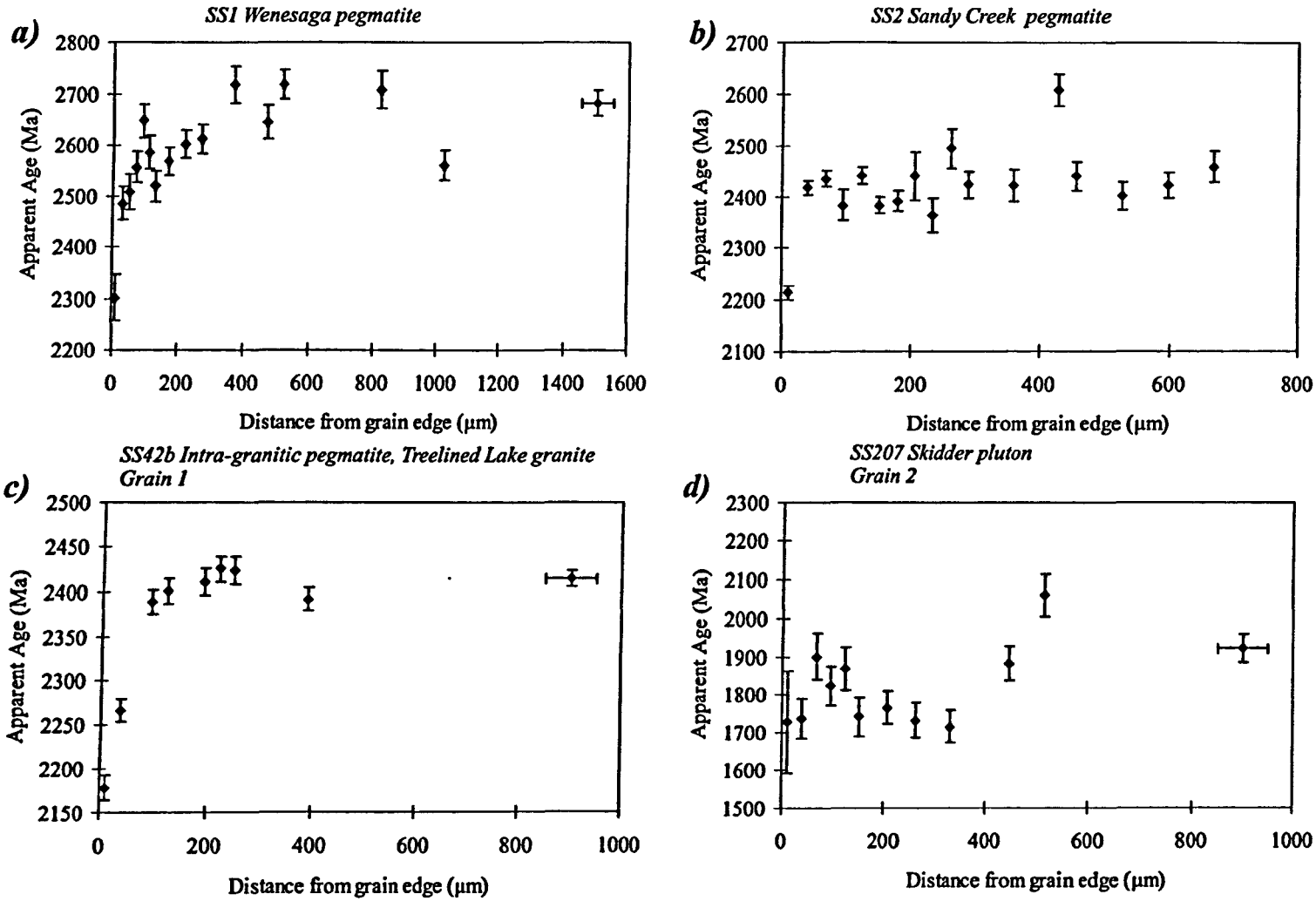

Figure 5.15 $^{40}Ar/^{39}Ar$ apparent age profiles from rare-element pegmatites in the western Superior Province. Vertical error bars represent 1 sigma age uncertainty, horizontal bars indicate width of ablation pit.

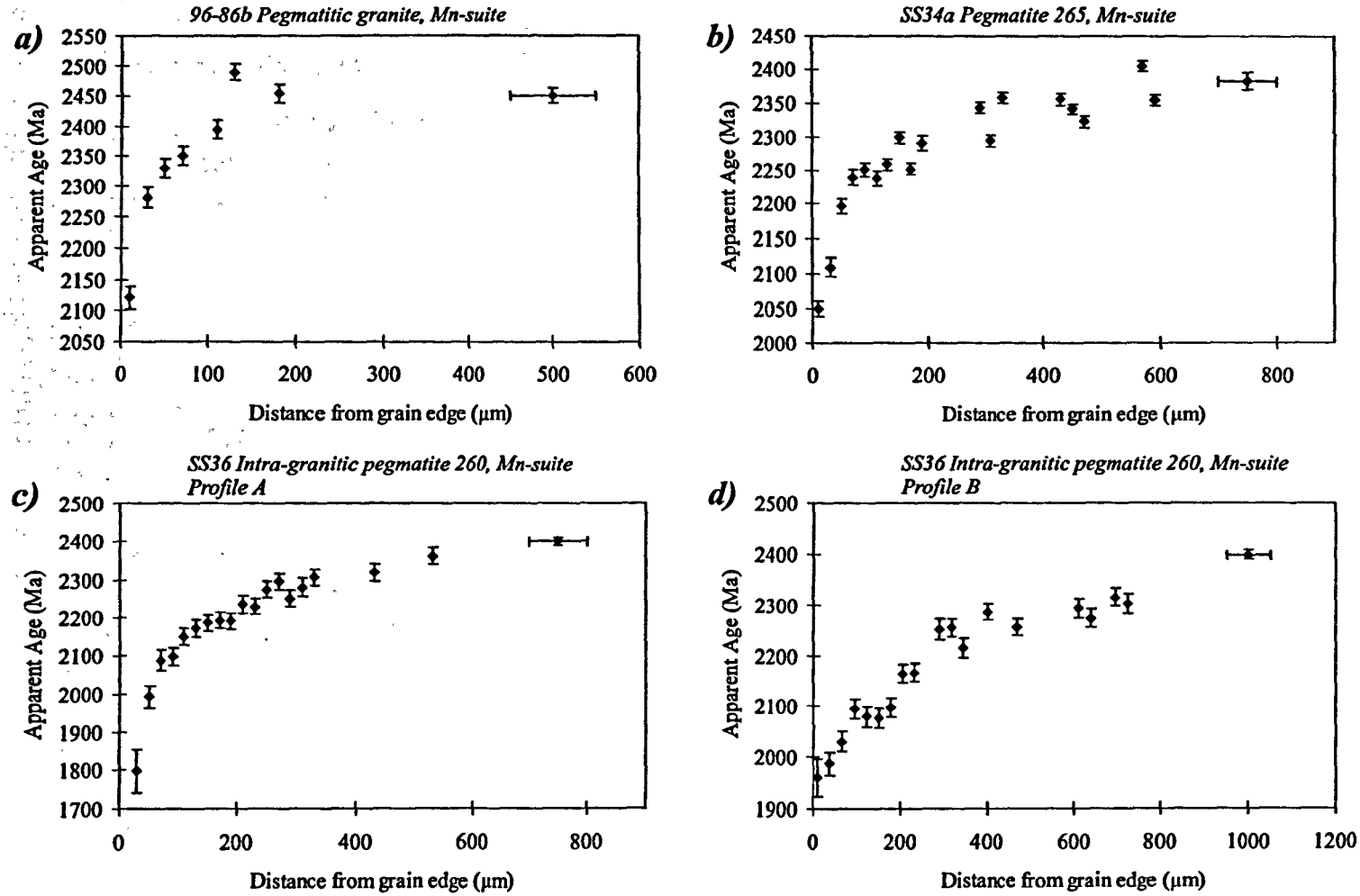

Figure 5.16 $^{40}Ar/^{39}Ar$ apparent age profiles from the Separation Rapids group rare-element pegmatites in the western Superior Province. Vertical error bars represent 1 sigma age uncertainty, horizontal bars indicate width of ablation pit.

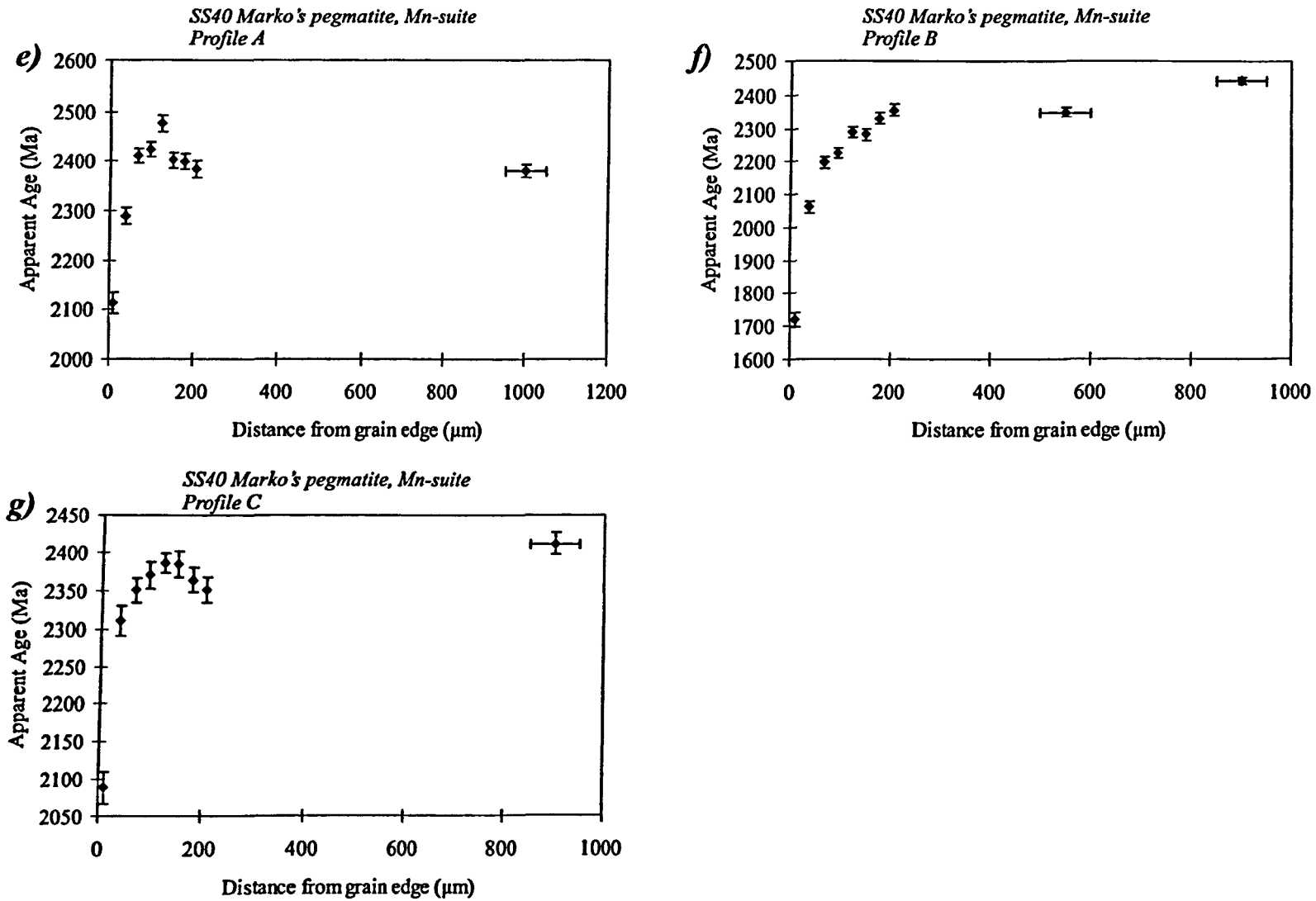

Figure 5.16 continued, $^{40}Ar/^{39}Ar$ apparent age profiles from the Separation Rapids group rare-element pegmatites in the western Superior Province. Vertical error bars represent 1 sigma age uncertainty, horizontal bars indicate width of ablation pit.

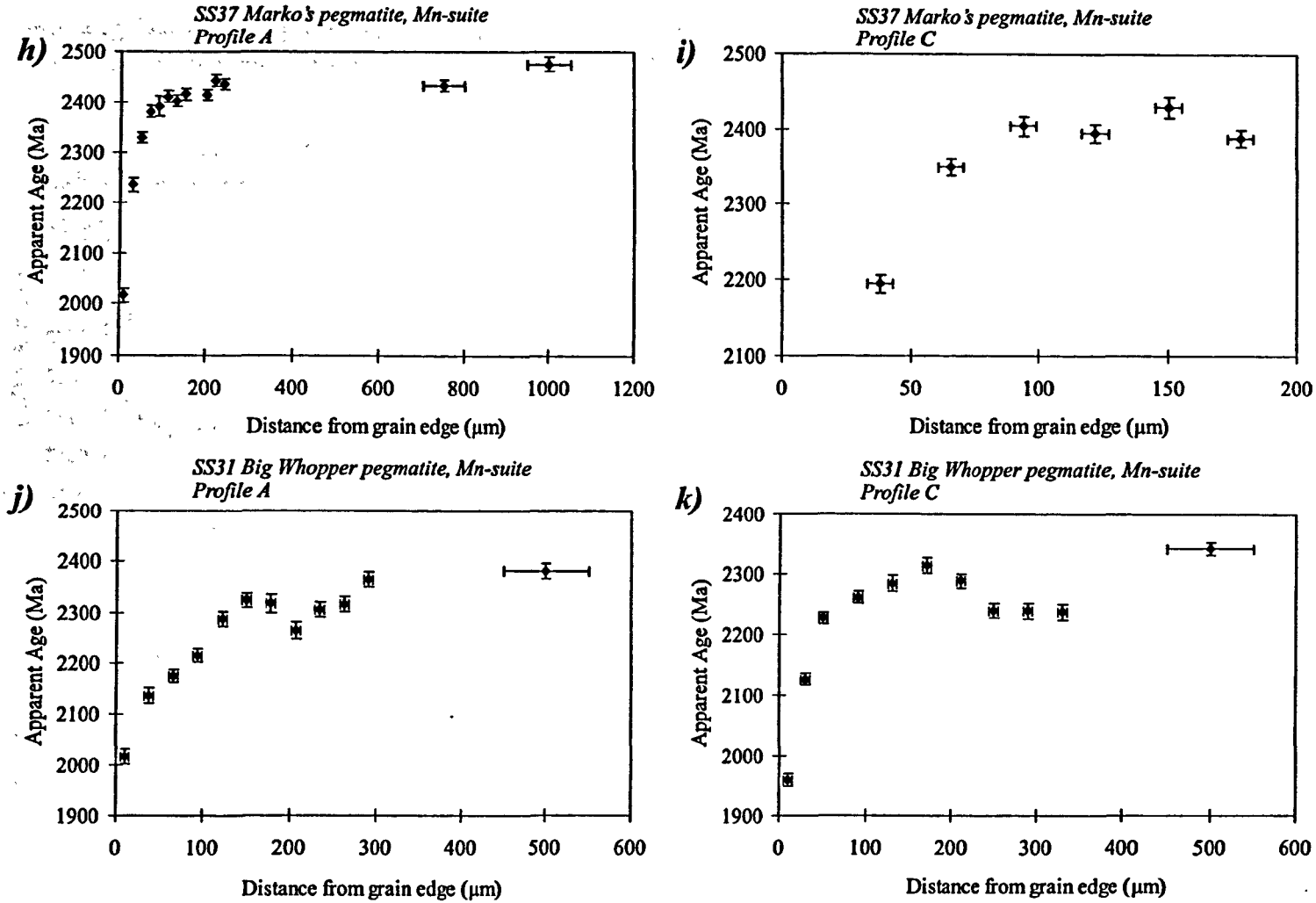

Figure 5.16 continued, $^{40}Ar/^{39}Ar$ apparent age profiles from the Separation Rapids group rare-element pegmatites in the western Superior Province. Vertical error bars represent 1 sigma age uncertainty, horizontal bars indicate width of ablation pit.

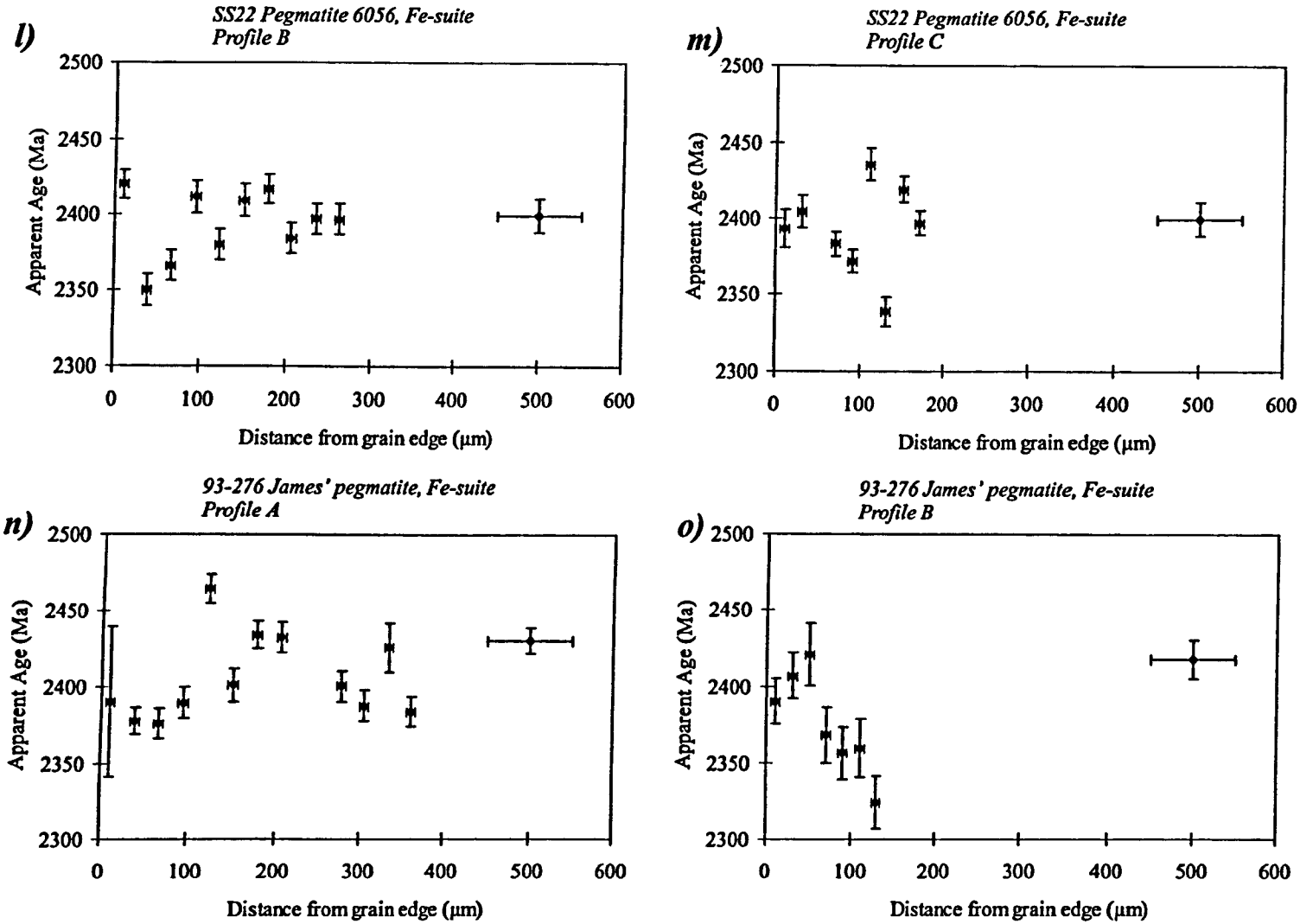

Figure 5.16 continued, $^{40}Ar/^{39}Ar$ apparent age profiles from the Separation Rapids group rare-element pegmatites in the western Superior Province. Vertical error bars represent 1 sigma age uncertainty, horizontal bars indicate width of ablation pit.

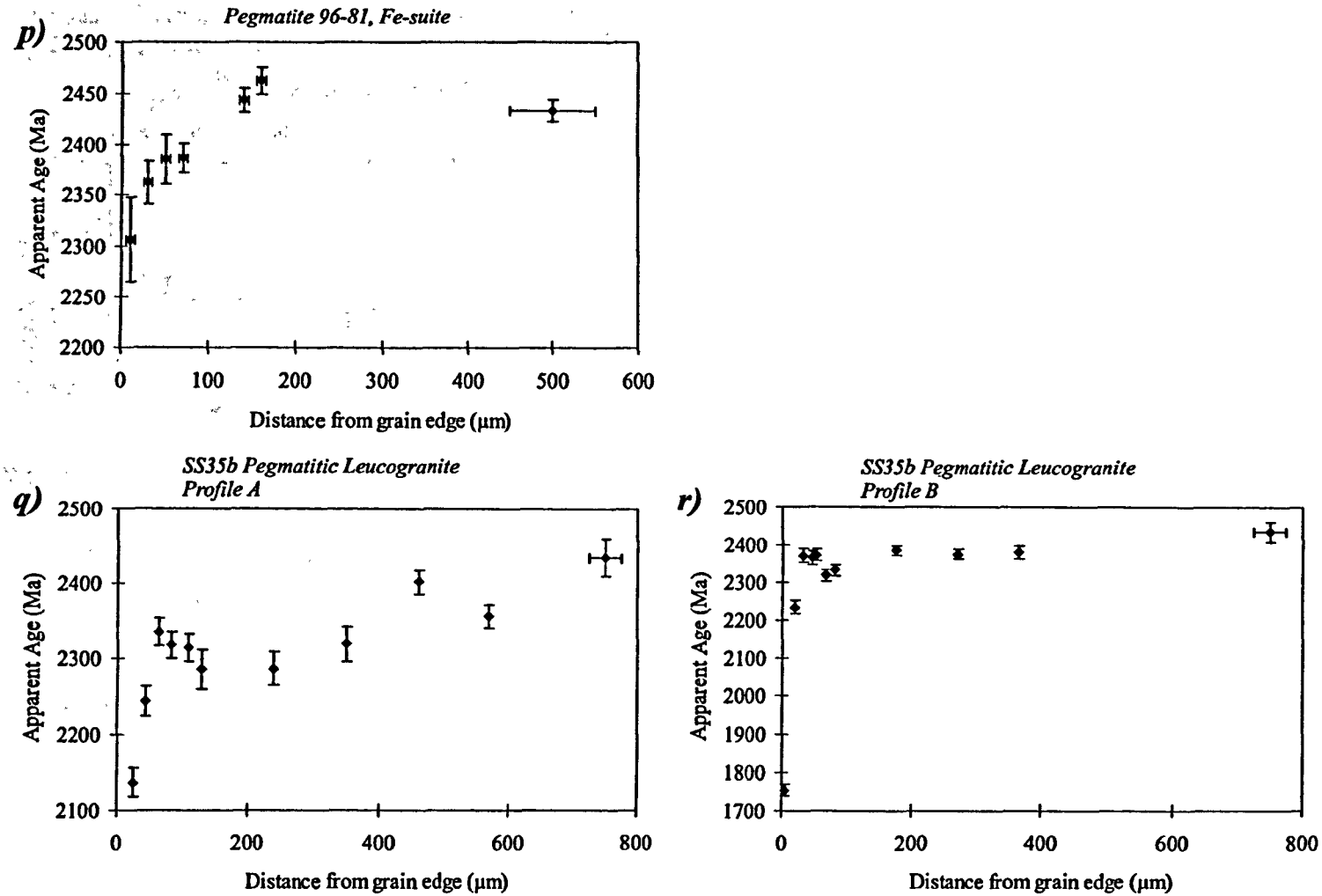

Figure 5.16 continued, $^{40}Ar/^{39}Ar$ apparent age profiles from the Separation Rapids group rare-element pegmatites in the western Superior Province. Vertical error bars represent 1 sigma age uncertainty, horizontal bars indicate width of ablation pit.

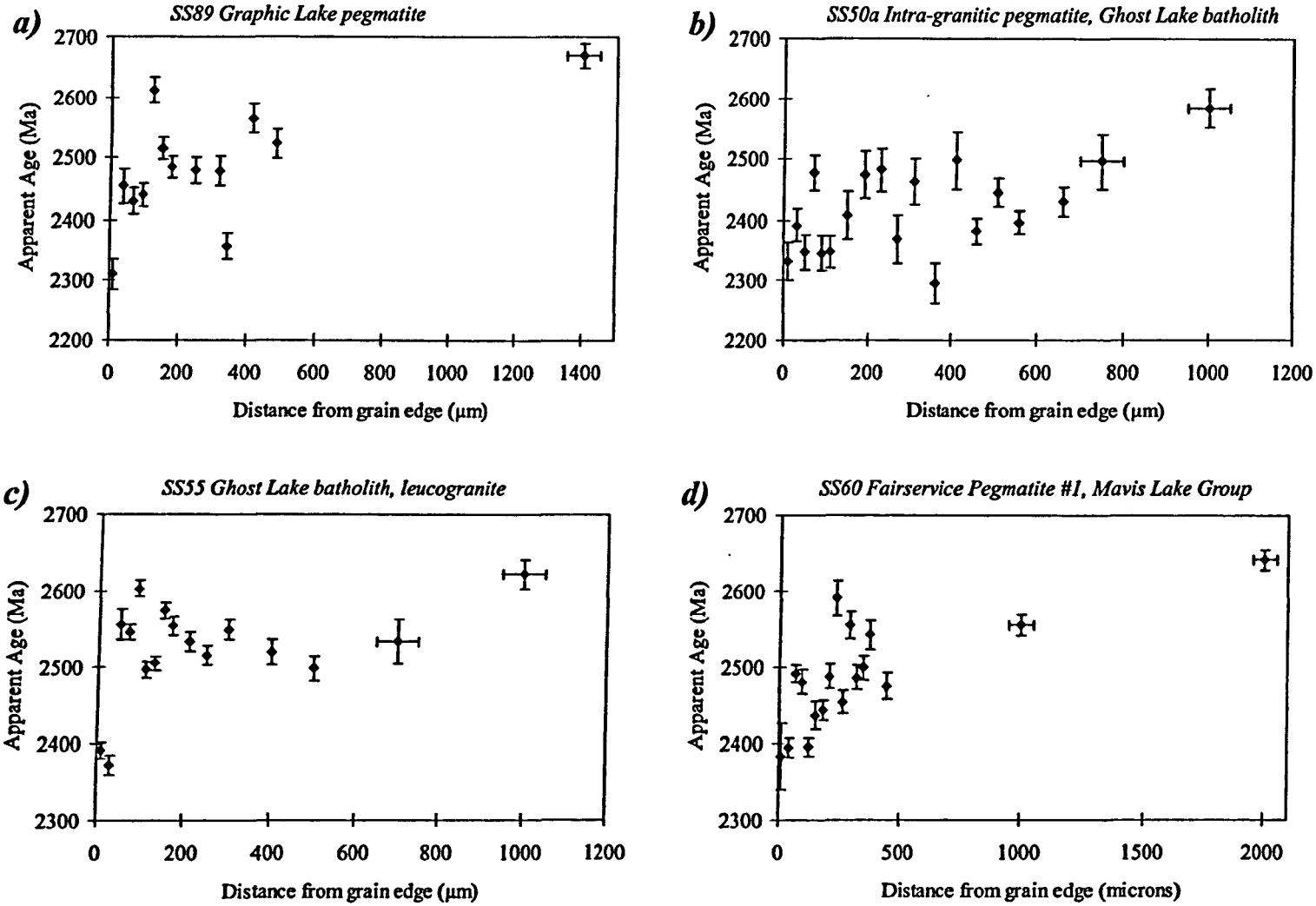

Figure 5.17 $^{40}Ar/^{39}Ar$ apparent age profiles from rare-element pegmatites in the western Superior Province. Vertical error bars represent 1 sigma age uncertainty, horizontal bars indicate width of ablation pit.

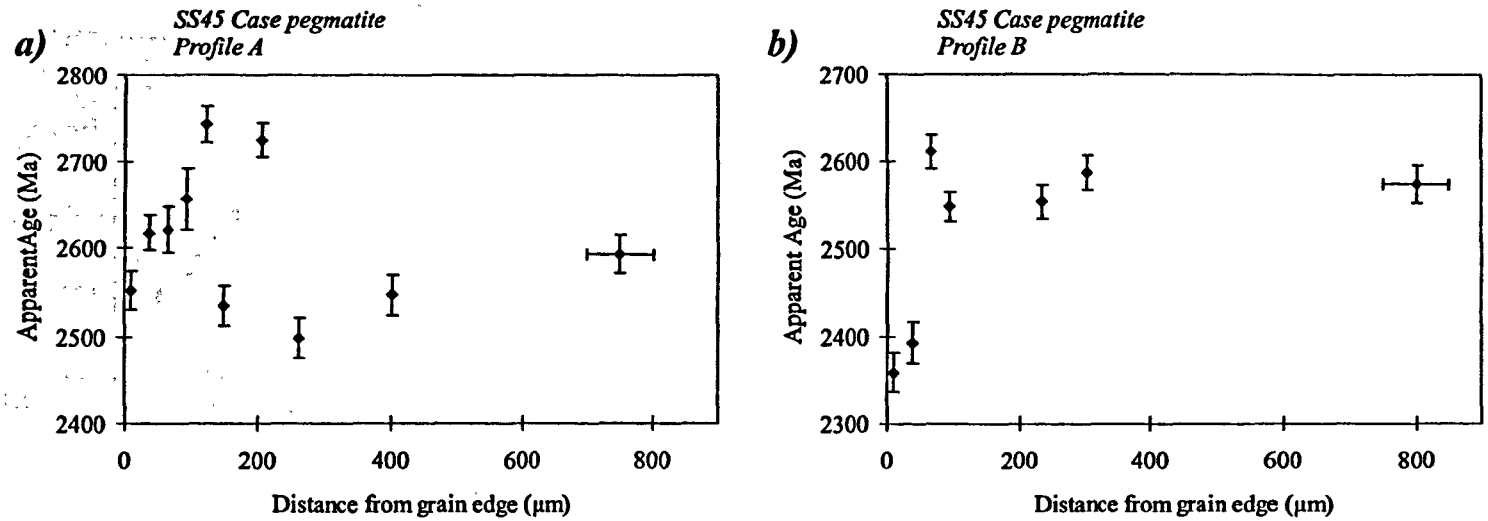

Figure 5.18 $^{40}Ar/^{39}Ar$ apparent age profiles from the Case pegmatite in the southern Superior Province. Vertical error bars represent 1 sigma age uncertainty, horizontal bars indicate width of ablation pit.

the grain edge although there is considerable scatter within the 2.5 - 2.3Ga range (figure 5.17b).

The apparent age profile for the pegmatitic leucogranite unit (GLB-7) of the Ghost Lake batholith (sample SS55) has a stepped pattern with younger ages only at the very edge of the grain (figure 5.17c). Apparent ages between 2.6 - 2.5Ga dominate the profile, offset by younger ages (2.4Ga) at the grain edge.

Sample SS60 is from Fairservice pegmatite #1 within the spodumene - beryl - tantalite zone of the Mavis Lake Group, located approximately 3.5km SE of the Ghost Lake batholith. Decreasing apparent ages between 2.6 - 2.4Ga, mostly occurs within 500μm of the grain edge (figure 5.17d).

5.4.3 Southern Superior Province

- *Case pegmatite (Figure 5.18)*

This is an albite - spodumene type pegmatite located at the boundary between the northern and southern Abitibi greenstone belt. Two profiles were measured on a single grain from sample SS45; apparent ages fall in the range 2.75 - 2.35Ga. Profile B has a relatively well defined trend to the data with 2.6Ga ages over much of the profile falling to gradually younger ages (2.4Ga) at the grain edge.

5.4.4 Summary

Hodges *et al.* (1994), and Hodges and Bowring (1995) were among the first to document large intragrain $^{40}Ar/^{39}Ar$ apparent age variations in mica using a laser microprobe. In their study of the 1700Ma (U-Pb zircon) Crazy Basin monzogranite in Arizona, laser spot ages of muscovite ranged from 1650 ± 10Ma to 1270 ± 10Ma, with a broadly concentric zoning of ages (oldest in the centre of the grain). Hodges and Bowring (1995) attributed the 300 - 400Ma age variations in mica to slow cooling of the host terrain.

This study has found intragrain age variations that are comparable to and even exceed those shown by Hodges *et al.* (1994), and Hodges and Bowring (1995). Apparent age profiles from white micas within peraluminous granites and rare-element pegmatites of the Superior Province display $^{40}Ar/^{39}Ar$ intragrain age variations commonly >400Ma and in some cases up to 800Ma (sample SS73, Severn River

pluton). It is difficult to reconcile an 800Ma age variation within a single mica crystal with a simple slow cooling model, since this would require an extremely stable crust. Importantly, the high spatial resolution of the UV-laser microprobe (10-15μm beam diameter), has made it possible to compare measured profiles with theoretical thermal histories using the DIFFARG program (Wheeler 1996).

Distinctive patterns emerge from apparent age profiles of micas within and between different pegmatite suites that require an explanation in terms of thermal history or otherwise (i.e. chemical variation). Most notably, apparent age profiles from pegmatites throughout much of the Superior Province have apparent ages in the range 2.8 - 1.8Ga. In contrast, those pegmatites located along the southern boundary of the English River Subprovince and in the adjacent Separation Rapids greenstone belt have maximum apparent ages of 2.45Ga. This is best displayed in the cumulative frequency plot of all $^{40}Ar/^{39}Ar$ data measured in this study (figure 5.19). Mica ages from the Separation Lake area have a skewed population with an abrupt cut-off at 2.45Ga, whereas mica from all other regions analysed exhibit a symmetrical population with a peak at 2.6Ga and a tail of ages down to 1.8Ga.

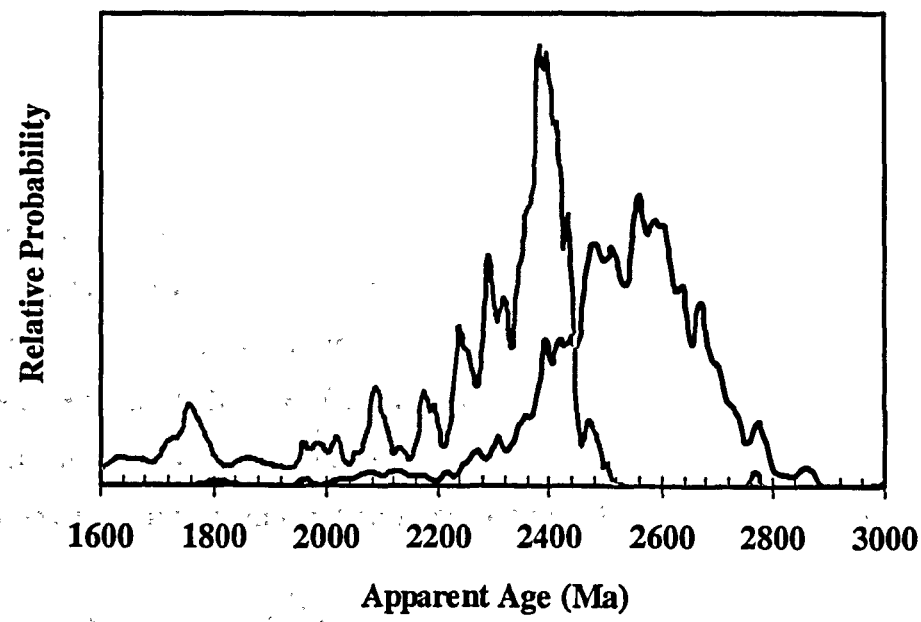

Figure 5.19 Cumulative frequency of $^{40}Ar/^{39}Ar$ apparent ages from the Separation Lake area (light grey line) and all other samples analysed (black line).

5.5 Thermochronology models using DIFFARG; slow cooling or episodic re-heating?

DIFFARG (Wheeler 1996) is a computer program, written in the Matlab 4.1 interpreted language, which uses a finite difference algorithm to simulate argon diffusion profiles. The user is able to define any linear thermal history e.g. temperature decrease with time to simulate slow cooling or a temperature pulse to simulate re-heating. Known parameters such as mineral species and grain size must also be specified. DIFFARG calculates the spatial concentration of radiogenic argon ($^{40}Ar^*$) within a given mineral, which is presented in graphical form showing the relationship between apparent age and distance from the grain boundary. In this way, the program is especially useful for interpreting $^{40}Ar/^{39}Ar$ profiles measured with the UV laser microprobe. Numerical models can be compared to measured data, which permits the user to model quantitative constraints on the T-t history of specific diffusion profiles.

It should be noted that diffusion parameters of muscovite are poorly constrained because of the narrow temperature range (~600 - 700°C) over which it is possible to experimentally measure argon diffusion in muscovite (McDougall and Harrison 1999). The observation that muscovite often yields older apparent ages than biotite in slowly cooled rocks has led to an ascribed 'nominal' closure temperature of 350°C for muscovite (Hames and Bowring 1994). However, in terrains that have undergone a complex (re-heated) or prolonged (slow cooling) thermal history, argon is effectively retained in the centre of the crystal at higher temperatures than at the grain boundary. In this case, single mineral grains exhibit a range of closure temperatures from core to rim.

Thermal pulses can be modelled using DIFFARG. In the simplest form of this case, the modelled temperature rises instantaneously to the thermal maximum and held at this temperature for a specified duration before instantaneously falling back to zero. Such 'flat top' thermal pulses are unlikely to occur in nature and more probably display a gaussian profile with temperatures rising exponentially over time to a thermal peak and then decreases exponentially back to zero. Similarly, cooling rates are assumed to vary linearly with time, whereas they are more realistically hyperbolic. These simplifications of geological processes are a reminder of the limitations of theoretical modelling, but the results from DIFFARG are surprisingly robust because of the logarithmic behaviour of diffusion. Therefore, DIFFARG provides a useful way to

interpret the general features of the apparent age profiles and to distinguish between slow cooling and episodic re-heating.

5.5.1 Results from DIFFARG modelling

In fitting a hypothetical thermal history to an apparent age profile measured on the UV laser microprobe, an empirical approach was followed. The ages of thermal events modelled are constrained by the apparent age profiles, although knowledge of any regional geological events is extremely valuable in the process of determining a T-t history from an apparent age profile. Proterozoic events surrounding and affecting the Superior Province are listed in section 1.5.

Sample SS70 (Severn River pegmatite) is a good example of a well defined profile and is characteristic of many of the apparent age profiles measured in this study. Initially, hypothetical thermal histories involving slow cooling from the emplacement age were considered (figure 5.20a). However, it is apparent that even extreme rates of slow cooling (e.g. 0.5°C/Ma) cannot account for the variation in $^{40}Ar/^{39}Ar$ apparent age.

Figure 5.20b shows hypothetical thermal histories that include discrete re-heating events coincident with some of the major Proterozoic events affecting the Superior Province. None of these theoretical profiles fits the measured data, which is very steep within 200μm of the grain boundary. However, there are two models that match with at least part of the profile. Thermal history 1 (TH1) models re-heating at 2450Ma and Thermal history 2 (TH2) models re-heating at 1850Ma. Incorporating these two events into a single theoretical thermal history model produces an almost perfect fit to the apparent age profile (Figure 5.21a). Importantly, the second event must be of a lower temperature than the first in order that the first event is not completely 'overprinted'. Varying the temperature and duration of the older re-heating event (TH5, TH6, TH7) can account for most of the scatter in the data. However, plotting the first 300μm from the grain edge in detail reveals that these theoretical profiles provide only a broad approximation to the intricacies of the apparent age profile (figure 5.21b). Variations in the profile gradient such as the 'local plateau' corresponding with an apparent age of 2.45Ga and anomalous data points are not accounted for by these hypothetical thermal history models. In particular, two measurements that fall below the local plateau may result from defects in the crystal that have lost argon via short-circuit diffusion (see figure 5.5).

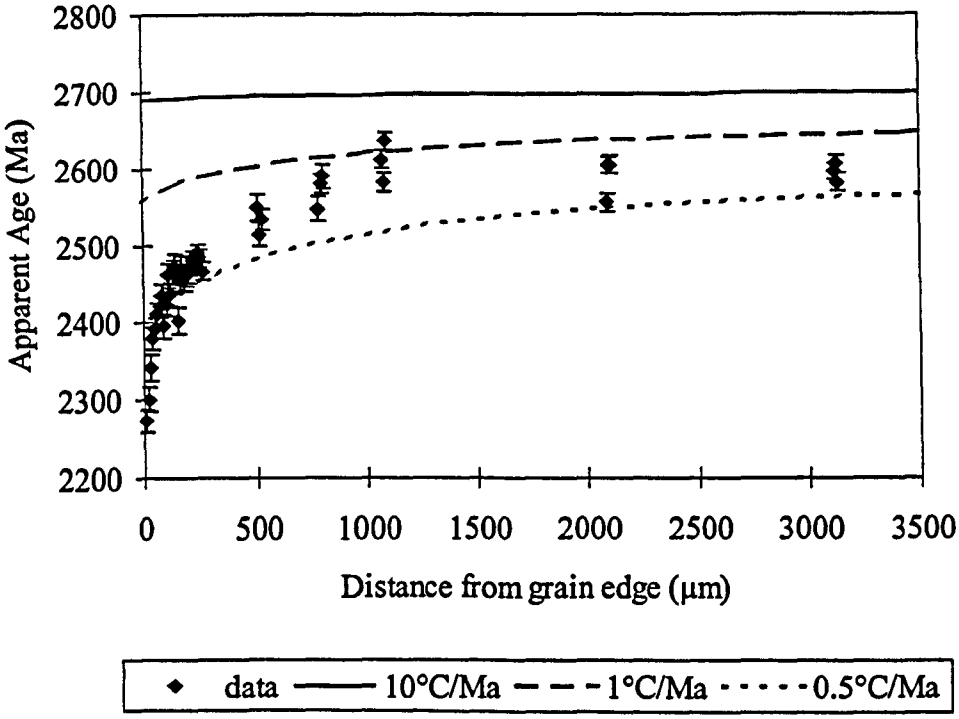

Figure 5.20a Apparent age profile with theoretical slow cooling models for sample SS70 (Severn River pegmatite).

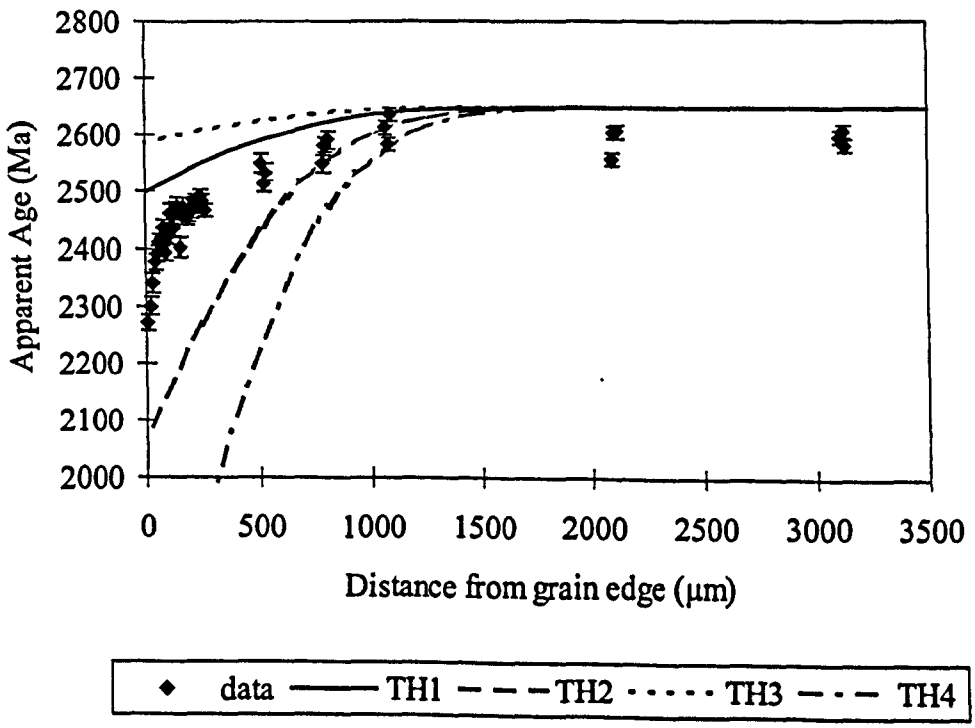

Figure 5.20b Apparent age profile with theoretical re-heating models for sample SS70 (Severn River pegmatite).
Thermal History 1 : 450°C pulse, 2450 - 2440Ma;, Matachewan-Hearst dyke swarm.
Thermal History 2 : 450°C pulse, 1850 - 1840Ma;, Trans-Hudson orogeny.
Thermal History 3 : 450°C pulse, 2570 - 2560Ma;, brittle faulting in Western SP.
Thermal History 4 : 450°C pulse, 2100 - 2090Ma;, Nipigon dyke swarm.

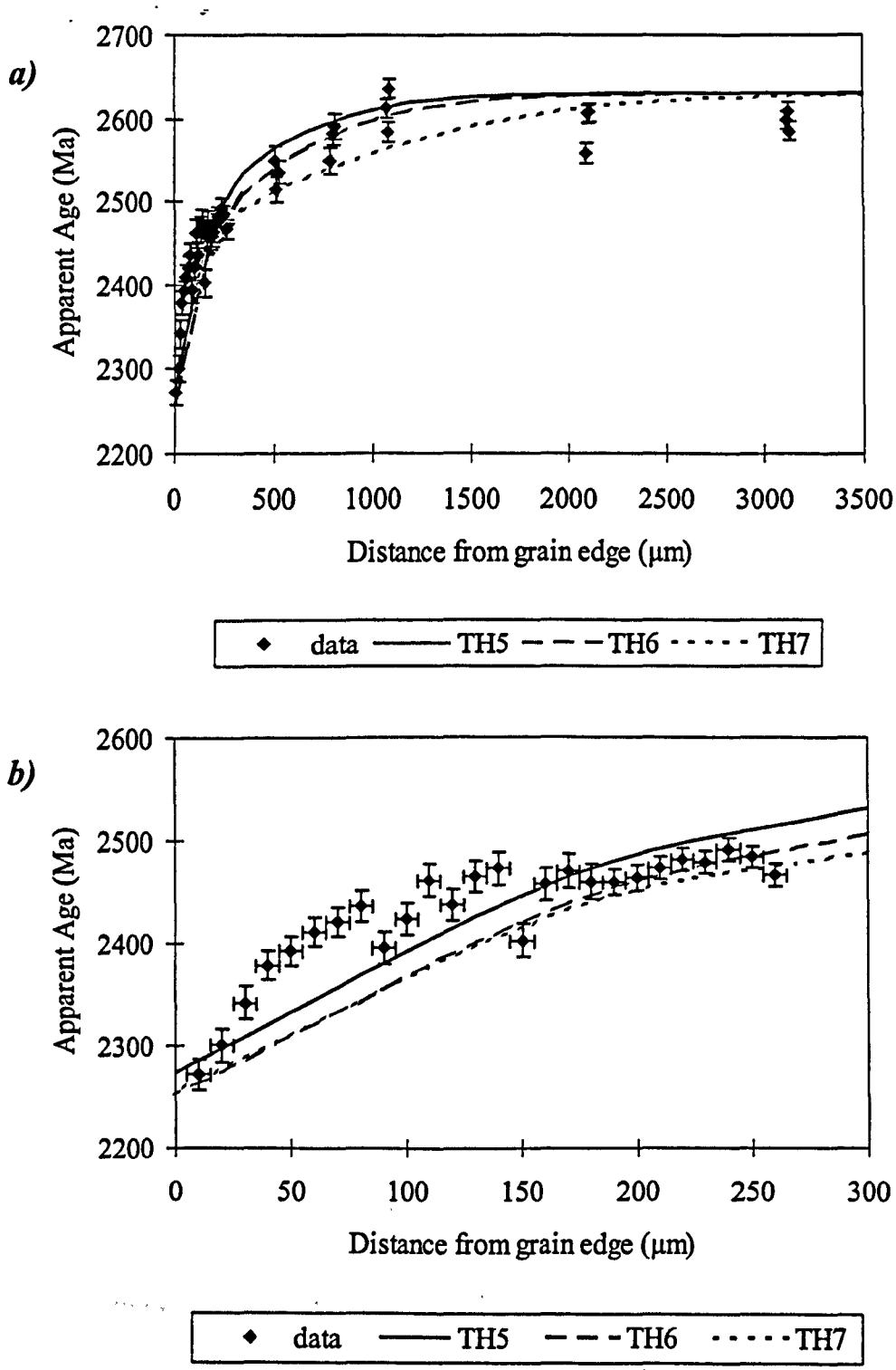

Figure 5.21 Apparent age profile with theoretical models for sample SS70 (Severn River pegmatite), (a) full profile; (b) first 300μm of the same profile in detail.

Thermal History 5 : 450°C pulse, 2450 - 2440Ma; 400°C pulse, 1850 - 1840Ma

Thermal History 6 : 425°C pulse, 2450 - 2400Ma; 400°C pulse, 1850 - 1840Ma

Thermal History 7 : 475°C pulse, 2450 - 2440Ma; 400°C pulse, 1850 - 1840Ma

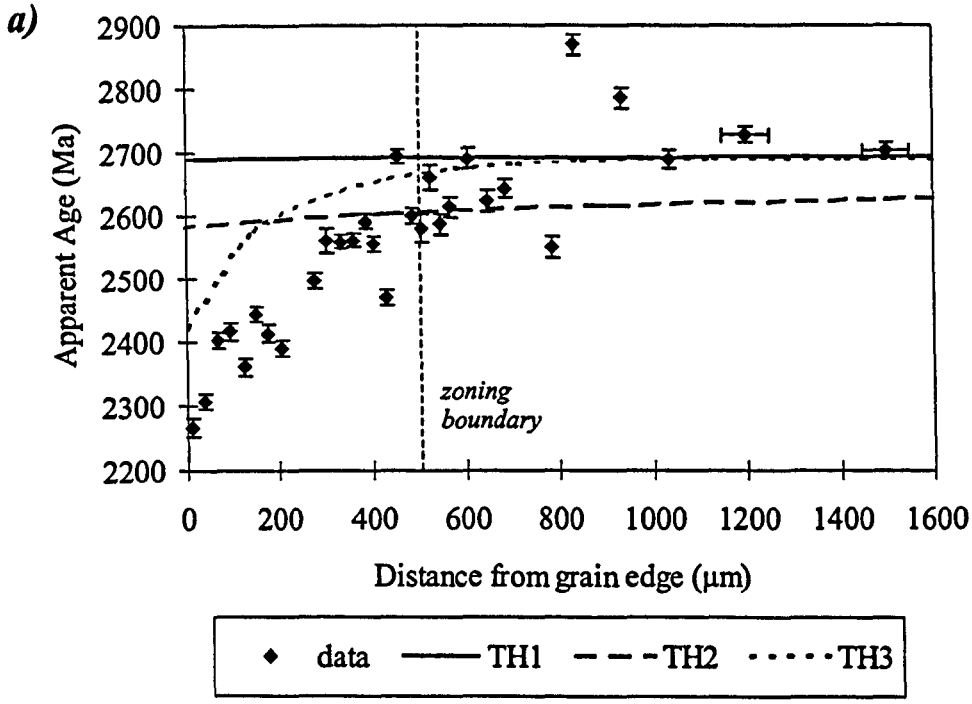

Figure 5.22a Apparent age profile with theoretical models for sample SS20 (Pakeagama Lake pegmatite).
Thermal History 1 : 10°C/Ma slow cooling
Thermal History 2 : 1°C/Ma slow cooling
Thermal History 3 : 425°C pulse, 2450 - 2440Ma; 375°C pulse, 1850 - 1840Ma

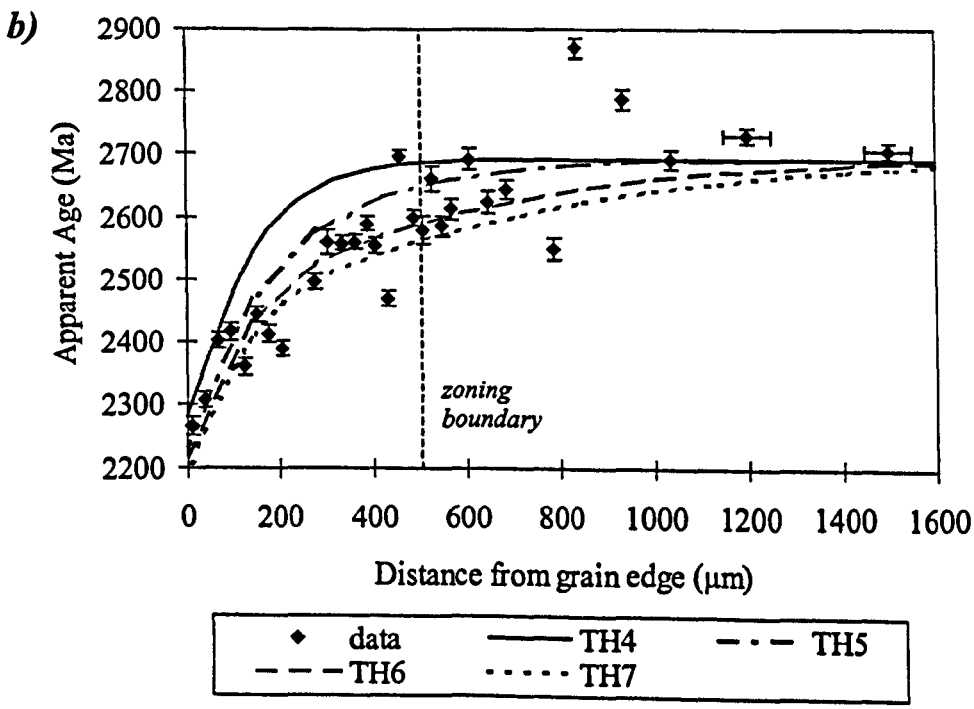

Figure 5.22b Apparent age profile with theoretical models for sample SS20 (Pakeagama Lake pegmatite).
Thermal History 4 : 400°C pulse, 2450 - 2440Ma; 400°C pulse, 1850 - 1840Ma
Thermal History 5 : 400°C pulse, 2450 - 2400Ma; 400°C pulse, 1850 - 1840Ma
Thermal History 6 : 450°C pulse, 2450 - 2440Ma; 400°C pulse, 1850 - 1840Ma
Thermal History 7 : 425°C pulse, 2450 - 2400Ma; 400°C pulse, 1850 - 1840Ma

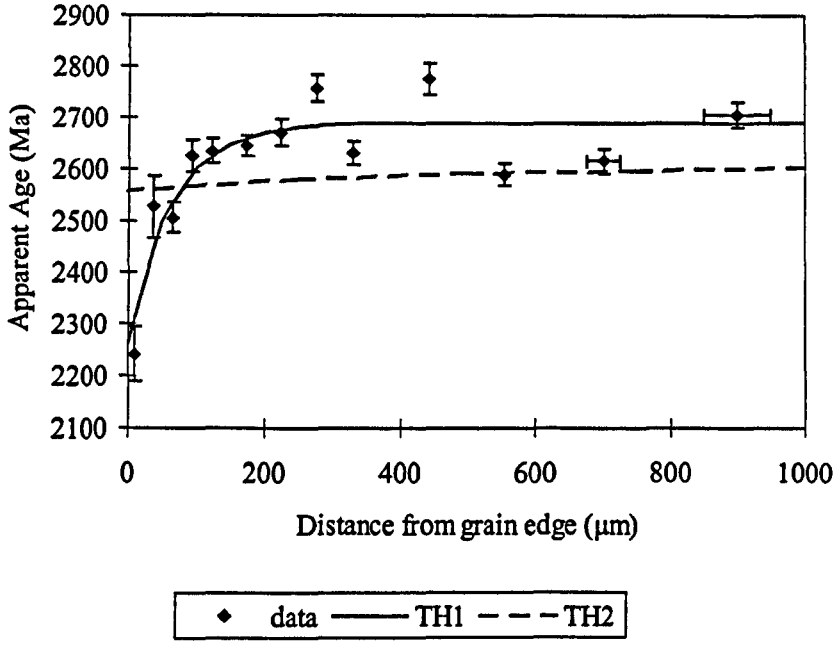

Figure 5.23 Apparent age profile A with theoretical models for sample SS106a (Pakeagama Lake pegmatite).
Thermal History 1 : 400°C pulse, 2450 - 2440Ma; 375°C pulse, 1850 - 1840Ma
Thermal History 2 : 1°C/Ma slow cooling

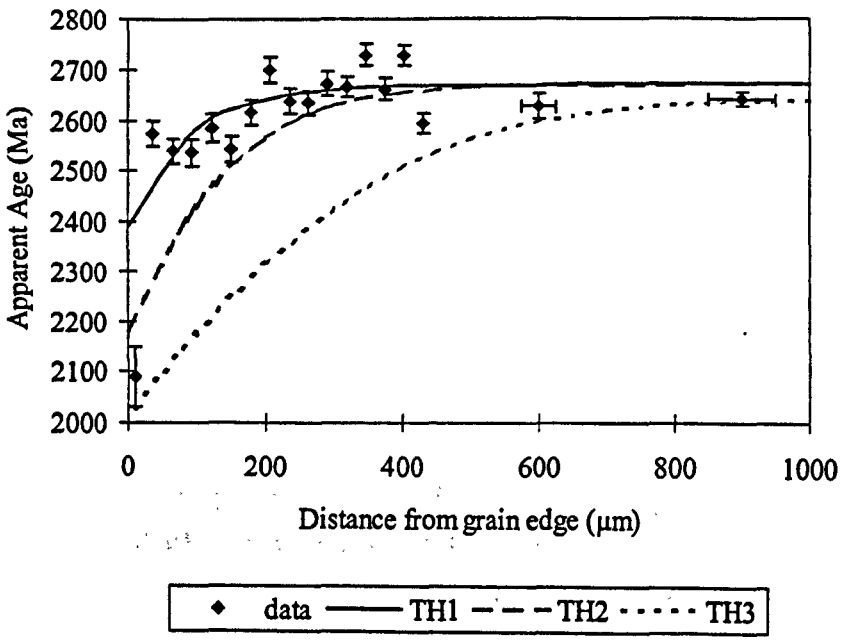

Figure 5.24 Apparent age profile with theoretical models for sample SS107 (Pakeagama Lake pegmatite).
Thermal History 1 : 400°C pulse, 2450 - 2440Ma; 375°C pulse, 1850 - 1840Ma
Thermal History 2 : 400°C pulse, 2450 - 2400Ma; 400°C pulse, 1850 - 1840Ma
Thermal History 3 : 400°C pulse, 2450 - 2440Ma; 425°C pulse, 1850 - 1840Ma

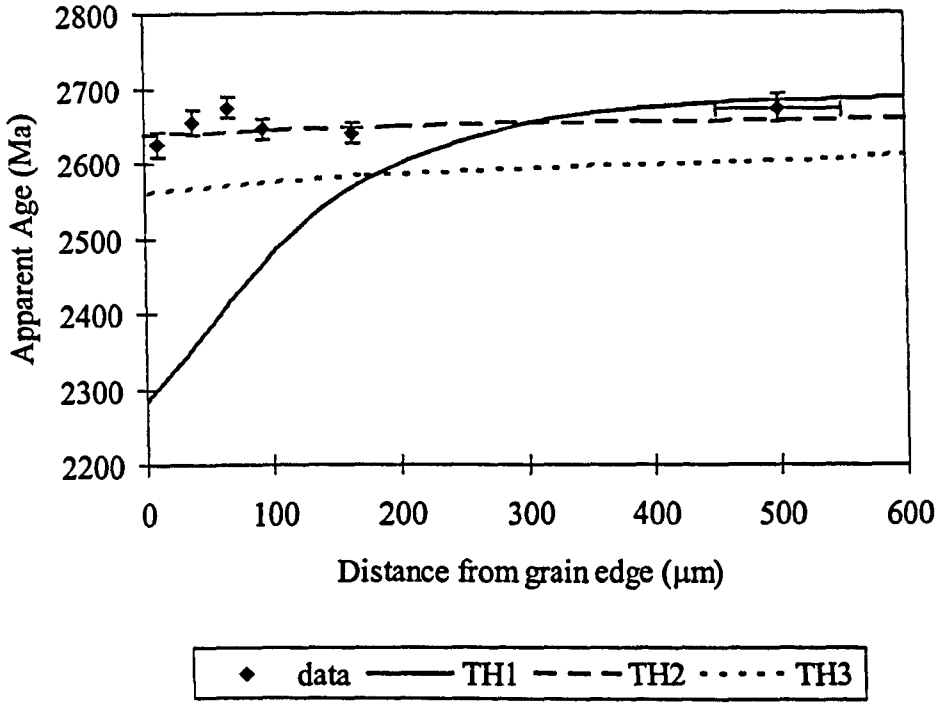

Figure 5.25 Apparent age profile B with theoretical models for sample 98FWB38 (Pakeagama Lake pegmatite).
Thermal History 1 : 400°C pulse, 2450 - 2440Ma; 400°C pulse, 1850 - 1840Ma
Thermal History 2 : 2°C/Ma slow cooling.
Thermal History 3 : 1°C/Ma slow cooling.

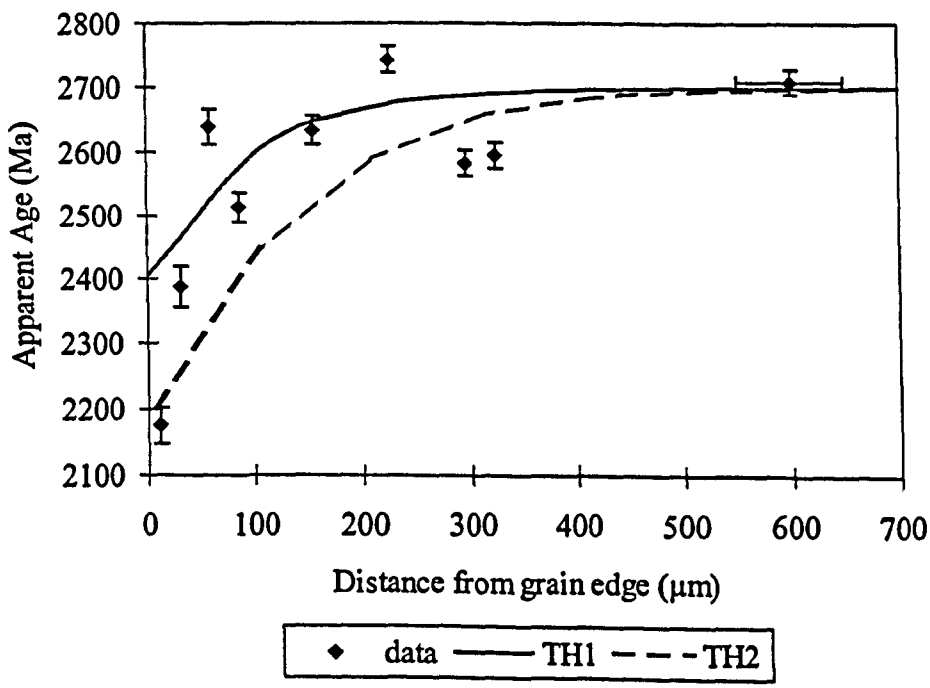

Figure 5.26 Apparent age profile with theoretical models for sample SS111 (Margot Lake pegmatite).
Thermal History 1 : 400°C pulse, 2450 - 2440Ma; 375°C pulse, 1850 - 1840Ma
Thermal History 2 : 400°C pulse, 2450 - 2440Ma; 400°C pulse, 1850 - 1840Ma

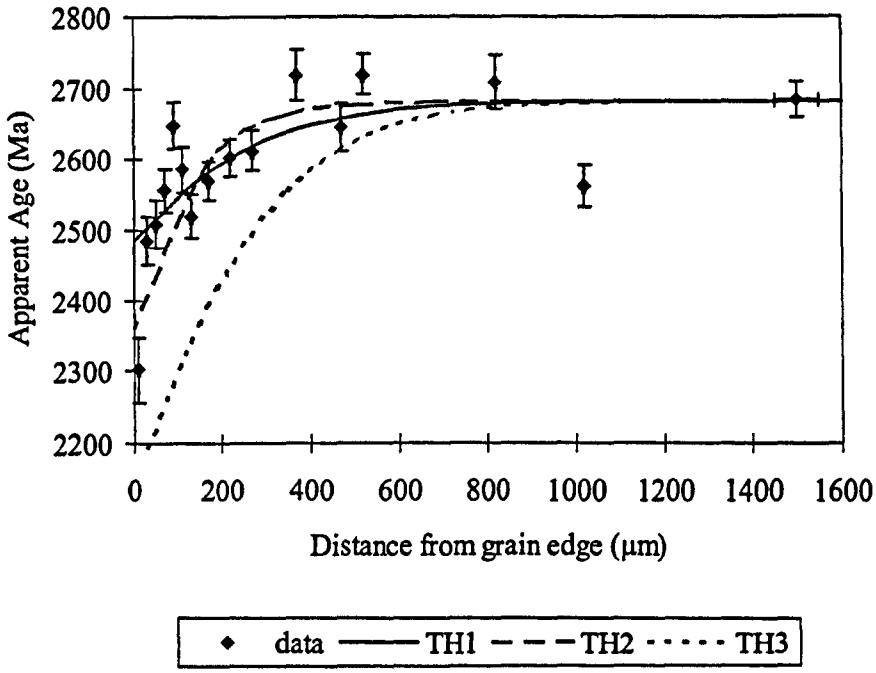

Figure 5.27 Apparent age profile with theoretical models for sample SS1 (Wenesaga pegmatite).
Thermal History 1 : 425°C pulse, 2400 - 2390Ma; 350°C pulse, 1850 - 1840Ma
Thermal History 2 : 400°C pulse, 2450 - 2440Ma; 400°C pulse, 1850 - 1840Ma
Thermal History 3 : 375°C pulse, 2450 - 2440Ma; 425°C pulse, 1850 - 1840Ma

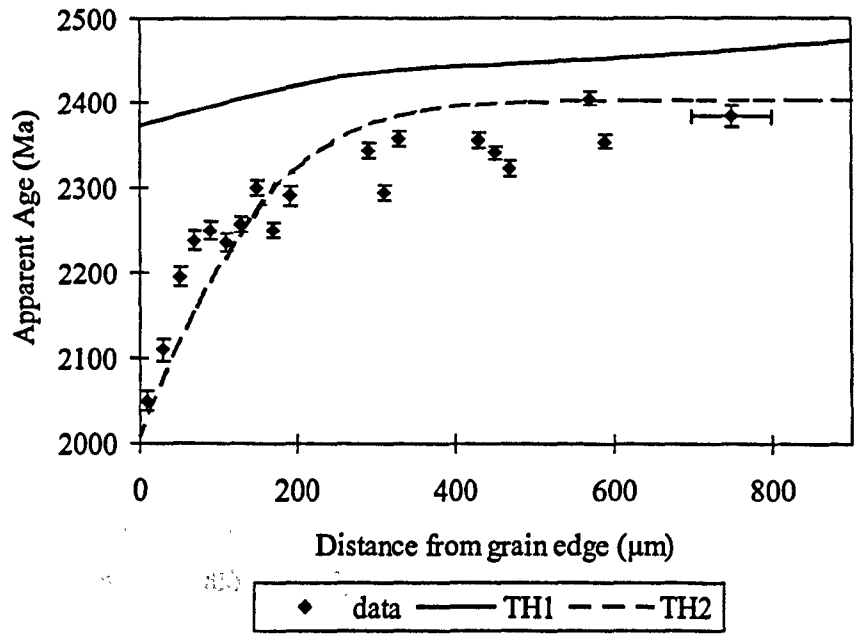

Figure 5.28 Apparent age profile with theoretical models for sample SS34a (Pegmatite 265; Mn-suite, Separation Rapids group).
Thermal History 1 : 450°C pulse, 2450 - 2400Ma; 400°C pulse, 1850 - 1840Ma
Thermal History 2 : 500°C pulse, 2450 - 2400Ma; 400°C pulse, 1850 - 1840Ma

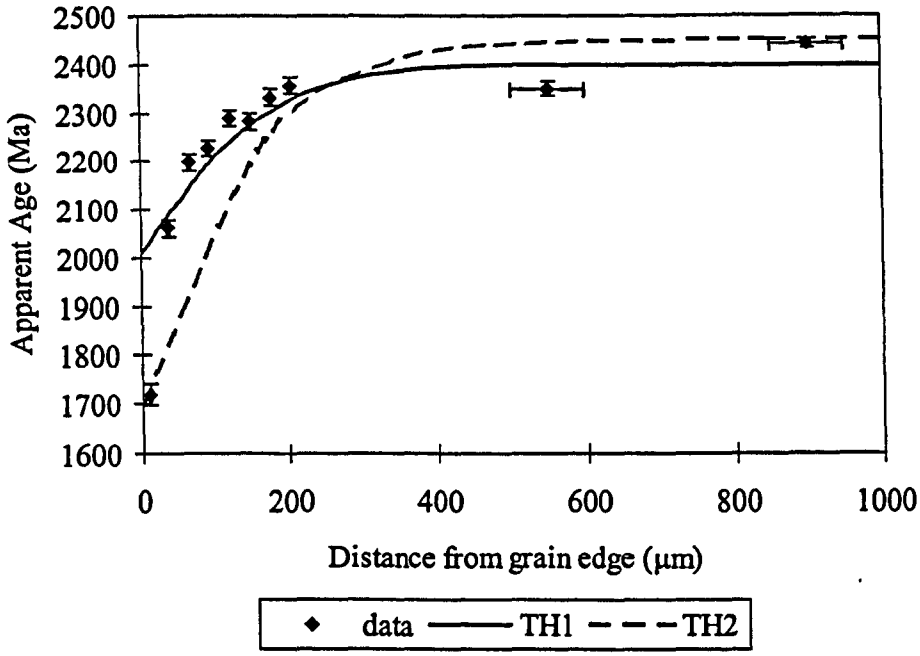

Figure 5.29 Apparent age profile with theoretical models for sample SS40 profile B (Marko's pegmatite; Mn-suite, Separation Rapids group).
Thermal History 1 : 550°C pulse, 2450 - 2400Ma; 400°C pulse, 1850 - 1840Ma
Thermal History 2 : 550°C pulse, 2450 - 2440Ma; 400°C pulse, 1850 - 1840Ma; 400°C pulse, 500 - 490Ma

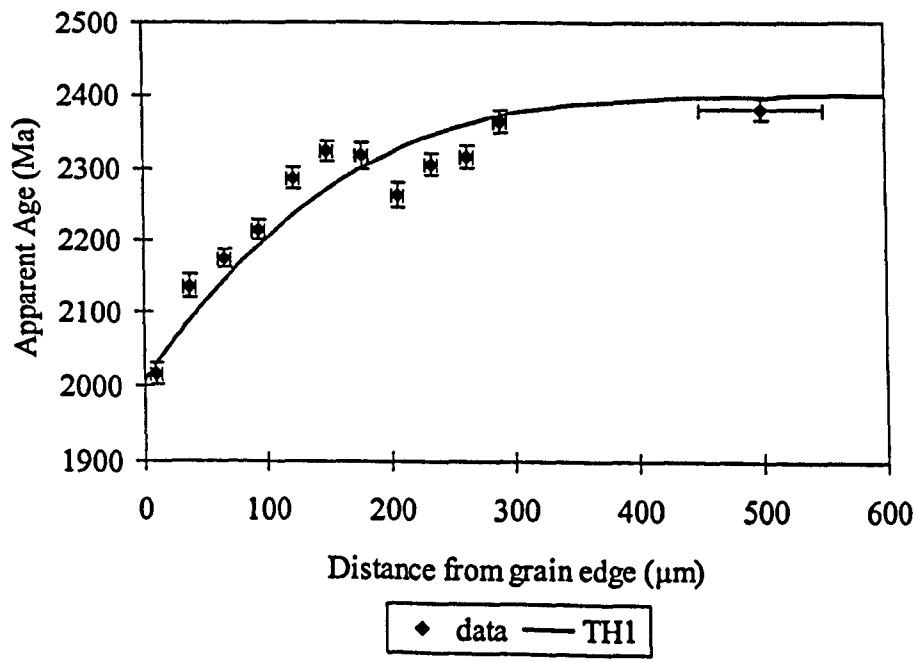

Figure 5.30 Apparent age profile with theoretical models for sample SS31 profile A (Big Whopper Pegmatite; Mn-suite, Separation Rapids group).
Thermal History 1 : 550°C pulse, 2450 - 2400Ma; 400°C pulse, 1850 - 1840Ma

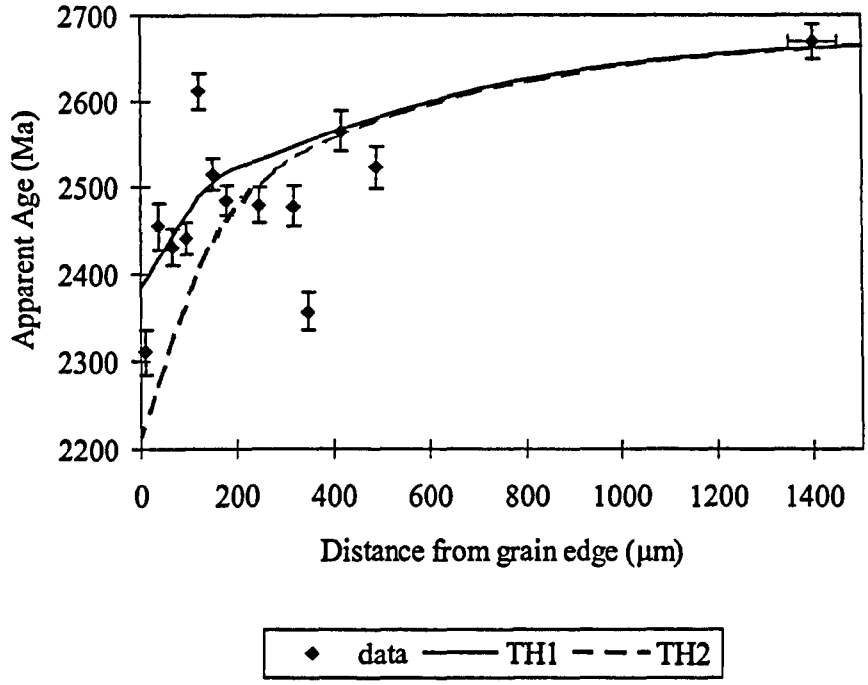

Figure 5.31 Apparent age profile with theoretical models for sample SS89 (Graphic Lake pegmatite).
Thermal History 1 : 450°C pulse, 2450 - 2440Ma; 375°C pulse, 1850 - 1840Ma
Thermal History 2 : 450°C pulse, 2450 - 2440Ma; 400°C pulse, 1850 - 1840Ma

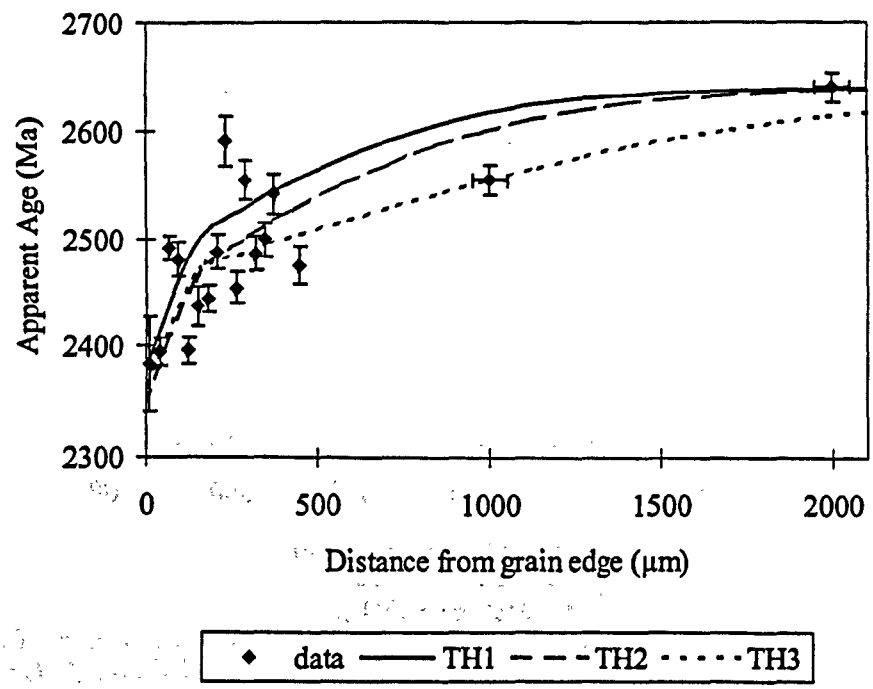

Figure 5.32 Apparent age profile with theoretical models for sample SS60 (Pegmatite #1, Mavis Lake group).
Thermal History 1 : 450°C pulse, 2450 - 2440Ma; 375°C pulse, 1850 - 1840Ma
Thermal History 2 : 425°C pulse, 2450 - 2400Ma; 375°C pulse, 1850 - 1840Ma
Thermal History 3 : 475°C pulse, 2450 - 2440Ma; 375°C pulse, 1850 - 1840Ma

Sample SS20 (Pakeagama Lake pegmatite) also displays a well defined profile of decreasing apparent ages towards the grain edge, although the data is more scattered than SS70. Figure 5.22a shows that slow cooling is again unable to account for the shape of the profile. Modelling of discrete re-heating events at 2450Ma and 1850Ma shows that this is a more likely scenario. However, the theoretical profile is not a perfect match to the data, indicating that either the temperature or duration of the re-heating must have been greater than in thermal history 3. Figure 5.22b shows four thermal histories with varying temperatures and duration for the 2450Ma event. Scatter amongst the data precludes determination of the exact temperature and duration of the re-heating events, although modelling suggests that it was between 400 - 450°C and lasted for a period of 10 - 50Ma.

Figure 5.23 shows that a hypothetical thermal history including discrete re-heating events at 2450Ma and 1850Ma that can largely account for the apparent age profile A from sample SS106a (Pakeagama Lake pegmatite). Samples SS107 and 98FWB38 display quite different apparent age profiles from other samples in the Pakeagama Lake suite that are not matched by re-heating models. Figure 5.24 shows a single measurement at the grain edge of SS107, which is much younger than apparent ages in the rest of the profile and is difficult to fit into theoretical profiles. Similarly, figure 5.25 shows that profile B from sample 98FWB38 does not indicate any significant re-heating of the grain has occurred. Instead, simple linear cooling models can adequately describe the measured apparent age profile. This is obviously in contrast with the thermal history implied by apparent age profiles from other samples of the Pakeagama Lake suite and is discussed further in the summary below.

The apparent age profile of mica from the Margot Lake pegmatite (SS111) is broadly consistent with theoretical models that include the re-heating events at 2450Ma and 1850Ma (figure 5.26).

Apparent age profiles matched with theoretical models are shown for the pegmatites of the western Superior Province in figures 5.27 - 5.32. The Wenesaga pegmatite is located on the northern boundary of the English River Subprovince (ERS). Theoretical profiles are compared with the measured profile of mica in figure 5.27, which indicates a similar thermal history to pegmatites in the NW Superior province, with circa 400°C re-heating at 2450Ma and 1850Ma.

In contrast, theoretical modelling must account for the maximum apparent ages being no older than 2.45Ga in the Separation Rapids pegmatite group. Figure 5.28 shows the

apparent age profile from sample SS34a compared with theoretical profiles produced by re-heating at 2450Ma, 450°C (TH1) and 500°C (TH2), followed by 400°C re-heating at 1850Ma. It is evident that the 2450Ma re-heating in TH1 (450°C) is not of sufficient temperature to reset ages in the core of the mica to 2450Ma. Increasing the temperature of the 2450Ma event to 500°C (TH2) has the effect of completely resetting the apparent age even within the grain core, which matches the data from the profile. This indicates that the temperature of re-heating during the 2450Ma event must have been 500°C or greater in the Separation Lake area (south of the ERS).

Theoretical profiles suggest that samples with much larger grain sizes (e.g. SS40, 10mm grain size) require temperatures up to 550°C during the 2450Ma re-heating event to fit with measured apparent ages (figure 5.29). It is worth noting a limitation of the DIFFARG program is that it does not take account of diffusion that may occur along crystal defects. These short-circuit pathways can lower the effective diffusion dimension (Layer *et al.* 1987), the closure temperature, and thus the degree of heating required to completely reset the grain (Lee 1995). This is confirmed by the observation that the effective diffusion dimension is 1-2mm, in micas from this study. In view of this, all hypothetical thermal histories shown here should be regarded as maximum estimates of re-heating temperatures.

Mica sample SS31 from the Big Whopper pegmatite has a grain size of 2mm and displays maximum apparent ages of 2.35Ga. Theoretical models indicate temperatures of 550°C during the 2450Ma re-heating event are required to produce this profile (figure 5.30).

Slightly scattered age profiles from the Graphic Lake pegmatite (SS89) and Mavis Lake group, Fairservice pegmatite #1 (SS60) can be matched by theoretical profiles with 425 - 450°C re-heating at 2450Ma and a slightly lower temperature 375°C event at 1850Ma (figures 5.31 - 5.32). It should be noted that there is considerable scatter amongst the data in both profiles, which may indicate crystal defects causing enhanced argon loss.

5.5.2 Summary

Theoretical modelling using DIFFARG suggests that slow cooling cannot account for the majority of apparent age profiles measured in this study. However, many of the profiles that display large variations in apparent age (>300Ma) between

core and rim can be described by a thermal history that includes discrete re-heating events at 2450Ma and 1850Ma. Pegmatites located in the northwestern and the western Superior Province (excluding those on the southern boundary of the English River Subprovince and Separation Lake greenstone belt) display profiles that suggest 400 - 450°C re-heating at 2450Ma and ~400°C for the 1850Ma event. The Separation Rapids group pegmatites are located within the Separation Lake greenstone belt of the western Superior Province. Apparent age profiles in this area were thoroughly reset at 2450Ma and can only be matched by higher temperatures of re-heating (500 - 550°C) at 2450Ma.

A crucial part of this series of reheating events should be the consistency of age profiles because regional heating/metamorphism should affect all muscovite in the same way. If such a thermal history was regionally pervasive and of such magnitude, it is expected that micas from the same pegmatite group would have similar $^{40}Ar/^{39}Ar$ apparent age profiles. However, this is not the case. Samples such as SS70, SS20 have profiles with wide variations in apparent ages that decrease towards the grain boundaries. In contrast, some samples (SS106a, SS107) display young apparent ages at the very edge of the grain, which are difficult to fit to modelled thermal histories (figures 5.23, 5.24). In the case of sample 98FWB38 (figure 5.25), there is relatively little variation in apparent age (<100Ma) suggesting that argon systematics have seemingly been unaffected by *circa* 400°C re-heating. To explain these apparently contradictory results, it is necessary to look beyond volume diffusion and inferred thermal histories as the only mechanism for apparent age variation.

- *Experimental artefacts*

In part, scattered age variations could result from experimental artefacts. During analysis, it is possible that ablation pits excavate through the upper most sheet of mica and therefore sample underlying sheets of mica. As diffusion in micas is dominated by transfer of atoms parallel to cleavage, individual mica layers may have slightly different diffusion profiles. The result of sampling multiple mica sheets would be a mixed age profile, with anomalous apparent age variation.

Abrasion or removal of grain rims during preparation is unlikely to be a reason for the lack of large variations in apparent age at the grain edge, since all grains were hand picked direct from hand specimen, without any crushing required. Furthermore, obvious crystal growth boundaries were selected for analysis and several grains were

analysed from samples which display relatively little variation in apparent age, suggesting that the profiles are representative of each sample.

- *Short-circuit diffusion and multi-domain diffusion*

A number of apparent age profiles measured in this study exhibit features that indicate the possibilty of short-circuit diffusion. Apparent ages that deviate from the main profile trends are noted in several samples, most notably SS70, SS20, SS2, SS31, SS89. It is conceivable that these anomalous apparent ages result from enhanced diffusion (producing young ages). Importantly, measured profiles do not display increasing ages towards the grain edge, which would be expected if excess argon was introduced from the grain boundary. Rather, any anomalous 'old' ages probably result from build up of excess argon within crystal defects or inclusions that do not reach the grain boundary.

Despite the large grain size of pegmatitic mica, crystals probably contain defects and chemical boundaries that effectively divide the grain in to several sub-grains or diffusion domains. This would have a similar effect to that predicted by multipath diffusion, creating steps in the age profiles. Sample SS70 is a good example of a profile with a step or 'local plateau', which could be explained by the presence of different domain boundaries within the grain. It is not possible to distinguish between short-circuit diffusion and multi domain diffusion from the present data. In cases where partitioning into short-circuit paths is dominant the two mechanisms are identical.

Whilst short-circuit diffusion and multi-domain diffusion models offer an explanation for departures from simple volume diffusion profiles, these mechanisms cannot adequately explain the large apparent age variations.

5.6 Compositional control on $^{40}Ar/^{39}Ar$ apparent ages

5.6.1 Alteration

The effects of chloritic alteration on apparent age variation within individual crystals was investigated using two diagrams that plot the component of argon derived from chlorine (^{38}Ar). Figure 5.33 shows $^{37}Ar/^{38}Ar$ *versus* $^{39}Ar/^{38}Ar$ diagrams and apparent age *versus* ^{38}Ar diagrams for selected samples analysed in this study. There is no obvious correlation, which indicates that chloritic alteration is not responsible for the apparent age variations. Furthermore, electron microprobe data (Chapter 3) reveals low concentrations (often below detection limit) of chlorine in mica from this study.

5.6.2 F - $(OH)_{-1}$ substitution

As discussed earlier in section 5.2.4, crystal - chemical effects on the diffusion of argon within micas are predicted by Dahl's ionic porosity model. In this insightful study of age, retentivity and compositional effects, Dahl (1996) convincingly shows a crystal-chemical connection between fluorine content and K - O bond strength within the interlayer sites of trioctahedral micas. Since the K - O bond strength is a determining factor for loss of radiogenic isotopes, Dahl's model predicts that apparent ages of coexisting micas, dioctahedral (e.g. muscovite) and trioctahedral (e.g. biotite, lepidolite), will vary according to fluorine concentration.

During the course of this study, backscaterred electron (BSE) imaging of mica revealed distinctive zoning in mica from several samples of the Pakeagama Lake pegmatites (Chapter 3). Muscovite cores (dioctahedral) are replaced at the grain boundaries by fluorine-rich lepidolite (trioctahedral). Combined with the large apparent age variations within the outer few hundred microns of some mica grains, this suggested a relationship between chemical variation and $^{40}Ar/^{39}Ar$ apparent ages.

To test this hypothesis, a number of samples from the Pakeagama Lake pegmatites were re-examined using the electron microprobe. Unfortunately, this had to be undertaken on new grains because the previously irradiated mica grains could not be handled for the length of time needed to prepare the grains for electron microprobe analysis. However, polished thin sections were already available from the same hand specimens from which the mica grains were separated for $^{40}Ar/^{39}Ar$ analysis.

SS70 Severn River pegmatite

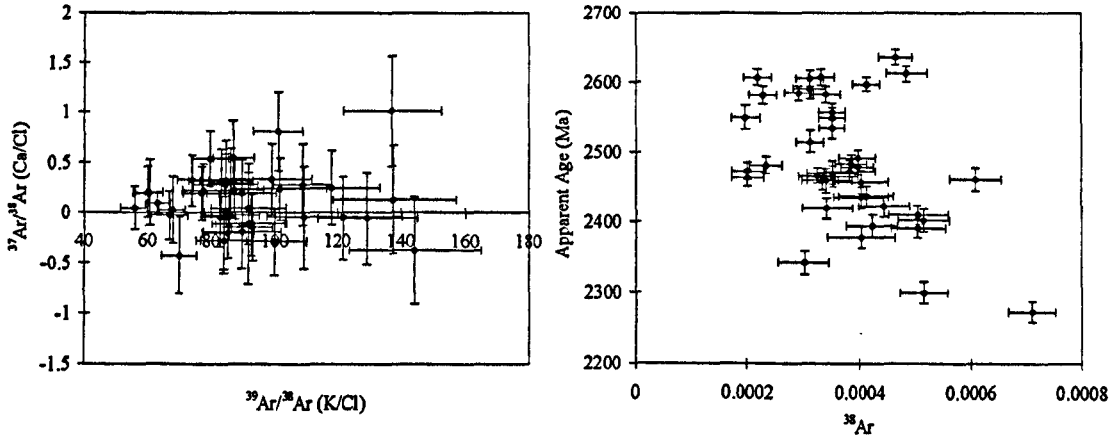

SS20 Pakeagama Lake pegmatite

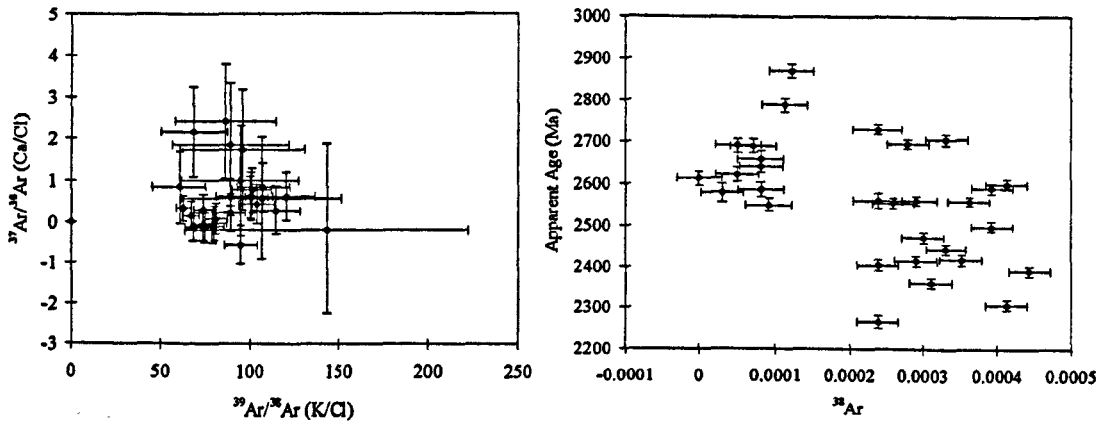

SS107 Pakeagama Lake pegmatite

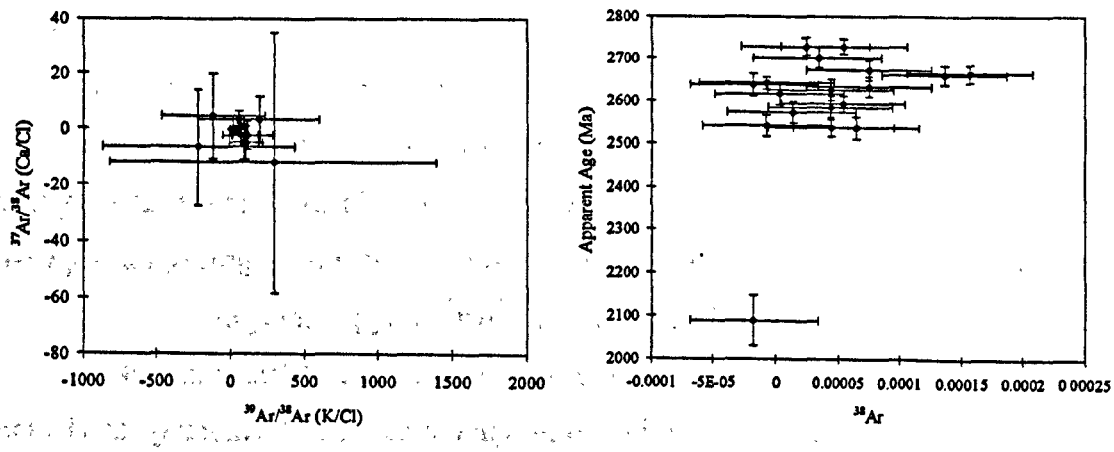

Figure 5.33 $^{37}Ar/^{38}Ar$ versus $^{39}Ar/^{38}Ar$ and apparent age versus ^{38}Ar for selected mica samples.

SS34a Separation Rapids pegmatite group

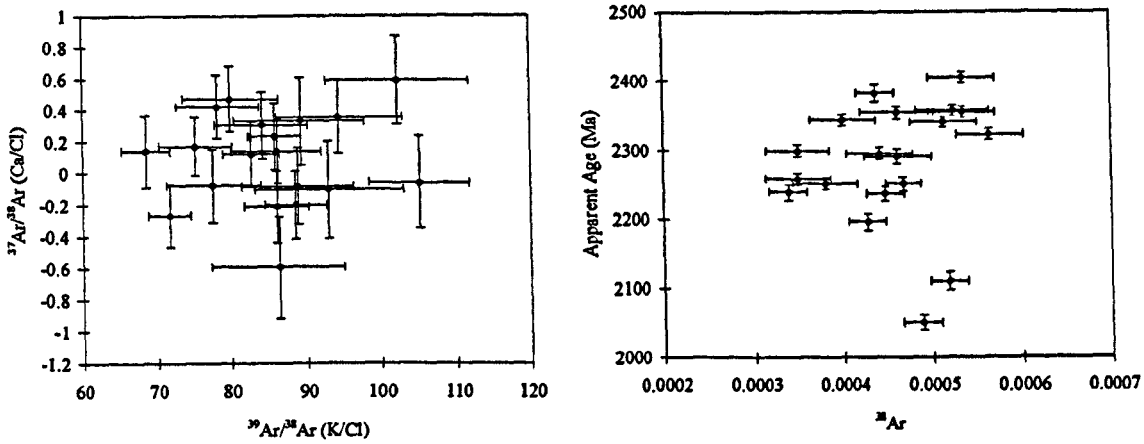

SS36 Separation Rapids pegmatite group

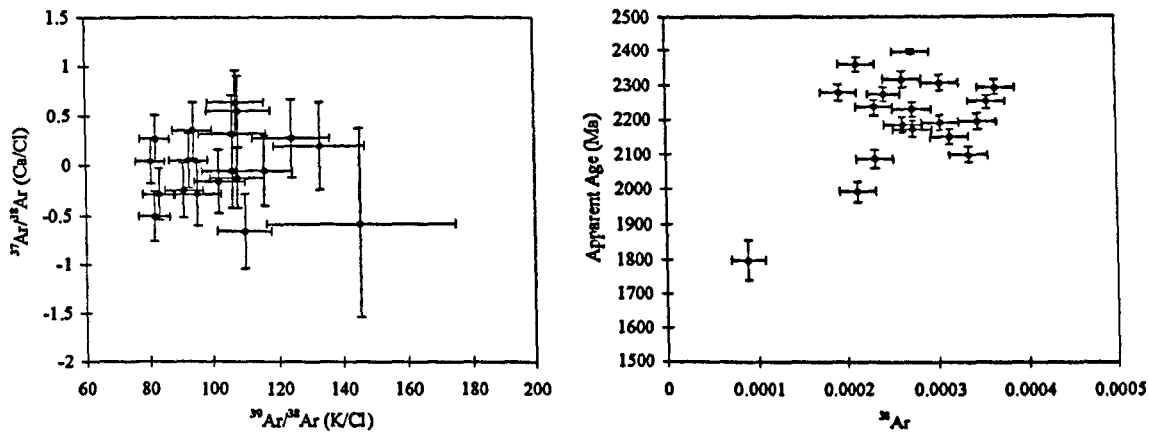

SS1 Wenesaga pegmatite

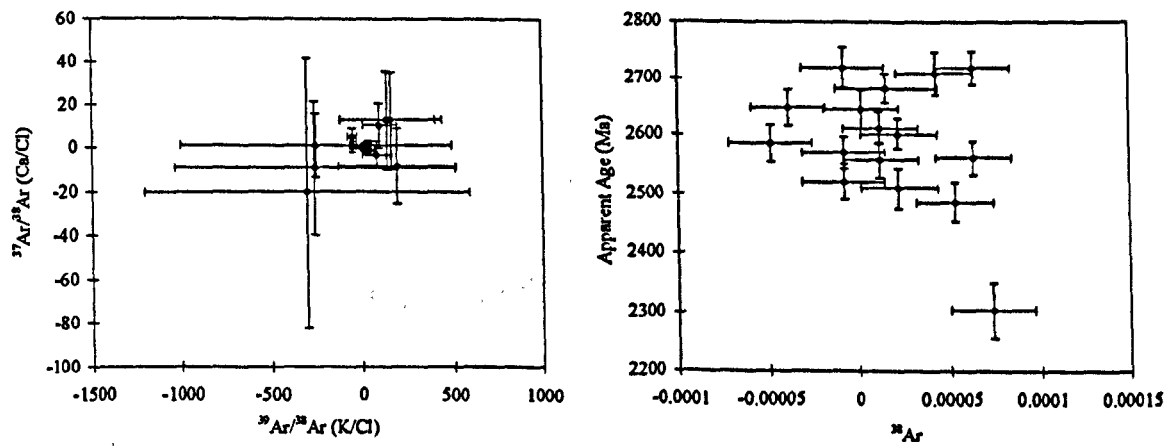

Figure 5.33 continued, $^{37}Ar/^{38}Ar$ versus $^{39}Ar/^{38}Ar$ and apparent age versus ^{38}Ar for selected mica samples.

a)

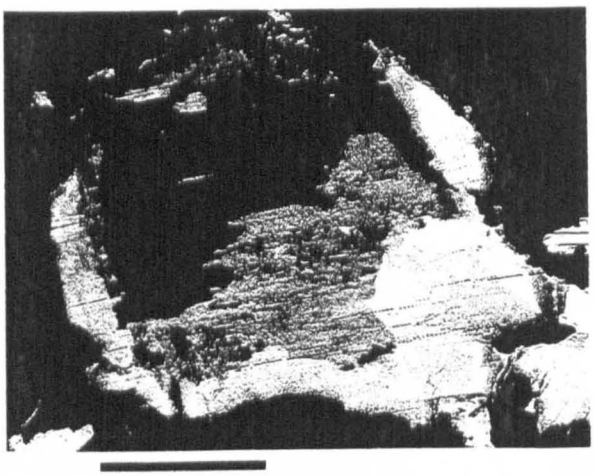

b)

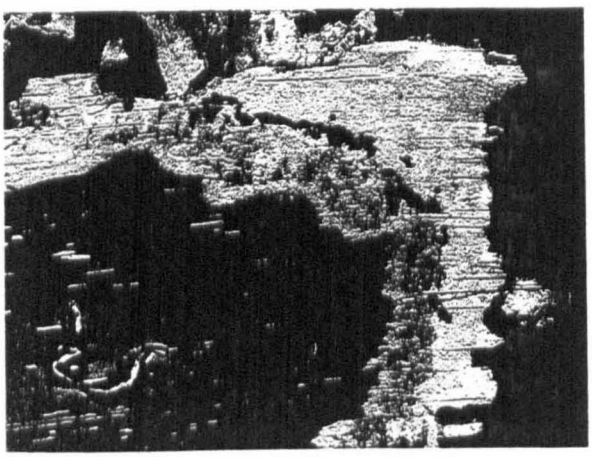

c)

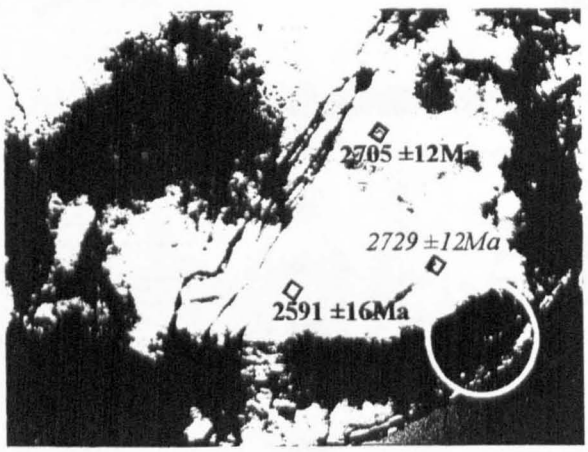

Figure 5.34a) and b)Backscattered electron images of mica from the Pakeagama Lake pegmatite. All images are taken from sample SS20, mica from the K-feldspar + petalite zone. Note the fluorine-rich rims (bright areas) are present on all grain boundaries, usually ~500μm wide.
c) transmitted light microscope image of mica grain used for UV laser ablation. Location of profile is outlined by the circle, which was continued further after this image was taken. All scale bars are 500μm.

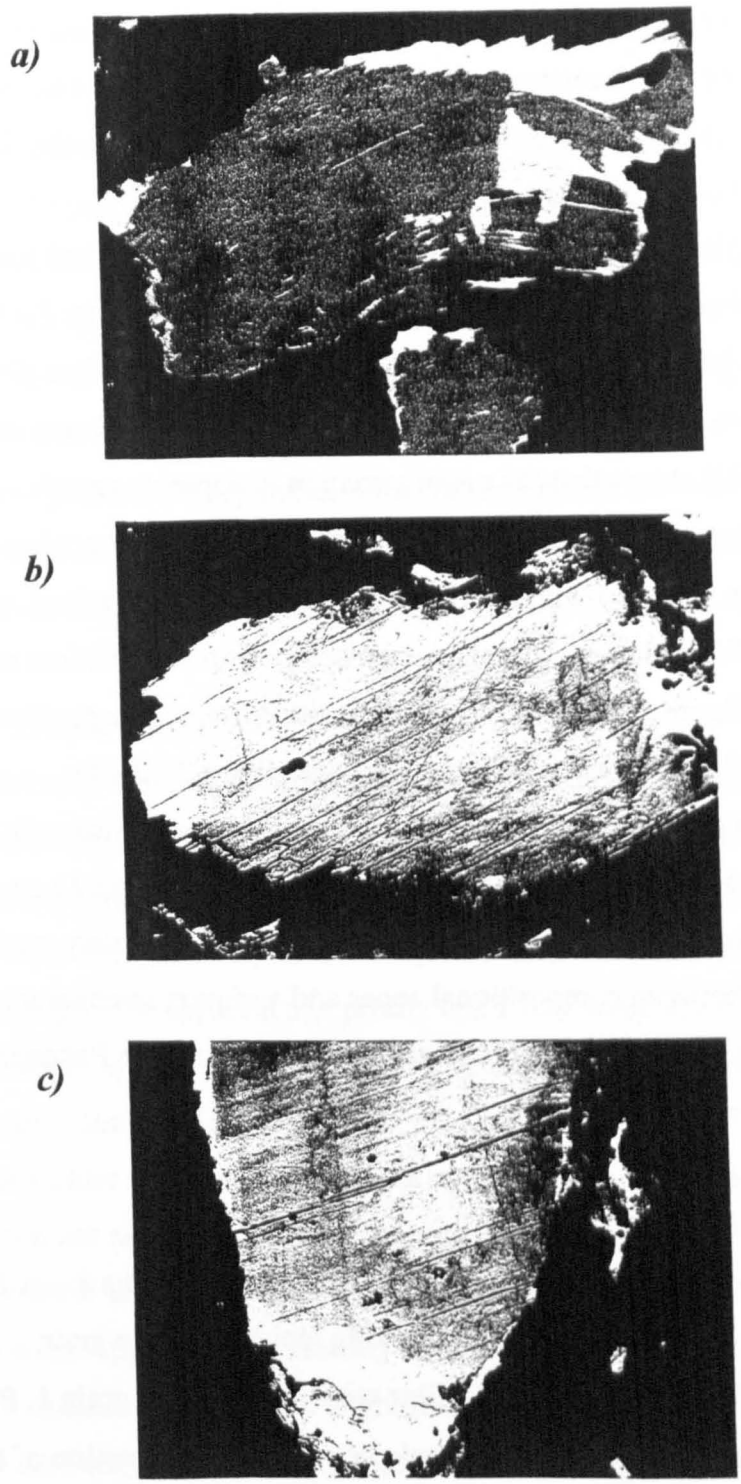

Figure 5.35 Backscattered electron images of mica from the Pakeagama Lake pegmatite. a) sample SS107, mica from the layered spodumene + quartz pegmatite-aplite; b) and c) sample 98FWB38, mica from the tourmaline + muscovite aplite dyke. Note the fluorine-rich rims (bright areas) are not present on all grain boundaries as in sample SS20 shown in figure 5.34. All images are at the same scale.

Backscattered electron (BSE) images revealed the length scale of zoning. The chemical variation is discussed in chapter 3, which shows dramatic increases in fluorine (up to 7 wt%), Li, Cs and Rb. A corresponding decrease in H_2O is also evident, although this cannot be measured directly on the electron microprobe, rather it is estimated from F - $(OH)_{-1}$ substitution.

Mica from sample SS20 (Pakeagama Lake pegmatite) was selected since it has distinct zoning, exhibiting a sharp boundary between core and rim (figure 5.34a, b). The distance from the grain boundary at which this compositional change takes place is on the order of 400 - 500μm. A close comparison with the $^{40}Ar/^{39}Ar$ profile measured from sample SS20 (figure 5.22) shows that the major variation in apparent age also occurs within 500μm of the grain edge. Figure 5.34c shows that this chemical zoning can also be seen in the mica grain analysed with the UV laser microprobe. In contrast, samples such as SS107 and 98FWB38 have a very thin or no compositionally distinct rim along most grain boundaries (figure 5.35). Correspondingly, the apparent age profiles are distinguished by relatively little variation in apparent age (figure 5.13k, l).

These observations suggest that where F-rich rims are present along the grain boundaries of mica, there is likely to be a large variation in apparent age. In contrast, where F-rich rims are absent, variation in apparent age should be relatively small.

The relationship between compositional zones and variation in apparent age was then tested directly using two mica grains from sample SS117 from the Pakeagama Lake pegmatite.

- *SS117 Grain 1 (figure 5.36)*

Backscattered electron (BSE) imaging and X-ray mapping of this 2mm diameter grain reveals a muscovite core replaced by fluorine-rich lepidolite at the grain boundaries (figure 5.36). Two apparent age profiles were measured on grain 1. Profile A extends a distance of 750μm inwards from the grain boundary. The direction of the profile runs perpendicular to the cleavage trace (NE-SW, visible in BSE image). The lowest apparent age from profile A occurs at the grain boundary, 2.4Ga. Ages increase, with some scatter up to 2.65Ga at a distance of 150μm, followed by a decrease in ages to 2.42Ga at 350μm from the grain edge. Notably, this 'trough' of younger apparent ages coincides with the compositional boundary, at a distance of 400μm from the grain edge. From this point, inwards to the centre of the grain, ages increase systematically to 2.65Ga. A single point lies above the emplacement age of the pegmatite (2673 ±10Ma),

which probably contains excess argon. Notably, there are some anomalous points that deviate from the generally smooth profile. It is likely that these analyses coincide with cleavage planes.

Profile B has a length of 850μm from the grain boundary into the core. The direction of the profile runs parallel to cleavage and does not cross any visible cleavage planes (figure 5.36). Apparent ages increase evenly from 2400Ma at the grain boundary to 2650Ma at a distance of ~200μm, and then decrease to 2500Ma at the compositional boundary, between 350-500μm. Ages increase within the core, up to 2660Ma, but exhibit a complicated pattern.

These profiles clearly indicate that the compositional zones act as sub-grains or diffusion domains. The 'troughs' of young apparent ages at ~400μm from the grain boundary coincide with the boundary between muscovite and F-rich lepidolite.

- *SS117 Grain 2 (figure 5.37)*

Markedly different apparent age profiles are observed in grain 2, which has a diameter of 5mm. Muscovite is again replaced by lepidolite at the grain boundaries. Profile A has a length of 550μm. The fluorine X-ray map reveals that this part of the grain that has a comparitively thin (~100μm) F-rich rim (fluorine X-ray map). Correspondingly, the apparent age profile has a very steep age gradient close to the grain boundary. Apparent ages increase from 2.2Ga to 2.6Ga within the first 100μm of the grain edge. Inwards from this point, ages fall in the range 2.7 - 2.9Ga, which is significantly older than the emplacement age of the pegmatite indicating a component of excess argon has penetrated along a fracture or cleavage plane.

Profile B is sited adjacent to profile A, where there is a wider F-rich lepidolite rim (~250μm). Apparent ages steadily increase from 2.15Ga at the grain boundary up to 2.6Ga at a distance of 250μm. A slight jump in the profile is coincident with the boundary between muscovite and lepidolite. Average ages within the muscovite core region are 2.67Ga, concordant with the emplacement age of the pegmatite. This indicates that the fluorine-rich lepidolite rim is less Ar-retentive than the muscovite.

Profile C has a length of 575μm and runs oblique to the grain boundary (figure 5.37). Ages increase from 2.3Ga to 2.5Ga within the first 100μm of the profile. Between 100μm and 300μm, ages are constant at 2.5Ga, forming a local plateau. The BSE image in figure 5.37 shows the orientation of the ablation tracks, which intersect the muscovite-lepidolite boundary on more than one analysis. Thus, the local plateau is

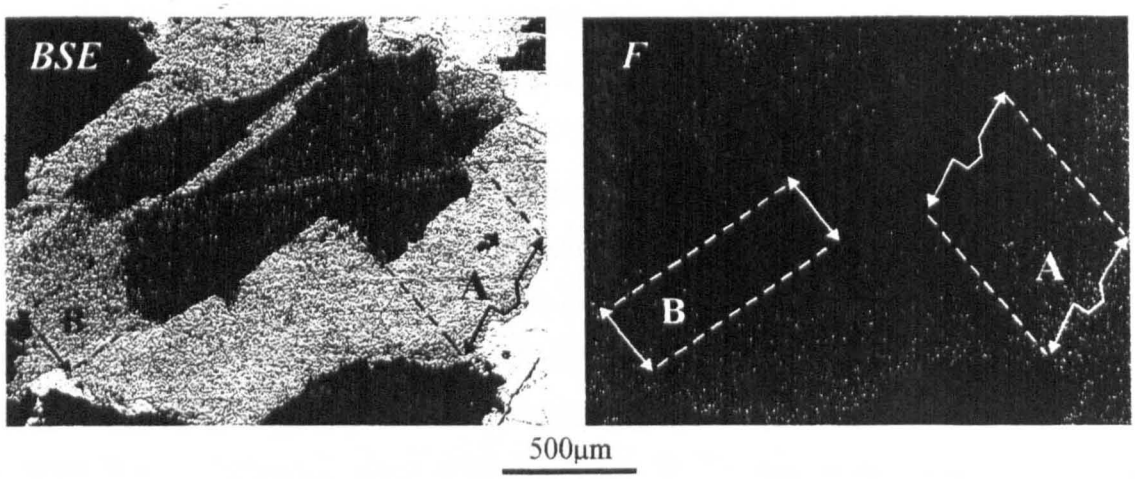

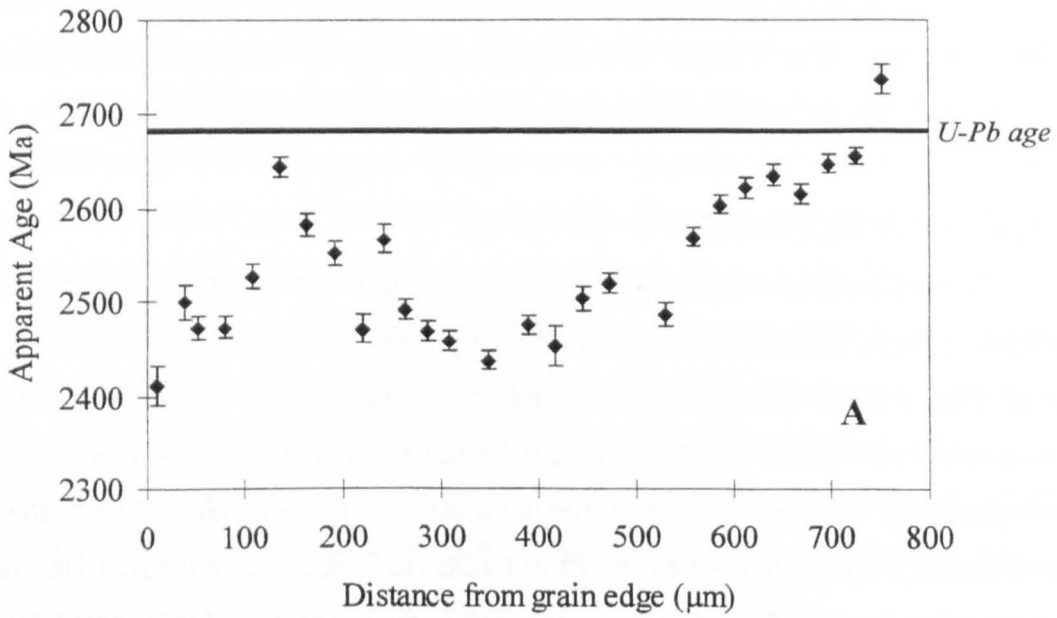

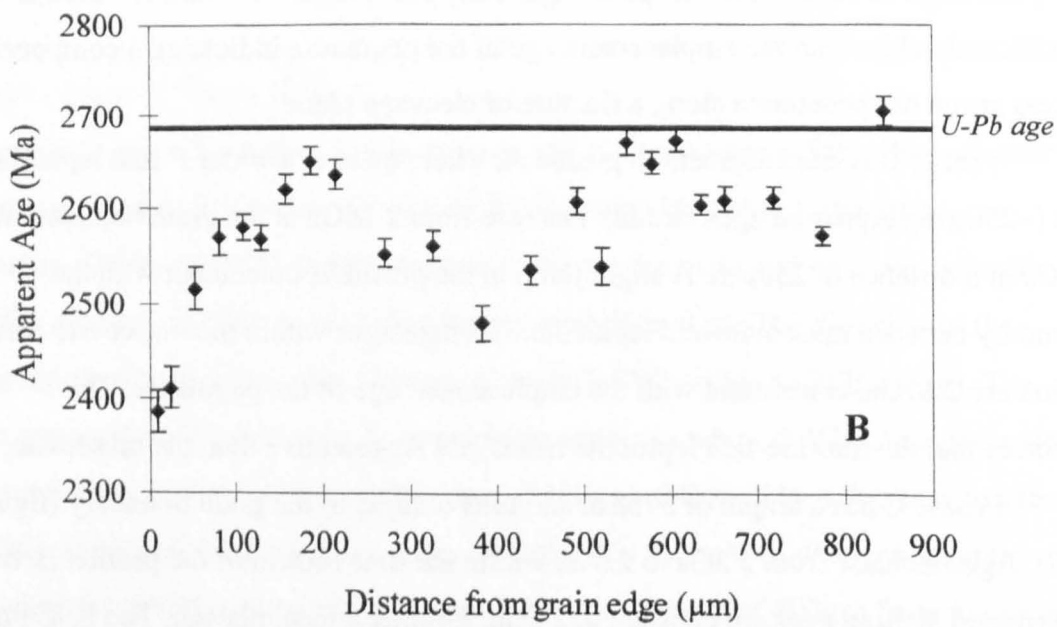

Figure 5.36 Backscattered electron image and X-ray map of fluorine for sample SS117 mica from the Pakeagama Lake pegmatite. Apparent age profiles from the locations highlighted in the BSE image and X-Ray map. Rim contains maximum fluorine concentration of 7.4 wt%. U-Pb tantalite age of 2673 ±10Ma (2 sigma, inc. decay constant uncertainty) from Chapter 4.

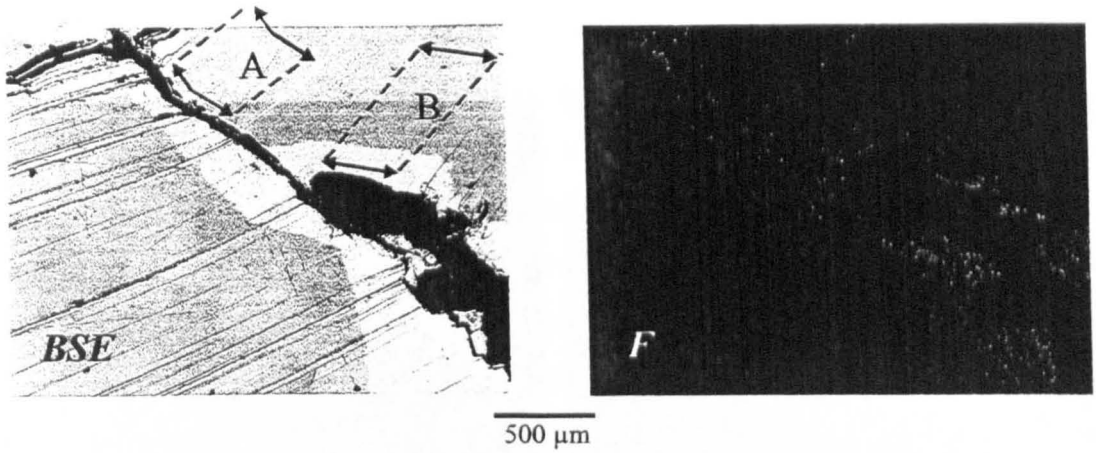

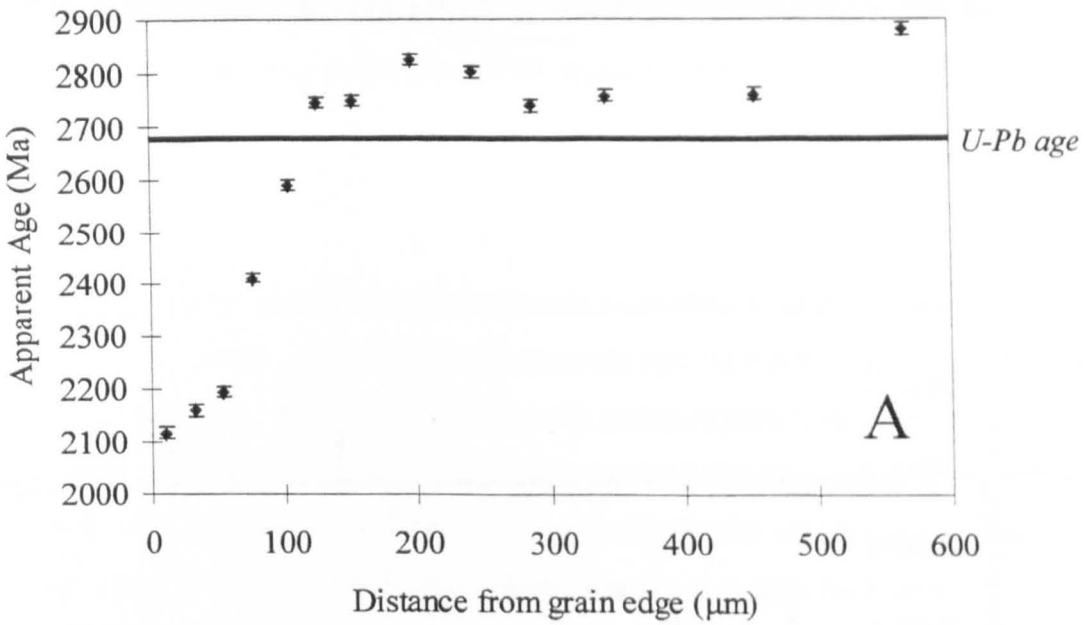

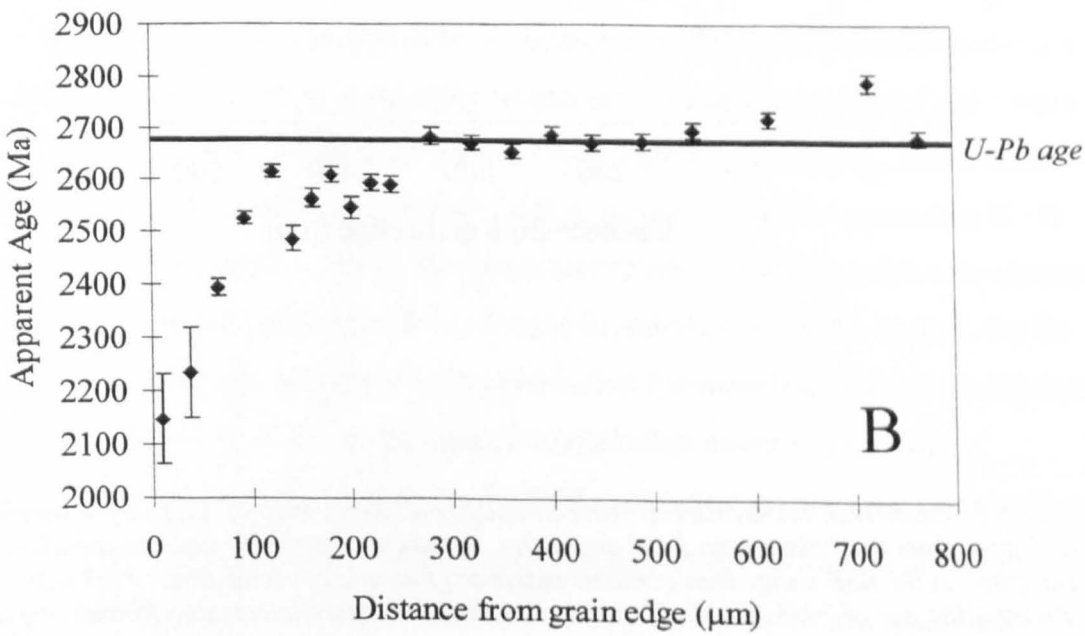

Figure 5.37 Backscattered electron image and X-ray map of fluorine for sample SS117 mica from the Pakeagama Lake pegmatite. Apparent age profiles from the locations highlighted in the BSE image. Rim contains maximum fluorine concentration of 6.3 wt%. U-Pb tantalite age of 2673 ±10Ma (2 sigma, inc. decay constant uncertainty) from Chapter 4.

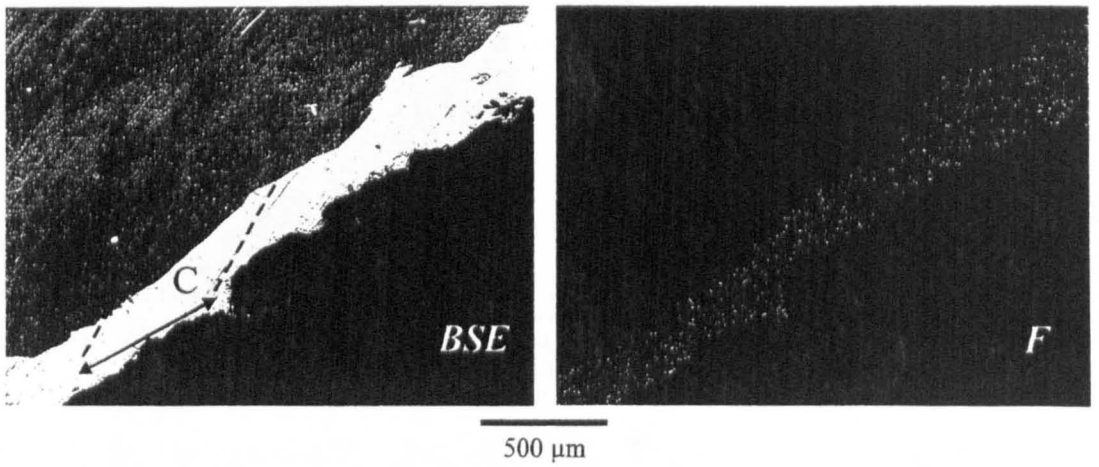

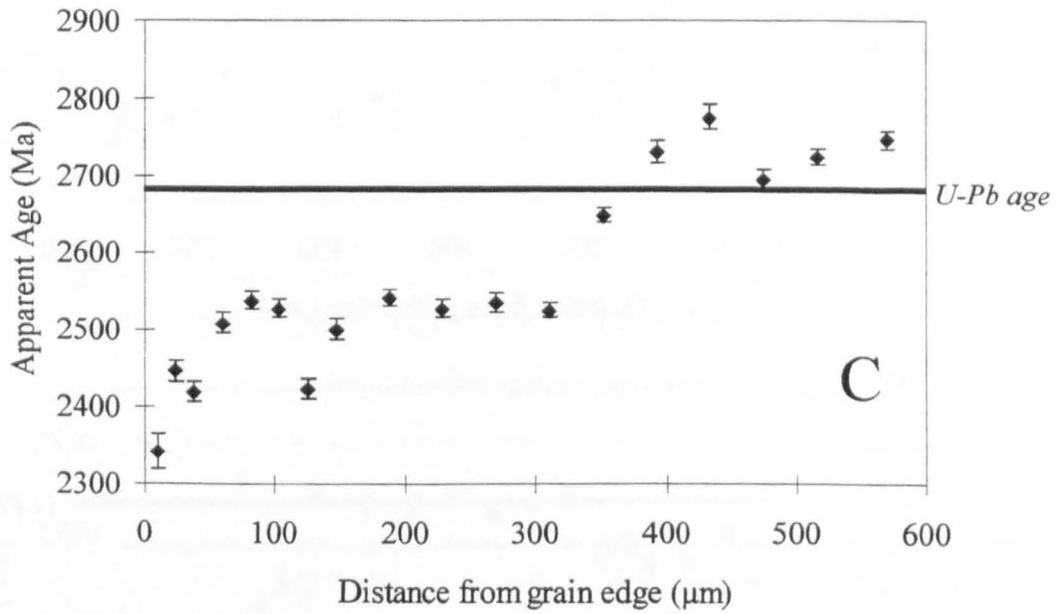

Figure 5.37 continued, backscattered electron image and X-ray map of fluorine for sample SS117 mica from the Pakeagama Lake pegmatite. Apparent age profile from the location highlighted in the BSE image.Rim contains maximum fluorine concentration of 6.3 wt%. U-Pb tantalite age of 2673 ±10Ma (2 sigma, inc. decay constant uncertainty) from Chapter 4.

produced because of repeated sampling of this boundary. Inwards to the centre of the grain, the muscovite core shows increasing apparent ages from 2.5 - 2.8Ga.

The differences between profile A and B from grain 2 indicate that the width of the F-rich lepidolite rim has a direct affect on the shape of the apparent age profile. Where a thin F-rich rim is present, the apparent age gradient is steep, and where a wider F-rich rim occurs, there is a gradual increase in apparent ages. As shown in profile C, profiles oriented sub-parallel to compositional zones may yield mixed ages between the two zones acting as separate diffusion domains. This has important implications for thermal history modelling as the shape of the profile determines the temperature, timing and duration of the re-heating event needed to simulate the profile.

5.6.3 Summary

The observations made here point towards a correlation between increased F content, inferred F - $(OH)_{-1}$ substitution and apparent age variation measured in mica as predicted by Dahl (1996). However, the relatively young apparent ages that are correlated with F - $(OH)_{-1}$ substitution in the Pakeagama Lake pegmatites are apparently contradictory to the predictions of Dahl's ionic porosity model which suggests higher closure temperatures (T_c) and hence older $^{40}Ar/^{39}Ar$ apparent ages for F-rich trioctahedral micas relative to muscovite.

One explanation for this apparent contradiction to the ionic porosity model is a difference between the barium availability within the metapelitic rocks of Dahl's work and rare-element enriched melts. Dahl shows that progressive F - $(OH)_{-1}$ substitution leads to the systematic partitioning of Ba^{2+}, which is responsible for increasing K - O bond strength in trioctahedral micas. Barium concentrations within Li-rich rare-element pegmatites are however, often very low, <2 ppm (London *et al.* 1988). Indeed, the Ba content of micas analysed in this study is often below the detection limit of the electron microprobe (Chapter 3). Thus, in the case of trioctahedral micas (zinnwaldite, lepidolite) from rare-element pegmatites, F - $(OH)_{-1}$ substitution does not necessarily lead to the systematic partitioning of Ba^{2+} perhaps simply due to a low availability of Ba within peraluminous melts. Instead, Cs is more likely to substitute into lepidolite (*see* Chapter 3). Unfortunately, diffusion parameters for lepidolite are not known, but a comparison with biotite closure temperature is most applicable, inferred from the lack of Ba^{2+} substitution. Therefore, the closure temperature for lepidolite is estimated here

as being similar to the nominal T_c for 'average' trioctahedral mica (biotite), 280°C (Harrison *et al.* 1985).

The implications for thermal history are clearly shown in figure 5.38. The apparent age profile of sample SS20 is modelled using the DIFFARG parameters for trioctahedral mica (biotite). Re-heating may only need to reach 350°C (as opposed to 450°C for muscovite parameters) in order to cause enhanced diffusion rates and produce the large apparent age variations in the outer few hundred microns of zoned muscovite - lepidolite grains.

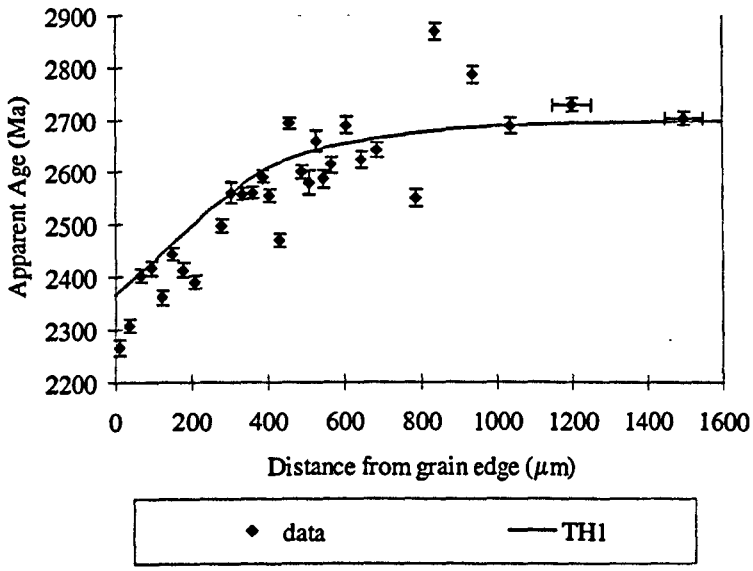

Figure 5.38 Apparent age profile for sample SS20 (Pakeagama Lake pegmatite). Note that the theoretical model uses the DIFFARG parameters for biotite so that the thermal pulse temperature needed to produce the apparent age profile can be evaluated for trioctahedral micas.
Thermal History 1 : 350°C, 2450 - 2440Ma; 350°C, 1850 - 1840Ma.

The apparent age profiles from the Separation Rapids pegmatites are more difficult to interpret. As noted in section 5.4.2, the Mn-suite and Fe-suite pegmatites display significantly different $^{40}Ar/^{39}Ar$ mica apparent age profiles. Micas from the Mn-suite commonly have well defined age profile trends and large apparent age variations, often younger than 2.1Ga at the grain edge. In contrast, Fe-suite pegmatites have micas with relatively little variation in apparent age, usually between 2.4 - 2.3Ga. Tindle and Breaks (1998) concluded that composition of the rare-element enriched melts from which these two pegmatite suites crystallised was significantly different. The Mn-suite

pegmatites crystallised from a fluorine-rich melt, indicated by bulk rock chemical analyses containing up to 8.5 wt% F. In contrast, the Fe-suite pegmatites are considered to have crystallised from a relatively fluorine-poor melt.

Electron microprobe analysis and backscattered electron images of mica (Chapter 3) show that compositional zoning is present in mica from the Mn-suite, but not the Fe-suite Separation Rapids pegmatites. However, this is not widespread. Fluorine enriched mica compositions and a rare species of Cs-mica, *nanpingite,* tend to occur sporadically along cleavage planes, fractures and in small aggregates (A.G. Tindle, *pers. comm.*). It is unclear what effects this may have on the diffusion characteristics of mica.

5.7 Implications for the regional thermal history

Investigation of regional cooling histories in the western Superior Province using $^{40}Ar/^{39}Ar$ geochronology has only recently been considered (Hanes and Archibald 1998). These authors undertook step-heating of bulk mineral separates (amphibole, mica and K-feldspar) and selective laser spot-dating on samples that had been previously dated by the U-Pb method. Hanes and Archibald (1998) reported varied $^{40}Ar/^{39}Ar$ apparent ages from the different subprovinces, within subprovinces and even within individual grains. In particular, 2.6Ga ages obtained in the granite-greenstone Uchi Subprovince contrasted with 2.37 - 2.47Ga ages in the western part of the high metamorphic grade English River and Winnipeg River Subprovinces.

The interpretation favoured by Hanes and Archibald (1998) was one of differential terrain uplift at or around 2.45Ga, in which the younger $^{40}Ar/^{39}Ar$ apparent ages could be explained by slower cooling in regions that were more deeply buried. Hanes and Archibald also suggested that south-side up tilting of the English River Subprovince exhumed deeper parts of the crust (i.e. eastern Lac Seul and Umfreville - Conifer Lakes granulite zones) along the southern boundary of the English River Subprovince because 2.45Ga apparent ages were also found proximal to the English River - Winnipeg River Subprovince boundary (figure 5.6).

In this study, apparent age profiles from rare-element pegmatites within the NW Superior Province do not reflect slow cooling, but can be modelled by a thermal history that includes a 2450Ma re-heating event that reached at least 350°C for a period of 10 -

50Ma. This re-heating event could conceivably have resulted from major basaltic underplating of the lithosphere associated with the emplacement of the Matachewan - Hearst dyke swarm at 2.45Ga (Heaman 1997). Mafic magmatism was centred on the southern Superior Province but may have had a much larger extent than the presently exposed dyke swarm. Indeed, Heaman (1997) suggested that the Matachewan magmatism would have caused thermal metamorphism and heating at the base of the crust and that this may have lasted for 30Ma with a progressive westward younging of magmatism.

The proposed re-heating at 2.45Ga had the most pronounced effect on pegmatites in the Separation Lake greenstone belt and southern boundary of the English River Subprovince, in the western Superior Province. Mica $^{40}Ar/^{39}Ar$ ages in this region were completely reset to 2.45Ga from the 2649 ± 8Ma and 2644±10Ma crystallisation ages determined by U-Pb columbite-tantalite geochronology for the Separation Rapids Fe-suite and Mn-suite pegmatites, respectively. Data from this study suggest that the southern boundary of the English River Subprovince and the adjacent Separation Lake greenstone belt experienced higher temperature re-heating during the 2.45Ga event. Theoretical modelling of apparent age profiles indicates that temperatures reached 500 - 550°C, based on muscovite diffusion parameters.

Reasons for disproportionately high temperatures recorded in the southern portion of the English River Subprovince and adjacent Separation Lake greenstone belt are unclear. The English River subprovince (ERS) has been interpreted as a fore-arc sedimentary prism (Breaks 1991). Recent seismic investigations have revealed that the folded metasedimentary rocks of the ERS are significantly thinner towards the south (Cruden and Hynes 1999). This might explain why re-heating had a greater effect on mica $^{40}Ar/^{39}Ar$ apparent ages in the Separation Rapids pegmatites and the Treelined Lake pegmatite compared with micas from pegmatites in the northern ERS. The Wenesaga (SS1) and Sandy Creek (SS2) pegmatites display maximum apparent ages of 2.65Ga and 2.5Ga respectively.

Further interpretation of seismic lines and the positive gravity anomaly coincident with the length of the ERS led Nitescu and Cruden (2001) to propose a dense linear body located in the mid- to lower crust. If this interpretation is correct, the emplacement of such a dense body (gabbro?) at 2.45Ga may well have caused the prominent heating and resetting of $^{40}Ar/^{39}Ar$ apparent ages in mica from pegmatites of the southern English River Subprovince and adjacent Separation Lake greenstone belt.

Partial disturbance of the $^{40}Ar/^{39}Ar$ systematics at 1850Ma is also indicated by the apparent age profiles of mica from the pegmatites analysed in this study. Theoretical modelling of these measured profiles suggests that the temperature reached during this event was between 375 - 400°C. Corfu and Ayres (1984) reported similar zircon lower intercept ages from batholiths of the North Caribou Terrain. Corfu and Ayres (1984) suggested that compressive stresses within the Superior Province, caused by the Trans Hudson Orogeny along its margins, reactivated major fault zones and resulted in partial disturbance of U-Pb systematics. This seems a plausible explanation for partial disturbance of $^{40}Ar/^{39}Ar$ systematics in mica from rare-element pegmatites located along tectonic boundaries. Indeed, Hanes and Archibald (1998) also found similar (1.7 - 1.9Ga) apparent ages from K-feldspar step heating experiments from a transect across the English River Subprovince and related this to final uplift during the Trans-Hudson Orogeny.

5.8 Conclusions

Based on $^{40}Ar/^{39}Ar$ apparent age profiles measured in this study, moderate temperature re-heating has caused partial disturbances to $^{40}Ar/^{39}Ar$ systematics of mica within rare-element pegmatites of the Superior Province.

Theoretical modelling using DIFFARG suggests that slow cooling cannot account for the majority of apparent age profiles measured in this study. Many of the profiles that display large variations in apparent age (>300Ma) between core and rim can be described by a thermal history that includes discrete re-heating events at 2450Ma and 1850Ma. Pegmatites located in the northwestern and the western Superior Province (excluding those on the southern boundary of the English River Subprovince and Separation Lake greenstone belt) display profiles that suggest a minimum 350°C re-heating at 2450Ma and ~300°C for the 1850Ma event. The Separation Rapids group pegmatites are located within Separation Lake greenstone belt of the western Superior Province. Apparent age profiles in this area were thoroughly reset at 2450Ma and can only be matched by higher temperatures of re-heating (500 - 550°C).

The episodes of re-heating are concordant with two major Proterozoic events affecting the Superior Province;

1. Emplacement of the 2450±2Ma Matachewan - Hearst dyke swarm associated with major basaltic underplating of the lithosphere and thermal metamorphism of the crust as proposed by Heaman (1997).
2. Fault reactivation and disturbance to isotopic systems during the Trans-Hudson Orogeny, 1860 - 1790Ma (Machado 1990).

However, there are several complications to the theoretical modelling of apparent age profiles and hence the thermal histories inferred from them. Crystal defects observed within mica grains are of crucial importance as they are associated with scattered intragrain apparent age variations.

Chemical zoning, in particular F - $(OH)_{-1}$ substitution, appears to directly correspond with variation in apparent ages. It is clear that the compositionally distinct muscovite cores and lepidolite rims act as individual diffusion domains or alternatively, the boundary between these zones could be interpreted as short-circuit pathways. Furthermore, F - $(OH)_{-1}$ substitution has often been proposed as a mechanism to increase argon retention and apparent ages in trioctahedral micas (Grove 1993, reported in Harrison and McDougall 1999). However, F-rich lepidolite rims analysed in this study yield younger, rather than older apparent ages, compared with the muscovite cores. This may be explained by a low availability of barium within peraluminous melts. In the case of trioctahedral micas (zinnwaldite/ lepidolite) from rare-element pegmatites, F - $(OH)_{-1}$ substitution does not necessarily lead to the systematic increase in Ba^{2+}. This confirms the prediction of Dahl's ionic porosity model i.e. Ba^{2+} is responsible for increasing K - O bond strength in trioctahedral micas. It is clear that thermochronology studies using mica age profiles need to incorporate detailed compositional measurements.

6. Conclusions

The major conclusions that can be drawn from this study relate to the geochemistry of micas, and the $^{40}Ar/^{39}Ar$ and U-Pb geochronology of rare-element pegmatites. Also, there are wider implications for the post-orogenic thermal history of the Superior Province and geochronology studies using both isotopic methods.

6.1 Mica geochemistry

- Mica from rare-element pegmatites is characterised by compositional zoning with muscovite cores and F-, Li- and Rb-rich zinnwaldite/ lepidolite rims. The zinnwaldite/ lepidolite rims texturally replace the original muscovite and were most likely precipitated from a F-, Li- and Rb-rich residual melt-fluid phase during the late-magmatic to hydrothermal period of pegmatite formation.

- Mica compositional variations within the Pakeagama Lake pegmatite reveal the extent of replacement by residual fluids within each of the internal zones, with increasing effect in the sequence; layered (spodumene + quartz) pegmatite-aplite → blocky K-feldspar (potassic) zone → K-feldspar + petalite zone → Quartz-rich wall zone → tourmaline + muscovite aplite dykes → spodumene + quartz core zone.

- Mica from the Separation Rapids pegmatite group exhibits similar compositional zoning (muscovite cores, zinnwaldite rims) but is not widespread, occurring in the Mn-suite pegmatites, but not the Fe-suite pegmatites. This indicates that the Mn-suite pegmatites crystallised from a chemically distinct (higher fluorine content) melt than the Fe-suite pegmatites.

6.2 Mica $^{40}Ar/^{39}Ar$ geochronology

- Micas from rare-element pegmatites of the Superior Province yield intragrain apparent age variations up to 800Ma within single crystals. Theoretical slow cooling models do not match the measured $^{40}Ar/^{39}Ar$ profiles and cannot account for the large apparent age variations. Theoretical thermal history models that produce the best fit to apparent age profiles include two re-heating events: a minimum 350°C re-heating at ~2450Ma and *circa* 300°C re-heating at 1850Ma, both for a period of at least 10Ma. These apparent ages are concordant with two major Proterozoic events affecting the Superior Province; intrusion of the Matachewan - Hearst dyke swarms and the Trans Hudson Orogeny, respectively.

- All mica from the Separation Rapids pegmatites and other pegmatites located in the southern portion of the English River Subprovince exhibit maximum apparent ages of 2.45Ga, which contrasts with maximum apparent ages of 2.6 - 2.7Ga from other locations in the Superior Province. This suggests that the 2450Ma re-heating event must have been at a higher temperature (500°C) in the southern English River Subprovince and adjacent Separation Lake greenstone belt.

- Extreme compositional variations in micas form individual diffusion domains, the boundaries of which may act as pathways for short-circuit diffusion. Backscattered electron images and compositional profiles obtained with the electron microprobe, combined with $^{40}Ar/^{39}Ar$ profiles measured with the UV-laser probe show that apparent ages decrease towards the boundary between the muscovite (dioctahedral) and lepidolite (trioctahedral) compositional zones.

- Younger apparent ages towards the grain boundaries are associated with trioctahedral, F-rich zinnwaldite/ lepidolite. This apparently contradicts ionic porosity models which predict higher closure temperatures resulting from the substitution of F for OH within the interlayer sites of mica. This may be explained by low barium concentration in rare-element pegmatite melts, which means that K - O bond strength is not increased by F - OH substitution in this case. The zinnwaldite/ lepidolite rims probably have similar diffusion characteristics to F-poor biotite (Harrison *et al.* 1985), and thus have a lower closure temperature than

coexisting muscovite. This is an important implication for thermochronology studies using mica apparent ages. Clearly, such studies need to incorporate compositional measurements.

6.3 U-Pb columbite-tantalite geochronology

- Primary crystallisation of tantalite and emplacement of the Pakeagama Lake pegmatite occurred at 2673 ±8Ma. Tantalite from the lepidolite vein cross-cutting the core zone yields a 2664 ±8Ma age from the magmatic grain core using LA-MC-ICP-MS and range of $^{207}Pb/^{206}Pb$ ages between 2659 ±1Ma and 2638 ±1Ma from TIMS analyses indicating disturbance to the U-Pb system by residual fluids/ sub-solidus metasomatic processes lasting for ~30Ma.

- Columbite from the Separation Rapids pegmatites yields crystallisation ages of 2649 ±4Ma (Fe-suite) and 2644 ±8Ma (Mn-suite) from TIMS analyses, confirming the link with the 2646 ±2Ma Separation Rapids pluton (Larbi *et al.* 1999). Precipitation of a residual fluid phase and/or sub-solidus processes lasted until 2628 ±4Ma within the Separation Rapids pluton. Columbite from a recrystallised assemblage within the Big Mack pegmatite yields a minimum estimate of 2588 ±2Ma for the age of localised ductile deformation.

- LA-MC-ICP-MS analyses of the magmatic grain core indicates primary columbite crystallisation at 2665 ±10Ma in Fairservice pegmatite #1, which is chemically associated with the Ghost Lake batholith. Replacement zones of the columbite exhibit normal discordance indicating a lead loss event at 2478 ±63Ma, which correlates with the re-heating event suggested from $^{40}Ar/^{39}Ar$ apparent age profiles.

- Reverse discordant data from U-Pb analyses of columbite-tantalite is probably created from sub-micron scale inclusions and U-Pb mobility within replacement zones of columbite-tantalite.

6.4 Future work

This work highlights several other possibilities for future research, most notably;

- *Further electron microprobe analysis of chemical variations in mica from rare-element pegmatites.*

  In particular, investigation into compositional zoning in muscovite-lepidolite series micas could yield petrogenetic information on complex, zoned pegmatite bodies. Such studies would also aid exploration in targeting sites for rare-element mineralisation.

- *Investigating the controls of compositional variation on the diffusion parameters of mica.*

  At present, there are few studies of the crystal-chemical controls on Ar diffusion and clearly there needs to be greater understanding of the effects of ionic substitution on the retention of isotopic components.

- *Developing techniques for U-Pb dating of columbite-tantalite by LA-MC-ICP-MS.*

  Work is in progress to refine the technique for laser ablation studies of columbite-tantalite. The columbite-tantalite series are important petrogenetic indicators in rare-element pegmatites and they have a great potential in providing constraints on the timescales of rare-element mineralisation processes.

References

Abella P. A., Corbella M., and Melgarejo J. C. (1995) Nb-Ta- minerals from the Cap de Creus pegmatite fiels, eastern Pyrenees: distribution and geochemical trends. *Mineralogy and Petrology* **55**, 53-69.

Baadsgaard H. and Cerný P. (1993) Winnipeg River pegmatite populations, southeastern Manioba. *Geological Association of Canada-Mineralogical Association of Canada Annual Meeting*, A5.

Barnett P. J. (1991) Quaternary Geology of Ontario. In *Geology of Ontario*, Special Volume 4 (ed. P. C. Thurston, H. R. Williams, R. H. Sutcliffe, and G. M. Stott), pp. 1011-1090. Ontario Geological Survey.

Beakhouse G. P. (1991) Winnipeg River Subprovince. In *Geology of Ontario*, Special Volume 4 (ed. P. C. Thurston, H. R. Williams, R. H. Sutcliffe, and G. M. Stott), pp. 279-302. Ontario Geological Survey.

Beakhouse G. P., Heaman L. M., and Creaser R. A. (1999) Geochemical and U-Pb zircon geochronological constraints on the development of a Late Archean greenstone belt at Birch Lake, Superior Province, Canada. *Precambrian Research* **97**, 77-97.

Bennett G., Dressler B. O., and Robertson J. A. (1991) The Huronian Supergroup and associated intrusive rocks. In *Geology of Ontario*, Special Volume 4 (ed. P. C. Thurston, H. R. Williams, R. H. Sutcliffe, and G. M. Stott). Ontario Geological Survey.

Blackburn C. E., Johns G. W., Ayer J. A., and Davis D. W. (1991) Wabigoon Subprovince. In *Geology of Ontario*, Special Volume 4 (ed. P. C. Thurston, H. R. Williams, R. H. Sutcliffe, and G. M. Stott), pp. 303-382. Ontario Geological Survey.

Blackburn C. E. and Young J. B. (1993) Geology of the Separation Lake Greenstone Belt., pp. 68-73. Ontario Geological Survey. Miscellaneous Paper 162.

Breaks F. W. (1991) English River Subprovince. In *Geology of Ontario*, Special Volume 4 (ed. P. C. Thurston, H. R. Williams, R. H. Sutcliffe, and G. M. Stott), pp. 239-278. Ontario Geological Survey.

Breaks F. W. (1993) Granite-related mineralization in northwestern Ontario: I. Raleigh Lake and Separation Rapids (English River) rare-element pegmatite fields. *Summary of Field Work and Other Activities 1993* Miscellaneous Paper **162**, 104-110.

Breaks F. W. and Janes D. A. (1991) Granite-related mineralization of the Dryden Area, Superior Province of northwestern Ontario. *Geological Association of Canada - Mineralogical Association of Canada*, Joint Annual Meeting, Field Trip B7 : Guidebook, pp. 71.

Breaks F. W. and Moore J. M. (1992) The Ghost Lake Batholith, Superior Province of Northwestern Ontario: A Fertile, S-Type, Peraluminous Granite - Rare-Element Pegmatite System. *Canadian Mineralogist* **30**, 835-875.

Breaks F. W. and Tindle A. G. (1996) Granite related mineralization in northwestern Ontario, IV. New rare-element pegmatite discoveries in the Separation Lake area., *Summary of Field Work and Other Activities* 1996, pp. 19-22. Ontario Geological Survey.

Breaks F. W. and Tindle A. G. (1997) Rare-metal exploration potential of the Separation Lake area: an emerging target for Bikita-type mineralization in the Superior Province of northwestern Ontario, Open File Report 5966, pp. 27. Ontario Geological Survey.

Breaks F. W. and Tindle A. G. (*in press*) Rare-element mineralization of the Separation Lake area, NW Ontario: geological, mineralogical and chemical characteristics of a new discovery of complex type (petalite subtype) pegmatites. In *Industrial Minerals of Canada*. Canadian Institute of Mining.

Breaks F. W., Tindle A. G., and Smith S. R. (1999a) Rare-metal mineralisation associated with the Berens River - Sachigo Subprovincial boundary, northwestern Ontario: Discovery of a new zone of complex-type, petalite subtype pegmatite and implications for future exploration. In *Summary of Field Work and Other Activities 1998*, Miscellaneous Paper 169, pp. 168-182. Ontario Geological Survey.

Breaks F. W., Tindle A. G., and Smith S. R. (1999b) Geology, mineralogy and exploration potential of the Big Mack pegmatite system : a newly discovered western extension of the Separation Rapids pegmatite group, NW Ontario., pp. 25-1 to 25-22. Ontario Geological Survey.

Card K. D. and Ciesielski A. (1986) Subdivisions of the Superior Province. *Geoscience Canada* **13**, 5-13.

Cerný P. (1990) Distribution, affiliation and derivation of rare-element granitic pegmatites in the Canadian Shield. *Geologische Rundschau* **79/2.**, 183-226.

Cerný P. (1991) Fertile Granites of Precambrian rare-element pegmatite fields: is geochemistry controlled by tectonic setting or source lithologies? *Precambrian Research.* **51**, 429-468.

Cerný P. (1992) Geochemical and petrogenetic features of mineralization in rare-element granitic pegmatites in the light of current research. *Applied Geochemistry* **7**, 393-416.

Cerný P. and Ercit T. S. (1985) Some recent advances in the mineralogy and geochemistry of Nb and Ta in rare-element granitic pegmatites. *Bull. Mineral.* **108**, 499-532.

Cerný P., Ercit T. S., and Vanstone P. J. (1998) Mineralogy and Petrology of the Tanco Rare-element Pegmatite Deposit, Southeastern Manitoba. *International Mineralogical Association, 17th General Meeting*, 74.

Cerný P., Fryer B. J., Longstaffe F. J., and Tammemagi H. Y. (1987) The Archean Lac du Bonnet batholith, Manitoba: Igneous history, metamorphic effects, and fluid overprinting. *Geochimica et Cosmochimica Acta* **51**, 421-438.

Cerný P. and Meintzer R. E. (1988) Fertile granites in the Archean and Proterozoic fields of rare-element pegmatites: crustal environment, geochemistry and petrogenetic relationships. In *Recent advances in the Geology of Granite Related Mineral Deposits* (ed. Taylor and Strong). The Canadian Institute of Mining and Metallurgy.

Cerný P., Novak M., and Chapman R. (1992) Effects of siilimanite-grade metamorphism and shearing on Nb-Ta oxide minerals in granitic pegmatites: Marsikov, northern Moravia, Czechoslovakia. *Canadian Mineralogist* **30**, 699-718.

Cerný P., Stanek J., Novak M., Baadsgaard H., Rieder M., Ottolini L., Kavalova M., and Chapman R. (1995) Geochemical and structural evolution of micas in the Rozna and Dobra Voda pegmatites, Czech Republic. *Mineralogy and Petrology* **55**, 177-201.

Černý P., Trueman D. L., Ziehlke D. V., Goad B. E., and Paul B. J. (1981) The Cat Lake - Winnipeg River and the Wekusko Lake Pegmatite Fields, Manitoba. *Economic Geology Report ER80-1*. Manitoba Department of Energy and Mines.

Chipera S. J. and Perkins D. (1988) Evaluation of biotite-garnet thermometers: application to the English River Subprovince, Ontario. *Contributions to Mineralogy and Petrology* **98**, 40-48.

Cooper D. G. (1964) The geology of the Bikita pegmatites. In *Geology of Some Ore Deposits in Southern Africa*, Vol. 2, pp. 441-462.

Corfu F. (1988) Differential response of U-Pb systems in coexisting accessory minerals, Winnipeg River Subprovince, Canadian Shield: implications for Archaean crustal growth and stabilization. *Contrib, Mineral. Petrol.* **98**, 312-325.

Corfu F. and Ayres L. D. (1984) U-Pb age and genetic significance of heterogeneous zircon populations in rocks from the Favourable Lake area, Northwestern Ontario. *Contributions to Mineralogy and Petrology* **88**, 86-101.

Corfu F. and Ayres L. D. (1991) Unscrambling the stratigraphy of an Archean greenstone belt: a U-Pb geochronological study of the Favourable Lake greenstone belt, northwestern Ontario, Canada. *Precambrian Research* **50**, 201-220.

Corfu F. and Davis D. W. (1991) A U-Pb Geochronological Framework for the Western Superior Province, Ontario. In *Geology of Ontario*, Special Volume 4 (ed. P. C. Thurston, H. R. Williams, R. H. Sutcliffe, and G. M. Stott), pp. 1335-1346. Ontario Geological Survey.

Corfu F., Davis D. W., Stone D., and Moore M. L. (1998) Chronostratigraphic constraints on the genesis of Archean greenstone belts, northwestern Superior Province, Ontario, Canada. *Precambrian Research* **92**, 277-295.

Corfu F., Krogh T. E., Kwok Y. Y., and Jensen L. S. (1989) U-Pb zircon geochmology in the southwestern Abitibi greenstone belt, Superior Province. *Can. J. Earth Sci.* **26**, 1747-1763.

Corfu F. and Stone D. (1998a) Age structure and orogenic significance of the Berens River composite batholiths, western Superior Province. *Canadian Journal of Earth Sciences* **35**(10), 1089-1109.

Corfu F. and Stone D. (1998b) The significance of titanite and apatite U-Pb ages: constraints for the post-magmatic thermal - hydrothermal evolution of a

batholithic complex, Berens River area, northwestern Superior Province. *Geochimica et Cosmochimica* **62**(17), 2979-2995.

Corfu F., Stott G. M., and Breaks F. W. (1995) U-Pb geochronolgy and evolution of the English River Subprovince, an Archean low P-high T metasedimentary belt in the Superior Province. *Tectonics* **14**(5), 1220-1233.

Corfu F. and Wood J. (1986) U-Pb zircon ages in supracrustal and plutonic rocks; North Spirit Lake area, northwestern Ontario. *Canadian Journal of Earth Sciences* **23**, 967-977.

Cruden A. R. and Hynes A. (1999) Western Superior Lithoprobe seismic reflection lines 2a and 2c: Comparison with surface geology and preliminary interpretation. In *1999 Western Superior Transect Fifth Annual Workshop, Lithoprobe report #70* (ed. Harrap R. and Helmstaedt H.), pp. 48-45. Lithoprobe Secretariat, University of British Columbia.

Dahl P. S. (1996) The crystal-chemical basis for Ar retention in micas: inferences from interlayer partitioning and implications for geochronology. *Contributions to Mineralogy and Petrology* **123**, 22-39.

Davis D. W. and Jackson M. C. (1988) Geochronology of the Lumby Lake greenstone belt: a 3Ga complex within the Wabigoon Subprovince, northwest Ontario. *Geol. Soc. Amer. Bull.* **100**, 818-824.

Davis D. W., Krogh T. E., Hinzer J., and Nakamura E. (1985) Zircon dating of polycyclic volcanism at Sturgeon Lake and implications for base metal mineralization. *Economic Geology* **80**, 1942-1952.

Davis D. W., Sutcliffe R. M., and Trowell N. F. (1988) Geochronological constraints on the tectonic evolution of a late Archean greenstone belt, Wabigoon Subprovince, northwest Ontario, Canada. *Precamb. Res.* **39**, 171-191.

Dingwell D. B., Hess K. U., and Knoche R. (1996) Granite and granitic pegmatite melts: volumes and viscosities. *Transactions of the Royal Society of Edinburgh: Earth Sciences.* **87**, 65-72.

Dodson M. H. (1973) Closure Temerature in Cooling Geochronological and Petrological Systems. *Contribuitons to Mineralogy and Petrology* **40**, 259-274.

Dodson M. H. (1986) Closure profiles in Cooling Systems. *Materials Science Forum* **7**, 145-154.

Ducharme Y., Stevenson R., and Machado N. (1997) Sm-Nd geochemistry and U-Pb geochronolgy of the Preissac and Lamotte leucogranites, Abitibi Subprovince. *Canadian Journal of Earth Sciences* **34**, 1059-1071.

Foord E. E., Cerný P., Jackson L. L., Sherman D. M., and Eby R. K. (1995) Mineralogical and geochemical evolution of micas from miarolitic pegmatites of the anorogenic Pikes Peak batholith, Colorado. *Mineralogy and Petrology* **55**, 1-26.

Gariepy C. and Allegre C. J. (1985) The lead isotope geochemistry and geochronology of late-kinematic intrusives from the Abitibi greenstone belt, and the implications for late Archean crustal evolution. *Geochimica et Cosmochimica Acta* **49**, 2371-2383.

Ginsburg A. I., Timofeyev I. N., and Feldman L. G. (1979) Principles of Geology of the Granitic Pegmatites. Nedra.

Goad B. E. and Cerný P. (1981) Peraluminous Pegmatitic Granites and Their Pegmatite Aureoles in the Winnipeg River District, Southeastern Manitoba. *Canadian mineralogist* **19**, 177-194.

Grove M. (1993) Thermal histories of southern California basement terranes. PhD. Diss., University of California.

Grove M. T. and Harrison T. M. (1996) $^{40}Ar^*$ diffusion in Fe-rich biotite. *American Mineralogist* **81**, 940-951.

Hames W. E. and Bowring S. A. (1994) An empirical evaluation of the argon diffusion geometry in muscovite. *Earth and Planetary Science Letters* **124**, 161-167.

Hames W. E. and Cheney J. T. (1997) On the loss of 40Ar* from muscovite during polymetamorphism. *Geochimica et Cosmochimica Acta* **61**(18), 3863-3872.

Hames W. E. and Hodges K. V. (1993) Laser 40Ar/30Ar Evaluation of Slow Cooling and Episodic Loss of 40Ar from a Sample of Polymetamorphic Muscovite. *Science* **261**, 1721-1723.

Hanes J. A. and Archibald D. A. (1998) Post-Orogenic Tectonothermal history of the Archean Western Superior Province of the Canadian Shield as Determined by Conventional and Laser Ar-Ar Dating. *Lithoprobe Report* **65**.

Harrap R. and Helmstaedt H. (1995) Lithoprobe Western Superior Transect, Second Annual Workshop, pp. 83. University of British Columbia.

Harrap R. and Helmstaedt H. (1999) Lithoprobe Western Superior Transect, Fifth Annual Workshop, pp. 168. University of British Columbia.

Harris N. B. W. and Goodwin A. M. (1976) Archean rocks from the eastern Lac Seul region of the English River gneiss belt, northwestern Ontario, part I: petrography, chemistry and metamorphism. *Can, J. Earth Sci.* **13**, 1201-1211.

Harrison T. M. (1990) Some observations on the interpretation of feldspar 40Ar/39Ar results. *Chemical Geology* **80**, 219-229.

Harrison T. M., Duncan I., and McDougall I. (1985) Diffusion of 40Ar in biotite: Temperature, pressure and compositional effects. *Geochimica et Cosmochimica Acta* **49**, 2461-2468.

Harrison T. M. and FitzGerald J. D. (1986) Exsolution in hornblende and its consequences for 40Ar/39Ar age spectra and closure temperature. *Geochimica et Cosmochimica Acta* **50**, 247-253.

Harrison T. M., Heizler M. T., and Lovera O. M. (1993) In vacuo crushing experiments and K-feldspar thermochronometry. *Earth and Planetary Science Letters* **117**, 169-180.

Heaman L. M. (1997) Global Mafic Magmatism at 2.45Ga: Remnants of an Ancient Large Igneous Province? *Geology* **25**(4), 299-302.

Heizler M. T., Lux D. R., and Decker E. R. (1988) The age and cooling history of the Chain of Ponds pluton and the Big Island Pond plutons and the Spider Lake granite, west-central Maine and Quebec. *Am. J. Sci.* **288**, 925-952.

Hodges K. V. and Bowring S. A. (1995) 40Ar/39Ar thermochronology of isotopically zoned micas: Insights from the southwestern USA Proterozoic orogen. *Geochimica et Cosmochimica Acta* **59**(15), pp 3205-3220.

Hodges K. V., Hames W. E., and Bowring S. A. (1994) 40Ar/39Ar age gradients in micas from a high temperature-low pressure metamorphic terrain: Evidence for very slow cooling and implications for the interpretation of age spectra. *Geology* **22**, 55-58.

Hoffman P. F. (1989) Precambrian geology and tectonic history of North America. In *The Geology of North America: an Overview*, Vol. A, pp. 447-512. Geological Society of America.

Horn I., Rudnick R., and McDonough W. F. (2000) Precise elemental and isotope ratio determination by simultaneous solution nebulization and laser ablation-ICP-MS: application to U-Pb geochronolgy. *Chemical Geology* **164**, 281-301.

Horstwood M. S. A., Foster G. L., Parrish R. R., and Noble S. R. (2001) Developments in U-Pb geochronology by LA-MC-ICP-MS. *GAC-MAC Joint Annual Meeting 2001.*

Icenhower J. and London D. (1995) An experimental study of element partitioning among biotite, muscovite, and coexisting peraluminous silicic melt at 200MPa (H_2O). *American Mineralogist* **80**, 1229-1251.

Jackson S. L. and Fyon J. A. (1991) The Western Abitibi Subprovince in Ontario. In *Geology of Ontario*, Special Volume 4 (ed. P. C. Thurston, H. R. Williams, R. H. Sutcliffe, and G. M. Stott), pp. 405-475. Ontario Geological Survey.

Jahns R. H. and Burnham C. W. (1969) Experimental studies of pegmatite genesis: I. A model for the derivation and crystallisation of granitic pegmatites. *Economic Geology* **64**, 943-864.

Jolliff B. L., Papike J. J., and Shearer C. K. (1987) Fractionation trends in mica and tourmaline as indicators of pegmatite internal evolution: Bob Ingersoll pegmatite, Black Hills, South Dakota. *Geochimica et Cosmochimica Acta* **51**, 519-534.

Jolliff B. L., Papike J. J., and Shearer C. K. (1992) Petrogenetic relationships between pegmatite and granite based on geochemistry of muscovite in pegmatite wall zones, Black Hills, South Dakota, USA. *Geochimica et Cosmochimica Acta* **56**, 1915-1939.

Kamineni D. C., Stone D., and Peterman Z. E. (1990) Early Proterozoic deformation in the western Superior province, Canadian Shield. *Geological Society of America Bulletin* **102**, 1623-1634.

Kelley S. P. (1995) Ar-Ar dating by laser microprobe. In *Microprobe Techniques in the Earth Sciences* (ed. P. J. Potts, J. F. W. Bowles, and J. M. B. Reed). Chapman & Hall.

Kelley S. P., Arnaud N. O., and Turner S. P. (1994) High spatial resolution $^{40}Ar/^{39}Ar$ investigations using an ultra-violet laser probe extraction technique. *Geochimica et Cosmochimica Acta* **58**, 3519-3525.

Kelley S. P., Bartlett J. M., and Harris N. B. W. (1997) Pre-metamorphic ages from biotite inclusions in garnet. *Geochimica et Cosmochimica Acta* **61**(18), 3873-3878.

Kelley S. P. and Turner G. (1991) Laser probe 40Ar-39Ar measurements of loss profiles from the Giants Range Granite, northern Minnesota, USA. *Earth and Planetary Science Letters* **107**, 634-648.

Kosler J., Tubrett M., and Sylvester P. (*in press*) Application of laser ablation ICP-MS to U-Th-Pb dating of monazite. *Geostandards Newsletter.*

Krogh T. E., D.W. D., and Corfu F. (1984) Precise U-Pb zircon and baddeleyite ages for the Sudbury area. In *The Geology and Ore Deposits of the Sudbury Structure*, Special Volume 1, pp. 431-446. Ontario Geological Survey.

Krogh T. E., Harris N. B. W., and Davis G. L. (1976) Archean rocks from the eastern Lac Seul region of the English river Gneiss Belt, northwestern Ontario, part 2. Geochronolgy. *Canadian Journal of Earth Sciences* **13**, 1212-1215.

Krogstad E., Walker R. J., Nabalek P. I., and Russ-Nabalek C. (1993) Lead isotopic evidence for mixed sources of Proterozoic granites and pegmatites, Black Hills, South Dakota, USA. *Geochimica et Cosmochimica Acta* **57**, 4677-4685.

Langford F. F. and Morin J. A. (1976) The Development of the Superior Province of Nortwestern Ontario by Merging Island Arcs. *American Journal of Science* **276**, 1023-1034.

Larbi Y., Stevenson R., Breaks F. W., Machado N., and Gariepy C. (1999) Age and isotopic composition of late Archean leucogranites: implications for continental collision in the western Superior Province. *Canadian Journal of Earth Sciences* **36**, 495-510.

Layer P. W., Hall C. M., and York D. (1987) The derivation of $^{40}Ar/^{39}Ar$ age spectra of single grains of hornblende and biotite by laser step-heating. *Geophysical Research Letters* **14**(7), 757-760.

Lee J. K. W. (1995) Multipath diffusion in geochronology. *Contributions to Mineralogy and Petrology* **120**, 60-82.

Li X.-h., Liang X.-r., Sun M., Guan H., and Malpas J. G. (2001) Precise 206Pb/238U age determination on zircons by laser ablation microprobe-inductively coupled plasma-mass spectrometry using continuous linear ablation. *Chemical Geology* **175**, 209-219.

Lo C.-H., Lee J. K. W., and Onstott T. C. (2000) Argon release mechanisms of biotite in vacuo and the role of short-circuit diffusion and recoil. *Chemical Geology* **165**, 135-166.

London D. (1984) Experimental phase equilibria in the system $LiAlSiO_4$-Si_2O-H_2O: a petrogenetic grid for lithium-rich pegmatites. *American Mineralogist* **69**, 995-1004.

London D. (1985) Origin and Significance of Inclusions in Quartz: A Cautionary Example From the Tanco Pegmatite, Manitoba. *Economic Geology* **80**, 1988-1995.

London D. (1986) Magmatic-hydrothermal transition in the Tanco rare-element pegmatite: Evidence from fluid inclusions and phase equilibrium experiments. *American Mineralogist* **71**, 376-395.

London D. (1987) Internal differentiation of rare-element pegmatites: Effects of boron, phosphorus and fluorine. *Geochimica et Cosmochimica Acta* **51**, 403-420.

London D. (1992) The application of experimental petrology to the genesis and crystallisation of granitic pegmatites. *Canadian Mineralogist* **30**(Granitic pegmatites), 499-540.

London D. (1996) Granitic pegmatites. *Transactions of the Royal Society of Edinburgh: Earth Sciences* **87**, 305-319.

London D., Hervig R. L., and Morgan VI G. B. (1988) Melt-vapor solubilities and element partitioning in peraluminous granite - pegmatite systems: experimental results with Macusani glass at 200 MPa. *Contributions to Mineralogy and Petrology* **99**, 360-373.

London D., Morgan G. B., Babb H. A., and Loomis J. L. (1993) Behaviour and effects of phosphorus in the system Na_2O-K_2O-Al_2O_3-SiO_2-P_2O_5-H_2O at 200MPa (H_2O). *Contrib. Mineral. Petrol.* **113**, 450-465.

London D., Morgan G. B., and Hervig R. L. (1989) Vapor-undersaturated experiments in the system macasunite-H2O, at 200MPa, and the internal differentaiation of granitic pegmatites. *Contrib. Mineral. Petrol.* **102**, 1-17.

Lovera O. M., Grove M., and Harrison T. M. (1997) Systematic analysis of K-feldspar (super 40) Ar/ (super 39) Ar step heating results; I, Significance of activation energy determinations. *Geochimica et Cosmochimica Acta* **65**(15), 3171-3192.

Lovera O. M., Richter F. M., and Harrison T. M. (1989) The 40Ar/39Ar Thermochronometry for Slowly Cooled Samples Having a Distribution of Diffusion Domain Sizes. *Journal of Geophysical Research* **94**(B12), 17,917-17,935.

Lovera O. M., Richter F. M., and Harrison T. M. (1991) Diffusion Domains Determined by 39Ar Released During Step Heating. *Journal of Geophysical Research* **96**(B2), 2057-2069.

Ludwig K. R. (2000) Isoplot/Ex version 2.22, pp. 53. Berkely Geochronology Center.

McDougall I. and Harrison T. M. (1999) *Geochronology and Thermochronology by the $^{40}Ar/^{39}Ar$ method.* Oxford University Press.

Menard T., Cruden A. R., Davis D., and Robin P.-Y. F. (1997) Himilayan-style metamorphism and tectonics between 2700 and 2650Ma in the Winnipeg River and Wabigoon Subprovinces near Dryden. *Lithoprobe Report #63.*

Nitescu B. and Cruden A. R. (2001) Gravity models of the English River Subprovince: implications for its deep structure and tectonic origin. Preliminary Abstracts Lithoprobe Western Superior Transect/Western Superior NATMAP, Joint Annual Workshop.

Nunes P. D. and Wood J. (1980) Geochronology of the North Spirit Lake area, District of Kenora., pp. 7-13. Ontario Geological Survey. Miscellaneous Paper No. 92

Osmani I. (1991) Proterozoic Mafic Dike Swarms in the Superior Province of Ontario. In *Geology of Ontario*, Special Volume 4 (ed. P. C. Thurston, H. R. Williams, R. H. Sutcliffe, and G. M. Stott), pp. 661-683. Ontario Geological Survey.

Pan Y. and Breaks F. W. (1997) Rare-Earth Elements in Fluorapatite, Separation Lake Area, Ontario: Evidence for S-Type Granite - Rare-Element Pegmatite Linkage. *Canadian Mineralogist* **35**, 659-671.

Pan Y., Fleet M. E., and Heaman L. (1998) Thermo-tectonic evolution of an Archean accretionary complex: U-Pb geochronological constraints on granulites from the Quetico Subprovince, Ontario, Canada. *Precambrian Research* **92**, 117-128.

Pan Y. and Therens C. (1997) Geochemistry of Granitoids in the English River Subprovince, Separation Lake Area. *Lithoprobe Report #63.*

Parrish R., Nowell G., Noble S. R., Horstwood M. A., Timmermann H., Shaw P., and Bowen I. (1999) LA-PIMMS: A New Method of U-Th-Pb Geochronology Using Micro-Sampling Techniques. *EUG X.*

Parsons I., Brown W. L., and Smith J. V. (1999) 40Ar/39Ar thermochronology using alkali feldspars: real thermal history or mathematical mirage of microtexture? *Contributions to Mineralogy and Petrology* **136**, 92-110.

Partington G. A., McNaughton N. J., and Williams I. S. (1995) A Review of the Geology, Mineralization and Geochronolgy of the Greenbushes Pegmatite, Western Australia. *Economic Geology* **90**, 616-635.

Pickles C. S., Kelley S. P., Reddy S. M., and Wheeler J. (1997) Determination of high spatial resolution argon isotope variations in metamorphic biotites. *Geochimica et Cosmochimica Acta* **61**(18), 3809-3833.

Roda E., Pesquera A., and Velasco F. (1995) Micas of the muscovite-lepidolite series from the Fregenda pegmatites (Salamanca, Spain). *Mineralogy and Petrology* **55**, 145-157.

Romer R. L. and Smeds S.-A. (1994) Implications of U-Pb ages of columbite-tantalites from granitic pegmatites for the Palaeoproterozoic accretion of 1.90-1.85 Ga magmatic arcs to the Baltic Shield. *Precambrian Research* **67**, 141-158.

Romer R. L. and Smeds S.-A. (1997) U-Pb columbite chronolgy of post-kinematic Palaeoproterozoic pegmatites in Sweden. *Precambrian Research* **82**, 85-99.

Romer R. L. and Smeds S. A. (1996) U-Pb columbite ages of pegmatites from Sveconorwegian terranes in southwestern Sweden. *Precambrian Research* **76**, 15-30.

Romer R. L., Smeds S.-A., and Cerny P. (1996) Crystal-chemical and genetic controls of U-Pb systematics of columbite-tantalite. *Mineralogy and Petrology* **57**, 243-260.

Romer R. L. and Wright J. E. (1992) U-Pb dating of columbites: A geochronologic tool to date magmatism and ore deposits. *Geochimica et Cosmochimica Acta* **56**, 2137-2142.

Sanborn-Barrie M. (1988) Geology of the tectonic boundary zone between the English river and Winnipeg River Subprovinces, northwestern Ontario. In *Summary of Field Work and Other Activities 1988*, Vol. Miscallaneous Paper 141, pp. 98-107. Ontario Geological Survey.

Scaillet S., Feraud G., Ballevre M., and Amouric M. (1992) Mg/Fe and [(Mg,Fe) Si-Al_2] compositional controls on argon behaviour in high pressure white micas: A 40Ar/39Ar continuous laser-probe study from the Dora-Maira nappe of the internal western Apls, Italy. *Geochimica et Cosmochimica Acta* **56**, 2851-2872.

Shearer C. K. and Papike J. J. (1988) Pegmatite-wallrock interaction, holmquistite-bearing amphibolite, Edison pegmatites, Black Hills, South Dakota. *American Mineralogist* **73**, 324-337.

Shearer C. K., Papike J. J., Simon S. B., and Laul J. C. (1986) Pegmatite-wallrock interactions, Black Hills, South Dakota: interaction between pegmatite derived fluids and quartz-mica schist wallrock.. *American Mineralogist* **71**, 518-539.

Stevenson R. (1995) Crust and Mantle evolution in the Late Archean: evidence from a Sm-Nd isotopic study of the North Spirit Lake greenstone belt, northwestern Ontario, Canada. *Geol. Soc. Amer. Bull.* **107**, 1458-1467.

Stone D. (1998) Precambrian Geology of the Berens River Area, Northwest Ontario, Ontario Geological Survey. *Open File Report 5963*, pp. 116.

Sylvester P. J. (1998) Post-collisional strongly peraluminous granites. *Lithos* **45**, 29-44.

Tagirov B. and Schott J. (2001) Aluminum speciation in crustal fluids revisited. *Geochimica et Cosmochimica Acta* **65**(21), 3965-3992.

Thurston P. C. (1991) Northwestern Superior Province: Review and Terrane Analysis. In *Geology of Ontario*, Special Volume 4 (ed. P. C. Thurston, H. R. Williams, R. H. Sutcliffe, and G. M. Stott), pp. 81-144. Ontario Geological Survey.

Timmins E. A., Turek A., and Symons D. T. A. (1985) U-Pb zircon geochronolgy and palaeomagnetism of the Bird River greenstone belt, Manitoba. *GAC-MAC Joint Annual Meeting*, 62.

Tindle A. G. and Breaks F. W. (1998) Oxide minerals of the Separation Rapids rare-element granitic pegmatite group, northwestern Ontario. *Canadian Mineralogist* **36**, 609-635.

Tindle A. G. and Breaks F. W. (2000) Columbite-tantalite mineral chemistry from rare-element granitic pegmatites: Separation Lake area, N.W. Ontario, Canada. *Mineralogy and Petrology* **70**, 165-198.

Tindle A. G., Breaks F. W., and Selway J. B. (in press) Compositional evolution of tourmaline in petalite-subtype granitic pegmatites from the Pakeagama Lake and Separation Lake areas of northwestern Ontario, Canada. *Canadian Mineralogist.*

Tindle A. G. and Webb P. C. (1990) Estimation of lithium contents in trioctahedral micas using electron microprobe data : application to micas from granitic rocks. *European Journal of Mineralogy* **2**, 595-610.

Tischendorf G. (1997) On Li-bearing micas: estimating Li from electron microprobe analyses and an improved diagram for graphical representation. *Mineralogical Magazine* **61**, 809-834.

Tomlinson K. Y., Hughes D. J., Thurston P. C., and Hall R. P. (1998) Plume magmatism and crustal growth at 2.9 to 3.0 Ga in the Steep Rock and Lumby

Lake area, Western Superior Province. *Lithos* Thematic edition: Plumes and crustal growth.

Villa I. M. (1988) Comments on "Argon diffusion in partially outgassed alkali feldspars: Insights from $^{40}Ar/^{39}Ar$ analysis" by P.K. Zeitler. *Chemical Geology* **73**, 255-267.

Webber K. J., Simmons W. B., Falster A. U., and Foord E. E. (1999) Cooling rates and crystallisation dynamics of shallow level pegmatite-aplite dikes, San Diego County, California. *American Mineralogist* **84**, 708-717.

Wheeler J. (1996) DIFFARG: A Program for Simulating Argon Diffusion Profiles in Minerals. *Computers & Geosciences* **22**(8), 919-929.

Wise M. A. (1995) Trace element chemistry of lithium-rich micas from rare-element granitic pegmatites. *Mineralogy and Petrology* **55**, 203-215.

Woods S. A. and Williams-Jones A. E. (1993) Theoretical studies of the alteration of spodumene, petalite, eucryptite and pollucite in granitic pegmatites: exchange reactions with alkali feldspars. *Contrib. Mineral. Petrol.* **114**, 255-263.

Appendix A – Electron microprobe data

Chemical analyses of micas were performed on a wavelength dispersive Cameca SX100 electron probe microanalyser at The Open University. Samples were prepared as polished thin sections which were carbon coated to provide a conductive layer to minimise charge build-up under the electron beam. An operating voltage of 20kV and probe current of 20nA (measured on a Faraday cage) were used for quantitative analyses. The electron beam diameter was set at 10μm in order to minimise sample decomposition. Calibration used the following standards: feldspar (Si, K, Al), bustamite (Mn, Ca), willemite (Zn), haematite (Fe), forsterite (Mg), rutile (Ti), jadeite (Na), synthetic potassium chlorite (Cl), synthetic LiF (F). Calibrations were cross-checked with a Kaersutite amphibole with reproducility averaging better than 2% (2σ).

Due to the large data set obtained from electron microprobe analyses, this appendix is presented on CD-ROM as a series of spreadsheets using Microsoft Excel. The spreadsheets are arranged with one worksheet for each individual sample which provides the most useful and easy access to the large dataset. Mica data from the Pakeagama Lake pegmatite and the Separation Rapids pegmatite group is presented on the disc labelled 'Appendix A'.

Appendix B – U-Pb techniques

Laboratory procedure for U-Pb isotopic analysis of columbite-tantalite

All isotopic analyses using TIMS were performed at GFZ Potsdam using the procedures described by Romer and Wright (1992) and Romer and Smeds (1996), summarised here.

Relatively large (1 to 5mm dimensions) columbite grains were crushed between two steel plates. Approximately 20 fragments were hand picked under a binocular microscope, avoiding obvious inclusions, surface fractures and defects; then placed in alcohol.

The samples were then placed on a hot plate at 120°C and leached in 20%HF for 20 minutes which visibly removes surface contamination, dissolves metamict parts of the columbite and removes inclusions such as feldspars and sulphides. Samples were then washed with 6 N HCl for 1 hour on the hot plate, followed by 7 N HNO_3 for 10 minutes, distilled H_2O for 5 minutes and finally rinsed with distilled acetone and placed on the hot plate to dry for 5 minutes.

Samples were ideally split into 6 fractions, aliquoted to beakers and weighed. A mixed $^{205}Pb + ^{235}U$ tracer was added and weighed.

Columbite dissolves easily in 40%HF placed on a hot plate overnight in Teflon beakers. HSO_4 is added prior to the ion exchange chemistry since it has a high evaporation temperature and thus keeps Nb and Ta in solution preventing the columns from clogging.

Ion Exchange Chemistry

250μL columns were used with AG1-8X resin and cleaned with a full reservoir volume (RV) of distilled H_2O, followed by a full reservoir volume of 6 N HCl. These are repeated with half reservoir volume, then rinsed with ¼ RV distilled H_2O. The following procedure is then used;

- 3 N HCl, 4 column volumes (CV) to condition columns.
- Load sample (with HSO_4) + 5 drops 3 N HCl.

- Wash with 3 N HCl, 4 CV.
- Elute U with 0.8 N HBr, 6-8 CV, catch in beakers. Add 2 drops of 0.025 N H_3PO_4 to the beakers and place on a hot plate at 250°C for 1hr to concentrate U.
- 3 N HCl, 8-10 drops to wash.
- Elute Pb with 6 N HCl, 6-8 CV. Add 2 drops 0.025 N H_3PO_4 and place beakers on a hot plate at 250°C for 1hr.
- Distilled H_2O, 2 CV.
- 7 N HNO_3, 4 CV to condition column.
- Load Sample, U concentrate (plus 2 drops of 7 N HNO_3 to remove HBr).
- Wash with 7 N HNO_3, 6 CV.
- 6 N HCl, 6 CV.
- Elute U with 0.1 N HCl, 6 CV, catch in beakers and place open on a hot plate at 120°C, overnight.

Appendix C – $^{40}Ar/^{39}Ar$ methods and data

Sample preparation and loading

The majority of samples analysed in this study were large >1cm mineral separates that were hand-picked direct from the sample or using a low powered binocular microscope. Clear grains that appeared to have unbroken and unaltered edges were selected preferentially in an attempt to reduce the possibility of analysing grains with edges damaged by the preparation process or natural alteration. Thick sections were also prepared. The "thick" section preparation technique is similar to that of a thin section except the resultant section is 100-150 μm thick and is attached to its glass slide by *Canada Balsam* rather than epoxy resin. The sections were subsequently heated to soften the *Canada Balsam* and removed from their glass slide. Each section was then cleaned to remove the resin and broken into smaller pieces suitable for packing into irradiation cylinders.

Both section and separate samples need to be cleaned prior to irradiation and analysis, as the presence of grease from the preparation stage potentially adds hydrocarbons to the analysis, which can interfere with the isotope measurements. Cleaning also removes contaminants, some of which may contain potassium that potentially effects the $^{40}Ar/^{39}Ar$ ratio. Samples were cleaned twice in methanol in an ultrasonic bath for 5 minutes, and then for a further 5 minutes in de-ionised water to remove the methanol. They were left to dry overnight before packing in aluminum foil for irradiation. Standards were packed similarly, and spaced regularly between samples in the irradiation cylinders. Following irradiation, samples remained at the reactor until their radiation levels fall to a safe level. Samples were irradiated at the McMaster University reactor, Canada.

After irradiation the samples and standards are loaded into an ultra high vacuum laser port and baked overnight at 120 °C using a 250 W heat lamp to remove any absorbed atmospheric argon and water vapour from the sample surface.

Principles of the ^{40}Ar-^{39}Ar dating technique

Radiogenic dating systems are based on the constant decay of a parent isotope and the accumulation of a stable daughter isotope. The calculated age reflects radiogenic ingrowth following the closure of the system to the incorporation or loss of either the parent or daughter species. The ^{40}Ar-^{39}Ar dating technique is, like the K-Ar system, based on the decay of the radiogenic parent species ^{40}K to its daughter, ^{40}Ar.

^{40}K has a half-life of 1250 Ma, 89.5% decaying to ^{40}Ca by electron (β^-) emission, and 10.5% decaying to ^{40}Ar predominantly by orbital electron capture. As both daughter products are stable, the ratios of both $^{40}Ca/^{40}K$ and $^{40}Ar/^{40}K$ could theoretically be used to obtain dates. However, ^{40}Ca is an abundant element in nature and distinguishing ^{40}Ca produced by decay of ^{40}K from naturally present ^{40}Ca is only possible in the oldest, potassium-rich rocks. In contrast, ^{40}Ar is only ever present in trace amounts and dating based on the production of ^{40}Ar from ^{40}K can be applied to geological problems.

The fundamental difference between the ^{40}Ar-^{39}Ar dating technique and the K-Ar system is the measurement of potassium. In the ^{40}Ar-^{39}Ar technique, ^{39}K is transformed to ^{39}Ar by fast neutron bombardment during irradiation in a nuclear reactor.

Isotopes of K undergo very little fractionation in nature and, therefore, the $^{39}K/^{40}K$ ratio may be regarded as essentially constant, and is conventionally assumed to be 0.0001167 (Steiger and Jäger 1977). Therefore, the $^{40}Ar/^{39}Ar$ ratio is proportional to the $^{40}Ar/^{40}K$ – the daughter to parent ratio - in the sample, and can be used to calculate the age. Although the ^{39}Ar produced is radioactive and ultimately decays to ^{39}K by beta emission with a half-life of 269 years, the effect is minimal between the irradiation time and the analysis, which is generally less than a year.

The amount of ^{39}Ar produced from ^{39}K during irradiation is a function of ^{39}K in the sample, proportional to a dimensionless irradiation parameter, J. The J value is specific to each sample within a given irradiation, and is calculated by including standard minerals of known age within the collection of samples to be dated. The inclusion of such standards, which have precise ages based on numerous repeat analyses and calibration to the K-Ar and/or U-Pb dating method, effectively monitors the neutron flux. Each reactor has a different spectrum and level of neutron flux, and the flux varies depending on the location of the samples within the reactor. The neutron flux gradient is significant along the length and breadth of the sample containing tube, and standards

are interspersed between samples in order to monitor these variations. The value of J appropriate for the samples irradiated will depend on their location relative to the standards during irradiation - small sample sizes are generally irradiated to ensure that the neutron flux across minerals from an individual sample is constant.

The apparent age of the sample is calculated as :

$$age = \frac{1}{\lambda}\ln\left\{\left(\frac{^{40}Ar^{*}}{^{39}Ar}\right)J + 1\right\}$$

The age is a function of the measured $^{40}Ar^*/^{39}Ar$ ratio of the sample (where *denotes the ^{40}Ar resulting purely from radiogenic ingrowth), the J value for the irradiation, and• , the combined decay constant for ^{40}K, comprising the decay of ^{40}Ar to ^{40}Ca by beta emissions, the decay of ^{40}K to ^{40}Ar by electron capture and gamma emission, and the decay of ^{40}K to ^{40}Ar by electron capture. This has a value of $5.543 \times 10^{-10}yr^{-1}$.

In an "ideal" radiometric dating technique, the measured abundance of the daughter species would reflect solely its accumulation by decay of the parent species since the system first became closed to their exchange. In many isotope systems, this assumption is not strictly valid, as there is already a significant abundance of daughter species present within the system. In the ^{40}Ar-^{39}Ar dating system, the argon released from a sample during laser ablation or step heating will ideally reflect a mixture of two components: trapped argon, present initially or absorbed into the sample during preparation, and the argon which accumulated from the decay of radiogenic ^{40}K, following closure of the system. The radiogenic $^{40}Ar^*/^{39}Ar$ ratio can be calculated by subtracting the "initial" ^{40}Ar component, assuming that it has the same $^{40}Ar/^{36}Ar$ value as present-day air (295.5). This approach may be complicated by the presence of an initial component with a non-atmospheric $^{40}Ar/^{36}Ar$ value, or by spatial heterogenities in the composition of this component.

Irradiation and interference reactions

The amount of ^{39}Ar produced from the transmutation of ^{39}K during irradiation is proportional to several parameters unique to the irradiation: the length of time of the irradiation, the neutron flux density at a specified energy and the neutron capture cross-section of ^{39}K for neutrons of that energy. These factors, the $^{39}K/^{40}K$ ratio, and the combined decay constant for ^{39}K define the dimensionless parameter J in the age equation. The irradiation procedure induces not only the production of ^{39}Ar, but also a series of interfering reactions that result from the neutron bombardment of K, Ar, Cl and Ca. The magnitude of the interference reactions varies with the neutron flux energy, and correction factors may be calculated for different nuclear reactors (McDougall and Harrison 1999) based on the irradiation of mineral salts. Correction factors for the McMaster reactor are given below. If samples have high calcium contents, a correction must be made for the decay of ^{37}Ar (produced from ^{40}Ca) in the period between sample irradiation and analysis, as ^{37}Ar has a half-life of 35 days. In order to achieve the maximum analytical precision, the neutron flux of the irradiation must be optimised carefully so that a measurable amount of ^{39}Ar is produced while the amounts of isotopes derived from interfering reactions (which will also increase with the neutron flux) is minimised. The most important aspects to be considered in this are the sample's approximate age and K/Ca ratio. Older samples require higher irradiation fluxes to obtain low $^{40}Ar/^{39}Ar$ ratios, and higher Ca minerals such as amphibole are more prone to interference reactions.

Correction factors for the McMaster University reactor are as follows:

Ca correction : $^{39}Ar/^{37}Ar = 0.000651$

: $^{36}Ar/^{37}Ar = 0.000254$

K correction : $^{40}Ar/^{39}Ar = 0.0156$

Table of irradiation packages showing the J-value, sample numbers and standards used as fluence monitors.

Irradiation #	**McMaster 6**	**McMaster 8**	**McMaster 14**
J- value	0.04693 ±0.00023	0.00995 ±0.00004975	0.0132 ±0.000066
End date of irradiation	21/11/98	27/01/00	16/02/01
Irradiation duration (hours)	203	50	50
Samples	SS40, SS38, SS34a, SS22, SS70, SS42b, SS37, SS31, SS36, SS35b, SS20, 98FWB38	SS1, SS2, SS107, 98-21a, SS73, SS89, SS111, SS207, SS50A, SS60, SS55, SS100, SS45, SS94, SS115, SS116, SS106a	SS117
Standard/ Age	Hb3gr hornblende, 1079 ± 1Ma (1σ). (Roddick 1983)	GA-1550 biotite, 98.8 ± 0.5Ma (1σ) (Renne *et al.* 1998; McDougall and Harrison 1999)	GA-1550 biotite, 98.8 ± 0.5Ma (1σ)

Calculation of errors

The precision on the age obtained from a ^{40}Ar-^{39}Ar analysis depends on several factors. The magnitude of the uncertainty is frequently dependent on the amount of argon extracted from within the sample, as large samples are less affected by blank corrections and errors on the blanks. The error in the calculated age (1 sigma) can be calculated using the following expression:

$$\sigma_t^2 = \frac{J^2\sigma_R^2 + R^2\sigma_J^2}{\lambda^2(1+RJ)^2}$$

where σ_t is the final error on the age, J is the irradiation parameter discussed in sections 3.2.1 and 3.1.2, R is the $^{40}Ar^*/^{39}Ar$ ratio, λ is the combined decay constant of ^{40}K, σ_R is the error on the $^{40}Ar^*/^{39}Ar$ ratio as measured and σ_J is the error on the J value, taken here as ± 0.5%.

Argon extraction by ultra-violet laser probe

Currently there are two main types of lasers in use for geochronological studies: continuous wave (CW) and pulsed systems. Continuous wave systems are the most common and operate by the continuous pumping of lamps within the laser cavity to achieve a continuous coherent beam. They are versatile and can be used for both slow heating and instantaneous melting and produce pit sizes varying from 50-250 μm diameter. The disadvantage of these lasers is that local heating of the surrounding material may occur, and in some cases, the analysis may reflect a mixture of gas from different minerals, and possibly, a mixture of ages. In contrast, pulsed lasers such as the ultra-violet system produce high-power densities that last for a few nanoseconds to microseconds. The Q-switched UV-laser system generates short wavelength (266nm) pulses, which produces a small beam diameter (10-15μm) and avoids large-scale heating of the sample.

A *Spectron Laser Systems SL401* was used as the UV source for sample ablation in this study. The technique for analysis is described by Kelley *et al.* (1994) and is summarised here. The beam is directed into a customised *Leica DM* microscope by high-reflectance oxide coated mirrors. The laser port holds the samples under vacuum and is fitted with a fused silica window which allows transmission of the UV beam. A 1mm thick sapphire window is placed between the laser port and the sample to prevent ablated material from coating the outer window. Samples are observed using a CCD camera, coaxial with the laser beam. A programmable automated stage allows the beam to be rastered across the sample.

Analysis technique

Square pit analyses were performed by rastering the beam over an area with dimensions of 100 x 100μm. For apparent age profiles, linear pits were ablated with a width equivalent to the beam diameter and over a length of 400 – 500μm. The following analysis follows a traverse immediately adjacent to the previous at a measured distance, and so on. In this way a profile can be constructed from the edge of the grain inwards.

Following gas extraction, argon is purified using two *SAES AP 10* getters, with one operated at 400 °C and another at room temperature. The 'clean' gas is then equilibrated via automated valves into a *MAP 215-50* noble gas spectrometer.

Mass spectrometry

Isotopic analysis was carried out using a *MAP 215-50* noble gas spectrometer with a secondary electron multiplier detector. The mass spectrometer scanned peaks at masses 35, 36, 37, 38, 39, 40 and 41. Peaks at 36-40 are argon and 35 and 41 peaks were analysed so that build-up of chlorine and hydrocarbons in the spectrometer could be measured, respectively. Peaks were measured ten times during one analysis, and peak intensities were extrapolated back to the inlet time to correct for argon adsorption onto the spectrometer walls.

Blank levels in the system were determined by running the system in the same way as for a sample analysis but without operating the laser. Blanks were run after every second sample run, and blank corrections were made by averaging the values

obtained during each day of analysis. Average blank levels were $^{40}Ar = 7 \times 10^{-12}$cc, $^{39}Ar = 1 \times 10^{-14}$cc, $^{36}Ar = 1 \times 10^{-13}$cc.

A correction for mass spectrometer discrimination is also required. Discrimination can cause the atmospheric $^{40}Ar/^{36}Ar$ ratio to be measured as a different value to the accepted 295.5. Discrimination varies with time and between spectrometers, and may be determined by the analysis of glasses known to contain air only. For the *MAP 215-50* noble gas spectrometer of this study a discrimination value of 282 was used, based on measurements of air-rich samples (S.P. Kelley, unpublished).

Sample/ Run	$^{40}Ar/^{39}Ar$	$^{38}Ar/^{39}Ar$	$^{37}Ar/^{39}Ar$	$^{36}Ar/^{39}Ar$	Total ^{39}Ar (cc)x10^{-12}	$^{40}Ar^{*}/^{39}Ar$	Age (Ma)	±
SS73								
100sq no.1	301.62	0.0240	-0.0770	-0.0284	1.0551	310.01	2539	24
100sq no.2	322.82	0.0072	-0.0278	-0.0219	0.9572	329.30	2622	22
100sq no.3	319.97	0.0037	-0.0385	-0.0164	0.9722	324.83	2603	20
traverseA 1	168.93	-0.0013	-0.1772	-0.0148	0.7765	173.29	1808	37
traverseA 2	199.13	0.0230	0.0060	0.0048	1.3591	197.71	1962	22
traverseA 3	268.74	0.0126	-0.0010	-0.0157	1.0188	273.38	2370	21
traverseA 4	262.10	0.0037	-0.0531	0.0021	0.9629	261.49	2312	26
traverseA 5	298.40	0.0078	-0.0872	-0.0066	1.0562	300.35	2496	39
traverseA 6	346.98	0.0129	0.0128	0.0156	0.9908	342.35	2676	23
traverseA 7	305.16	0.0150	0.0344	-0.0022	1.1633	305.79	2520	19
traverseA 8	294.05	0.0228	-0.0516	0.0017	1.1680	293.54	2465	19
traverseA 9	297.07	0.0257	0.0029	0.0016	1.2146	296.59	2479	18
traverseA 10	301.06	0.0113	0.0152	-0.0022	1.1307	301.72	2502	19
traverseA 11	297.61	0.0256	-0.0718	0.0090	1.2193	294.93	2471	23
traverseB 1	211.15	-0.0012	-0.0064	-0.0185	0.8650	216.61	2073	29
traverseB 2	224.02	0.0120	0.0247	-0.0066	1.0654	225.96	2125	25
traverseB 3	288.18	0.0326	-0.0447	-0.0141	0.6363	292.36	2459	44
traverseB 4	264.83	0.0576	0.0532	-0.0049	0.9206	266.28	2336	31
traverseB 5	316.49	0.0087	0.0731	0.0170	0.7948	311.48	2545	33
traverseB 6	301.66	0.0027	-0.0388	0.0000	0.8508	301.66	2502	33
traverseB 7	307.75	0.0237	0.0769	0.0154	0.8740	303.19	2509	32
traverseB 8	377.98	0.0570	-0.0745	0.0393	0.6876	366.37	2771	37

Sample/ Run	$^{40}Ar/^{39}Ar$	$^{38}Ar/^{39}Ar$	$^{37}Ar/^{39}Ar$	$^{36}Ar/^{39}Ar$	Total ^{39}Ar (cc)x10^{-12}	$^{40}Ar^{*}/^{39}Ar$	Age (Ma)	±
SS70								
100 sq No 1	122.20	0.0410	0.0061	0.1858	32.6344	67.31	2571	11
100 sq No 2	68.62	0.0112	0.0007	0.0064	17.8240	66.74	2560	15
100 sq No 3	68.98	0.0125	0.0047	0.0043	17.0554	67.72	2580	15
100 sq No 4	62.66	0.0118	0.0077	-0.0004	18.1146	62.79	2477	16
100 sq No 5	64.90	0.0094	0.0034	0.0020	20.7814	64.31	2509	14
100 sq No 6	58.99	0.0117	-0.0003	-0.0004	21.3391	59.11	2396	14
100 sq No 7	67.23	0.0114	0.0041	0.0006	16.2492	67.05	2566	16

Sample/ Run	$^{40}Ar/^{39}Ar$	$^{38}Ar/^{39}Ar$	$^{37}Ar/^{39}Ar$	$^{36}Ar/^{39}Ar$	Total ^{39}Ar (cc)x10^{-12}	$^{40}Ar^{*}/^{39}Ar$	Age (Ma)	±
SS70								
traverseA 1	62.20	0.0158	0.0015	0.0285	20.2705	53.79	2273	15
traverseA 2	55.51	0.0118	0.0001	0.0019	19.6706	54.96	2300	16
traverseA 3	57.26	0.0082	-0.0004	0.0017	16.4701	56.75	2342	16
traverseA 4	58.50	0.0099	0.0024	0.0006	18.4105	58.33	2379	14
traverseA 5	59.36	0.0117	-0.0025	0.0015	19.3900	58.92	2392	14
traverseA 6	60.67	0.0117	-0.0004	0.0031	19.5259	59.76	2411	14
traverseA 7	61.04	0.0085	0.0021	0.0028	18.1199	60.20	2420	15
traverseA 8	61.23	0.0108	-0.0012	0.0012	16.7888	60.88	2435	15
traverseA 9	59.49	0.0115	0.0026	0.0015	16.6248	59.06	2395	16
traverseA 10	60.81	0.0119	-0.0034	0.0017	16.7982	60.31	2423	15
traverse A 11	62.04	0.0179	0.0007	-0.0002	15.3265	62.09	2462	16
traverse A 12	60.64	0.0118	0.0033	-0.0010	15.7249	60.94	2437	16
traverse A 13	62.65	0.0101	0.0034	0.0013	15.6593	62.28	2466	16
traverse A 14	62.49	0.0112	0.0022	-0.0005	15.4296	62.63	2473	16
traverse A 15	61.06	0.0150	-0.0004	0.0056	15.5187	59.40	2403	17
traverse A 16	62.56	0.0120	0.0038	0.0022	15.0734	61.91	2458	16
traverse A 17	61.73	0.0109	0.0005	-0.0027	14.5344	62.52	2471	17
traverse A 18	62.61	0.0111	-0.0021	0.0021	13.7939	62.00	2460	18
traverse A 19	61.79	0.0119	-0.0034	-0.0006	12.6629	61.98	2459	12
traverse A 20	63.17	0.0073	0.0010	0.0033	12.4848	62.19	2464	12
traverse A 21	62.67	0.0069	-0.0026	0.0001	13.0659	62.64	2474	12
traverse A 22	62.66	0.0077	-0.0005	-0.0013	13.4971	63.03	2482	11
traverse A 23	62.74	0.0130	0.0025	-0.0006	13.7362	62.92	2480	11
traverse A 24	63.13	0.0129	0.0028	-0.0012	13.8768	63.50	2492	11
traverse A 25	63.74	0.0125	0.0068	0.0020	13.8627	63.15	2484	11
traverse A 26	62.54	0.0100	-0.0029	0.0007	14.5985	62.34	2467	11
traverse A 27	67.05	0.0109	-0.0012	0.0027	8.1627	66.25	2550	17
traverse A 28	64.02	0.0143	-0.0061	-0.0019	9.8078	64.58	2515	15
traverseA 29	65.64	0.0147	0.0004	0.0004	10.7545	65.53	2535	14
traverseA 30	70.62	0.0165	0.0033	0.0149	9.6016	66.21	2549	15
traverseA 31	67.79	0.0092	-0.0005	-0.0001	11.2326	67.80	2581	13
traverseA 32	68.14	0.0118	0.0038	-0.0004	11.8465	68.27	2591	15
traverseA 33	69.16	0.0167	0.0034	-0.0007	13.1214	69.37	2613	12
traverseA 34	67.98	0.0116	0.0034	0.0003	13.2198	67.89	2583	12
traverseA 35	70.57	0.0135	0.0044	0.0000	15.5351	70.58	2637	11
traverseA 36	68.53	0.0108	-0.0016	0.0064	14.7055	66.64	2558	12
traverseA 37	68.92	0.0099	0.0080	-0.0004	14.1150	69.03	2606	11
traverseA 38	69.47	0.0073	0.0074	0.0013	13.4776	69.09	2607	12
traverseA 39	68.60	0.0121	-0.0006	0.0000	15.4085	68.61	2598	10
traverseA 40	69.42	0.0115	0.0063	0.0010	12.9714	69.13	2608	11
traverseA 41	67.66	0.0092	0.0025	-0.0010	14.1993	67.95	2584	11

Sample/ Run	$^{40}Ar/^{39}Ar$	$^{38}Ar/^{39}Ar$	$^{37}Ar/^{39}Ar$	$^{36}Ar/^{39}Ar$	Total ^{39}Ar (cc)x10^{-12}	$^{40}Ar^{*}/^{39}Ar$	Age (Ma)	±
SS20								
100sq#1	69.13	0.0106	-0.0049	0.0028	8.8327	68.30	2591	16
100sq#2	77.60	0.0111	-0.0047	-0.0005	12.9768	77.75	2772	11
100sq#3	74.73	0.0125	-0.0006	0.0021	11.9559	74.12	2705	12
100sq#4	156.18	0.0087	0.0037	0.0005	13.9977	156.04	3823	10
100sq#5	74.89	0.0093	0.0077	-0.0018	11.5643	75.41	2729	12
100sq#6	68.40	0.0132	-0.0012	0.0005	13.3497	68.25	2590	11
traverseA 1	53.71	0.0100	0.0061	0.0006	10.8091	53.53	2266	15
traverseA 2	55.53	0.0145	-0.0016	0.0009	12.7997	55.27	2308	13
traverseA 3	59.90	0.0087	0.0024	0.0016	12.3568	59.41	2403	13
traverseA 4	60.07	0.0136	-0.0010	0.0002	11.6809	60.01	2416	13
traverseA 5	57.26	0.0112	0.0068	-0.0009	12.4686	57.52	2360	13
traverseA 6	61.00	0.0126	-0.0013	-0.0010	11.8161	61.28	2444	13
traverseA 7	60.15	0.0105	-0.0061	0.0009	12.4128	59.88	2413	13
traverseA 8	59.40	0.0159	0.0052	0.0020	12.5852	58.82	2390	12
traverseA 9	63.82	0.0135	0.0040	0.0002	13.1120	63.77	2498	12
traverseA 10	67.56	0.0083	0.0051	0.0026	12.9208	66.79	2561	19
traverseA 11	66.38	0.0123	0.0009	-0.0012	13.2565	66.73	2560	11
traverseA 12	67.58	0.0097	0.0042	0.0025	13.5362	66.84	2562	11
traverseA 13	68.82	0.0133	-0.0019	0.0019	13.2705	68.26	2591	11
traverseA 13a	66.37	0.0099	0.0075	-0.0006	11.8207	66.54	2555	13
traverseA 13b	63.02	0.0113	0.0025	0.0017	12.0212	62.53	2471	12
traverseA 14	74.13	0.0100	0.0060	0.0020	12.5899	73.55	2694	12
traverseA 15	69.68	0.0149	0.0024	0.0031	12.4873	68.77	2601	12
traverseA 16	66.30	0.0058	0.0153	-0.0049	2.3827	67.74	2580	22
traverseA 17	69.95	0.0112	0.0208	-0.0063	3.2917	71.80	2660	19
traverseA 18	67.10	0.0104	0.0181	-0.0033	3.5294	68.07	2587	17
traverseA 19	69.60	0.0000	0.0303	0.0006	3.3057	69.43	2614	16
traverseA 20	71.98	0.0069	0.0000	-0.0048	3.3290	73.41	2691	16
traverseA 21	70.50	0.0070	-0.0014	0.0020	3.2964	69.92	2624	17
traverseA 22	69.20	0.0105	0.0104	-0.0059	3.5015	70.93	2644	15
traverseA 23	66.11	0.0116	0.0280	-0.0007	3.5807	66.33	2551	16
traverseA 24	85.43	0.0164	0.0135	0.0073	3.3616	83.28	2870	16
traverseA 25	78.37	0.0145	0.0313	-0.0007	3.4921	78.59	2787	16
traverseA 26	72.74	0.0094	0.0053	-0.0021	3.4409	73.35	2690	16

Sample/ Run	$^{40}Ar/^{39}Ar$	$^{38}Ar/^{39}Ar$	$^{37}Ar/^{39}Ar$	$^{36}Ar/^{39}Ar$	Total ^{39}Ar (cc)x10^{-12}	$^{40}Ar^{*}/^{39}Ar$	Age (Ma)	±
SS94								
100sqno. 1	373.70	0.0089	0.0126	0.0228	1.4634	366.97	2773	26
100sqno. 2	346.49	-0.0003	-0.0266	0.0199	1.6749	340.61	2668	34
100sqno. 3	2611.33	1.3954	0.0348	8.1303	2.3409	208.81	2028	33
100sqno. 4	344.40	0.0197	0.0246	0.0142	2.0304	340.21	2667	20
100sqno. 5	467.59	0.0069	-0.0087	0.0096	2.5389	464.76	3116	16
100sqno. 6	344.09	0.0116	0.0435	-0.0150	2.2869	348.51	2701	19
50sqno. 7	442.18	0.0033	-0.0143	0.0015	1.2294	441.74	3041	26
traverseA 1	300.77	0.0224	-0.0068	-0.0010	2.5929	301.07	2499	17
traverseA 2	309.09	0.0141	0.0002	0.0114	2.5299	305.73	2520	18
traverseA 3	310.10	0.0161	0.0200	0.0007	2.4939	309.89	2538	17
traverseA 4	291.52	0.0178	-0.0118	0.0008	2.2464	291.28	2455	21
traverseA 5	337.70	-0.0023	-0.0039	-0.0179	2.1654	342.98	2678	22
traverseA 6	308.78	0.0096	0.0529	0.0047	2.3049	307.40	2527	28
traverseA 7	319.28	0.0259	-0.0063	0.0030	2.0709	318.38	2575	23
traverseA 8	304.49	0.0055	-0.0686	-0.0050	2.3544	305.96	2521	18
traverseA 9	305.75	0.0082	0.0400	0.0134	2.1474	301.79	2502	21
traverseA 10	291.63	0.0165	0.0095	0.0268	2.4219	283.72	2419	22
traverseA 11	308.23	-0.0105	-0.0225	-0.0033	2.1789	309.21	2535	19

Sample/ Run	$^{40}Ar/^{39}Ar$	$^{38}Ar/^{39}Ar$	$^{37}Ar/^{39}Ar$	$^{36}Ar/^{39}Ar$	Total ^{39}Ar (cc)x10^{-12}	$^{40}Ar^{*}/^{39}Ar$	Age (Ma)	±
SS106a								
100sq no.1	346.81	0.0302	-0.0357	-0.0102	1.3854	349.83	2706	26
100sq no.2	310.81	-0.0021	-0.0324	-0.0063	1.5294	312.67	2550	20
100sq no.3	317.02	0.0034	0.0557	0.0049	1.6958	315.56	2563	17
traverseA 1	249.63	-0.0055	0.0154	0.0066	0.5844	247.68	2242	53
traverseA 2	307.01	0.0790	0.1049	-0.0014	0.4718	307.42	2527	60
traverseA 3	305.32	0.0426	0.0184	0.0085	0.9803	302.81	2507	29
traverseA 4	332.04	0.0186	-0.0070	0.0065	1.2819	330.11	2625	32
traverseA 5	329.44	0.0067	0.0321	-0.0092	1.5428	332.16	2634	24
traverseA 6	331.73	-0.0171	0.0240	-0.0094	1.5023	334.51	2643	19
traverseA 7	336.99	-0.0047	-0.0862	-0.0138	1.3409	341.08	2670	27
traverseA 8	362.41	0.0195	-0.0252	-0.0004	1.3315	362.53	2756	27
traverseA 9	328.96	0.0162	-0.0380	-0.0088	1.6019	331.55	2631	21
traverseA 10	360.12	-0.0012	-0.1063	-0.0256	1.4295	367.67	2776	31
traverseA 11	317.58	0.0047	0.0133	-0.0145	1.5878	321.88	2590	22
traverseA 12	320.49	0.0046	-0.0288	-0.0250	1.6392	327.89	2616	23
traverseB 1	260.35	0.0265	0.1450	-0.0343	0.8046	270.48	2356	51
traverseB 2	286.23	0.0165	0.0107	0.0129	2.4036	282.43	2413	20
traverseB 3	301.96	0.0148	-0.0537	0.0084	2.0681	299.46	2492	24
traverseB 4	354.06	0.0165	0.0040	0.0021	1.8489	353.43	2720	19
traverseB 5	357.56	0.0130	0.0197	0.0110	1.9887	354.30	2724	25
traverseB 6	327.29	0.0062	0.0203	-0.0003	1.9374	327.38	2614	18
traverseB 7	332.89	0.0021	0.0867	0.0196	1.3454	327.09	2612	25
SS115								
100sqno. 1	341.26	-0.0002	-0.0211	0.0007	2.5084	341.07	2670	16
100sqno. 2	369.18	-0.0002	0.0159	0.0023	2.6855	368.50	2779	17
100sqno. 3	324.09	0.0192	-0.0201	0.0005	3.0911	323.93	2599	14
100sqno. 4	396.01	0.0334	0.0063	0.1286	3.1610	358.00	2738	14
100sqno. 5	319.34	0.0015	-0.0010	0.0037	2.8393	318.23	2575	21
100sqno. 6	401.67	0.0261	0.0150	0.1459	3.1563	358.54	2740	15
traverseA 1	255.91	-0.0334	-0.0685	0.0020	0.8395	255.33	2281	52
traverseA 2	250.71	0.0128	-0.0187	0.0055	3.5572	249.07	2249	14
traverseA 3	288.71	0.0173	0.0201	0.0053	3.7063	287.15	2435	14
traverseA 4	283.18	0.0068	0.0164	0.0038	3.9767	282.05	2412	13
traverseA 5	284.28	0.0111	-0.0020	0.0017	3.6831	283.79	2420	14
traverseA 6	296.32	0.0025	0.0005	0.0031	3.4686	295.41	2473	14
traverseA 7	282.71	0.0096	0.0377	0.0135	3.7902	278.73	2396	14

Sample/ Run	$^{40}Ar/^{39}Ar$	$^{38}Ar/^{39}Ar$	$^{37}Ar/^{39}Ar$	$^{36}Ar/^{39}Ar$	Total ^{39}Ar (cc)x10^{-12}	$^{40}Ar^{*}/^{39}Ar$	Age (Ma)	±
SS115								
traverseB 1	310.51	0.0039	-0.0114	0.0328	2.2427	300.80	2498	23
traverseB 2	313.69	0.0195	0.0483	0.0243	2.1074	306.52	2523	21
traverseB 3	327.87	0.0468	0.0450	0.0396	1.8603	316.17	2566	25
traverseB 4	325.08	0.0701	0.0979	0.0280	1.5060	316.82	2568	28
traverseB 5	304.03	0.0435	0.1192	0.0295	1.5806	295.32	2473	26
SS116								
G1 100sq no.1	352.92	0.0207	0.0820	-0.0101	0.8332	355.92	2730	30
G1 100sq no.2	322.01	0.0089	0.0127	0.0098	1.4299	319.10	2578	21
G1 100sq no.3	354.03	0.0180	-0.0299	0.0139	1.9800	349.91	2706	14
G1 100sq no.4	341.25	0.0238	0.0404	0.0003	1.6909	341.15	2671	18
G1 100sq no.5	325.81	0.0153	0.0157	0.0025	2.0359	325.08	2604	17
G1 100sq no.6	387.66	0.0219	0.0335	-0.0052	1.6303	389.19	2857	28
G1 traverseA1	326.03	0.0087	-0.0148	0.0104	0.9218	322.96	2595	32
G1 traverseA2	346.76	0.0281	0.0205	0.0249	1.1083	339.41	2664	24
G1 traverseA3	361.29	0.0108	-0.0386	0.0081	1.1782	358.88	2742	22
G2 100sq no.1	322.19	0.0010	-0.0189	-0.0126	1.4863	325.92	2607	19
G2 100sq no.2	315.89	0.0117	0.0040	-0.0111	2.1016	319.16	2579	23
G2 100sq no.3	351.71	0.0146	-0.0300	-0.0049	1.9991	353.14	2719	15
G2 100sq no.4	370.98	-0.0016	-0.0511	-0.0242	1.8872	378.14	2816	43
G2 100sq no.5	328.21	0.0031	-0.0212	-0.0164	1.9664	333.06	2637	18
G2 traverseA 1	301.36	0.0064	-0.0032	-0.0031	1.6774	302.29	2505	19
G2 traverseA 2	313.99	0.0236	-0.0069	-0.0005	1.4303	314.14	2557	22
G2 traverseA 3	350.71	0.0449	0.0119	0.0025	1.4723	349.96	2706	20
G2 traverseA 4	313.64	0.0069	0.0141	0.0082	1.5608	311.22	2544	24
G2 traverseA 5	363.36	0.0238	-0.0166	-0.0069	1.4210	365.39	2767	18
G2 100sq no.5	328.21	0.0031	-0.0212	-0.0164	1.9664	333.06	2637	18

Sample/ Run	$^{40}Ar/^{39}Ar$	$^{38}Ar/^{39}Ar$	$^{37}Ar/^{39}Ar$	$^{36}Ar/^{39}Ar$	Total ^{39}Ar (cc)x10^{-12}	$^{40}Ar^{*}/^{39}Ar$	Age (Ma)	±
98-21a								
100sqno.1	328.27	0.0243	0.0143	0.0292	3.1442	319.65	2581	23
100sqno.2	326.32	0.0156	0.0118	0.0150	3.4239	321.90	2590	19
100sqno.3	339.65	0.0246	-0.0111	0.0637	2.9252	320.83	2586	22
100sqno.4	326.40	0.0135	0.0022	0.0005	3.9507	326.27	2609	19
G1traverseB 1	343.29	0.0048	-0.1922	0.0190	0.5711	337.69	2656	101
G1traverseB 2	292.89	-0.0055	-0.0983	0.0016	1.1631	292.42	2460	59
G1traverseB 3	305.60	0.0014	-0.0092	-0.0257	2.0348	313.18	2553	31
G1traverseB 4	313.44	0.0032	-0.0139	-0.0012	2.3238	313.78	2555	27
G1traverseB 5	294.74	0.0180	-0.0495	0.0033	1.9416	293.78	2466	34
G2100sqno.1	331.32	0.0107	0.0193	0.0197	3.2840	325.49	2606	22
G2100sqno.2	333.73	0.0185	0.0021	0.0102	4.1278	330.71	2628	16
G2100sqno.3	320.94	0.0113	-0.0264	0.0077	4.3283	318.67	2576	16
G2traverseA 1	348.09	-0.0031	0.0012	0.0132	3.5405	344.19	2683	21
G2traverseA 2	331.29	0.0089	-0.0174	0.0177	2.8972	326.06	2608	22
G2traverseA 3	319.06	0.0099	-0.0031	0.0050	3.0743	317.58	2572	22
G2traverseA 4	330.49	0.0115	0.0058	-0.0053	3.0370	332.06	2633	21
SS100								
100sq 1	366.79	-0.0126	0.0879	-0.0753	1.0755	389.04	2856	17
100sq 2	665.39	0.0307	0.0798	0.0644	1.4670	646.35	3618	17
100sq 3	322.10	0.0419	-0.0262	0.0236	1.7190	315.14	2561	17
100sq 4	306.30	0.0236	0.0236	0.0094	1.9080	303.51	2510	10
100sq 5	367.51	0.0072	0.0866	0.0038	2.0106	366.39	2771	35
100sq 6	326.54	0.0005	0.0152	-0.0211	1.9881	332.76	2636	37
traverseA 1	224.73	0.0083	-0.0144	-0.0183	2.2851	230.14	2148	42
traverseA 2	296.30	0.0141	-0.0166	0.0107	1.9791	293.15	2463	40
traverseA 3	321.27	0.0051	-0.0170	0.0016	1.9296	320.79	2586	40
traverseA 4	323.69	0.0188	0.0314	-0.0007	1.9611	323.89	2599	39
traverseA 5	309.30	0.0139	-0.0141	-0.0007	2.0061	309.50	2537	38
traverseA 6	344.37	0.0164	0.0062	0.1019	1.9746	314.26	2557	41
traverseA 7	335.75	-0.0069	0.0017	-0.0205	1.8261	341.79	2673	40
traverseA 8	329.45	0.0099	0.0087	-0.0171	1.9161	334.51	2643	38
traverseA 9	319.67	0.0163	0.0515	-0.0052	1.9836	321.21	2587	37
traverseA 10	317.38	0.0047	0.0442	0.0015	2.1096	316.94	2569	36
traverseA 11	306.71	0.0101	0.0324	0.0149	2.3211	302.30	2505	35

Sample/ Run	$^{40}Ar/^{39}Ar$	$^{38}Ar/^{39}Ar$	$^{37}Ar/^{39}Ar$	$^{36}Ar/^{39}Ar$	Total ^{39}Ar (cc)x10^{-12}	$^{40}Ar^{*}/^{39}Ar$	Age (Ma)	±
SS107								
100sqno. 1	293.07	-0.0080	-0.0333	-0.0026	2.7031	293.82	2466	18
100sqno. 2	290.31	0.0033	-0.0025	0.0186	3.2531	284.80	2424	15
100sqno. 3	334.59	-0.0009	0.0003	0.0019	3.4255	334.03	2641	14
100sqno. 4	316.66	0.0144	0.0003	0.0043	3.6073	315.38	2562	14
50sqno. 5	333.55	-0.0041	0.0029	0.0058	1.9105	331.84	2632	23
50sqno. 6	336.22	0.0107	-0.0215	0.0036	1.8546	335.17	2646	23
50sqno. 7	325.98	0.0115	-0.0258	-0.0144	1.7241	330.25	2626	25
50sqno. 8	295.93	-0.0081	0.0874	-0.0311	1.5235	305.14	2517	37
traverseA 1	212.94	-0.0085	-0.0386	-0.0222	0.9176	219.51	2089	60
traverseA 2	316.75	0.0034	-0.0411	-0.0040	1.7474	317.92	2573	24
traverseA 3	308.21	0.0103	-0.0491	-0.0059	1.9246	309.96	2539	23
traverseA 4	311.27	0.0154	-0.0357	0.0059	1.8826	309.53	2537	26
traverseA 5	318.53	0.0117	-0.0583	-0.0067	1.7008	320.51	2584	27
traverseA 6	313.87	-0.0017	-0.0161	0.0105	1.9199	310.78	2542	26
traverseA 7	325.57	0.0007	-0.0137	-0.0083	1.9245	328.02	2616	25
traverseA 8	347.19	0.0090	-0.0209	-0.0041	1.6915	348.40	2700	25
traverseA 9	337.43	-0.0045	0.0297	0.0143	1.7194	333.21	2638	26
traverseA 10	324.05	0.0196	0.0642	-0.0276	1.7193	332.21	2634	24
traverseA 11	345.86	0.0166	0.0028	0.0144	2.0224	341.62	2673	24
traverseA 12	341.14	0.0319	-0.0222	0.0050	2.2089	339.66	2665	20
traverseA 13	357.05	0.0053	0.0164	0.0055	2.0037	355.42	2728	22
traverseA 14	336.64	0.0292	0.0005	-0.0076	2.0970	338.88	2661	22
traverseA 15	355.91	0.0108	-0.0256	0.0029	2.2742	355.05	2727	19
traverseA 17	317.31	0.0101	-0.0240	-0.0177	2.4187	322.55	2593	20

Sample/ Run	$^{40}Ar/^{39}Ar$	$^{38}Ar/^{39}Ar$	$^{37}Ar/^{39}Ar$	$^{36}Ar/^{39}Ar$	Total ^{39}Ar (cc)x10^{-12}	$^{40}Ar^{*}/^{39}Ar$	Age (Ma)	±
98FWB38								
Grain 1								
100sq #1	71.85	0.0133	0.0028	-0.0015	7.3858	72.28	2670	31
100sq #2	72.65	0.0117	0.0002	0.0011	14.6485	72.32	2670	17
100sq #3	72.76	0.0139	0.0005	0.0002	13.9819	72.70	2678	18
100sq #4	71.88	0.0095	0.0075	-0.0014	14.2569	72.30	2670	18
traverseA #1	70.61	0.0106	0.0038	-0.0004	14.8769	70.74	2640	17
traverseA #2	73.59	0.0122	-0.0007	-0.0007	15.5995	73.80	2699	16
traverseA #3	71.80	0.0120	0.0026	-0.0015	16.5597	72.24	2669	16
traverseA #4	73.63	0.0110	0.0004	0.0012	17.6459	73.28	2689	14
traverseA #5	70.39	0.0116	-0.0017	0.0005	14.8350	70.24	2630	17
Grain 2								
100sq#1	73.92	0.0109	0.0019	0.0002	15.4037	73.87	2700	16
100sq#2	77.58	0.0103	0.0021	0.0011	14.3968	77.25	2763	16
100sq#3	72.58	0.0124	0.0008	0.0002	14.2196	72.53	2674	17
100sq#4	72.71	0.0103	0.0016	-0.0010	15.3244	73.01	2684	16
100sq#5	68.73	0.0139	-0.0006	-0.0021	9.1781	69.35	2612	20
traverseB #1	70.13	0.0118	0.0019	0.0005	15.4037	69.99	2625	16
traverseB #2	71.34	0.0123	-0.0014	-0.0007	15.0727	71.55	2656	17
traverseB #3	72.47	0.0110	-0.0008	-0.0001	12.8048	72.50	2674	14
traverseB #4	71.21	0.0070	0.0045	0.0006	12.9073	71.03	2645	13
traverseB #5	70.98	0.0109	0.0010	0.0006	12.4738	70.80	2641	14

Sample/ Run	$^{40}Ar/^{39}Ar$	$^{38}Ar/^{39}Ar$	$^{37}Ar/^{39}Ar$	$^{36}Ar/^{39}Ar$	Total ^{39}Ar (cc)x10^{-12}	$^{40}Ar^{*}/^{39}Ar$	Age (Ma)	±
SS117								
Grain 1								
50sq 1	250.27	0.0107	0.0067	0.0023	4.1721	249.59	2629	11
50sq 2	237.23	0.0100	0.0275	0.0041	4.4937	236.00	2552	12
50sq 3	241.41	0.0118	-0.0009	0.0034	4.1674	240.41	2578	11
50sq 4	249.92	0.0103	-0.0127	0.0083	3.8831	247.47	2617	11
Traverse A 1	214.40	0.0186	0.0344	0.0064	2.0277	212.50	2411	21
Traverse A 2	229.70	0.0165	0.0271	0.0091	3.4122	227.02	2499	18
Traverse A 3	226.29	0.0157	0.0232	0.0128	4.1767	222.50	2472	12
Traverse A 4	223.91	0.0173	0.0060	0.0043	4.0416	222.63	2473	11
Traverse A 5	233.93	0.0114	-0.0019	0.0075	4.1302	231.71	2527	12
Traverse A 6	253.28	0.0217	-0.0091	0.0034	3.8691	252.29	2644	12
Traverse A 7	242.10	0.0145	0.0090	0.0031	4.2047	241.19	2582	12
Traverse A 8	235.38	0.0176	-0.0008	-0.0022	4.2327	236.04	2552	13
Traverse A 9	224.86	0.0121	-0.0135	0.0086	4.6383	222.31	2471	15
Traverse A 10	238.23	0.0061	0.0170	-0.0011	4.6475	238.55	2567	15
Traverse A 11	225.48	0.0121	-0.0015	-0.0010	5.0205	225.77	2492	10
Traverse A 12	224.32	0.0086	0.0104	0.0081	4.9272	221.92	2469	10
Traverse A 13	220.97	0.0158	0.0084	0.0026	5.0298	220.20	2458	10
Traverse A 14	217.64	0.0125	-0.0110	0.0027	4.8527	216.85	2438	10
Traverse A 15	226.37	0.0137	0.0261	0.0112	4.7640	223.05	2476	10
Traverse A 16	216.95	0.0136	-0.0364	-0.0084	2.6105	219.42	2454	21
Traverse A 17	228.04	0.0172	-0.0122	0.0014	3.6780	227.63	2503	12
Traverse A 18	230.43	0.0076	-0.0028	0.0001	4.6569	230.39	2519	11
Traverse A 19	223.06	0.0112	-0.0040	-0.0060	4.3959	224.83	2486	13
Traverse A 20	238.41	0.0090	-0.0017	-0.0017	4.9786	238.91	2569	9
Traverse A 21	244.53	0.0112	0.0019	-0.0016	5.2536	245.00	2604	10
Traverse A 22	247.78	0.0186	-0.0058	-0.0015	5.3935	248.24	2622	12
Traverse A 23	248.82	0.0051	0.0037	-0.0060	5.1603	250.59	2635	11
Traverse A 24	250.83	0.0128	-0.0067	0.0128	5.3096	247.03	2615	11
Traverse A 25	252.87	0.0092	0.0249	0.0001	5.3374	252.83	2647	9
Traverse A 26	252.30	0.0092	-0.0118	-0.0066	5.3562	254.25	2655	9
Traverse A 27	270.14	0.0117	0.0092	0.0019	5.0251	269.58	2737	15

Sample/ Run	$^{40}Ar/^{39}Ar$	$^{38}Ar/^{39}Ar$	$^{37}Ar/^{39}Ar$	$^{36}Ar/^{39}Ar$	Total ^{39}Ar (cc)x10^{-12}	$^{40}Ar^{*}/^{39}Ar$	Age (Ma)	±
SS117								
Grain 1								
Traverse B 0	208.81	0.0140	-0.0060	0.0010	3.1559	208.51	2386	22
Traverse B I	210.00	0.0087	-0.0211	-0.0081	3.4776	212.41	2410	22
Traverse B A	226.65	0.0026	-0.0269	-0.0103	2.7364	229.71	2515	23
Traverse B 1	238.83	0.0209	-0.0291	-0.0004	2.9928	238.96	2569	20
Traverse B 2	239.57	0.0153	0.0026	-0.0039	4.9785	240.72	2579	14
Traverse B 3	240.01	0.0071	0.0073	0.0043	4.9086	238.73	2568	14
Traverse B 4	248.46	0.0130	0.0172	0.0017	4.4611	247.95	2620	16
Traverse B 5	252.17	0.0199	0.0049	-0.0042	4.5404	253.43	2650	14
Traverse B 6	250.19	0.0197	0.0198	-0.0015	3.8784	250.63	2635	16
Traverse B 7	236.87	0.0126	0.0128	0.0029	4.2233	236.02	2552	15
Traverse B 8	238.62	0.0083	0.0074	0.0040	4.2001	237.44	2561	16
Traverse B 9	228.24	0.0111	-0.0168	0.0151	4.3773	223.77	2480	18
Traverse B 10	235.66	0.0169	0.0180	0.0087	4.5217	233.10	2535	14
Traverse B 11	244.07	0.0099	0.0234	-0.0053	4.4517	245.65	2607	14
Traverse B 12	231.39	0.0219	0.0042	-0.0083	3.2549	233.84	2540	19
Traverse B 13	257.17	0.0060	0.0173	0.0000	4.2152	257.17	2671	14
Traverse B 14	252.20	0.0053	-0.0171	-0.0028	4.7933	253.03	2648	11
Traverse B 15	258.10	0.0052	-0.0130	0.0018	4.8912	257.55	2673	13
Traverse B 16	244.11	0.0110	0.0165	-0.0034	5.2407	245.13	2604	11
Traverse B 17	244.74	0.0086	-0.0065	-0.0048	5.6230	246.16	2610	13
Traverse B 18	247.49	0.0149	-0.0143	0.0033	5.4180	246.51	2612	11
Traverse B 19	239.67	0.0061	-0.0105	0.0008	5.6370	239.43	2572	10
Traverse B 20	262.87	0.0114	-0.0167	-0.0029	4.6488	263.73	2706	15
Grain 2								
100sq 1	252.54	0.0198	0.0221	-0.0023	5.7243	253.21	2649	11
100sq 2	254.88	0.0089	0.0207	-0.0006	6.5541	255.06	2659	10
100sq 3	260.61	0.0108	0.0162	0.0014	6.6706	260.19	2687	11
100sq 4	259.95	0.0081	0.0026	-0.0015	5.1004	260.40	2688	12
100sq 5	250.28	0.0093	0.0035	0.0016	6.4103	249.81	2630	11

Sample/ Run	$^{40}Ar/^{39}Ar$	$^{38}Ar/^{39}Ar$	$^{37}Ar/^{39}Ar$	$^{36}Ar/^{39}Ar$	Total ^{39}Ar (cc)x10^{-12}	$^{40}Ar^{*}/^{39}Ar$	Age (Ma)	±
SS117								
Grain 2								
TraverseA 1	169.19	0.0239	0.0158	0.0001	6.2884	169.16	2117	11
TraverseA 2	174.38	0.0128	0.0133	-0.0017	7.4491	174.89	2159	10
TraverseA 3	179.65	0.0151	0.0083	-0.0005	8.1018	179.80	2194	9
TraverseA 4	213.04	0.0110	0.0025	0.0011	8.6565	212.72	2412	9
TraverseA 5	243.91	0.0117	0.0155	0.0039	9.3044	242.75	2591	10
TraverseA 6	270.62	0.0123	0.0112	-0.0030	8.8383	271.51	2747	9
TraverseA 7	271.59	0.0136	0.0135	-0.0009	9.3277	271.86	2749	9
TraverseA 8	287.41	0.0118	0.0160	0.0022	6.4795	286.77	2824	10
TraverseA 9	281.62	0.0064	0.0175	-0.0021	6.1905	282.24	2802	11
TraverseA 10	272.06	0.0109	0.0212	0.0069	6.6193	270.03	2739	12
TraverseA 11	272.91	0.0146	0.0264	-0.0020	6.5028	273.50	2757	10
TraverseA 12	272.29	0.0082	0.0110	-0.0061	6.5168	274.10	2760	11
TraverseA 13	296.19	0.0194	0.0085	-0.0063	6.3164	298.06	2880	12
TraverseB 0	177.46	0.0317	0.1931	0.0141	0.7278	173.30	2147	85
TraverseB 1	202.56	0.0253	-0.1072	0.0574	0.7279	185.59	2234	83
TraverseB 2	210.33	0.0089	-0.0033	0.0026	5.7018	209.56	2392	16
TraverseB 3	229.28	0.0106	0.0055	-0.0069	5.6458	231.33	2525	13
TraverseB 4	245.81	0.0091	0.0125	-0.0042	5.0538	247.05	2615	13
TraverseB 5	226.30	0.0072	-0.0108	0.0054	3.3385	224.71	2486	23
TraverseB 6	234.81	0.0025	-0.0150	-0.0107	4.2195	237.97	2564	18
TraverseB 7	247.37	0.0127	0.0133	0.0044	5.1658	246.08	2610	15
TraverseB 8	235.63	0.0169	0.0024	0.0023	3.8745	234.94	2546	20
TraverseB 9	240.47	0.0021	-0.0093	-0.0093	4.8442	243.21	2593	16
TraverseB 10	242.95	0.0115	0.0247	0.0008	5.7204	242.72	2591	15
TraverseB 11	260.59	0.0091	-0.0058	0.0029	4.6810	259.74	2685	17
TraverseB 12	259.77	0.0067	-0.0118	0.0072	4.9934	257.64	2673	15
TraverseB 13	254.48	0.0130	0.0163	-0.0009	5.0632	254.74	2658	15
TraverseB 14	261.71	0.0381	0.0250	0.0038	4.7508	260.59	2689	16
TraverseB 15	261.14	0.0152	0.0399	0.0110	4.9139	257.90	2675	15
TraverseB 16	259.65	0.0149	0.0191	0.0036	5.0352	258.60	2678	16
TraverseB 17	260.34	0.0199	0.0454	-0.0073	4.9232	262.51	2699	15
TraverseB 18	263.60	0.0104	0.0202	-0.0099	4.9839	266.54	2721	15
TraverseB 19	276.45	0.0088	-0.0140	-0.0112	4.8349	279.75	2789	16
TraverseB 20	259.14	0.0091	0.0325	-0.0026	5.1890	259.91	2686	15

Sample/ Run	$^{40}Ar/^{39}Ar$	$^{38}Ar/^{39}Ar$	$^{37}Ar/^{39}Ar$	$^{36}Ar/^{39}Ar$	Total ^{39}Ar (cc)x10^{-12}	$^{40}Ar^{*}/^{39}Ar$	Age (Ma)	±
SS117								
Grain 2								
TraverseC 1	203.16	0.0131	-0.0162	0.0053	4.1289	201.59	2341	23
TraverseC 2	218.87	0.0055	-0.0014	0.0023	5.6765	218.20	2446	13
TraverseC 3	213.15	0.0125	0.0044	-0.0022	6.5109	213.79	2419	12
TraverseC 4	228.33	0.0194	0.0081	-0.0008	6.3570	228.57	2509	13
TraverseC 5	233.90	0.0096	0.0147	0.0013	6.5947	233.53	2538	11
TraverseC 6	232.10	0.0107	0.0052	0.0012	7.1961	231.76	2528	11
TraverseC 7	213.75	0.0107	0.0008	-0.0030	7.6623	214.64	2424	12
TraverseC 8	228.74	0.0085	0.0088	0.0054	7.3965	227.15	2500	13
TraverseC 9	235.18	0.0183	0.0165	0.0036	7.2473	234.10	2541	11
TraverseC 10	233.45	0.0185	0.0137	0.0060	7.3872	231.68	2527	11
TraverseC 11	233.34	0.0087	0.0078	0.0011	7.7834	233.02	2535	12
TraverseC 12	231.80	0.0104	0.0157	0.0013	9.6294	231.40	2525	10
TraverseC 13	253.64	0.0135	0.0034	0.0015	8.4501	253.19	2649	10
TraverseC 14	266.14	0.0128	0.0203	-0.0084	4.6762	268.62	2732	14
TraverseC 15	277.23	0.0083	0.0156	-0.0005	6.0793	277.39	2777	16
TraverseC 16	262.88	0.0057	0.0118	0.0027	7.2587	262.09	2697	12
TraverseC 17	268.57	0.0113	0.0081	0.0036	7.7575	267.49	2726	10
TraverseC 18	272.92	0.0113	0.0111	0.0041	6.9137	271.72	2748	11

Sample/ Run	$^{40}Ar/^{39}Ar$	$^{38}Ar/^{39}Ar$	$^{37}Ar/^{39}Ar$	$^{36}Ar/^{39}Ar$	Total ^{39}Ar (cc)x10^{-12}	$^{40}Ar^{*}/^{39}Ar$	Age (Ma)	±
SS111								
100sq no.1	332.04	0.0251	0.0237	0.0327	0.9626	322.38	2592	17
100sq no.2	370.43	0.0067	-0.0745	0.0053	0.8554	368.87	2781	27
100sq no.3	337.25	0.0304	-0.0109	0.0791	1.2516	313.88	2556	16
100sq no.4	346.81	0.0150	0.0732	-0.0136	0.9952	350.82	2710	19
100sq no.5	3807.22	1.9098	-0.0555	11.6019	0.7389	378.84	2818	39
100sq no.6	1228.23	0.5189	0.0209	3.2178	1.3076	277.36	2389	29
traverseA no.0	237.92	0.0156	-0.0219	0.0093	1.3426	235.17	2176	26
traverseA no.1	273.77	-0.0079	-0.0564	-0.0118	0.8438	277.27	2389	32
traverseA no.2	329.79	0.0271	0.0064	-0.0130	1.1141	333.63	2640	27
traverseA no.3	314.29	0.0219	0.0917	0.0337	1.1700	304.32	2514	23
traverseA no.4	334.46	0.0414	0.0758	0.0068	1.1747	332.46	2635	22
traverseA no.5	361.76	0.0217	-0.0094	0.0068	1.1794	359.75	2745	21
traverseA no.6	317.97	0.0328	0.0222	-0.0075	1.3425	320.18	2583	20
traverseA no.7	320.64	0.0335	-0.0015	-0.0076	1.3146	322.89	2595	20

Sample/ Run	$^{40}Ar/^{39}Ar$	$^{38}Ar/^{39}Ar$	$^{37}Ar/^{39}Ar$	$^{36}Ar/^{39}Ar$	Total ^{39}Ar (cc)x10^{-12}	$^{40}Ar^*/^{39}Ar$	Age (Ma)	±
SS1								
100sq. no.1	332.30	0.0210	-0.0340	0.0080	0.9976	329.93	2624	24
100sq. no.2	339.43	0.0121	0.0261	-0.0010	0.9696	339.74	2665	27
100sq. no.3	310.65	0.0204	-0.0016	-0.0152	1.2540	315.13	2561	31
100sq. no.4	344.85	0.0070	0.0864	0.0034	1.0301	343.86	2682	25
100sq. no.5	305.38	-0.0106	0.0067	-0.0265	1.0582	313.20	2553	22
traverseA 1	255.59	0.0438	0.0253	-0.0132	0.7593	259.48	2302	46
traverseA 2	294.82	0.0258	0.0011	-0.0107	0.9318	297.99	2485	33
traverseA 3	308.79	0.0115	-0.0398	0.0191	0.8899	303.15	2508	34
traverseA 4	309.44	0.0061	0.0748	-0.0157	0.9271	314.06	2556	30
traverseA 5	332.17	-0.0202	-0.0939	-0.0116	0.8619	335.59	2648	32
traverseA 6	317.67	-0.0237	-0.0087	-0.0108	0.9271	320.86	2586	32
traverseA 7	303.96	-0.0038	0.0346	-0.0058	0.9504	305.67	2520	31
traverseA 8	308.26	-0.0033	0.0672	-0.0296	1.0996	317.00	2569	28
traverseA 9	324.42	0.0098	0.0965	-0.0010	1.0483	324.71	2602	27
traverseA 10	324.24	0.0052	-0.0454	-0.0092	1.0810	326.97	2612	28
traverseA 11	354.05	-0.0039	-0.0039	0.0038	0.9178	352.93	2718	35
traverseA 12	326.59	0.0010	-0.0589	-0.0283	0.9878	334.96	2645	34
traverseA 13	348.45	0.0303	-0.0182	-0.0153	0.9458	352.98	2718	28
traverseA 14	344.73	0.0199	-0.0222	-0.0194	0.9784	350.47	2708	38
traverseA 15	314.60	0.0271	0.0354	-0.0010	1.0576	314.88	2560	29
SS2								
100sq no.1	300.16	0.0161	-0.0143	-0.0113	1.8569	303.51	2510	16
100sq no.2	306.54	0.0050	-0.0713	-0.0054	1.3954	308.12	2530	19
100sq no.3	451.68	0.1177	-0.0111	0.6148	2.7985	270.00	2354	14
100sq no.4	296.28	0.0051	-0.0237	-0.0073	2.2718	298.43	2487	13
100sq no.5	291.49	0.0136	-0.0104	0.0271	2.5421	283.47	2418	17

Sample/ Run	$^{40}Ar/^{39}Ar$	$^{38}Ar/^{39}Ar$	$^{37}Ar/^{39}Ar$	$^{36}Ar/^{39}Ar$	Total ^{39}Ar (cc)x10^{-12}	$^{40}Ar^*/^{39}Ar$	Age (Ma)	±
SS2								
traverseA 1	250.27	0.0177	0.0132	0.0261	2.4675	242.55	2215	14
traverseA 2	283.46	0.0179	0.0273	0.0007	2.1925	283.26	2417	13
traverseA 3	291.69	0.0098	0.0368	0.0155	2.1225	287.10	2435	15
traverseA 4	286.22	0.0183	0.0025	0.0343	2.1459	276.10	2383	29
traverseA 5	289.63	0.0192	0.0529	0.0038	1.5631	288.50	2442	17
traverseA 6	274.01	0.0144	0.0108	-0.0068	1.7543	276.03	2383	16
traverseA 7	277.32	0.0126	-0.0161	-0.0018	1.6518	277.85	2392	21
traverseA 8	288.53	0.0143	-0.0290	0.0013	0.9650	288.13	2440	47
traverseA 9	272.35	0.0064	0.0312	0.0009	1.4404	272.09	2364	33
traverseA 10	295.91	0.0232	-0.0044	-0.0140	1.1934	300.05	2494	38
traverseA 11	284.81	0.0386	0.0025	0.0008	1.5523	284.57	2423	26
traverseA 12	285.42	0.0292	0.0412	0.0041	1.4217	284.22	2422	31
traverseA 13	322.32	-0.0035	-0.0005	-0.0127	1.3146	326.08	2608	31
traverseA 14	291.13	0.0095	0.0844	0.0102	1.4497	288.12	2440	29
traverseA 15	280.96	0.0056	0.0024	0.0035	1.6595	279.93	2401	27
traverseA 16	283.08	0.0000	0.0241	-0.0046	1.6735	284.44	2423	25
traverseA 17	294.05	0.0184	0.0328	0.0068	1.5057	292.03	2458	31
SS42b								
Grain 1								
100sq #1	64.42	0.0117	0.0029	0.0013	42.4187	64.03	2503	8
100sq #2	60.01	0.0100	0.0029	0.0007	35.9158	59.81	2412	9
100sq #3	60.19	0.0129	0.0038	0.0009	35.2119	59.92	2414	9
100sq #4	60.28	0.0138	0.0014	0.0014	24.4111	59.88	2413	10
100sq #5	58.61	0.0087	-0.0102	-0.0033	14.3980	59.60	2407	14
100sq #6	59.38	0.0106	-0.0082	-0.0005	15.7918	59.52	2405	13
traverseA 1	51.15	0.0098	0.0021	0.0040	18.5328	49.98	2179	14
traverseA 2	54.41	0.0096	-0.0061	0.0029	17.4420	53.55	2267	13
traverseA 3	59.07	0.0146	-0.0086	0.0010	15.6007	58.79	2389	14
traverseA 4	58.87	0.0123	-0.0061	-0.0015	14.3887	59.30	2400	14
traverseA 5	66.01	0.0141	-0.0110	0.0211	14.1603	59.78	2411	15
traverseA 6	59.26	0.0113	-0.0075	-0.0039	13.5823	60.40	2425	14
traverseA 7	59.43	0.0102	-0.0140	-0.0031	12.7572	60.33	2423	15
traverseA 8	59.49	0.0093	-0.0028	0.0020	12.9623	58.91	2392	13

Sample/ Run	$^{40}Ar/^{39}Ar$	$^{38}Ar/^{39}Ar$	$^{37}Ar/^{39}Ar$	$^{36}Ar/^{39}Ar$	Total ^{39}Ar (cc)x10^{-12}	$^{40}Ar^{*}/^{39}Ar$	Age (Ma)	±
SS42b								
Grain 2								
2. 100sq #1	58.69	0.0125	0.0073	0.0015	13.6941	58.24	2376	13
2. 100sq #2	67.38	0.0116	0.0056	0.0163	21.9591	62.56	2472	10
2. 100sq #3	63.37	0.0132	0.0029	0.0076	17.4514	61.11	2440	11
2. 100sq #4	61.12	0.0074	0.0000	0.0012	16.9852	60.76	2433	12
2. 100sq #5	66.01	0.0136	-0.0039	0.0215	14.9994	59.66	2408	13
traverseA 1	61.33	0.0106	-0.0208	-0.0003	5.2614	61.41	2447	27
traverseA 2	60.31	0.0158	-0.0155	0.0033	7.6155	59.32	2401	20
traverseA 3	59.84	0.0146	-0.0093	0.0024	8.8461	59.14	2397	17
traverseB 1	52.64	0.0124	-0.0059	0.0100	9.3402	49.69	2171	18
traverseB 2	60.49	0.0162	-0.0068	0.0201	8.0024	54.56	2291	20
traverseB 3	59.72	0.0148	-0.0067	0.0178	7.4896	54.45	2288	21
traverseB 4	58.13	0.0130	-0.0029	0.0187	7.8625	52.61	2244	21
SS207								
Grain 1								
100sq. no.1	198.81	0.0181	-0.0263	0.1031	0.7202	168.35	1775	38
100sq. no.2	186.21	0.0279	0.0845	0.0197	0.7994	180.40	1854	34
50sq. no. 3	149.60	0.0112	0.0595	0.0269	0.7528	141.66	1587	30
traverse A 1	149.54	0.0417	0.3557	0.0110	0.2027	146.29	1621	92
traverse A 2	160.53	0.0228	0.1164	-0.0203	0.7761	166.53	1763	35
traverse A 3	170.94	0.0390	-0.0173	0.0118	0.5710	167.45	1769	36
traverse A 4	173.66	0.0508	0.0502	0.0918	0.7109	146.54	1623	31
traverse A 5	151.20	0.0143	-0.0108	-0.0074	0.9160	153.37	1672	31
traverse A 6	160.90	-0.0114	-0.0268	-0.0179	0.8787	166.20	1761	24
traverse A 7	159.96	-0.0068	0.0048	0.0370	0.7901	149.02	1641	36
traverse A 8	172.20	0.0176	0.0296	0.0091	0.7435	169.52	1783	37
traverse A 9	143.91	-0.0139	0.1634	0.0406	0.7201	131.92	1512	42
traverse A 10	153.47	0.0586	-0.0020	0.0059	0.3799	151.72	1660	56

Sample/ Run	$^{40}Ar/^{39}Ar$	$^{38}Ar/^{39}Ar$	$^{37}Ar/^{39}Ar$	$^{36}Ar/^{39}Ar$	Total ^{39}Ar (cc)x10^{-12}	$^{40}Ar^{*}/^{39}Ar$	Age (Ma)	±
SS207								
Grain 2								
100sq. no.1	195.12	0.0047	-0.0317	-0.0113	0.9733	198.46	1967	37
100sq. no.2	190.35	0.0135	-0.0212	-0.0019	1.0245	190.93	1921	36
100sq. no.3	209.46	0.0198	-0.0638	0.0229	0.6982	202.69	1992	52
traverseB 1	163.94	0.0472	-0.2610	0.0086	0.2927	161.40	1728	136
traverseB 2	167.53	-0.0063	0.1198	0.0157	0.7308	162.89	1738	53
traverseB 3	192.61	-0.0209	-0.0605	0.0174	0.6609	187.46	1899	60
traverseB 4	178.29	-0.0063	0.0263	0.0096	0.7308	175.47	1822	52
traverseB 5	191.29	0.0000	-0.0385	0.0300	0.6842	182.43	1867	56
traverseB 6	167.83	-0.0059	0.0650	0.0146	0.7867	163.51	1742	52
traverseB 7	164.71	0.0101	-0.0189	-0.0072	0.9080	166.83	1765	43
traverseB 8	178.22	0.0159	-0.0093	0.0546	0.8707	162.10	1733	47
traverseB 9	160.44	0.0099	-0.0235	0.0027	0.9266	159.64	1716	43
traverseB 11	187.11	0.0111	-0.0098	0.0084	0.8287	184.61	1881	45
traverseB 12	213.20	0.0146	0.0592	-0.0032	0.6329	214.14	2059	54
96-86b								
100sq #1	61.71	0.0109	0.0023	0.0005	15.4851	61.56	2450	13
100sq #2	61.27	0.0120	0.0036	0.0002	17.5735	61.22	2443	12
100sq #3	62.08	0.0126	0.0033	0.0012	17.3777	61.72	2454	12
100sq #4	64.07	0.0139	0.0014	0.0088	18.7156	61.46	2448	12
100sq #5	63.01	0.0110	0.0060	-0.0001	15.7461	63.03	2482	13
traverseA #1	47.47	0.0108	0.0067	-0.0009	11.3876	47.73	2121	18
traverseA #2	55.03	0.0116	0.0074	0.0029	13.4107	54.16	2281	16
traverseA #3	56.99	0.0132	0.0054	0.0026	13.1823	56.21	2330	15
traverseA #4	57.98	0.0140	0.0013	0.0030	13.0704	57.09	2350	15
traverseA #5	58.21	0.0140	0.0012	-0.0028	5.9151	59.04	2395	15
traverseA #6	63.23	0.0158	-0.0025	-0.0005	6.1248	63.38	2490	13
traverseA #7	61.54	0.0112	0.0013	-0.0005	5.7612	61.70	2453	15
traverseB #1	60.38	0.0100	-0.0024	-0.0009	7.6978	60.64	2430	16
traverseB #2	60.47	0.0170	0.0122	0.0057	6.7048	58.78	2389	17

	$^{40}Ar/^{39}Ar$	$^{38}Ar/^{39}Ar$	$^{37}Ar/^{39}Ar$	$^{36}Ar/^{39}Ar$	Total ^{39}Ar (cc)x10^{-12}	$^{40}Ar^{*}/^{39}Ar$	Age (Ma)	±
SS34a								
100sq #1	59.90	0.0142	0.0059	0.0000	10.1070	59.90	2358	15
100sq #2	60.14	0.0118	0.0015	0.0022	12.1725	59.48	2349	13
100sq #3	62.69	0.0146	0.0020	0.0056	13.5450	61.03	2383	12
100sq #4	61.39	0.0117	-0.0009	0.0032	14.1840	60.46	2370	13
traverseA 1	47.79	0.0121	0.0015	0.0027	18.1980	46.99	2050	11
traverseA 2	49.70	0.0139	-0.0037	0.0013	16.7625	49.30	2109	13
traverseA 3	52.67	0.0116	-0.0024	-0.0005	16.5870	52.83	2196	11
traverseA 4	54.64	0.0095	-0.0005	0.0000	16.0020	54.64	2239	11
traverseA 5	55.44	0.0116	0.0028	0.0010	18.0945	55.15	2251	10
traverseA 6	54.77	0.0113	-0.0022	0.0008	17.8740	54.54	2236	11
traverseA 7	55.33	0.0107	-0.0011	-0.0004	14.6420	55.46	2258	8
traverseA 8	57.01	0.0116	-0.0069	-0.0008	13.5745	57.25	2299	9
traverseA 9	56.18	0.0112	0.0037	0.0034	15.2806	55.18	2251	8
traverseA 10	56.91	0.0129	-0.0010	0.0002	16.1850	56.87	2290	11
traverseA 11	59.85	0.0098	0.0058	0.0021	18.4458	59.23	2343	8
traverseA 12	58.45	0.0112	-0.0009	0.0047	17.6907	57.06	2295	9
traverseA 13	60.13	0.0125	0.0059	0.0009	18.8654	59.88	2358	8
traverseA 14	61.21	0.0116	0.0017	0.0049	20.6927	59.76	2355	8
traverseA 15	59.37	0.0119	0.0036	0.0008	19.4387	59.13	2341	7
traverseA 16	58.96	0.0133	0.0023	0.0022	19.1497	58.30	2323	9
traverseA 17	64.54	0.0128	0.0055	0.0085	18.8281	62.02	2404	8
traverseA 18	60.17	0.0106	0.0038	0.0015	19.6485	59.73	2354	8
SS36								
100sq #1	60.23	0.0100	-0.0005	0.0029	15.0693	59.38	2347	8
100sq #2	61.51	0.0091	-0.0060	-0.0008	13.4984	61.74	2398	9
100sq #3	60.25	0.0097	-0.0045	0.0006	11.7736	60.06	2362	11
100sq #4	80.41	0.0087	-0.0057	-0.0015	12.6033	80.87	2768	8
100sq #5	60.67	0.0101	0.0035	0.0017	17.8643	60.17	2364	9

Sample/ Run	$^{40}Ar/^{39}Ar$	$^{38}Ar/^{39}Ar$	$^{37}Ar/^{39}Ar$	$^{36}Ar/^{39}Ar$	Total ^{39}Ar (cc)x10^{-12}	$^{40}Ar^{*}/^{39}Ar$	Age (Ma)	±
SS36								
traverseA 1	32.35	0.0107	-0.0258	-0.0268	1.6248	40.26	1865	191
traverseA 2	37.83	0.0069	-0.0040	-0.0005	5.8902	37.98	1798	57
traverseA 3	43.72	0.0094	0.0030	-0.0038	10.1648	44.85	1993	29
traverseA 4	48.12	0.0094	-0.0005	-0.0011	11.1391	48.43	2087	26
traverseA 5	48.17	0.0120	-0.0033	-0.0024	12.5609	48.87	2098	23
traverseA 6	50.29	0.0108	0.0006	-0.0023	13.1575	50.97	2150	21
traverseA 7	51.75	0.0098	-0.0015	-0.0006	12.6028	51.92	2174	23
traverseA 8	51.62	0.0093	0.0060	-0.0027	12.7473	52.42	2186	22
traverseA 9	51.42	0.0122	-0.0062	-0.0045	12.7054	52.74	2194	22
traverseA 10	53.00	0.0110	-0.0026	0.0012	12.5003	52.64	2191	22
traverseA 10a	53.76	0.0093	0.0051	-0.0026	11.3395	54.54	2236	23
traverseA 10a	54.35	0.0093	-0.0011	0.0005	13.2927	54.22	2229	21
traverseA 10a	55.28	0.0086	-0.0004	-0.0031	12.7007	56.19	2275	21
traverseA 10a	56.19	0.0124	0.0006	-0.0029	13.2554	57.06	2295	20
traverseA 11	57.69	0.0122	0.0034	0.0084	13.1063	55.22	2252	21
traverseA 12	55.66	0.0075	0.0015	-0.0026	11.5213	56.43	2280	23
traverseA 13	56.46	0.0106	0.0038	-0.0037	12.9058	57.56	2306	21
traverseA 14	57.99	0.0105	-0.0029	-0.0003	11.3395	58.07	2317	23
traverseA 15	60.04	0.0080	0.0022	0.0001	11.8989	60.00	2360	21
traverseB 1	44.39	0.0075	-0.0088	0.0026	6.6805	43.64	1960	36
traverseB 2	44.50	0.0129	-0.0100	-0.0005	11.3514	44.64	1987	22
traverseB 4	47.09	0.0107	-0.0066	0.0028	12.4096	46.26	2030	20
traverseB 5	48.53	0.0085	-0.0024	-0.0008	12.9177	48.75	2095	19
traverseB 6	48.31	0.0103	0.0089	0.0006	13.3419	48.13	2079	20
traverseB 7	47.97	0.0091	-0.0014	-0.0001	13.0902	47.99	2075	18
traverseB 8	49.62	0.0116	-0.0018	0.0028	12.6240	48.80	2096	20
traverseB 9	51.71	0.0134	-0.0112	0.0006	12.9969	51.53	2164	18
traverseB 10	51.90	0.0108	-0.0059	0.0010	13.1368	51.62	2166	18
traverseB 11	55.14	0.0150	-0.0015	-0.0001	11.6078	55.17	2251	20
traverseB 12	62.87	0.0175	0.0027	0.0256	12.1112	55.31	2254	19
traverseB 13	56.28	0.0090	-0.0007	0.0091	11.7616	53.58	2214	19
traverseB 14	56.82	0.0107	0.0027	0.0006	13.7568	56.65	2285	16
traverseB 15	56.01	0.0128	-0.0006	0.0022	13.6076	55.35	2255	17
traverseB 16	73.54	0.0213	0.0000	0.0560	12.1205	57.00	2293	18
traverseB 17	58.66	0.0101	-0.0051	0.0087	12.3257	56.09	2272	18
traverseB 18	59.72	0.0163	0.0033	0.0061	12.4235	57.93	2314	18
traverseB 19	58.91	0.0111	0.0017	0.0052	11.1603	57.38	2302	19

Sample/ Run	$^{40}Ar/^{39}Ar$	$^{38}Ar/^{39}Ar$	$^{37}Ar/^{39}Ar$	$^{36}Ar/^{39}Ar$	Total ^{39}Ar (cc)x10^{-12}	$^{40}Ar^*/^{39}Ar$	Age (Ma)	±
SS40								
100sq #1	59.98	0.0078	0.0022	0.0006	11.2662	59.81	2412	14
100sq #2	59.31	0.0133	0.0058	0.0032	12.0897	58.38	2380	13
100sq #3	57.31	0.0110	0.0066	0.0008	13.2912	57.06	2350	14
100sq #4	77.74	0.0093	0.0097	0.0008	13.3002	77.49	2768	12
100sq #5	58.32	0.0109	0.0023	0.0020	15.2492	57.73	2365	12
100sq #6	61.50	0.0134	0.0021	0.0010	12.7506	61.21	2443	10
traverseA 1	48.88	0.0122	0.0043	0.0048	7.9632	47.46	2114	21
traverseA 2	54.92	0.0130	0.0105	0.0014	10.9467	54.50	2290	16
traverseA 3	60.02	0.0131	-0.0049	0.0006	10.5237	59.83	2412	15
traverseA 4	60.18	0.0100	-0.0010	-0.0006	10.6047	60.37	2424	15
traverseA 5	62.70	0.0098	0.0048	-0.0002	9.8847	62.76	2476	16
traverseA 6	59.33	0.0087	-0.0002	-0.0002	10.1232	59.40	2403	16
traverseA 7	60.25	0.0117	0.0067	0.0034	9.8172	59.23	2399	16
traverseA 8	58.64	0.0071	0.0103	0.0002	9.8352	58.57	2384	17
traverseB 1	34.52	0.0104	0.0032	0.0019	10.6227	33.96	1719	21
traverseB 2	45.60	0.0121	-0.0019	0.0002	10.2897	45.53	2062	17
traverseB 3	51.16	0.0099	0.0007	0.0015	10.2627	50.70	2197	17
traverseB 5	52.43	0.0159	0.0047	0.0018	11.1942	51.89	2227	16
traverseB 6	55.20	0.0118	0.0025	0.0024	10.1682	54.48	2289	15
traverseB 7	54.67	0.0116	0.0023	0.0017	9.1602	54.16	2282	18
traverseB 8	56.36	0.0107	-0.0075	0.0003	8.6427	56.28	2331	18
traverseB 9	57.11	0.0147	-0.0087	-0.0008	8.4402	57.35	2356	17
traverseC 1	47.04	0.0113	-0.0087	0.0018	7.6140	46.52	2089	22
traverseC 2	55.57	0.0104	0.0080	0.0006	7.4205	55.39	2311	19
traverseC 3	57.26	0.0092	0.0006	0.0005	8.3925	57.10	2350	16
traverseC 4	57.65	0.0096	0.0027	-0.0011	8.5275	57.96	2370	18
traverseC 5	60.09	0.0137	0.0008	0.0048	12.1770	58.67	2386	12
traverseC 6	59.72	0.0082	-0.0020	0.0038	8.3655	58.61	2385	17
traverseC 7	57.69	0.0132	-0.0014	0.0000	9.2385	57.69	2364	16
traverseC 8	57.12	0.0070	-0.0083	0.0000	9.1350	57.12	2351	17

Sample/ Run	$^{40}Ar/^{39}Ar$	$^{38}Ar/^{39}Ar$	$^{37}Ar/^{39}Ar$	$^{36}Ar/^{39}Ar$	Total ^{39}Ar (cc)x10^{-12}	$^{40}Ar^*/^{39}Ar$	Age (Ma)	±
SS37								
100sq #1	58.95	0.0120	-0.0056	0.0017	13.0031	58.45	2381	12
100sq #2	102.65	0.0333	0.0021	0.1350	12.9938	62.75	2476	14
100sq #3	63.12	0.0155	0.0005	0.0004	9.8146	63.00	2481	14
100sq #4	60.23	0.0137	0.0044	0.0007	12.4344	60.03	2417	13
100sq #5	60.68	0.0143	-0.0038	-0.0001	9.6608	60.70	2431	15
100sq #7	61.21	0.0123	-0.0061	0.0015	14.2562	60.76	2433	11
100sq #8	58.76	0.0112	0.0025	0.0014	12.3636	58.36	2379	10
traverseA 1	43.61	0.0112	0.0010	-0.0007	13.6045	43.82	2016	13
traverseA 2	52.02	0.0087	0.0043	-0.0007	13.7956	52.22	2235	13
traverseA 3	56.26	0.0103	-0.0038	0.0003	14.2571	56.18	2329	11
traverseA 4	58.37	0.0090	0.0007	-0.0004	13.3574	58.48	2382	11
traverseA 5	59.04	0.0103	-0.0013	0.0003	13.8655	58.95	2393	19
traverseA 6	60.06	0.0121	0.0014	0.0010	13.3527	59.77	2411	12
traverseA 7	58.92	0.0124	0.0016	-0.0016	14.1685	59.41	2403	11
traverseA 8	59.70	0.0120	0.0026	-0.0010	13.8142	60.00	2416	12
traverseA 9	60.42	0.0082	-0.0012	0.0016	11.5296	59.96	2415	11
traverseA 10	61.17	0.0132	-0.0074	0.0000	11.0075	61.17	2442	12
traverseA 11	60.54	0.0125	-0.0059	-0.0012	11.5856	60.89	2436	11
traverseB 1	63.88	0.0129	0.0010	0.0159	8.7606	59.18	2398	15
traverseB 2	58.56	0.0126	-0.0152	-0.0024	7.4834	59.27	2400	15
traverseB 3	60.66	0.0072	0.0025	0.0000	7.3389	60.66	2431	15
traverseC a1	42.43	0.0022	0.0650	-0.0343	1.0504	52.56	2243	103
traverseC 1a	50.44	0.0118	-0.0008	-0.0004	10.7651	50.56	2193	12
traverseC 2	57.16	0.0087	-0.0106	0.0004	10.2710	57.03	2349	12
traverseC 3	59.75	0.0144	0.0121	0.0009	9.7908	59.48	2404	14
traverseC 4	59.18	0.0087	-0.0056	0.0005	9.7722	59.04	2395	12
traverseC 5	61.44	0.0111	-0.0106	0.0027	7.8652	60.63	2430	14
traverseC 6	58.99	0.0126	-0.0074	0.0007	10.6202	58.77	2388	11

Sample/ Run	$^{40}Ar/^{39}Ar$	$^{38}Ar/^{39}Ar$	$^{37}Ar/^{39}Ar$	$^{36}Ar/^{39}Ar$	Total ^{39}Ar (cc)x10^{-12}	$^{40}Ar^*/^{39}Ar$	Age (Ma)	±
SS31								
Grain 1								
100sq #1	59.82	0.0156	-0.0044	0.0031	13.5887	58.91	2336	13
100sq #2	60.90	0.0117	-0.0016	-0.0003	11.7987	60.98	2382	14
traverseA 1	45.65	0.0127	-0.0035	-0.0002	13.1039	45.72	2016	15
traverseA 2	50.76	0.0120	-0.0001	0.0012	12.3534	50.40	2136	15
traverseA 3	51.71	0.0113	0.0003	-0.0009	13.8451	51.97	2175	13
traverseA 4	53.37	0.0097	-0.0050	-0.0009	13.7472	53.63	2215	13
traverseA 5	56.58	0.0099	-0.0012	-0.0006	12.1716	56.76	2288	14
traverseA 6	58.09	0.0102	-0.0021	-0.0009	13.1086	58.36	2324	14
traverseA 7	57.26	0.0075	0.0024	-0.0028	9.1976	58.09	2318	18
traverseA 8	55.92	0.0111	0.0041	0.0005	10.8477	55.76	2265	17
traverseA 9	57.96	0.0102	0.0024	0.0013	11.2719	57.58	2306	15
traverseA 10	58.16	0.0135	0.0003	0.0005	11.9898	58.01	2316	14
traverseA 11	60.25	0.0090	0.0023	0.0001	11.7614	60.22	2365	14
Grain 2								
100sq #1	58.65	0.0098	-0.0033	0.0037	20.7536	57.54	2306	10
100sq #2	59.98	0.0107	0.0014	0.0028	21.5088	59.16	2342	10
100sq #3	60.34	0.0093	0.0004	0.0039	19.8492	59.19	2342	11
traverseB 1	55.97	0.0117	-0.0035	0.0257	6.7083	48.38	2086	26
traverseB 2	52.09	0.0131	-0.0029	0.0126	17.3087	48.38	2085	13
traverseB 3	67.49	0.0172	-0.0016	0.0524	17.2061	52.01	2176	12
traverseB 4	89.15	0.0282	0.0063	0.1096	19.4297	56.76	2288	11
traverseC 1	43.93	0.0116	-0.0004	0.0010	23.1030	43.63	1960	10
traverseC 2	50.32	0.0110	0.0047	0.0011	21.0240	49.99	2126	10
traverseC 3	54.14	0.0113	0.0029	-0.0001	21.5880	54.18	2228	10
traverseC 4	55.90	0.0121	0.0014	0.0008	22.9538	55.65	2262	10
traverseC 5	56.44	0.0083	0.0098	-0.0007	16.6094	56.65	2285	13
traverseC 6	57.64	0.0114	0.0050	-0.0011	15.3555	57.96	2315	12
traverseC 7	57.32	0.0133	0.0002	0.0017	16.6794	56.82	2289	12
traverseC 8	55.12	0.0105	0.0023	0.0012	15.8310	54.76	2242	12
traverseC 9	54.92	0.0119	0.0061	0.0007	14.7961	54.72	2241	13
traverseC 10	54.85	0.0133	0.0052	0.0007	14.6236	54.64	2239	13

Sample/ Run	$^{40}Ar/^{39}Ar$	$^{38}Ar/^{39}Ar$	$^{37}Ar/^{39}Ar$	$^{36}Ar/^{39}Ar$	Total ^{39}Ar (cc)x10^{-12}	$^{40}Ar^*/^{39}Ar$	Age (Ma)	±
SS22								
100sq #1	77.86	0.0193	-0.0025	0.0544	10.5431	61.79	2399	11
100sq #2	61.14	0.0085	0.0014	-0.0007	10.4405	61.35	2390	11
100sq #3	60.71	0.0097	0.0023	-0.0007	10.0816	60.92	2380	11
100sq #4	60.95	0.0112	0.0079	-0.0019	8.7204	61.50	2393	13
100sq #5	60.03	0.0116	-0.0065	-0.0027	7.6203	60.83	2379	13
traverseA 1	60.71	0.0057	-0.0148	-0.0166	1.7886	65.62	2480	46
traverseA 2	62.00	0.0074	-0.0179	0.0054	1.9844	60.39	2369	47
traverseA 3	62.42	0.0104	-0.0087	0.0027	4.0728	61.64	2396	23
traverseB 1	63.12	0.0096	-0.0020	0.0012	12.9997	62.77	2420	9
traverseB 2	60.09	0.0110	0.0004	0.0020	12.2306	59.50	2349	11
traverseB 3	61.29	0.0154	-0.0060	0.0035	12.0627	60.25	2366	10
traverseB 4	61.86	0.0126	-0.0018	-0.0017	12.1327	62.37	2412	11
traverseB 5	60.72	0.0134	0.0008	-0.0006	12.4030	60.89	2380	10
traverseB 6	62.66	0.0098	0.0001	0.0013	11.3402	62.27	2409	11
traverseB 7	62.67	0.0097	-0.0007	0.0002	11.9695	62.62	2417	10
traverseB 8	61.25	0.0109	-0.0015	0.0005	11.5034	61.09	2384	10
traverseB 9	61.83	0.0109	0.0001	0.0005	12.3657	61.68	2397	10
traverseB 10	61.28	0.0114	-0.0022	-0.0013	12.2399	61.67	2397	10
traverseC 1	61.97	0.0176	-0.0011	0.0015	4.0919	61.51	2393	13
traverseC 2	63.03	0.0087	-0.0063	0.0034	7.1825	62.03	2404	11
traverseC 3	60.78	0.0130	0.0006	-0.0009	7.9843	61.04	2383	8
traverseC 4	61.19	0.0077	-0.0063	0.0023	8.7022	60.51	2372	8
traverseC 5	63.58	0.0108	0.0006	0.0002	7.5415	63.51	2436	11
traverseC 6	59.07	0.0104	0.0006	0.0002	7.3504	58.99	2338	10
traverseC 7	62.10	0.0133	0.0000	-0.0021	7.8398	62.71	2419	9
traverseC 8	61.93	0.0121	0.0018	0.0008	7.4343	61.68	2397	8

Sample/ Run	$^{40}Ar/^{39}Ar$	$^{38}Ar/^{39}Ar$	$^{37}Ar/^{39}Ar$	$^{36}Ar/^{39}Ar$	Total ^{39}Ar (cc)x10^{-12}	$^{40}Ar^*/^{39}Ar$	Age (Ma)	±
93-276								
100sq#1	74.17	0.0190	0.0008	0.0366	14.5436	63.35	2489	10
100sq#2	74.27	0.0192	0.0024	0.0452	16.5574	60.91	2436	8
100sq#3	87.20	0.0307	-0.0024	0.0917	14.1008	60.10	2418	13
100sq#4	67.24	0.0120	-0.0059	0.0195	15.7837	61.49	2449	8
100sq#5	64.49	0.0120	-0.0001	0.0131	14.5623	60.63	2430	8
traverseA 1	60.87	0.0214	0.0078	0.0069	1.5099	58.84	2390	49
traverseA 2	58.51	0.0131	-0.0017	0.0007	14.7627	58.30	2378	9
traverseA 3	58.68	0.0099	0.0027	0.0015	12.5904	58.22	2376	10
traverseA 4	60.80	0.0091	0.0038	0.0067	11.6255	58.82	2390	10
traverseA 5	62.12	0.0111	0.0039	-0.0003	11.2479	62.21	2464	10
traverseA 6	60.28	0.0128	0.0027	0.0032	13.0100	59.33	2401	11
traverseA 7	61.41	0.0113	0.0090	0.0020	13.8956	60.81	2434	9
traverseA 8	61.01	0.0130	0.0071	0.0009	11.3038	60.74	2432	10
traverseA 9	68.15	0.0157	-0.0105	0.0299	11.4811	59.31	2401	10
traverseA 10	59.45	0.0137	0.0053	0.0024	11.7327	58.74	2388	10
traverseA 11	61.05	0.0148	0.0034	0.0021	11.5509	60.44	2426	16
traverseA 12	59.48	0.0133	0.0036	0.0031	12.1009	58.57	2384	10
traverseB 1	62.43	0.0134	0.0019	0.0121	9.4925	58.86	2390	15
traverseB 2	63.30	0.0112	0.0073	0.0125	10.5879	59.60	2407	15
traverseB 3	89.36	0.0271	0.0190	0.0986	6.2293	60.22	2421	20
traverseB 4	68.21	0.0157	0.0121	0.0349	6.3785	57.89	2369	18
traverseB 5	61.74	0.0119	0.0113	0.0148	6.8400	57.37	2357	17
traverseB 6	61.01	0.0159	0.0102	0.0118	6.2667	57.51	2360	19
traverseB 7	60.02	0.0076	0.0103	0.0137	7.0451	55.96	2324	17
96-81	**Grain 2**							
100sq#1	62.75	0.0122	0.0007	0.0049	14.0049	61.32	2445	11
100sq#2	61.40	0.0107	0.0003	0.0040	16.8671	60.21	2421	10
100sq#3	77.13	0.0171	0.0035	0.0554	16.7412	60.76	2433	10
100sq#4	61.16	0.0112	-0.0028	0.0011	16.4709	60.83	2434	10
traverseA 1	58.12	0.0114	0.0155	0.0099	3.2227	55.18	2306	41
traverseA 2	59.83	0.0121	0.0015	0.0075	6.0942	57.62	2362	21
traverseA 3	62.73	0.0106	0.0044	0.0139	5.2178	58.63	2385	24
traverseA 4	61.81	0.0142	0.0053	0.0105	9.4412	58.70	2387	15
traverseA 5	67.63	0.0129	0.0011	0.0216	16.0420	61.24	2443	12
traverseA 6	62.36	0.0110	-0.0026	0.0009	10.5041	62.09	2462	13

Sample/ Run	$^{40}Ar/^{39}Ar$	$^{38}Ar/^{39}Ar$	$^{37}Ar/^{39}Ar$	$^{36}Ar/^{39}Ar$	Total ^{39}Ar (cc)x10^{-12}	$^{40}Ar^*/^{39}Ar$	Age (Ma)	±
96-81								
Grain 2								
100sq#1	62.61	0.0130	0.0017	0.0083	19.1233	60.17	2420	9
100sq#2	60.38	0.0099	0.0050	0.0012	19.9623	60.04	2417	9
100sq#3	59.63	0.0091	0.0019	0.0017	21.3748	59.12	2396	9
traverseA#1	47.56	0.0123	0.0073	0.0037	3.7494	46.46	2087	39
traverseA#2	47.72	0.0181	0.0458	0.0160	2.2857	43.01	1993	64
SS35b								
50 μm sq 1	180.88	0.0877	0.0105	0.4063	10.3044	60.83	2435	26
traverseA 1	34.41	0.0147	-0.0291	0.0047	2.2212	33.03	1689	163
traverseA 2	48.69	0.0140	0.0011	0.0012	15.5114	48.33	2137	19
traverseA 3	52.89	0.0129	0.0029	0.0011	16.8306	52.55	2243	20
traverseA 4	56.82	0.0107	0.0052	0.0013	14.6956	56.43	2335	19
traverseA 5	55.53	0.0135	0.0011	-0.0005	15.3622	55.67	2318	18
traverseA 6	55.78	0.0131	0.0008	0.0010	15.4881	55.50	2314	18
traverseA 7	54.47	0.0136	0.0008	0.0006	10.5048	54.30	2285	26
traverseA 8	55.22	0.0147	0.0014	0.0030	12.6119	54.34	2286	22
traverseA 9	62.45	0.0138	0.0023	0.0228	11.7262	55.72	2319	23
traverseA 10	65.62	0.0122	0.0005	0.0212	9.2385	59.36	2402	16
traverseA 11	72.98	0.0197	0.0039	0.0530	10.4038	57.32	2356	15
traverseB 1	35.04	0.0095	0.0011	0.0002	12.8232	34.99	1753	15
traverseB 2	51.16	0.0083	0.0058	-0.0034	8.5905	52.16	2234	17
traverseB 3	57.71	0.0069	0.0049	-0.0008	8.3201	57.95	2370	17
traverseB 4	57.63	0.0068	-0.0053	-0.0003	8.5159	57.71	2365	17
traverseB 5	58.37	0.0106	0.0075	0.0012	9.7792	58.03	2372	15
traverseB 6	55.63	0.0111	0.0070	-0.0002	9.7839	55.70	2318	15
traverseB 7	55.97	0.0100	0.0084	-0.0011	10.3386	56.29	2332	16
traverseB 8	58.50	0.0138	0.0039	-0.0002	11.5506	58.56	2384	13
traverseB 9	58.11	0.0126	0.0076	-0.0002	10.7628	58.18	2376	13
traverseB 10	59.13	0.0135	0.0084	0.0025	9.7093	58.38	2380	17

Sample/ Run	$^{40}Ar/^{39}Ar$	$^{38}Ar/^{39}Ar$	$^{37}Ar/^{39}Ar$	$^{36}Ar/^{39}Ar$	Total ^{39}Ar (cc)x10^{-12}	$^{40}Ar^*/^{39}Ar$	Age (Ma)	±
SS89								
100sq no.1	340.76	0.0130	-0.0052	0.0028	1.4224	339.94	2666	22
100sq no.2	304.96	0.0103	-0.0041	-0.0028	1.7860	305.79	2520	21
100sq no.3	339.86	0.0242	-0.0079	-0.0033	1.5203	340.84	2669	21
100sq no.4	332.76	0.0215	0.0032	0.0253	1.9305	325.27	2605	19
100sq no.5	329.50	0.0078	0.0087	0.0175	1.7626	324.31	2601	17
traverseA 1	255.16	-0.0072	-0.0781	-0.0198	1.0076	261.00	2309	25
traverseA 2	289.47	0.0106	-0.0315	-0.0061	1.0542	291.27	2454	27
traverseA 3	284.41	0.0102	-0.0219	-0.0058	1.1008	286.13	2431	21
traverseA 4	286.80	-0.0020	-0.0292	-0.0050	1.2919	288.27	2441	18
traverseA 5	324.38	-0.0022	0.0479	-0.0091	1.2080	327.06	2612	21
traverseA 6	304.22	0.0015	-0.0010	-0.0014	1.3572	304.64	2515	18
traverseA 7	296.52	0.0188	-0.0078	-0.0048	1.3339	297.94	2485	17
traverseA 8	297.27	0.0147	0.0023	0.0018	1.3898	296.72	2479	21
traverseA 9	340.01	0.0341	-0.0225	0.1469	1.2733	296.60	2479	23
traverseA 10	272.01	0.0118	-0.0010	0.0053	1.3432	270.45	2356	22
traverseA 11	314.38	0.0064	0.0297	-0.0062	1.0309	316.22	2566	23
traverseA 12	308.44	0.0110	-0.0326	0.0070	1.0169	306.39	2523	25

Sample/ Run	$^{40}Ar/^{39}Ar$	$^{38}Ar/^{39}Ar$	$^{37}Ar/^{39}Ar$	$^{36}Ar/^{39}Ar$	Total ^{39}Ar (cc)x10^{-12}	$^{40}Ar^*/^{39}Ar$	Age (Ma)	±
SS50a								
100sq. no.1	283.91	0.0055	-0.0697	-0.0555	0.7235	300.32	2496	44
100sq. no.2	459.06	0.0356	-0.0222	-0.0424	0.6303	471.58	3138	38
100sq. no.3	311.69	0.0046	-0.0419	-0.0150	0.8773	316.14	2565	36
100sq. no.4	302.97	0.0178	0.1132	-0.0042	1.0031	304.22	2513	43
100sq. no.5	315.20	-0.0103	-0.0098	-0.0185	0.9566	320.67	2585	33
traverseA 1	305.47	0.0381	0.0045	0.0145	0.9519	301.19	2500	34
traverseA 2	341.90	0.0603	0.0470	-0.0082	1.0591	344.33	2684	36
traverseA 3	427.17	0.0091	0.1199	-0.0235	0.9472	434.10	3015	38
traverseB 1	265.62	0.0075	0.0709	0.0002	1.1523	265.55	2332	32
traverseB 2	283.65	0.0191	0.0385	0.0194	1.1756	277.92	2392	28
traverseB 3	268.63	0.0033	0.0567	0.0002	1.1989	268.56	2347	29
traverseB 4	291.68	0.0153	0.0349	-0.0152	1.1663	296.17	2477	29
traverseB 5	268.19	0.0067	0.0033	0.0002	1.2875	268.12	2345	29
traverseB 6	264.67	-0.0078	0.0034	-0.0140	1.2642	268.81	2348	27
traverseB 7	276.74	-0.0007	0.0479	-0.0156	0.8493	281.34	2408	40
traverseB 8	291.06	-0.0113	0.0259	-0.0152	0.8680	295.56	2474	37
traverseB 9	294.37	0.0200	0.1632	-0.0098	0.8912	297.27	2482	34
traverseB 10	273.11	0.0087	-0.0049	0.0003	0.9845	273.02	2368	41
traverseB 11	296.20	0.0252	0.0201	0.0104	0.8913	293.12	2463	37
traverseB 12	254.24	0.0040	0.0358	-0.0131	1.0078	258.11	2295	34
traverseB 13	296.49	0.0070	0.0219	-0.0144	1.2316	300.74	2498	47
traverseB 14	318.50	0.0270	0.0837	0.1445	1.6837	275.80	2382	22
traverseB 15	286.35	0.0285	0.0361	-0.0101	1.7583	289.33	2446	23
traverseB 16	278.15	-0.0003	0.0536	-0.0024	1.7769	278.86	2396	20
traverseB 17	285.52	-0.0004	0.0341	-0.0024	1.7257	286.24	2431	23

Sample/ Run	$^{40}Ar/^{39}Ar$	$^{38}Ar/^{39}Ar$	$^{37}Ar/^{39}Ar$	$^{36}Ar/^{39}Ar$	Total ^{39}Ar (cc)x10^{-12}	$^{40}Ar^*/^{39}Ar$	Age (Ma)	±
SS55								
100sq no.1	331.06	0.0218	0.0000	0.0133	1.2679	327.12	2612	22
100sq no.2	323.08	0.0062	-0.0304	0.0053	1.4964	321.52	2589	23
100sq no.3	306.70	0.0160	0.0190	0.0055	1.4404	305.09	2517	18
100sq no.4	317.20	0.0000	-0.0493	-0.0038	1.4778	318.32	2575	18
100sq no.5	297.36	-0.0113	-0.0084	-0.0007	1.6316	297.56	2483	19
100sq no.6	331.46	0.0112	-0.0139	0.0075	1.6409	329.23	2621	18
100sq no.7	284.60	0.0114	0.0339	-0.0091	1.6129	287.28	2436	21
traverseA 1	275.65	0.0215	-0.0169	-0.0072	2.3927	277.79	2391	11
traverseA 2	272.11	0.0084	-0.0238	-0.0057	2.2716	273.78	2372	12
traverseA 3	308.70	0.0115	-0.0175	-0.0173	1.2646	313.81	2555	20
traverseA 4	309.99	0.0193	-0.0035	-0.0053	2.4160	311.57	2546	10
traverseA 5	320.98	0.0199	0.0022	-0.0131	2.3508	324.86	2603	11
traverseA 6	298.50	0.0091	0.0055	-0.0067	2.6025	300.47	2496	10
traverseA 7	300.85	0.0071	-0.0031	-0.0048	2.6957	302.26	2504	9
traverseA 8	316.62	0.0075	0.0003	-0.0051	2.5372	318.11	2574	10
traverseA 9	311.20	0.0100	0.0079	-0.0073	2.3741	313.36	2553	12
traverseA 10	307.49	0.0143	-0.0037	-0.0036	2.2948	308.57	2532	13
traverseA 11	306.36	0.0123	0.0320	0.0061	2.2994	304.55	2515	12
traverseA 12	309.99	0.0146	0.0427	-0.0077	2.2528	312.27	2549	13
traverseA 13	302.72	0.0166	0.0224	-0.0097	2.2622	305.57	2519	17
traverseA 14	299.52	0.0182	0.0224	-0.0041	2.0664	300.72	2497	16
traverseA 15	302.30	-0.0071	-0.0792	-0.0214	1.0794	308.63	2533	29
SS60								
100sqno.1	331.66	0.0268	-0.0212	0.0255	1.3076	324.13	2600	49
100sqno.2	310.94	0.0419	0.0088	0.0133	1.4940	307.02	2526	42
100sqno.3	305.77	0.0146	0.0089	0.0104	2.7014	302.70	2506	15
100sqno.4	313.59	0.0054	-0.0100	0.0194	3.0743	307.86	2529	15
100sqno.5	323.97	0.0117	-0.0051	0.0297	3.3727	315.20	2561	15
100sqno.6	340.92	0.0128	-0.0432	0.0238	3.4520	333.89	2641	13
100sqno. 7	314.36	0.0124	-0.0093	0.0020	2.8133	313.77	2555	14
100sqno. 8	314.83	0.0111	-0.0046	0.0070	2.7387	312.76	2551	16

Sample/ Run	$^{40}Ar/^{39}Ar$	$^{38}Ar/^{39}Ar$	$^{37}Ar/^{39}Ar$	$^{36}Ar/^{39}Ar$	Total ^{39}Ar (cc)x10^{-12}	$^{40}Ar^*/^{39}Ar$	Age (Ma)	±
SS60								
traverseA 1	271.32	-0.0826	0.0198	-0.0165	0.7482	276.20	2384	43
traverseA 2	280.75	0.0159	-0.0084	0.0077	3.6477	278.47	2395	12
traverseA 3	299.10	0.0170	0.0053	-0.0008	4.5054	299.32	2491	11
traverseA 4	296.15	0.0112	-0.0084	-0.0025	3.1070	296.90	2480	16
traverseA 5	279.43	0.0052	-0.0301	0.0025	4.0533	278.69	2396	11
traverseA 6	292.02	0.0068	0.0111	0.0157	3.7875	287.37	2436	18
traverseA 7	292.81	0.0084	0.0211	0.0133	4.1511	288.89	2443	12
traverseA 8	301.40	0.0051	0.0443	0.0102	3.2094	298.40	2487	16
traverseA 9	317.21	0.0055	-0.0228	-0.0162	2.1467	322.01	2591	22
traverseA 10	292.76	0.0220	-0.0013	0.0055	2.6361	291.12	2454	15
traverseA 11	314.57	0.0258	-0.0056	0.0025	2.2446	313.83	2555	18
traverseA 12	297.12	0.0138	0.0296	-0.0036	2.1932	298.18	2486	16
traverseA 13	304.04	0.0174	0.0245	0.0104	2.2725	300.97	2499	16
traverseA 14	305.98	-0.0009	0.0743	-0.0162	2.1605	310.76	2542	19
traverseA 15	299.32	0.0274	0.0264	0.0123	2.2818	295.68	2475	18
SS45								
100sq no.1	323.01	0.0203	-0.0413	0.0272	0.5194	314.96	2560	35
100sq no.2	294.83	0.0016	-0.0494	0.0008	0.8038	294.59	2470	19
100sq no.3	311.66	-0.0040	-0.0039	-0.0371	0.8318	322.63	2593	22
100sq no.4	318.41	0.0228	0.0963	0.0007	0.8643	318.20	2574	22
100sq no.5	305.19	-0.0092	0.0121	0.0479	0.8597	291.05	2453	29
traverseA 1	306.91	-0.0093	0.0231	-0.0205	0.8457	312.97	2552	22
traverseA 2	322.94	0.0397	0.0771	-0.0181	0.9622	328.28	2617	20
traverseA 3	330.45	0.0142	-0.0030	0.0048	1.0695	329.03	2620	27
traverseA 4i	344.50	0.0107	-0.0637	0.0236	0.9810	337.52	2656	35
traverseA 5	356.24	0.0015	0.0432	-0.0096	0.8737	359.07	2742	21
traverseA 6	314.10	0.0055	0.0139	0.0173	1.0788	309.00	2534	22
traverseA 7	354.67	0.0109	-0.0222	0.0007	0.9670	354.47	2724	20
traverseA 8	302.56	0.0139	-0.0487	0.0060	0.7482	300.78	2498	22
traverseA 9	313.43	0.0127	-0.0280	0.0055	0.8135	311.79	2547	23
traverseB 1	277.43	0.0362	-0.0260	0.0214	1.0512	271.10	2359	22
traverseB 2	274.95	0.0124	-0.0038	-0.0112	1.2050	278.26	2394	24
traverseB 3	324.21	0.0100	0.0000	-0.0087	1.0372	326.77	2611	19
traverseB 4	308.85	0.0049	-0.0155	-0.0115	1.1771	312.24	2549	17
traverseB 5	313.40	0.0334	-0.0546	0.0000	0.9999	313.40	2554	19
traverseB 6	325.33	0.0012	-0.0370	0.0137	0.9859	321.28	2588	19